Coded-OFDM based Massive MIMO communications

Ditsapon Chumchewkul

Thesis submitted for the degree of
Doctor of Philosophy

School of Engineering
Newcastle University
Newcastle upon Tyne
United Kingdom

November 2023

Acknowledgements

I've very proud to study in Newcastle University, School of Engineering, Intelligent Sensing and Communications Group from 2019 to 2023, and complete this thesis. This achievement would not have been possible without support from several people and organizations. Therefore, I would like to utilize this section to express my gratitude to them.

First of all, I would like to thank my supervisors, Prof.Dr.Charalampos Tsimenidis and Prof.Jeffrey Neasham, expert researchers in digital communication and signal processing. They dedicated their time to support me during the past years. Moreover, I received constructive suggestions from the panel, Dr.Martin Johnston and Prof.Nick Wright. The information motivated me to conduct the research work in this thesis. In addition, my family, colleague, and friends from Thailand and other countries always assisted me during the past 4 years. I will never forget it and would like to utilize this space to thank you all.

My education and research work in the United Kingdom were supported by the scholarship ST G 5671 from Thailand's National Science and Technology Development Agency, and the EPSRC under project EP/R002665/1, Full-Duplex For Underwater Acoustic Communications. I additionally received kindness from the office of the civil service commission, the office of educational affairs, the royal Thai embassy, Rajamangala university of technology Rattanakosin, and Newcastle university to organize almost anything for my education. I would like to express my gratitude to them, and I will utilize the knowledge from this PhD programme in a constructive way.

Although conducting research during the Covid-19 pandemic would be the worst experience in my life, the situation forced me to create parts of this thesis in a small room by using limited resources. It would not possible to live and study during the crisis without excellent suggestions, IT supports, and health care services from graduate school, school of engineering, PGR admin teams, the office of educational affairs, the royal Thai embassy, Newgate court, and national health service in England. I would like to thanks them all for their hard working during the tough times.

Abstract

This thesis aims to analyze the performance of the maximal-ratio combining (MRC) and zero-forcing (ZF) detections in the orthogonal frequency-division multiplexing (OFDM) based massive multiple-input, multiple-output (MMIMO) system over the frequency-selective Rayleigh fading channel. Binary and quadrature phase shift keying (BPSK, QPSK), and M-ary quadrature amplitude modulation (QAM) schemes are focused by this research work. The mathematical expression of the co-channel interference (CCI) and effective noise (EN) for MRC detection is derived, and is chosen to analyze the probability distribution function (PDF) of the CCI and EN, bit error probability (BEP), PDF of signal-to-interference-plus-noise ratio (SINR), and outage probability of the output SINR. Furthermore, by assuming that the diagonal components of the Gram matrix approaches a constant, this thesis proves that the PDF of the CCI and EN for BPSK and QPSK modulation tends to the Gaussian distribution, whereas the PDF for M-QAM approaches the combination of scaled Gaussian distribution, i.e., the Gaussian mixture model (GMM). Thus, the analysis for the performance metrics is then simplified by utilizing the approximate PDFs. Monte-Carlo simulation results confirm that the outcome from the derived equation and the approximation closely matched those obtained by simulation.

Moreover, there are deviations between the Gaussian distribution and the exact PDF of the CCI and EN, especially in a higher E_b/N_0 region. Thus, an enhanced soft-output MRC detection is proposed for the coded-OFDM-MMIMO system. The detector utilizes the derived PDF of CCI and EN instead of the conventional Gaussian distribution to produce soft-information in forms of the log-likelihood ratio (LLR) for iterative decoders. Newton's method is additionally chosen to simplify the computation for the LLRs. According to the numerical results, the proposed detector provided a better bit error rate (BER) performance than that of the classical, low-complexity, soft-output detections, especially at a higher E_b/N_0 region.

Likewise, the performance metrics for the OFDM-MMIMO system, utilizing ZF detection, are derived in this thesis. The PDF of the EN and BEP for the detection were previously derived in a research work, thus, this thesis improves the accuracy for the derived equations by increasing the Neumann series expansion (NSE) to second order. The PDF of signal-to-noise ratio (SNR) and the outage probability of output SNR are then derived by employing the derived PDF of the EN. Furthermore, an asymptotic closed-form expression for the EN PDF, in forms of the Gaussian distribution, and the noise variance are derived in this thesis for simplifying the performance analysis.

In addition, the derived noise variance for ZF detection is chosen to estimate the LLR instead of the approximate noise variance for the low-complexity soft-output ZF detection. The requirement for real arithmetic operators of the proposed detection is thus

significantly reduced, whereas its BER is slightly lower than that of the classical detection. Focusing on a 10×200 coded-OFDM-MMIMO system, 97.81% of multiplications, required for producing the LLR from the estimated symbol, were minimized by utilizing the proposed detection. Therefore, the derived equations can be efficiently utilized for reducing the computational complexity of the soft-output ZF detection.

Contents

List of Figures

List of Tables

Nomenclature

APP	A posterior probability
AWGN	Additive white Gaussian noise
BEP	Bit error probability
BER	Bit error rate
BPSK	Binary phase shift-keying
BS	Base station
CCI	Co-channel interference
CDF	Cumulative distribution function
CIR	Channel impulse response
CFR	Channel frequency response
CP	Cyclic prefix
DFT	Discrete Fourier transform
EN	Effective noise
FFT	Fast Fourier transform
GS	Gauss Seidal
GMM	Gaussian mixture model
IBI	Inter-block interference
ICI	Inter-carrier interference
IFFT	Inverse fast Fourier transform
JI	Jacobi iteration
LDPC	Low-density parity-check
LLR	Log-likelihood ratio
MAP	Inter-block interference
MIMO	Multiple-input multiple-output
ML	Maximal likelihood
MMIMO	Massive multiple-input multiple-output
MMSE	Minimum mean-squared error detection
MAP	Maximum a posteriori
MRC	Maximal-ratio combining detection
MT	Mobile terminal
NSE	Neumann series expansion
OFDM	Orthogonal frequency-division multiplexing
OTFS	Orthogonal time frequency space modulation
PDF	Probability distribution function
PDP	Power delay profile
PEP	Pairwise error probability
PIC	Parallel interference cancellation
QAM	Quadrature amplitude modulation
QPSK	Quadrature phase shift keying
SINR	Signal-to-interference-plus-noise ratio
SNR	Signal-to-noise ratio
VN	Variable node
ZF	Zero-forcing detection

Nomenclature (Cont.)

5G	5-th generation
6G	6-th generation

List of Symbols

$\mathbf{d}$	Transmit information bits
$\hat{\mathbf{d}}$	Receive information bits
$\mathbf{D}_f$	Diagonal components of Gram matrix
$\mathbf{E}_f$	Off-diagonal components of Gram matrix
$\mathbf{G}_f$	Gram matrix
$\mathbf{H}_f$	Channel frequency response matrix
$\tilde{\mathbf{H}}_f$	Parity check matrix
$\mathbf{W}_f$	Noise vectors matrix
$\mathbf{X}_f$	Matrix of the transmit symbols in frequency domain
$\mathbf{Y}_f$	Matrix of the receive symbols in frequency domain
$\mathbf{\Psi}$	Matrix of the transmit symbols in time domain
ξ	Matrix of the receive symbols in time domain
$\mathbf{\Lambda}$	Matrix of the log-likelihood ratio
$d_{m,l}^{(f)}$	Component of $\mathbf{d}$
$\hat{d}_{m,l}^{(f)}$	Component of $\hat{\mathbf{d}}$
$D_{n,m}^{(f)}$	Component of $\mathbf{D}_f$
$E_{n,m}^{(f)}$	Component of $\mathbf{E}_f$
E_s	Average symbol energy
E_λ	Average symbol energy per dimension
E_b/N_0	Signal-to-noise ratio per bit
$G_{n,m}^{(f)}$	Component of $\mathbf{G}_f$
$H_{n,m}^{(f)}$	Component of $\mathbf{H}_f$
$h_{n,m,l}$	Channel impulse response
I	Number of iteration
K	Block size
N	Code word size
$X_m^{(f)}$	Component of $\mathbf{X}_f$
$Y_n^{(f)}$	Component of $\mathbf{Y}_f$
$W_n^{(f)}$	Component of $\mathbf{W}_f$
M	Number of constellation points
M_λ	Number of constellation points per dimension
N_{CP}	Number of CP symbols coefficients
N_l	Number of tap coefficients
$N_{\max}$	Maximal delay spread
N_t	Number of the transmit antennas
N_r	Number of the receive antennas
P_e	Bit error probability
P_s	Symbol error probability
R	Coding rate
$Z_m^{(f)}$	CCI and EN of linear symbol detection
$\Lambda_{m,q}^{(f)}$	Component of $\mathbf{\Lambda}$
$\Psi_{m,t}$	Component of $\mathbf{\Psi}$
$\xi_{n,t}$	Component of ξ

Ω	Mean of $D^{(f)}_{m,m}$

List of Symbols (Cont.)

τ	Constant to control power delay profile
γ_b	Signal-to-noise ratio per bit
γ_s	Signal-to-noise ratio per symbol
σ_h^2	Variance per dimension of CIR and CFR
σ_w^2	Variance per dimension of noise vectors
σ_z^2	Variance per dimension of Z_m^λ
$\Lambda_{m,q}$	Log-likelihood ratio
$\Gamma(x)$	Gamma function of x
$\Gamma(x,a)$	Incomplete Gamma function of x
$\delta(x)$	Unit impulse function of x
$p_x(x)$	Probability distribution function of x
$\nabla^n \bar{\Lambda}_{p,q}$	Divided differences
$\Phi_x(\omega)$	Characteristic function of $p_x(x)$
$\mathcal{N}(\bar{x}, \sigma_x^2)$	Gaussian random variable
$\mathcal{CN}(\bar{x}, 2\sigma_x^2)$	Complex-valued, Gaussian random variable
$\mathbb{E}(x)$	Expectation operator
$\Im(x)$	Imaginary part operator
$\Re(x)$	Real part operator
$\wp(x)$	Real or imaginary part operator

Chapter 1

Introduction

During the past years, there is a significant increasing in the global mobile data traffic, and the number was predicted to reach more than 4.39 zettabytes/month in 2030[1]. As a result, the 5-th generation (5G) cellular network has been deployed worldwide to enhance the data transmission rate to 10 Gb/s for the uplink and 20 Gb/s for the downlink. Due to the 5G has been expected to end in 2030, a number of researchers are focusing on the standardization for the 6-th generation (6G) cellular network, and massive multiple-input, multiple-output (MMIMO) has becomes a key to enhance data transmission rate and energy efficiency for 6G[2]. The technique employs multiple antennas for data communication between base station (BS) and mobile terminal (MT). Due to the fact that a very high frequency band is recommended for 5G and 6G, hundreds or thousands antennas can be installed at base station (BS). Focusing on an uplink transmission, multiple MTs transmit messages through the channel over the same time. As a result, the receive signal at the BS is interfered by the co-channel interference (CCI) from other antennas, and the BS requires spatial multiplexing technique to estimate the transmit messages from MTs. Several linear and non-linear multiple-input, multiple-output (MIMO) symbol detections have been developed for decades. However, the number of antennas at the BS is very large and computational complexity for the symbol detection significantly increases according to the size of the channel frequency response (CFR) matrix. As a result, linear symbol detections are recommended for the practical MMIMO system due to the computational complexity for the detection is significantly less than that of the non-linear detection. Moreover, if the number of receive antennas is much larger than that of the transmit antennas, the Gram matrix for the MMIMO system approaches diagonal matrix. As the results, an excellent results can be obtained by utilizing the linear symbol detections[3]. Furthermore, asymptotic inverse matrix operations can be efficiently utilized to reduce the operational complexity of the detection [4] [5].

This thesis discusses the performance of linear symbol detections in orthogonal frequency-division multiplexing (OFDM) based MMIMO system, in terms of the bit error probability (BEP) and the outage probability of the output signal-to-noise ratio (SNR). Maximal-ratio combining (MRC), zero-forcing (ZF), and minimum mean-squared error (MMSE)

are important linear symbol detections, and the performance for the detections in MIMO system was essentially derived by a number of research work. Several approximations were chosen to simplify the analysis in the work. Therefore, the analysis can be theoretically enhanced by employing more accurate calculation. Moreover, the effects of the CCI and the effective noise (EN) in the outcomes of linear symbol detections are generally assumed to be the complex-valued, zero-mean, Gaussian distribution, $\mathcal{CN}(0, 2\sigma_z^2)$. However, as far as the literature survey goes, there is no research work derive a closed-form expression for the probability distribution function (PDF) and noise variance. As the results, the computational complexity of the derived equations significantly increases according to the number of antennas. Thus, a compact closed-form expression for the PDF is still required to simplify the analysis.

1.1 Literature review

The performance analysis of MRC, ZF, and MMSE detections in MIMO system was previously discussed by a number of research work, and the information is now briefly summarized in this section. In addition, channel coding technique is generally chosen for enhancing reliability, and thus, reducing energy requirements for data transmission[6]. Therefore, the research work on soft-output linear symbol detections for the coded-MIMO system is additionally included in the section.

1.1.1 Performance analysis of MRC detection

Although the MRC detection is the least computational complexity linear symbol detector, and is suitable for practical system, the research work on the performance analysis for this type of detector in the multiple-input, multiple-output (MIMO) system is scarce. The PDF of the output signal-to-interference-plus-noise ratio (SINR), BEP, and outage probability of output SINR for MRC detection in Rayleigh flat fading channel were derived in [7]. The analysis was then extended to the MMIMO system over a slow flat Rayleigh fading channel model in [8], where the effects of the channel estimation errors were included in the work. It is worth noting that almost all of the research work in this area assumed that the PDF of the CCI and EN for MRC detection exhibited the Gaussian distribution and utilized the PDF of output SINR to derive the performance of MRC detection in MIMO system. On the contrary, the accurate and asymptotic PDFs of the the CCI and EN of the detection were proposed in [9]. The derived PDFs were then employed to analyze the performance metrics for the MIMO system, and improved the calculation for soft-output MRC detection.

1.1.2 Performance analysis of ZF detection

The ZF detection utilizes Moore-Penrose inverse matrix to estimate the transmit symbols, corresponding to the receive symbols. Although the BEP for the ZF detection is higher than that of the MMSE detection, the computational complexity of the ZF detection is less than that of the MMSE detection since the SNR information is not required by the detector [4]. Furthermore, the difference in BEP of ZF and MMSE detection at a higher SNR region is marginal. Therefore, the performance for the detection was focused by a number of research works. The authors in [10, 11] derived exponential tight bounds on BEP of the data communications, utilizing multiple antennas and optimal combining for flat and frequency-selective Rayleigh fading. The numerical results confirmed that user capacity can be significantly enhanced by increasing the number of the antennas. The BEP of the MIMO system using ZF detection was then analyzed under various fading channels in [12, 13]. The complex Wishart distribution and a derived probability distribution function (PDF) of SNR from [14] were employed to approximate the PDF of the Gram matrix and a closed-form expression for the BEP. The BEP of the system over uncorrelated Rayleigh fading channel was approximated in [15]. The authors assumed that the Gram matrix exhibited a diagonal matrix and utilized the Gaussian approximation to derive the BEP. The performance metrics for the ZF and MMSE detections over uncorrelated flat Rayleigh fading were extensively investigated in [16]. The interference-to-noise ratio and the output SNR at high SNR region were approximated. The equation for the latter was then utilized to derive a tight approximation of the BEP, outage probabilities, diversity-multiplexing gain trade-off for the system. The authors also demonstrated a gap between the performance of MMSE and ZF detection, which cannot be decreased at a higher SNR region. The gap was then rewritten in terms of a Hermitian quadratic form in [17], and the authors employed the equation to derive the PDF of SNR, the symbol error rate and the outage probabilities of the MMIMO system. A BEP analysis for the MIMO system over correlated Rician and Rayleigh fading was derived in [18]. The noncentral Wishart distributed matrix was utilized to approximate the distribution of the Gram matrix, and the authors proved that the PDF of the SNR can be approximated as an infinite linear summation of the Gamma distribution. Channel estimation is generally employed to the receiver to estimate the information, making a deviation between the actual and the estimated information. As a result, the effects of channel estimation errors in ZF detection and the BEP approximation were then investigated by a number of research works. In [19], the authors utilized Taylor expansion to approximate the pseudo-inverse of the channel matrix and employed Gaussian random variable to model the channel estimation errors. The SNR and the BEP for the system using M-PSK and M-QAM were then derived in the work. The authors also demonstrated that the PDF of the SNR exhibits the Chi-square distribution. The BEP analysis was then extended to the MMIMO system and a lower SNR region in [20]. Improved SNR and BEP analysis for M-QAM were introduced in the work. The BEP for MRC, ZF, and MMSE detection in MMIMO system using pilot

symbols to estimate the channel state information was derived in [21]. The average SNR and the BEP were derived in the work.

It is worth noting that the BEP analysis for the MIMO system using ZF detection and BPSK modulation over uncorrelated frequency-flat Rayleigh fading channel at high SNR region was previously proposed in [16]. The BEP for M-QAM and other type of modulation schemes was neglected in the paper, however, the readers can employ the PDF of the derive SNR to derive the BEP using the equations in [22, 23]. Although the outcome from the derived equation significantly matched the exact BEP, the distribution of the effective noise in the work was assumed to be the Gaussian distribution. Therefore, The authors in [24] utilized the Neumann series expansion (NSE) to approximate the inverse matrix operation as the Taylor series, and the effective noise PDF was then derived from the joint probability of the involved random variables. The BEP of the system with Gray-encoded M-QAM was analyzed utilizing the derived PDF. In addition, the pairwise error probability of the system was then determined from the PDF and was used to evaluate the upper-bounds of coded systems.

1.1.3 Performance analysis of MMSE detection

Although the ZF detection provides an excellent BEP performance to the MMIMO system, the effects of thermal noise in the detection are still neglected, making a noise enhancement to the outcome of the detector. Thus, the MMSE detection utilizes an algorithm to estimate the outcome, which is as close to the exact transmit symbol as possible[25]. As the results, the MMSE detection outperforms its BEP performance, compared to other linear symbol detections. During the past decades, research works derived the performance of the MIMO system, utilizing MMSE detection. The asymptotic PDF of SINR of MMSE detection in MIMO system over a correlated and uncorrelated Rayleigh flat-fading channel was derived in [26]. The Gamma distribution was chosen to simplify the analysis, and the BEP was then analyzed by utilizing the derived PDF. The authors in [27] derived the BEP of the MMSE detection in the MIMO system over the fast fading channel. The PDF of SINR for the system was proposed in the work, and employed to approximate the BEP for M-QAM in terms of the Q-function. The inter-carrier interference (ICI), caused by phase noise and channel estimation errors, in the OFDM-MIMO system degrades the performance of the OFDM-MIMO system. Thus, the SINR degradation in the system was derived in [28]. The achievable sum rate of the MMSE detection in the MIMO system was derived in [29]. The asymptotic analysis for a higher and lower SNR region was additionally included in the work. The performance of ZF and MMSE detection for a higher SNR region was essentially derived in [16]. The authors utilized the derived PDF of SNR for the detections to derive the BEP, outage probability, and diversity-multiplexing gain trade-off for the system. The effects of the channel estimation errors in the MIMO system, utilizing MMSE detection, was analyzed in [30]. The zero-mean circularly symmetric complex Gaussian random variables was chosen to represent the

errors from the channel estimator, and the authors derived the mathematical expression for the SNR and the BEP for BPSK modulation. Recently, the asymptotic performance analysis of MMSE detection in the MMIMO system was proposed in [31]. The SINR for the MMSE detection was rewritten as a combination of the SNR for ZF detection and a random variable. The asymptotic SINR, capacity, and the BEP for the MMSE detection were then derived from the equation.

1.1.4 Soft-output linear symbol detection

Despite the MMIMO system, channel coding is another important technique for improving reliability, and thus, reducing energy requirements for data transmission. Low-density parity-check (LDPC)[32][33] and turbo codes [34] are widely applied to wireless networks due to huge coding gain can be achieved by utilizing these channel coding techniques. The channel coding schemes significantly reduce the energy requirements in MMIMO systems. However, soft-information in forms of log-likelihood ratio (LLR) is generally required for iterative decoders, making a significantly increasing in computational complexity to the detector. As a result, a number of research works aims to reduce the computational complexity of soft-output linear detection in MMIMO system. Fang et. al., in [35], employed Neumann series approximation to reduce the complexity of inverse matrix operation in minimum mean square error-parallel interference cancellation (MMSE-PIC) detection. The complexity of the detector was significantly minimized by employing the approximate inverse matrix operation. A low-complexity joint iterative detection and decoding for MMSE detection was introduced in [36]. The Gram matrix was assumed to be a diagonal matrix, and an approximate equation for the detection was then proposed for the detector. An inversion-less MMSE detection was also introduced by the authors. The proposed detection outperformed conventional detection in terms of computational complexity and bit error rate (BER) performance. A technique to reduce the operation of soft-symbol estimation in soft-interference cancellation and MMSE detection was introduced in [37]. The authors utilized a polynomial to approximate the output of hyperbolic tangent function, and a simple mathematical operation was then applied to determine the product of the hyperbolic tangent functions. The use of this proposed technique decreased the number of multiplications in the detection without reducing their BER performance. Recently, a semi-iterative symbol detection method was proposed, in [38], to approximate the operation of MMSE detection. The authors utilized the Richardson approach in the detection to enhance the convergence rate along with an approximation. Simulation results confirmed that the proposed technique provides improved performance compared to classical iterative detection, and requires less number of iterations.

1.2 Research contributions

According to the literature survey on MRC detection, the BEP analysis for the detection in the MIMO system was recently proposed in [9]. The authors in the work derived PDF of the CCI and EN of MRC detection for M-PSK modulation and M-QAM, and the PDF was then utilized to analyze the BEP and mutual information. Although the outcomes from the analysis matched the exact BEP, there were still small deviations between the results. In addition, the CCI for the MIMO system in [9] was assumed to be the Gaussian distribution. However, the CCI is combination of product of CFR and transmit symbol vector, which are Gaussian and discrete uniform random variables, respectively. Therefore, more accurate PDF of the CCI could be theoretically utilized to enhanced the performance analysis. According to the information, this thesis derives more accurate PDF of the CCI and EN of MRC detection in the OFDM-MMIMO system, utilizing BPSK, QPSK, and M-QAM modulation. The mathematical expression for the CCI and EN is rewritten to minimize the correlation between the variables in the equation. Joint probabilities of involving random variables and other theorems in probability theory are then employed to derive the PDF of the CCI and EN. The BEP, PDF of output SINR, and outage probability of the output SINR are additionally analyzed by employing the derived PDF.

It is worth pointing out that a number of correlated variables in the original analysis for MRC detection was assumed to be independent random variables, resulting in small deviations between the analytical results and the actual PDF values. Thus, more accurate analysis is still required to analyze the performance metrics for the MRC detection. Furthermore, it is well known that the distribution of the received symbols in linear symbol detection tends to be a Gaussian distribution if there is no line-of-sight link between transmitter and receiver[39]. However, as far as the literature survey goes, there is no research work derives a closed-form expression for the PDF and the noise variance. Therefore, a mathematical expression for the Gaussian approximation is still required to simplify the performance analysis. According to the information, the derived PDF of CCI and EN for MRC detection and the performance analysis are enhanced in this thesis. The mathematical expression of CCI and EN in MRC detection involves with the diagonal elements of the Gram matrix, and the elements tends to a constant values if the number of the receive antennas is much larger than the number for the transmiter. Therefore, this approximation can be utilized to simplify the PDFs of CCI and EN for MRC detection. Variables, in the mathematical expression of the CCI and the EN, are assumed to be the constant, and the enhanced PDF of CCI and EN is then derived from the approximation. Moreover, this thesis firstly derives asymptotic closed-form expressions for the PDFs of the CCI and the EN. The work proves that the PDF of the CCI and the EN in the OFDM-MMIMO system, utilizing BPSK and QPSK modulation, converge to the Gaussian distribution. On the other hand, if Gray-coded M-QAM is employed by the system, the PDF tends to be a combination of Gaussian distributions, i.e., Gaussian

mixture model (GMM). The enhanced PDFs and the approximations are additionally utilized to derive the BEP, PDF of SINR, and outage probability of the output SINR.

In general, the classical soft-output MRC detection employs the Gaussian distribution to estimate the soft-information in forms of log-likelihood ratio (LLRs), corresponding to the estimated transmit symbols. Although the EN of MRC detection tends to be the Gaussian distribution, this is not the case for the CCI, especially when the system operates in the high E_b/N_0 region. Therefore, the derived PDF of CCI and EN for MRC detection is then chosen to the soft-output MRC detection to produce more accurate LLRs instead of assuming a classical Gaussian distribution. Due to the high computational complexity of the PDF, it is not suitable for using it in a symbol-by-symbol maximum a posterior (MAP) detector directly. Therefore, a polynomial is chosen to approximate the LLRs instead of the exact equation[24]. The enhanced soft-output MRC detector utilizes the Newton's method to produce coefficients in the polynomial[40].

Focusing on the performance analysis for ZF detection, the PDF of the EN and the BEP analysis for the detection over the OFDM-MMIMO system were derived in [24]. Although the analysis in the work provided accurate analytical results, only the 1^{st} order of Taylor's series was employed by the research work, and the Gram matrix was assumed to be a diagonal matrix. As a result, there is still a small deviation between the analytical results and the exact BEP. More accurate analytical results could be theoretically achieved if a higher order of Taylor's series is chosen for the analysis. Therefore, this thesis employs the NSE with the 2^{nd} order Taylor series to analyze the effect of noise in ZF detection and its PDF. The PDF is additionally utilized to determine the BEP, PDF of output SNR, and outage probability of the output SNR for the OFDM-MMIMO system. Moreover, this thesis proves that the PDF of the EN after the ZF detection in the OFDM-MMIMO system tends to the Gaussian distribution, and derives a closed-form expression of the noise variance. In practice, the analytical results from the approximate PDF are closely matching those from the exact equation if the number of the receive antennas is larger than 100, and the ratio of number of the receive antennas to that of the transmit antennas is larger than 10. As a result, the classical Gaussian distribution approximation can be also utilized to simplify the performance analysis of OFDM-MMIMO system for special cases.

Furthermore, this thesis utilizes the asymptotic PDF of the EN for ZF detection to reduce the computational complexity of the soft-output ZF detection. The derived noise variance is chosen to calculate the LLRs instead of the approximate noise variance. Since the PDF of the EN tends to become the Gaussian distribution, the BEP of the proposed detection is theoretically close to that of the classical detection, whereas its operational complexity can be significantly minimized.

In summary, the contributions from this research work are as follows.

1. This thesis derives accurate PDFs of the CCI and EN, BEP, PDF of SINR, outage probability of output SINR for MRC detection in the OFDM-MMIMO system,

utilizing BPSK, QPSK, and M-QAM modulation. The mathematical expression for the CCI and EN in the detection is rewritten, and the performance metrics are then derived from the equation.

2. The analysis in this thesis proves that the PDF of the CCI and EN for MRC detection, utilizing BPSK and QPSK modulation, approaches the Gaussian distribution. On the other hand, the PDF for M-QAM is approximated as the combination of Gaussian distribution. Thus, the BEP, PDF of SINR, outage probability of output SINR for the detection are then simplified in terms of the Q, exponential, and incomplete Gamma functions, respectively.

3. An enhanced soft-output MRC detection is additionally proposed in this thesis. The detector employs the derived PDF of the CCI and EN and the Newton's method to estimate the LLR instead of the Gaussian distribution. Due to the exact PDF of the CCI and EN is different from the Gaussian distribution, especially in a higher E_b/N_0 region, a higher BER performance could be theoretically achieved by utilizing the proposed soft-output MRC detection.

4. The performance of ZF detection in the OFDM-MMIMO system is analyzed in this thesis. The 2-nd order NSE is chosen to approximate the inverse matrix operator in the mathematical expression for the EN of the detection, and the PDF of the EN, BEP, PDF of SNR, and outage probability are then derived from the equation.

5. This research work proves that the PDF of the EN for ZF detection in the OFDM-MMIMO system approaches the Gaussian distribution, and derives a compact closed-form expression of the noise variance. The performance analysis for the BEP, PDF of SNR, and outage probability are then simplified by utilizing the asymptotic PDF of the EN.

6. A low-complexity soft-output ZF detection is proposed in this thesis, where the detector utilizes the derived noise variance to estimate the LLR instead of the approximate noise variance. Since the PDF of the EN for the detection approaches the Gaussian distribution, the computational complexity of the proposed detection is thus significantly reduced, whereas the BER is slightly lower than that of the classical detection.

1.3 Publications arising from this research

1. **D. Chumchewkul** and C. Tsimenidis, "Maximal-ratio combining detection in massive multiple-input multiple-output systems with accurate probability distribution function," *IET Electron. Lett.*, Vol. 59, No. 9, pp. 381-383, 2021.

2. **D. Chumchewkul** and C. Tsimenidis, "MRC Detection for LDPC-OFDM, Massive MIMO, NR-5G-based Systems Utilizing Accurate PDF of Effective Noise and Co-Channel Interference," in *Proc. IEEE Int. Conf. Commun.*, 2022, pp. 775-780.

3. **D. Chumchewkul** and C. Tsimenidis, "Probability of Bit Error of MRC Detection in OFDM-MMIMO Systems Utilizing Gaussian Mixture Model," in *Proc. Asia Pacific Conf. Commun.*, 2022, pp. 220-225.

4. **D. Chumchewkul** and C. C. Tsimenidis, "Closed-Form Bit Error Probability of ZF Detection for OFDM-M-MIMO Systems Using Effective Noise PDF," in *IEEE Access*, vol. 10, pp. 104384-104397, 2022.

5. **D. Chumchewkul**, C. Tsimenidis and S. Mumtaz, "Outage Probability Analysis of MRC Detection in OFDM-MMIMO System Utilizing Incomplete Gamma Function," in *Proc. IEEE Int. Conf. Commun. (Workshop)*, 2023, pp. 1826-1831.

1.4 Thesis outline

The remainder of this thesis is organized as follows. The principle of uncoded OFDM-MMIMO and coded-OFDM-MMIMO systems, the channel model, linear symbol detections, and channel coding techniques are briefly summarized in chapter 2. The mathematical expression of the CCI and EN for MRC detection is then utilized in chapter 3 to analyze the PDF of the CCI and EN, BEP, the PDF of SINR, and the outage probability of the output SINR for the OFDM-MMIMO system. The asymptotic analysis is additionally included in the chapter. The performance metrics for the OFDM-MMIMO system, utilizing ZF detection are then derived in chapter 4 by employing the mathematical expression for the EN. The asymptotic equations are additionally discussed in the chapter. Furthermore, the derived PDFs of the CCI and EN for MRC detection are chosen to enhance the performance of the soft-output MRC detection. Likewise, the asymptotic PDF of the EN for ZF detection is employed to simplify the computation of the soft-output ZF detector. The information, regarding the proposed soft-output MRC and ZF detections, are finally discussed in chapter 5.

1.5 Notation

The definition of mathematical symbols is clarified in this section. Matrix and vector variables in this paper are denoted as bold characters, e.g., $\mathbf{H}$, with element $H_{n,m}^{(f)}$. $\Re(H_{n,m}^{(f)})$ and $\Im(H_{n,m}^{(f)})$ represent the in-phase and quadrature components of $H_{n,m}^{(f)}$, respectively. The Hermitian transpose of $\mathbf{X}$ is denoted as $\mathbf{H}^{\dagger} = ((\mathbf{H})^T)^*$. $Q(x) = \frac{1}{\sqrt{2\pi}} \int_x^{\infty} \exp(-\frac{t^2}{2})dt$ be the Q-function. Furthermore, $\Gamma(x) = (x-1)!$ and $\Gamma(x,a) = (1/\Gamma(a)) \int_x^{\infty} t^{a-1} \exp(-t)dt$ denote the Gamma and upper incomplete Gamma function, respectively.

Chapter 2

Preliminaries

The principle of uplink uncoded OFDM-MMIMO and coded OFDM-MMIMO systems is summarized in this chapter. The next section explains the block diagram of an OFDM-MMIMO system. BPSK, QPSK, and M-QAM modulation schemes are chosen to this research work for generating the transmit symbol, and the methodology of the symbol mapper is introduced in section 2.2. Section 2.3 describes the operation of OFDM, which is employed by this research work to eliminate the effects of inter-block interference (IBI) caused by multi-path propagation. The mathematical models of the OFDM-MMIMO channel in time and frequency domain are then explained in section 2.4. The random variables in the equations describing the channel model are additionally declared in this section. Since the number of receive antennas is much larger than that of the transmit antennas, the Gram matrix tends to be a diagonal dominant matrix, where the off-diagonal components are very small. The distribution of the diagonal and off-diagonal components of the Gram matrix is summarized in section 2.5. Section 2.6 explains the operation of linear symbol detection to estimate the transmit symbols for the MMIMO systems under consideration. In addition, the principles of low-complexity linear symbol detection using inverse matrix operations or direct methods are described in section 2.7. Next, the system model of coded-OFDM-MMIMO system is summarized in section 2.8. The 5G NR LDPC codes are utilized in the system to evaluate the BEP performance. Therefore, the operation of the LDPC is then explained in section 2.9. Finally, the soft-output linear symbol detection is introduced in the section 2.10.

2.1 System model

Fig. 2.1 shows the block diagram of an uplink $N_t \times N_r$ OFDM-MMIMO system, where the number of transmit and receive antennas are denoted as N_t and N_r, respectively. Let N_f denotes the number of sub-carriers, the information bits at the transmitter $\mathbf{d} \in \mathbb{Z}^{N_t \times \log_2(M) N_f}$ are generated by the information source, and row-wise separated into N_t sub-streams for each transmitter. The element $d_{m,l}^{(f)}$ in $\mathbf{d}$ represents the l-th tuple of the information bit for the m-th transmitter of the f-th sub-carrier. Next, BPSK, QPSK, and

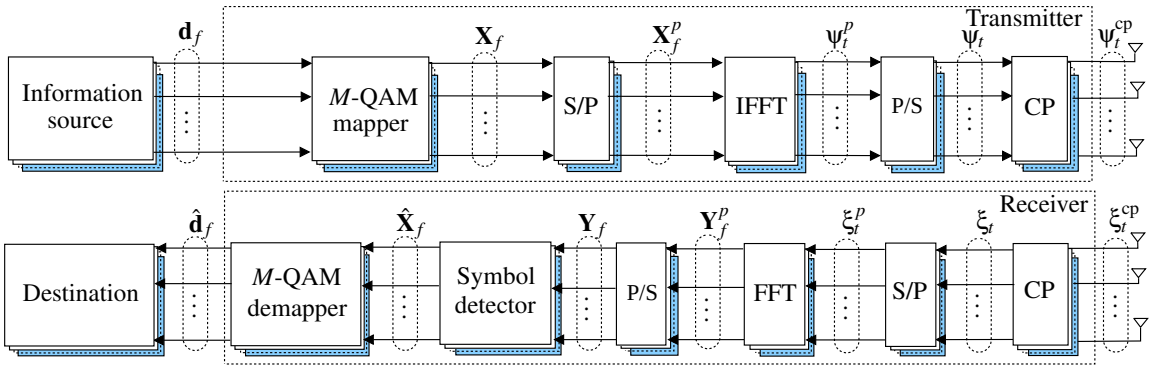

Figure 2.1: Block diagram of OFDM-MMIMO system.

M-QAM mappers are chosen for the system to produce the transmit symbols in frequency domain $\mathbf{X} \in \mathbb{C}^{N_t \times N_f}$, corresponding to $\mathbf{d}$. If the number of the constellation points is represented as M, the information bits for each transmitter are grouped into a $\log_2(M)$-tuples binary code. The information is then utilized by the mapper for producing $\mathbf{X}$. If the value of N_f is a power of two, the inverse fast Fourier transform (IFFT) operation can be employed by the OFDM modulator to produce the transmit symbols in time domain $\mathbf{\Psi} \in \mathbb{C}^{N_t \times N_f}$ from $\mathbf{X}$. Due to the occurrence of multi-path propagation in the MMIMO channel model, the transmitted symbols are impaired by the effects of IBI. Therefore, a cyclic prefix (CP) is appended at the start of the OFDM symbols during the process to obtain $\mathbf{\Psi}^{\mathrm{CP}} \in \mathbb{C}^{N_t \times (N_f + N_{\mathrm{CP}})}$, where N_{CP} denotes the number of appended CP samples. Finally, $\mathbf{\Psi}^{\mathrm{CP}}$ is transmitted through the MMIMO channel. Let $\xi^{\mathrm{CP}} \in \mathbb{C}^{N_r \times (N_f + N_{\mathrm{CP}})}$ denote the received samples at the receiver, then, per antenna, the CP samples are firstly removed from the received signal to obtain $\xi \in \mathbb{C}^{N_r \times N_f}$, which is transformed into frequency domain $\mathbf{Y} \in \mathbb{C}^{N_r \times N_f}$ by utilizing FFT operation per row. The receiver then utilizes the symbol detector to estimate the transmitted OFDM symbols $\hat{\mathbf{X}}$ from $\mathbf{Y}$. Finally, the received information bits $\hat{\mathbf{d}}$ are produced from the symbols utilizing the M-QAM demapper.

2.2 M-QAM mapper and demapper

The transmitter utilizes the M-QAM mapper to produce the transmit symbol for each transmitter corresponding to the information $\mathbf{d}$. The information bits for the m-th transmitter are packed in $\log_2(M)$-tuples of binary code. The mapper then produces the transmit symbol $X_m^{(f)}$ by matching $\{d_{m,l}^{(f)}\}_{l=1}^{\log_2(M)}$ with one of a M constellation points. Fig. 2.2 shows example of the constellation diagram for square-shaped, Gray-coded BPSK, QPSK, or, 16-QAM modulation. There are M constellation points in the diagrams, and each point in the diagram corresponds to a $\log_2(M)$-digits binary codes. In addition, if Gray-coded mapping is chosen to the system, the different between the binary codes for each two successive points in the constellation diagram is always 1 bits. Likewise, the receiver utilizes a symbol demapper to estimate the transmitted information from the received symbol $\hat{X}_m^{(f)}$. Since the in-phase and quadrature element of $X_m^{(f)}$ match the

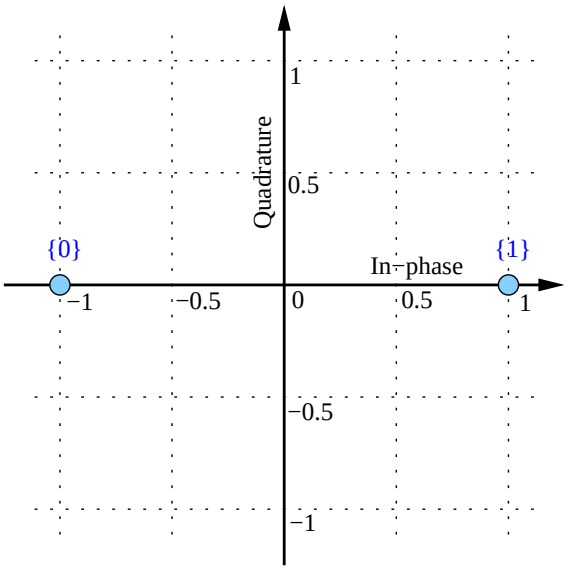

(a) BPSK.

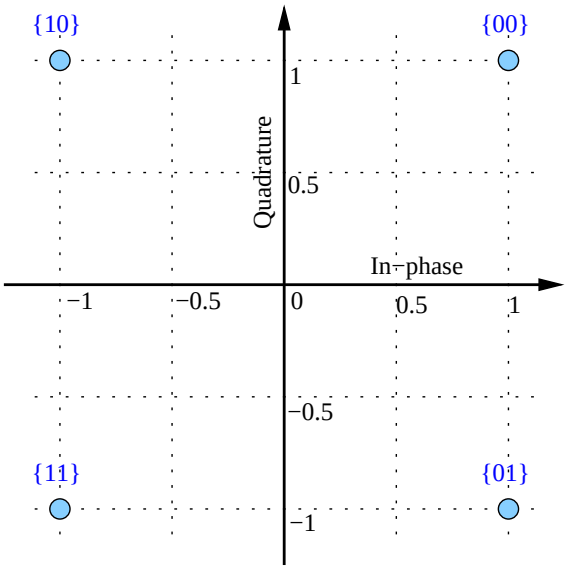

(b) QPSK.

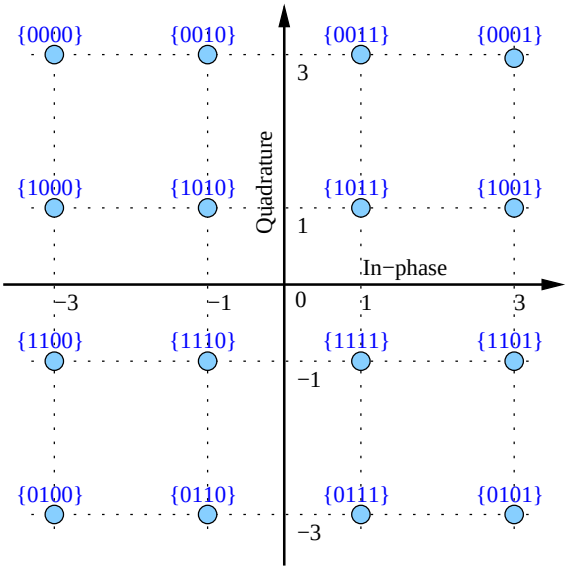

(c) 16-QAM.

Figure 2.2: Constellation points of square-shaped, Gray-coded, M-QAM waveform.

transmitted information, the estimated symbol $\hat{X}_m^{(f)}$, generated by the MMIMO detector, is then compared with the constellation points in terms of the euclidean distance. The nearest constellation point to $\hat{X}_m^{(f)}$ is chosen by the demapper and the binary code $\{\hat{d}_{m,l}^{(f)}\}_{l=1}^{\log_2(M)}$ corresponding to the point is then used as the outcome of the demapper. If Gray-coded M-QAM constellation points are chosen to the transmitter, the in-phase and quadrature components of $X_m^{(f)}$ independently match half of the binary codes. As a result, the demapper can use $\Re(X_m^{(f)})$ or $\Im(X_m^{(f)})$ to estimate $\hat{d}_{m,l}^{(f)}$ independently for this case.

2.3 OFDM

Orthogonal frequency division multiplexing (OFDM) is an important multi-carrier communication technique, which can improve spectral efficiency and reduce effects of IBI in wireless communications. The technique was proposed in 1960s [41], whereas the OFDM system using discrete Fourier transform (DFT) algorithm was later introduced in [42]. OFDM is widely applied for data communication standards, e.g., IEEE 802.11a/g/n/p, DVB-T and DVB-H [39]. Generally, the bandwidth of communication channel is separated into N_f multiple sub-channels, which use a different sub-carrier to transfer the information[43, 44]. Since the OFDM waveform employs multiple orthogonal carriers for data communication, the symbol for all N_f sub-carriers can be transmitted through the sub-channels over the same time. Sequence of transmit symbols for the m-th transmit antenna is firstly separated into N_f-symbol groups $\{X_m^{(f)}\}_{f=0}^{N_f-1}$. If N_f is a power of 2, an N_f-point IFFT operation can be utilized by the OFDM modulator to produce the transmit symbol in time domain $\{\Psi_{m,t}\}_{t=0}^{N_f-1}$ corresponding to $X_m^{(f)}$, i.e.,[45]

$$\Psi_{m,t} = \frac{1}{\sqrt{N_f}} \sum_{f=0}^{N_f-1} X_m^{(f)} e^{j\frac{2\pi ft}{N_f}}. \tag{2.1}$$

At the receiver, the OFDM demodulator uses ξ and discrete FFT converter to estimate the transmit symbols in frequency domain for the n-th receive antenna as

$$Y_n^{(f)} = \frac{1}{\sqrt{N_f}} \sum_{t=0}^{N_f-1} \xi_{n,t} e^{-j\frac{2\pi ft}{N_f}}. \tag{2.2}$$

The MMIMO channel model in time domain can be expressed as a convolutional integral of the transmit symbols and the CIR. As a result, the received symbol is generally interfered by the consecutive symbols, i.e., IBI. Therefore, dummy symbols are transmitted during the symbols to eliminate the effects of IBI[46]. CP is an example of the dummy symbol, which employ the last K samples of the OFDM symbols to be the CP symbols, and the operation of CP insertion is demonstrated in Fig. 2.3. If the number of CP symbols is chosen to be larger than the maximal delay spread, N_l, in (2.3), the

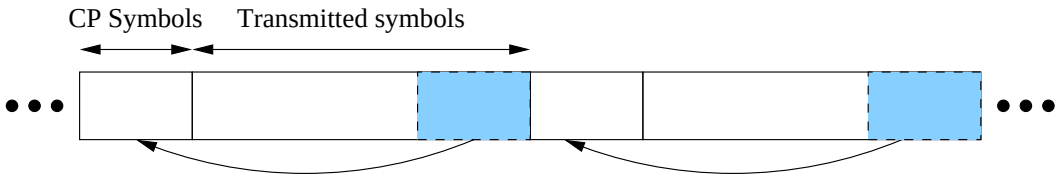

Figure 2.3: Utilizing CP symbols to eliminate the effects of IBI.

MMIMO channel model in frequency domain for each sub-carrier can be independently expressed as a flat-fading channel and a low-complexity one-tap equalizer can be applied to recover the transmitted symbol. It is worth nothing that the CP symbols, which are added by the OFDM modulator, are removed by the receiver since the symbols are not required by the OFDM demodulator for producing the output.

2.4 Channel model for the OFDM-MMIMO system

The mathematical model for an up-link data communication from mobile terminal (MT) to base station (BS) is summarized in this section. This thesis focuses on the system, where the MTs are pedestrians, moving slowly inside cellular network. Furthermore, there is no line-of-sight link between BS and MTs and the symbol time is higher than the maximal delay spread. Thus, frequency-selective Rayleigh fading channel is chosen by this thesis to simulate the propagation channel between transmit and receive antennas for this case[47], and the Doppler effects are neglected by the model. Section 2.4.1 and 2.4.2 describes the OFDM-MMIMO channel model in time and frequency domain, respectively, where random variables are chosen to demonstrate the propagation channel. Due to the fact that the mathematical expression of the MMIMO channel model in section 2.4.2 is complex, asymptotic OFDM-MMIMO channel model in frequency domain is chosen by this thesis for simplifying the derivation in chapter 3 and 4. The approximation is explained in section 2.4.3.

2.4.1 Channel model in time-domain

This section discusses the frequency-selective multi-path Rayleigh fading channel model and the tapped delay line channel model, which are chosen by this research work to demonstrate the OFDM-MMIMO system. According on the system model for the OFDM-MMIMO in Fig. 2.1, the transmit symbols with CP insertion, $\mathbf{\Psi}^{\mathrm{CP}}$, are generated by the transmit antennas, and the symbols are delivered to the receive antennas through the multi-path propagation. There are multiple propagation paths between transmit and receive antenna, utilizing various propagation delay and channel coefficient. Let $\{\Psi_{m,t}^{\mathrm{CP}}\}_{m=1}^{N_t}$ and $\{\xi_{n,t}^{\mathrm{CP}}\}_{m=1}^{N_r}$ represent elements in $\mathbf{\Psi}^{\mathrm{CP}}$ and ξ^{CP}, respectively, the received symbol at

the n-th receive antenna and the time t is given by

$$\xi_{n,t}^{\mathrm{CP}} = \sum_{m=1}^{N_t} \sum_{l=0}^{N_l-1} h_{n,m}^{(l)} \Psi_{m,t-l}^{\mathrm{CP}} + w_{n,t}, \tag{2.3}$$

where $h_{n,m}^{(l)}$ denotes the l-th tap coefficient of the channel impulse response (CIR) between the m-th transmit antenna and the n-th receive antenna. The number of tap coefficients is denoted as N_l. $w_{n,t}$ in (2.3) represents the complex-valued additive white Gaussian noise (AWGN) for the n-th receive antenna at the time t. According to (2.3), $\xi_{n,t}^{\mathrm{CP}}$ is generated from CIRs and $\Psi_{m,t-l}^{\mathrm{CP}}$ by employing various attenuation coefficient and propagation delay.

$w_{n,t}$ in (2.3) is generated from a complex-valued, zero-mean Gaussian random variable, $\mathcal{CN}(0, 2\sigma_{\tilde{w}}^2)$. Let $\gamma_b = E_b/N_0$ represent the signal-to-noise ratio (SNR) per bit, the variance per dimension $\sigma_{\tilde{w}}^2$ of $w_{n,t}$ is defined as

$$\sigma_{\tilde{w},\mathrm{uncoded}}^2 = \frac{N_t E_s}{2\log_2(M)\gamma_b}. \tag{2.4}$$

It is worth noting that the noise variance, $\sigma_{\tilde{w}}^2$, can be expressed in forms of N_0. If $E_s = \log_2(M)E_b$ and $\gamma_b = E_b/N_0$ are substituted in (2.4), the $\sigma_{\tilde{w}}^2$ becomes

$$\sigma_{\tilde{w},\mathrm{uncoded}}^2 = \frac{N_t N_0}{2}. \tag{2.5}$$

In addition to the channel model in (2.3), the magnitude of the CIR, $h_{n,m}^{(l)}$ decays according to the delay. Therefore, the CIR is generated from the Gaussian random variable and exponential function as

$$\tilde{h}_{n,m}^{(l)} = \varrho_{n,m,l} \exp\left(-\frac{l^\tau}{N_{\max}}\right), \tag{2.6}$$

where $\varrho_{n,m,l}$ represents the tap coefficient, exhibiting a $\mathcal{CN}(0,1)$. $N_{\max}$ and τ in (2.6) represents the maximum delay spread and a constant to control power delay profile (PDP), respectively. In order to normalize the total power of tap coefficients, σ_h^2 is 0.5 and $h_{n,m}^{(l)}$ is generated from $\tilde{h}_{n,m}^{(l)}$ as

$$h_{n,m}^{(l)} = \frac{\tilde{h}_{n,m}^{(l)}}{\sqrt{\sum_{k=0}^{N_l-1} |\tilde{h}_{n,m}^{(k)}|^2}}. \tag{2.7}$$

By utilizing the FFT operation, the channel frequency response (CFR) between the m-th transmit antenna and n-th receive antenna for the f-th sub-carrier can be evaluated from $h_{n,m}^{(t)}$ as

$$H_{n,m}^{(f)} = \sum_{k=0}^{N_f-1} h_{n,m}^{(k)} \exp\left(-j\frac{2\pi f k}{N_f}\right), \quad f = 0, 1, \cdots, N_f - 1. \tag{2.8}$$

$N_{\max} = 50$ and $\tau = 1.2$ were chosen to the simulation on this thesis since the magnitude of CFR in (2.8) fluctuates across all sub-carrier. Fig. 2.4 shows samples of CIR and CFR

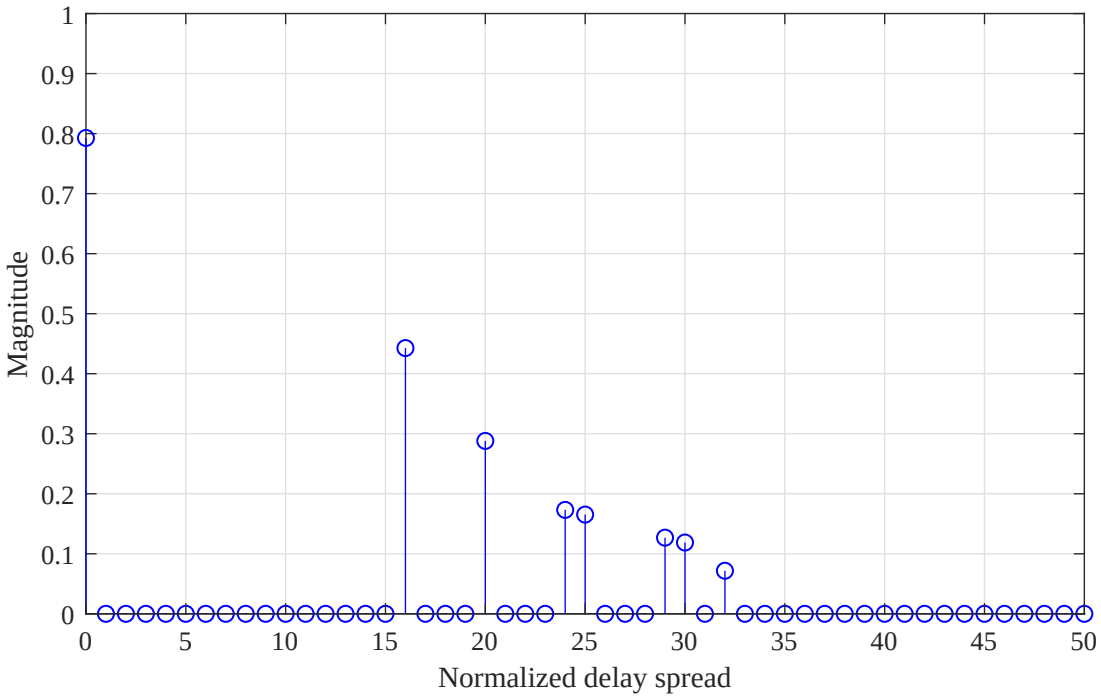

(a) CIR.

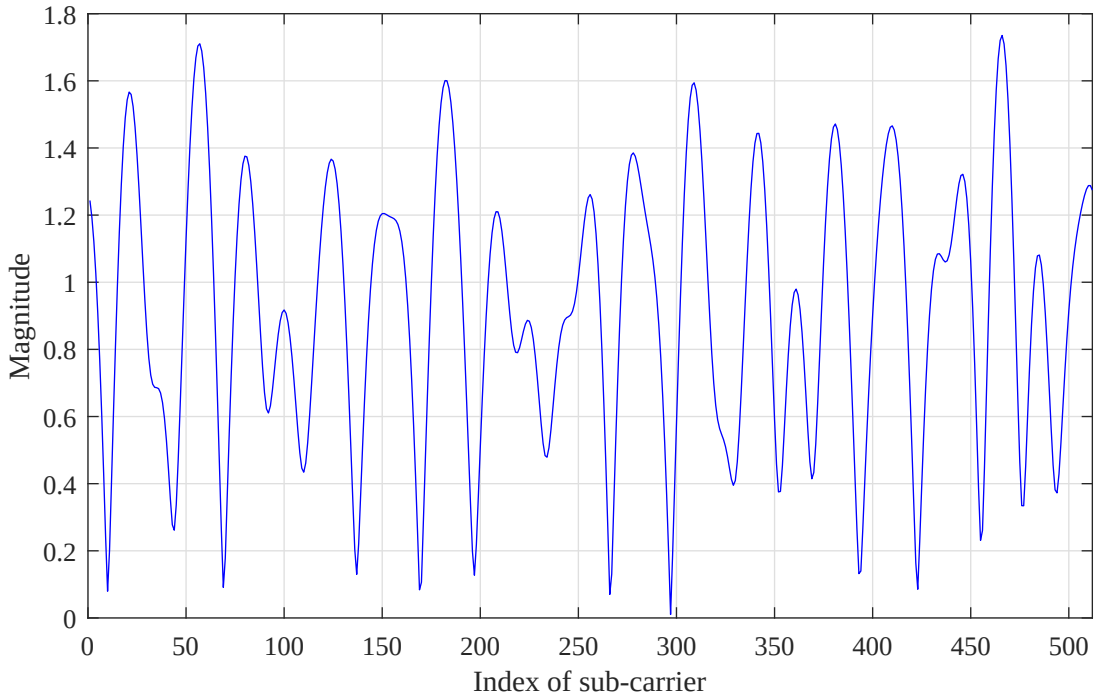

(b) CFR.

Figure 2.4: CIR and CFR for 10×100 OFDM-MMIMO system.

for a 10×100 OFDM-MMIMO system. τ and $N_{\max}$ were 1.2 and 50, respectively. $N_l = 8$ and $N_f = 512$ were chosen to the simulation. A closer look at the results reveals that the magnitude of $H_{n,m}^{(f)}$ exhibits a frequency-selective behaviour with several spectral nulls.

2.4.2 Channel model in frequency-domain

Generally, the CP symbols are added to the OFDM symbols for reducing the effects of IBI. If the number of CP symbols is larger than the maximum delay spread, $N_{\max}$, IBI is assumed to be completely eliminated for the OFDM demodulator. As a result, the receive symbol in frequency domain of the f-th sub-carrier for the n-th receive antenna is given by

$$Y_n^{(f)} = \sum_{m=1}^{N_t} H_{n,m}^{(f)} X_m^{(f)} + W_n^{(f)}, \quad n = 0, 1, \cdots, N_r. \tag{2.9}$$

$X_m^{(f)}$, $Y_n^{(f)}$, and $W_n^{(f)}$ in (2.9) denote the transmit symbol, the receive symbol, and the noise vector for the f-th sub-carrier, respectively. The symbols are calculated from the $\Psi_m^{(t)}$, $\xi_n^{(t)}$ and $w_n^{(t)}$ by using FFT operator, i.e.,

$$X_m^{(f)} = \sum_{k=0}^{N_f-1} \Psi_m^k \exp\left(-j\frac{2\pi fk}{N_f}\right), \quad f = 0, 1, \cdots, N_f - 1, \tag{2.10a}$$

$$Y_n^{(f)} = \sum_{k=0}^{N_f-1} \xi_n^k \exp\left(-j\frac{2\pi fk}{N_f}\right), \quad f = 0, 1, \cdots, N_f - 1, \tag{2.10b}$$

$$W_n^{(f)} = \frac{1}{\sqrt{N_f}} \sum_{k=0}^{N_f-1} w_n^k \exp\left(-j\frac{2\pi fk}{N_f}\right), \quad f = 0, 1, \cdots, N_f - 1. \tag{2.10c}$$

Since the path gain between the m-th transmit antenna and the n-th receive antenna in (2.9) only corresponds to $H_{n,m}^{(f)}$, the received symbols for the f-th sub-carrier can be rewritten in forms of a linear matrix equation as

$$\mathbf{Y}_f = \mathbf{H}_f \mathbf{X}_f + \mathbf{W}_f, \tag{2.11a}$$

$$\begin{bmatrix} Y_1^{(f)} \\ Y_2^{(f)} \\ \vdots \\ Y_{N_r}^{(f)} \end{bmatrix} = \begin{bmatrix} H_{1,1}^{(f)} & H_{1,2}^{(f)} & \cdots & H_{1,N_t}^{(f)} \\ H_{2,1}^{(f)} & H_{2,2}^{(f)} & \cdots & H_{2,N_t}^{(f)} \\ \vdots & \vdots & \cdots & \vdots \\ H_{N_r,1}^{(f)} & H_{N_r,2}^{(f)} & \cdots & H_{N_r,N_t}^{(f)} \end{bmatrix} \begin{bmatrix} X_1^{(f)} \\ X_2^{(f)} \\ \vdots \\ X_{N_t}^{(f)} \end{bmatrix} + \begin{bmatrix} W_1^{(f)} \\ W_2^{(f)} \\ \vdots \\ W_{N_r}^{(f)} \end{bmatrix}. \tag{2.11b}$$

$\mathbf{X}_f \in \mathbb{C}^{N_t \times 1}$ and $\mathbf{Y}_f \in \mathbb{C}^{N_r \times 1}$ in (2.11) denote the transmitted and received signal vectors in frequency domain for the f-th sub-carrier, with components $X_m^{(f)}$ and $Y_n^{(f)}$, respectively. $\mathbf{H}_f \in \mathbb{C}^{N_r \times N_t}$ is the CFR matrix of the f-th sub-carrier and its element is $H_{n,m}^{(f)}$. $\mathbf{W}_f \in \mathbb{C}^{N_r \times 1}$ in (2.11) represents the noise vector of the f-th sub-carrier, where its component is $W_n^{(f)}$.

2.4.3 Asymptotic channel model in frequency-domain

Although the OFDM-MMIMO channel model in frequency-domain on (2.11) can be chosen to demonstrate the channel model on the simulation software, several random variables are included in the equation, making a complication to the analysis. Therefore, asymptotic channel model of the OFDM-MMIMO system in frequency domain is chosen by this thesis to simplify the derivation. The asymptotic channel model in frequency-domain is identical to the exact linear matrix equation in (2.11). However, $H_{n,m}^{(f)}$ and $W_n^{(f)}$ in (2.11) are assumed to be the complex-valued, Gaussian random variables. According to the derivation in (2.8), $H_{n,m}^{(f)}$ exhibits a sum of Gaussian random variables, $h_{n,m}^{(t)}$. Thus, $H_{n,m}^{(f)}$ in (2.11) is assumed to be the complex-valued, Gaussian distribution, $\mathcal{CN}(0, 2\sigma_h^2)$. The variance per dimension for $H_{n,m}^{(f)}$ is determined by using the expectation in (2.8) [9], i.e.,

$$\sigma_h^2 = \frac{1}{2} \sum_{l=0}^{N_f-1} \mathbb{E}\left(|h_{n,m}^{(l)}|^2\right), \tag{2.12a}$$

$$\sigma_h^2 = 0.5, \tag{2.12b}$$

where $\mathbb{E}(.)$ denotes the expectation operator. Due to the total squared magnitude of the CIR in (2.12a) is normalized to unity by using (2.7), σ_h^2 becomes 0.5 for this case. Fig. 2.5 compares the PDF of in-phase component of $H_{n,m}^{(f)}$, i.e. $p_h(\Re(H_{n,m}^{(f)}))$, from the simulation results to that of the Gaussian distribution. N_f and the maximal delay spread was 1,024 and 50 symbols, respectively. $N_l = \{5, 10, 20, 40\}$. The results confirmed that the PDF of $\Re(H_{n,m}^{(f)})$ converged to the Gaussian distribution, especially in the system with a larger N_l. Focusing on the system using $N_l = 40$, the actual $p_h(\Re(H_{n,m}^{(f)}))$ at $\Re(H_{n,m}^{(f)}) = 0$ was 0.11, which was only 2.1×10^{-3} different from the Gaussian distribution. However, the deviation between the $\mathcal{N}(0, \sigma_h^2)$ and the exact PDF increased if N_l was smaller. The deviation in $p_h(\Re(H_{n,m}^{(f)}))$ for the system with $N_l = 5$ was 1.47×10^{-2}, which was 1.26×10^{-2} higher than that of $N_l = 40$.

Likewise, $W_n^{(f)}$ in (2.10) is a sum of complex-valued, Gaussian random variable, i.e., $w_{n,t}$. As the results, $W_n^{(f)} \simeq \mathcal{CN}(0, 2\sigma_w^2)$, and the noise variance per dimension is evaluated from the expectation in (2.10) as

$$\sigma_w^2 = \frac{1}{2N_f} \sum_{k=0}^{N_f-1} \mathbb{E}\left(|w_n^{(k)}|^2\right), \tag{2.13a}$$

$$\sigma_w^2 = \sigma_{\tilde{w}}^2. \tag{2.13b}$$

Eq. (2.13) proves that the noise variance per dimension for the $W_n^{(f)}$, σ_w^2, is identical to that of the $w_{n,t}$ in (2.4). Fig. 2.6 shows the simulation results for the PDF of the in-phase component of $W_n^{(f)}$ for a 10×100 OFDM-MMIMO system. 16-QAM was chosen as the modulation scheme for the system and the system operated at $E_b/N_0 = \{-10, -5, 0\}$ dB. The empirical results are also compared to the $\mathcal{N}(0, \sigma_w^2)$, using the noise variance,

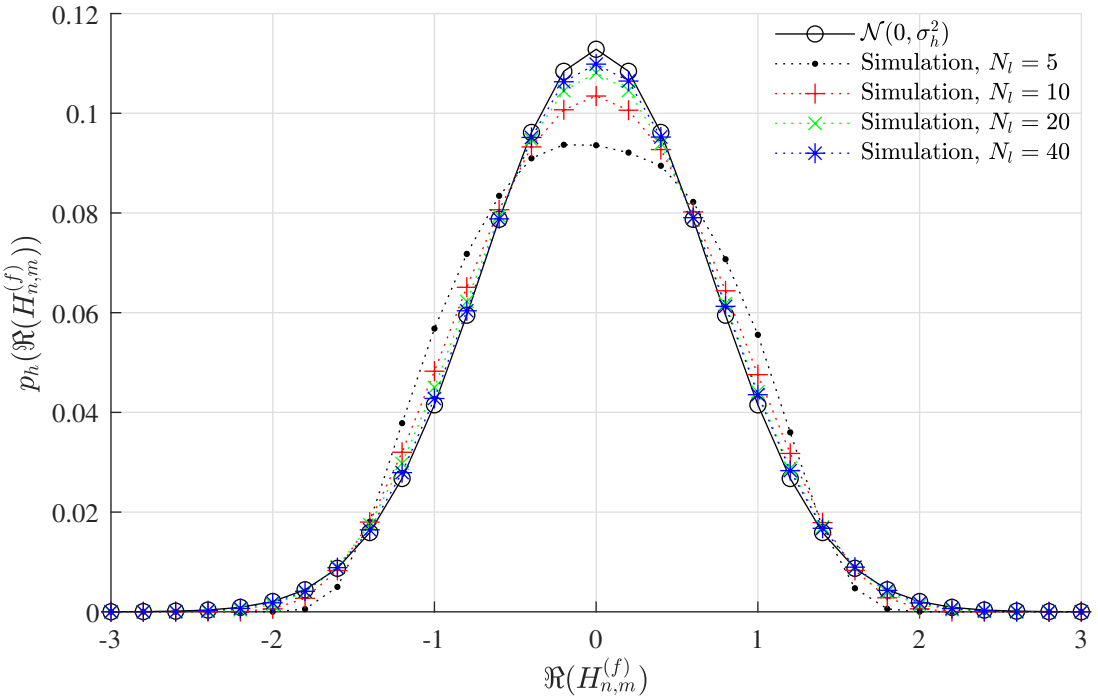

Figure 2.5: PDF of CFR.

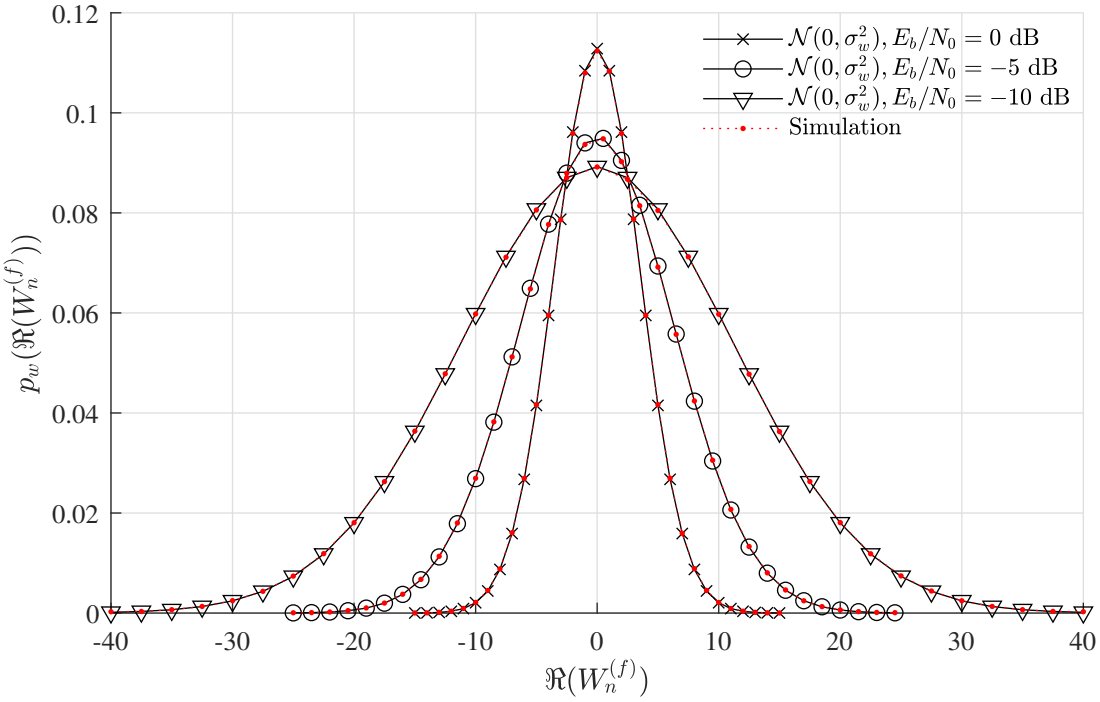

Figure 2.6: PDF of noise vectors.

σ_w^2, in (2.13). Evidently, the exact PDF of $\Re(W_n^{(f)})$ matched the Gaussian distribution. Focusing on the system with $E_b/N_0 = 0$ dB, the exact PDF at $\Re(W_n^{(f)}) = 0$ was 0.11 and the number was only 4.63×10^{-4} different from the Gaussian distribution. In addition, the empirical results were compared with the Gaussian distribution, utilizing a 2-sample Kolmogorov–Smirnov test with the significant level 5%, and the outcome confirmed that there is no significant difference between the PDFs.

2.5 Distribution of Gram matrix

The Gram matrix, $\mathbf{G}_f \in \mathbb{C}^{N_t \times N_t}$, is a matrix which is generally employed by linear symbol detectors to evaluate the output. The matrix for the MMIMO channel is written in terms of the CFR matrix as

$$\mathbf{G}_f = \mathbf{H}_f^{\dagger}\mathbf{H}_f, \tag{2.14a}$$

$$\mathbf{G}_f = \begin{bmatrix} H_{1,1}^{(f),*} & H_{2,1}^{(f),*} & \dots & H_{N_r,1}^{(f),*} \\ H_{1,2}^{(f),*} & H_{2,2}^{(f),*} & \dots & H_{N_r,2}^{(f),*} \\ \vdots & \vdots & \ddots & \vdots \\ H_{1,N_t}^{(f),*} & H_{2,N_t}^{(f),*} & \dots & H_{N_r,N_t}^{(f),*} \end{bmatrix} \begin{bmatrix} H_{1,1}^{(f)} & H_{1,2}^{(f)} & \dots & H_{1,N_t}^{(f)} \\ H_{2,1}^{(f)} & H_{2,2}^{(f)} & \dots & H_{2,N_t}^{(f)} \\ \vdots & \vdots & \ddots & \vdots \\ H_{N_r,1}^{(f)} & H_{N_r,2}^{(f)} & \dots & H_{N_r,N_t}^{(f)} \end{bmatrix}, \tag{2.14b}$$

where the Hermitian transpose of $\mathbf{H}_f$ is denoted as $\mathbf{H}_f^{\dagger}$. If N_r is chosen to be much larger than N_t, e.g., 10×200 system, the diagonal components of $\mathbf{G}_f$ dominate the matrix. As a result, $\mathbf{G}_f$ tends to be a diagonal matrix for this case[3]. Let $\mathbf{D}_f$ and $\mathbf{E}_f$ denote the diagonal and off-diagonal components of $\mathbf{G}_f$, respectively, $\mathbf{G}_f$ in (2.14) can be rewritten in terms of the matrices as

$$\mathbf{G}_f = \mathbf{D}_f + \mathbf{E}_f. \tag{2.15}$$

An element in $\mathbf{D}_f$ and $\mathbf{E}_f$ is represented as $D_{n,m}^{(f)}$ and $E_{n,m}^{(f)}$, respectively. The distribution of the diagonal and off-diagonal components of $\mathbf{G}_f$ are discussed in the next sub-sections.

2.5.1 Diagonal components of $\mathbf{G}_f$

$\mathbf{G}_f$, in (2.14), is a product of $\mathbf{H}_f^{\dagger}$ and $\mathbf{H}_f$. Therefore, the diagonal components of the Gram matrix, $\mathbf{D}_f$, in (2.14) can be expressed as

$$\mathbf{D}_f = \begin{bmatrix} \sum_{n=1}^{N_r} |H_{n,1}^{(f)}|^2 & 0 & 0 & \dots & 0 \\ 0 & \sum_{n=1}^{N_r} |H_{n,2}^{(f)}|^2 & 0 & \dots & 0 \\ 0 & 0 & \sum_{n=1}^{N_r} |H_{n,3}^{(f)}|^2 & \dots & 0 \\ \vdots & \vdots & \vdots & \ddots & \vdots \\ 0 & 0 & 0 & 0 & \sum_{n=1}^{N_r} |H_{n,N_t}^{(f)}|^2 \end{bmatrix}. \tag{2.16}$$

According to (2.16), the m-th diagonal component $D_{m,m}^{(f)}$ of $\mathbf{D}_f$ is a N_r times summation of the squared magnitude of $H_{n,m}^{(f)}$. Thus, $D_{m,m}^{(f)}$ can be rewritten in terms of real arithmetic operators as

$$D_{m,m}^{(f)} = \sum_{n=1}^{N_r} \Re(H_{n,m}^{(f)})^2 + \Im(H_{n,m}^{(f)})^2. \tag{2.17}$$

Evidently, $D_{m,m}^{(f)}$ in (2.17) is a combination of squared Gaussian random variables.

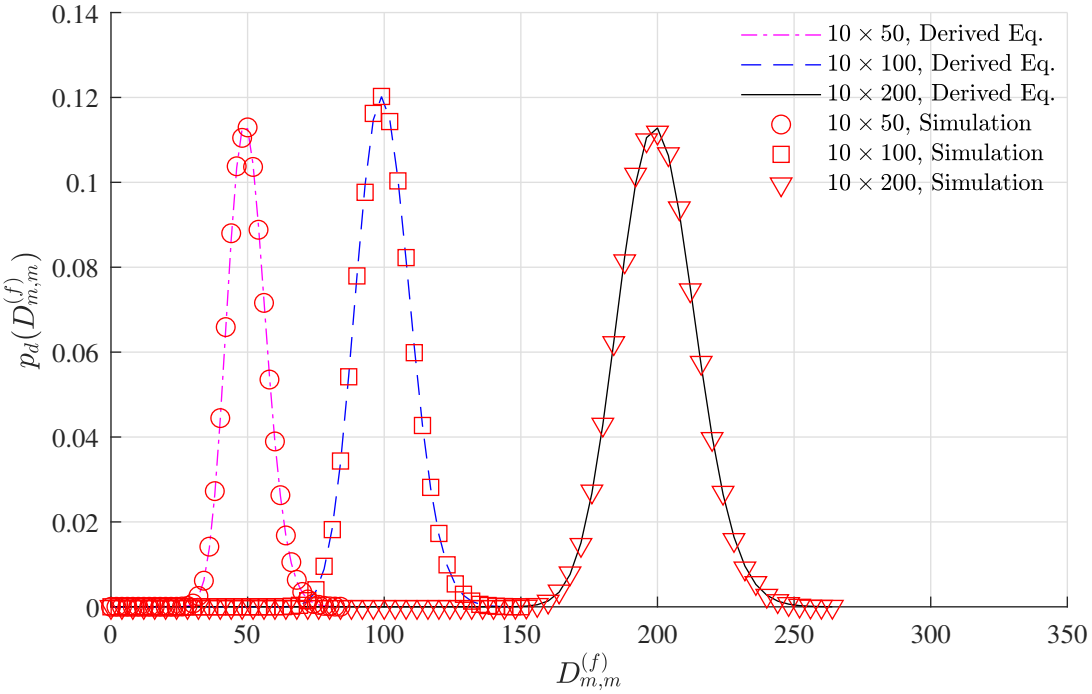

Figure 2.7: PDF of $D^{(f)}_{m,m}$ from (2.18).

Thus, $p_d(D^{(f)}_{m,m})$ exhibits the Chi-square distribution and the PDF of $D^{(f)}_{m,m}$ is given by [24]

$$p_d(D^{(f)}_{m,m}) = \frac{(D^{(f)}_{m,m})^{N_r-1}}{(2\sigma_h^2)^{N_r}\Gamma(N_r)} \exp\left(-\frac{D^{(f)}_{m,m}}{2\sigma_h^2}\right), \quad D^{(f)}_{m,m} > 0, \tag{2.18}$$

where the Gamma function of variable X is represented as $\Gamma(X)$. Moreover, if $N_r >> N_t$, the PDF of $D^{(f)}_{m,m}$ tends to be a $\mathcal{N}(2N_r\sigma_h^2, 2N_r\sigma_h^2)$ [48]. According to the Markov's theorem in (7-119) of [49], $D^{(f)}_{m,m}$ approaches a constant and the variance for the variable tends to zero. Therefore, $D^{(f)}_{m,m}$ can be approximated as the mean Ω, i.e.,

$$\Omega = 2N_r\sigma_h^2. \tag{2.19}$$

Fig. 2.7 demonstrates the PDF of $D^{(f)}_{m,m}$ from (2.18), where $N_t = 10$ and $N_r = \{50, 100, 200\}$. The outcome from the equation was also compared to that of the simulation results. According to the 2-sample Kolmogorov–Smirnov test with a significance level of 5%, there is no significant different in PDF between the exact and the derived PDF. Focusing on the simulation results for the 10×100 system on Fig. 2.7, the percentage of the occurrence of $D^{(f)}_{m,m}$, ranged from 85 to 115 was 86.76 percent. Furthermore, if $N_r \geq 100$, most of the variation of $D^{(f)}_{m,m}$ was less than 15 percent of its mean. The results demonstrate that the distribution of $D^{(f)}_{m,m}$ become smaller, compared to its mean in the system with a larger N_r.

2.5.2 Off-diagonal components of $\mathbf{G}_f$

According to the Gram matrix in (2.15), the off-diagonal components, $\mathbf{E}_f$, of the Gram matrix can be expressed as

$$\mathbf{E}_f = \begin{bmatrix} 0 & \sum_{k=1}^{N_r} H_{k,1}^{(f),*} H_{k,2}^{(f)} & \sum_{k=1}^{N_r} H_{k,1}^{(f),*} H_{k,3}^{(f)} & \dots & \sum_{k=1}^{N_r} H_{k,1}^{(f),*} H_{k,N_t}^{(f)} \\ \sum_{k=1}^{N_r} H_{k,2}^{*} H_{k,1}^{(f)} & 0 & \sum_{k=1}^{N_r} H_{k,2}^{(f),*} H_{k,3}^{(f)} & \dots & \sum_{k=1}^{N_r} H_{k,2}^{(f),*} H_{k,N_t}^{(f)} \\ \sum_{k=1}^{N_r} H_{k,3}^{(f),*} H_{k,1}^{(f)} & \sum_{k=1}^{N_r} H_{k,3}^{(f),*} H_{k,2}^{(f)} & 0 & \dots & \sum_{k=1}^{N_r} H_{k,3}^{(f),*} H_{k,N_t}^{(f)} \\ \vdots & \vdots & \vdots & \ddots & \vdots \\ \sum_{k=1}^{N_r} H_{k,N_t}^{(f),*} H_{k,1}^{(f)} & \sum_{k=1}^{N_r} H_{k,N_t}^{(f),*} H_{k,2}^{(f)} & \sum_{k=1}^{N_r} H_{k,N_t}^{(f),*} H_{k,3}^{(f)} & \dots & 0 \end{bmatrix}. \tag{2.20}$$

Off-diagonal elements, $E_{n,m}^{(f)}$ in (2.20) are combination of product of CFR, i.e., complex-valued, Gaussian random variables, $\mathcal{CN}(0, 2\sigma_h^2)$. Therefore, $E_{n,m}^{(f)}$ approaches the $\mathcal{CN}(0, 2\sigma_e^2)$, where the noise variance per dimension for $E_{n,m}^{(f)}$ is derived from the expectation of $E_{n,m}^{(f)}$[9], and results in

$$\sigma_e^2 = \frac{1}{2} \sum_{k=1}^{N_r} \mathbb{E}\left(|H_{k,1}^{(f),*}|^2 |H_{k,2}^{(f)}|^2 \right), \tag{2.21a}$$

$$\sigma_e^2 = 2N_r \sigma_h^4. \tag{2.21b}$$

Fig. 2.8 shows the simulation results for the $p_e(\Re(E_{m,n}^{(f)}))$ of the OFDM-MMIMO system. N_t was 10 and $N_r = \{50, 100, 200\}$. The empirical results are also compared to the $\mathcal{N}(0, \sigma_e^2)$ using the variance σ_e^2 in (2.21). The results confirm that the Gaussian approximation match the exact PDF. Focusing on the 10×200 system, the PDF from the Gaussian distribution at $\Re(E_{m,n}^{(f)}) = 0$ was 9.97×10^{-2}, and the number was only 3.22×10^{-5} different from the exact PDF.

2.6 Linear symbol detections

Focusing on the MMIMO channel model in (2.9), the transmitter sends the transmit symbols $\mathbf{X}_f$ from all transmit antennas over the same time slot. The symbols are interfered by the effects of thermal noise $\mathbf{W}_f$ and the CCI. Therefore, a symbol detection is required by the receiver to estimate the transmit symbols $\hat{\mathbf{X}}_f$ from $\mathbf{Y}_f$. Several MMIMO detection schemes can be chosen to the receiver, and the detections can be broadly classified into two groups according to the detection algorithm, i.e., linear and non-linear detections [25]. The latter employs non-linear algorithm to recover the transmitted symbol from the received signal. Maximal likelihood (ML) detection is an important algorithm for non-linear detection, where the received symbols are compared to the referenced signals corresponding to all possible constellation points. The nearest point is then utilized to produce the outcome for the detector.

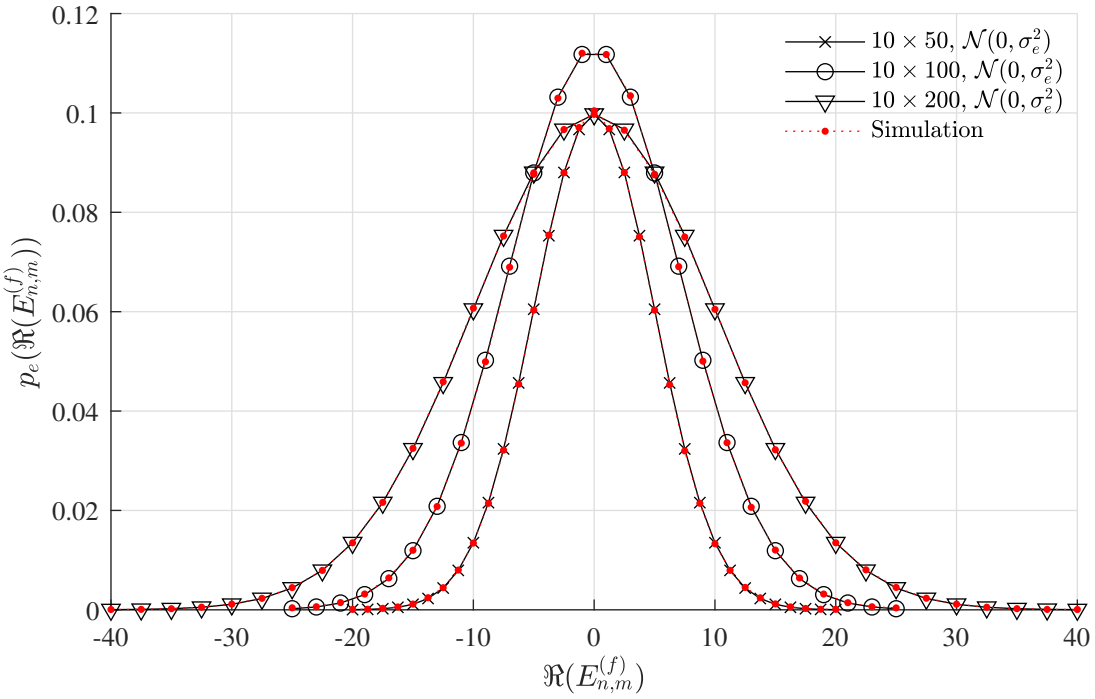

Figure 2.8: Gaussian approximation of $p_e(\Re(E_{n,m}^{(f)}))$.

Although ML detection provides an optimal BEP performance to the MMIMO system, the operational complexity of the detection increases exponentially according to the number of N_t and N_r. Therefore, linear symbol detection has been recommended for practical MMIMO system[4]. The detection employs inverse matrix operator to suppress the CCI from $\mathbf{Y}_f$. MRC, ZF, and MMSE detections are important algorithms for linear symbol detection. MRC detection requires the smallest computational complexity compared to other techniques since the detection directly multiply the $\mathbf{Y}_f$ with the Hermitian transpose of the CFR matrix to estimate the transmit symbols. However, the BEP of the system using the technique is higher that that of other detections since the interference from other transmit antennas is still neglected. On the other hand, ZF and MMSE detections utilize Moore-Penrose inverse of channel matrix to eliminate the interference, making a higher BEP performance, compared to that of MRC detection. Although the linear symbol detection cannot provide an optimal BEP performance to the system, the detector utilizes uncomplicated matrix operators to estimate the transmit symbol $\hat{\mathbf{X}}_f$ from $\mathbf{Y}_f$. The detector requires much less arithmetic operators than that of non-linear detection. In addition, if N_r is large enough, the effective channel becomes deterministic and the Gram matrix tends to be a diagonal matrix. This properties is called the "channel-hardening" and linear symbol detection provides an excellent BEP performance for this scenario[4]. Moreover, approximate inverse matrix operation and direct methods can be efficiently utilized to simplify the inverse matrix operation[50].

Fig. 2.9 compares the BER of the OFDM-MMIMO system where MRC, ZF, or MMSE detection are chosen to the system for estimating the transmitted symbol. $N_t = 10$ and N_r was $\{50, 100, 200\}$. The transmitter employed 16-QAM to produce the transmit symbol

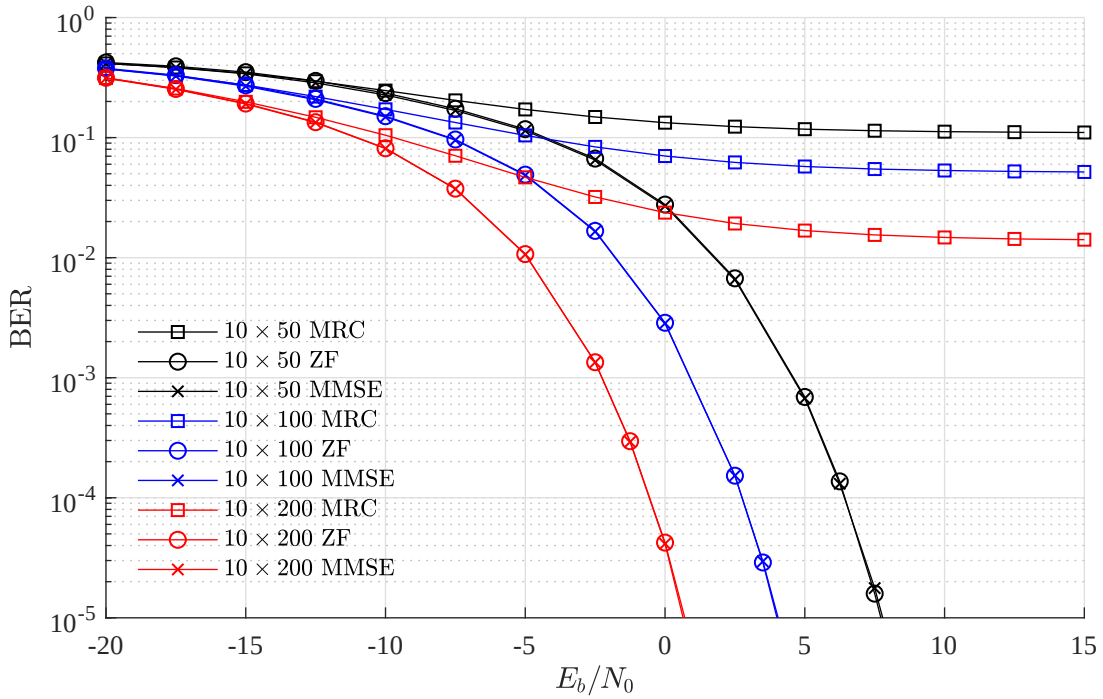

Figure 2.9: BER for OFDM-MMIMO system using linear symbol detection.

in the frequency domain. The block size utilization and the number of sub-carrier of the OFDM symbol were 1024 bits and 256 symbols, respectively. The results confirmed that the system using MRC detection obtained the highest BER, compared to the number for other detections. Focusing on the 10×200 system operating at $E_b/N_0 = 0$ dB. The BER for MRC detection was 1.93×10^{-2}, which was 1.92×10^{-2} higher than that of ZF detection. In addition, the deviation in BER between ZF and MMSE detection was marginal, and the difference for the 10×200 system at $E_b/N_0 = 0$ was only 9.6×10^{-7}. Furthermore, the results in Fig. 2.9 also demonstrated that an extra BER performance can be significantly achieved by increasing the number of receive antennas, N_r. Focusing on the 10×50 system where utilized MMSE detection, the system required the E_b/N_0 of 6.42 dB to maintain the BER at 10^{-4}. On the other hand, the E_b/N_0 for the 10×200 system was -0.57 dB, and this number was 6.99 dB smaller than that of the 10×50 system.

2.6.1 MRC detection

According to (2.11), the MMIMO channel can be expressed as a linear matrix equation. Thus, linear detection uses the equation to estimate the transmit symbol. MRC or Matched filter detection is the lowest computational complexity linear symbol detection, and employs a weight matrix to estimate $\tilde{\mathbf{X}}_f$ from $\mathbf{Y}_f$ as

$$\tilde{\mathbf{X}}_f = \mathbf{H}_f^{\dagger} \mathbf{Y}_f. \tag{2.22}$$

By substituting $\mathbf{Y}_f$ from (2.11) into (2.22), $\tilde{\mathbf{X}}_f$ becomes

$$\tilde{\mathbf{X}}_f = \mathbf{G}_f \mathbf{X}_f + \mathbf{H}_f^{\dagger} \mathbf{W}_f. \tag{2.23}$$

The first term in (2.23) corresponds to $\mathbf{X}_f$, and the term is multiplied by the diagonal components of the Gram matrix, $D_{m,m}^{(f)}$. Therefore, $\tilde{\mathbf{X}}_f$ is then normalized as

$$\hat{X}_m^{(f)} = \frac{\tilde{X}_m^{(f)}}{D_{m,m}^{(f)}}. \tag{2.24}$$

$\hat{X}_m^{(f)}$ in (2.24) represents the outcome of MRC detection and the receiver employs the symbol to estimate the transmitted message. It is worth noting that $\hat{X}_m^{(f)}$ is still interfered by the CCI and EN. If $\tilde{X}_m$ in (2.23) is substituted in (2.24), $\hat{X}_m^{(f)}$ can be rewritten as

$$\hat{X}_m^{(f)} = X_m^{(f)} + \underbrace{\frac{\sum_{k=1,k\neq m}^{N_t} E_{m,k}^{(f)} X_k^{(f)}}{D_{m,m}^{(f)}} + \frac{\sum_{n=1}^{N_r} H_{n,m}^{(f),*} W_n^{(f)}}{D_{m,m}^{(f)}}}_{Z_m^{(f),\mathrm{MRC}}}. \tag{2.25}$$

The second and the third terms in (2.25), $Z_m^{(f),\mathrm{MRC}}$, represent the effects of the CCI and the EN of MRC detection. Due to the effects of CCI in MRC detection cannot be eliminated by utilizing MRC algorithm, the BEP performance of the detection is less than other linear symbol detections. However, If N_r is large enough, the Gram matrix $\mathbf{G}_f$ tends to be a diagonal matrix and this term becomes smaller. As far as the literature survey goes, there is no research work derive exact PDF of the CCI and EN in MRC detection. Thus, the $Z_m^{(f)}$ is assumed to be the complex-valued, Gaussian distribution, $\mathcal{CN}(0, 2\sigma_z^2)$, where the variance per dimension for the variable is calculated from the mathematical expression of $Z_m^{(f)}$ in (2.25) as[9]

$$\sigma_{z,m}^2 = \frac{\sum_{k=1,k\neq m}^{N_t} \mathbb{E}\left(|E_{m,k}^{(f)} X_k^{(f)}|^2\right) + \sum_{n=1}^{N_r} \mathbb{E}\left(|H_{n,m}^{(f),*} W_n^{(f)}|^2\right)}{2\,\mathbb{E}\left(|D_{m,m}^{(f)}|^2\right)}. \tag{2.26}$$

The expectation of $D_{m,m}^{(f)}$ was previously derived in (2.19). $H_{m,n}^{(f)}$ and $W_n^{(f)}$ are complex-valued, Gaussian random variables, and the expectation for the squared magnitude for the variable approach the variance for the variable. After solving the equation, the variance per dimension of $Z_m^{(f)}$ becomes

$$\sigma_z^2 = \frac{E_s(N_t - 1)}{2N_r^2} + \frac{\sigma_w^2}{2N_r\sigma_h^2}. \tag{2.27}$$

The Gaussian approximation of the PDF of $\Re(Z_m^{(f)})$ in (2.27) for a 10×200 system was compared to that of the exact PDF, and the empirical results are shown in Fig. 2.10. 16-QAM was chosen to the system, and the system operated at $E_b/N_0 = \{-15, -5\}$ dB. Focusing on the results for $E_b/N_0 = -15$ dB, the derived PDF at $\Re(Z_m^{(f)}) = 0$

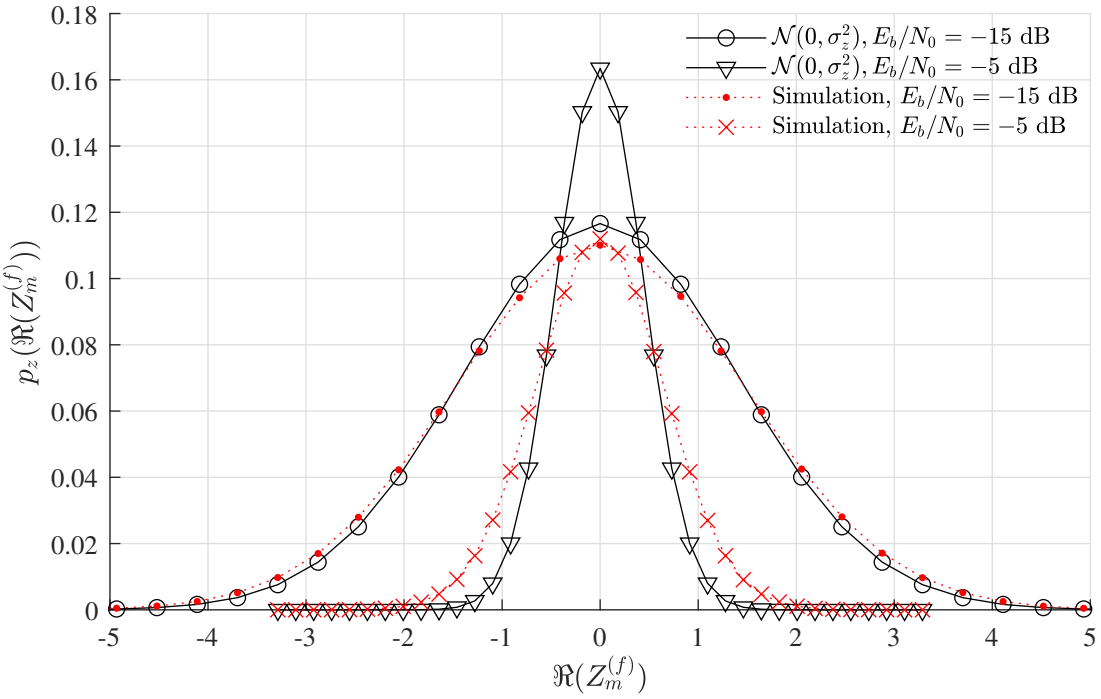

Figure 2.10: PDF of the CCI and the EN of OFDM-MMIMO system, utilizing MRC detection.

was 0.12, exhibiting 6.52×10^{-3} different from that of the exact PDF. Furthermore, the difference between the exact PDF and the Gaussian approximation for $E_b/N_0 = -5$ dB at $\Re(Z_m^{(f)}) = 0$ increased to 5.15×10^{-2}. Thus, there are deviations between the derived PDF and the exact results, especially in a higher E_b/N_0 region.

2.6.2 ZF detection

Zero forcing (ZF) detection uses the Moore-Penrose inverse of channel matrix to suppress the CCI between each transmitted signals. Focusing on the MMIMO channel model in (2.11), the relationship between $\mathbf{X}_f$ and $\mathbf{Y}_f$ is expressed as a linear matrix equation. If the effects of noise is neglected, the transmitted symbols can be estimated from $\mathbf{Y}_f$ utilizing an inverse matrix operator as[25]

$$\hat{\mathbf{X}}_f = (\mathbf{H}_f^{\dagger}\mathbf{H}_f)^{-1}\mathbf{H}_f^{\dagger}\mathbf{Y}_f. \tag{2.28}$$

$\hat{\mathbf{X}}_f$ in (2.28) corresponds to $\mathbf{X}_f$, generated by the transmitter, and the receiver utilizes the symbol to estimate the message. However, the symbol still receive the effects of thermal noise, caused by the MMIMO channel. If $\mathbf{Y}_f$ in (2.11) is substituted in (2.28), $\tilde{\mathbf{X}}_f$ can be rewritten as

$$\hat{\mathbf{X}}_f = \mathbf{X}_f + \mathbf{G}_f^{-1}\mathbf{H}_f^{\dagger}\mathbf{W}_f, \tag{2.29a}$$

$$= \mathbf{X}_f + \mathbf{Z}_f. \tag{2.29b}$$

The last term, $\mathbf{Z}_{f,\mathrm{ZF}} = \mathbf{G}_f^{-1}\mathbf{H}_f^{\dagger}\mathbf{W}_f$, in (2.29) represents the EN of the detection,

and its value depends on the CFR and the noise vectors of the MMIMO channel. Let $\mathbf{U}_f = \mathbf{G}_f^{-1}\mathbf{H}_f^{\dagger}$ with elements $U_{n,m}^{(f)}$, each element in $\mathbf{Z}_f$ becomes

$$Z_m^{(f)} = \sum_{n=1}^{N_r} U_{n,m}^{(f)} W_n^{(f)}. \tag{2.30}$$

2.6.3 MMSE detection

In frequency-selective channels with spectral nulls, the ZF detector tends to amplify the noise around the locations of the nulls. Therefore, if the detector is followed by a soft error correction decoder it can lead to numerical instability. Thus, MMSE detection be introduced to design the equalizer weight matrix that limits the noise enhancement due to channel inversion using information about SNR. The algorithm of MMSE detection aims to estimate $\hat{\mathbf{X}}$ while avoiding in instability [25], i.e.,

$$\tilde{\mathbf{X}}_f = \arg\min_{\mathbf{W}_f} E||\mathbf{X}_f - \mathbf{W}_f\mathbf{Y}_f||^2. \tag{2.31}$$

By setting partial derivatives for (2.31) to zero, the weight matrix becomes[27, 51]

$$\tilde{\mathbf{W}}_f = \left(\mathbf{H}_f^H\mathbf{H}_f + \frac{N_o}{E_s}\mathbf{I}\right)^{-1}\mathbf{H}_f^H, \tag{2.32}$$

where $N_0 = 2\sigma_w^2$ denotes the noise energy density and $\mathbf{I} \in \mathbb{Z}^{N_t \times N_t}$ is an $N_t \times N_t$ identity matrix. MMSE detection employs $\tilde{\mathbf{W}}_f$ to estimate the transmitted symbols from $\mathbf{Y}_f$. Let $\mathbf{K}_f = \mathbf{H}_f^H\mathbf{H}_f + \frac{N_o}{E_s}\mathbf{I}$, the outcome from the detection is generated as

$$\tilde{\mathbf{X}}_f = \mathbf{K}_f^{-1}\mathbf{H}_f^H\mathbf{Y}_f. \tag{2.33}$$

Although $\tilde{\mathbf{X}}_f$ in (2.33) matches the transmit symbol, the outcome from the equation is still scaled by the diagonal component of the weigh matrix. If $\mathbf{Y}_f$ in (2.11) is substituted in to (2.33), $\tilde{\mathbf{X}}_f$ can be rewritten as

$$\tilde{\mathbf{X}}_f = \acute{\mathbf{K}}_f\mathbf{X}_f + \breve{\mathbf{K}}_f\mathbf{W}_f, \tag{2.34}$$

where $\breve{\mathbf{K}}_f = \mathbf{K}_f^{-1}\mathbf{H}_f^H$ and $\acute{\mathbf{K}} = \breve{\mathbf{K}}_f\mathbf{H}_f$. According to (2.34), each m-th element in $\tilde{\mathbf{X}}_f$ can be expressed as

$$\tilde{X}_m^{(f)} = \acute{K}_{m,m}^{(f)} X_m^{(f)} + \sum_{n=1,n\neq m}^{N_t} \acute{K}_{m,n}^{(f)} X_n^{(f)} + \sum_{n=1}^{N_t} \breve{K}_{m,n}^{(f)} W_n^{(f)}. \tag{2.35}$$

Since X_m in the first term of (2.35) is multiplied by $\acute{K}_{m,m}^{(f)}$, $\tilde{X}_m^{(f)}$ is then divided by the

variable to normalize the first term in the equation, i.e.,

$$\hat{X}_m^{(f)} = \frac{\tilde{X}_m^{(f)}}{\acute{K}_{m,m}^{(f)}}. \tag{2.36}$$

In general, the EN samples in $\hat{X}_m^{(f)}$ exhibits a complex-valued, zero-mean, Gaussian distribution, and the mathematical expression for the EN can be derived by substituting $\tilde{X}_m$ from (2.35) into (2.36). As a result, $\hat{X}_m^{(f)}$ becomes

$$\hat{X}_m^{(f)} = X_m^{(f)} + \underbrace{\frac{\sum_{n=1,n\neq m}^{N_t} \acute{K}_{m,n}^{(f)} X_n^{(f)}}{\acute{K}_{m,m}^{(f)}} + \frac{\sum_{n=1}^{N_r} \breve{K}_{m,n} W_n^{(f)}}{\acute{K}_{m,m}^{(f)}}}_{Z_m^{(f),\mathrm{MMSE}}}, \tag{2.37a}$$

$$\hat{X}_m^{(f)} = X_m^{(f)} + Z_m^{(f),\mathrm{MMSE}}. \tag{2.37b}$$

2.7 Reducing computational complexity of MMSE detection

MMSE detection employs inverse matrix operation to generate the receive symbol and the dimension of $\mathbf{T}$ in (2.33) for the MMIMO system is very large, e.g., $\mathbb{Z}^{10\times 200}$. Generally, the inverse matrix operation employs the Cholesky factorization to decompose a matrix into an upper and a lower diagonal matrix. The matrixes are then utilized to evaluate the outcome of the inverse matrix operation[52]. The computational complexity of the Cholesky factorization is low since upper and lower diagonal matrixes require less arithmetic operators to evaluate the outcomes. However, the requirements in arithmetic operators to determine the outcome from the operation significantly increase according to the Gram matrix's size. Since N_r in the MMIMO system is chosen to be much larger than that of N_t, approximate inverse matrix operations and other direct methods can be efficiently applied for reducing the computational complexity[4, 25]. The approximation techniques are now summarized in this section. A number of variables are defined in this section to simplify the explanation. The variable $\mathbf{K}_f = \mathbf{H}_f^H \mathbf{H}_f + \frac{N_o}{E_s}\mathbf{I}$ was previously defined in section 2.6.3. The diagonal and off-diagonal components of $\mathbf{K}_f$ are denoted as $\mathbf{K}_{d,f}$ and $\mathbf{K}_{e,f}$, respectively. In addition, $\mathbf{K}_{l,f}$ denotes the lower triangle components of $\mathbf{K}_f$, and the upper triangle components is represents as $\mathbf{K}_{l,f}^{\dagger}$.

2.7.1 Neumann series expansion

The low-complexity MMSE detection using NSE was introduced in [52]. Inverse matrix operation in the work was approximated as a L-th order Taylor series, making a reduction in the computational complexity of MMSE detection. $\mathbf{K}_f^{-1}$ in (2.33) is now approximated

as

$$\mathbf{K}_f^{-1} \simeq \sum_{l=0}^{L-1} (-\mathbf{K}_{d,f}^{-1}\mathbf{K}_{e,f})^l \mathbf{K}_{d,f}^{-1}, \tag{2.38}$$

where the order of Taylor series is denoted as L. The difference between the exact outcome from the inverse matrix operation and the approximation in (2.38) depends on the order L of the Taylor series, and the order should large enough the minimize the difference. However, if $L > 4$, the NSE in (2.38) requires more arithmetic operators than that of the exact inverse matrix operation [25].

2.7.2 Gauss Seidel method

Gauss Seidel (GS) based MMSE detection was introduced in [51], and the authors employed an algorithm to evaluate the outcome for the detector without using inverse matrix operation. An equation to generate the initial solution to the GS method was also proposed in the work for enhancing the convergence rate. To simplify the explaination, $\mathbf{K}_f$ in (2.33) is separated into three terms as

$$\mathbf{K}_f = \mathbf{K}_{d,f} + \mathbf{K}_{l,f} + \mathbf{K}_{l,f}^{\dagger}. \tag{2.39}$$

$\mathbf{K}_{d,f}$ and $\mathbf{K}_{l,f}$, in (2.39), contain the diagonal components and the lower triangle components of $\mathbf{K}_f$, respectively. The last term in the equation demonstrates the upper elements in $\mathbf{K}_f$. GS based MMSE detection utilizes $\mathbf{Y}_f$ to estimate the transmit symbol iteratively, and the outcome for the k-th iteration is determined from $\mathbf{Y}_f$ and the outcome from the previous iteration, $\hat{\mathbf{X}}_f^{(k-1)}$, as

$$\hat{\mathbf{X}}_f^{(k)} = (\mathbf{K}_{d,f} + \mathbf{K}_{l,f})^{-1}(\mathbf{Y}_f - \mathbf{K}_{l,f}^{\dagger}\hat{\mathbf{X}}_f^{(k-1)}). \tag{2.40}$$

Due to the fact that $\mathbf{K}_f$ of the MMSE detection is a Hermitian positive definite, the outcome from the algorithm converge to $\mathbf{X}_f$[51]. Although inverse matrix operation is still required by (2.40), the operational complexity for the operation is small since the combination of $\mathbf{K}_{d,f}$ and $\mathbf{K}_{l,f}$ is a lower triangle matrix. Focusing on the first iteration, $k = 1$, the detector requires an initial solution $\hat{\mathbf{X}}_f^{(0)}$ to estimate the transmitted symbol. The authors, in [51], introduced an equation to evaluate the initial solution $\hat{\mathbf{X}}_f^{(0)}$ to enhance the convergence rate as

$$\hat{\mathbf{X}}_f^{(0)} = \mathbf{K}_{d,f}^{-1}\mathbf{H}^{\dagger}\mathbf{Y}. \tag{2.41}$$

Since $\mathbf{K}_{d,f}$ is a diagonal matrix, the computational complexity of the operation to generate $\mathbf{K}_{d,f}^{-1}$ is small. The GS method can be efficiently used to reduce the computational complexity of the detection from $\mathcal{O}(N_t^3)$ to $\mathcal{O}(N_t^2)$, which is lower than that of NSE algorithm. Moreover, its BEP performance close to the classical MMSE detection with a small number of iterations [51].

2.7.3 Jacobi iteration

A joint MMSE detection, utilizing Jacobi iteration (JI) was proposed for the MMIMO system in [53]. Let $\tilde{\mathbf{Y}}_f = \mathbf{H}_f^{\dagger}\mathbf{Y}_f$, $\hat{\mathbf{X}}_f$ in (2.32) can be rewritten as

$$\hat{\mathbf{X}}_f = \mathbf{K}_f^{-1}\tilde{\mathbf{Y}}_f. \tag{2.42}$$

The detector estimates $\mathbf{K}_f$ and $\tilde{\mathbf{Y}}_f$ from the received symbols and CFR, and the outcome of the process is then utilized to evaluate the transmit symbols iteratively. The outcome from the first iteration $\hat{\mathbf{X}}_f^{(0)}$ is generated as

$$\hat{\mathbf{X}}_f^{(0)} = \mathbf{K}_{d,f}^{-1}\tilde{\mathbf{Y}}_f. \tag{2.43}$$

The symbol is then utilized to evaluate $\mathbf{R}_f^{(0)}$ as

$$\mathbf{R}_f^{(0)} = \tilde{\mathbf{Y}}_f - \mathbf{K}_f\hat{\mathbf{X}}_f^{(0)}. \tag{2.44}$$

For the second iteration, the symbol $\hat{\mathbf{X}}_f^{(1)}$ is generated from the outcome from the first iteration, i.e.,

$$\hat{\mathbf{X}}_f^{(1)} = \hat{\mathbf{X}}_f^{(0)} + u\mathbf{R}_f^{(0)} + \mathbf{K}_{d,f}^{-1}(\mathbf{R}_f^{(0)} - u\mathbf{P}_f^{(0)}), \tag{2.45}$$

where $\mathbf{P}_f^{(0)}$ and u are given by

$$\mathbf{P}_f^{(0)} = \mathbf{K}_f\mathbf{R}_f^{(0)}, \tag{2.46a}$$

$$u = \frac{\mathbf{R}_f^{(0),\dagger}\mathbf{R}_f^{(0)}}{\mathbf{P}_f^{(0),\dagger}\mathbf{R}_f^{(0)}}. \tag{2.46b}$$

The detection estimates the outcome for the k-th iteration from $\tilde{\mathbf{Y}}_f$ and $\hat{\mathbf{X}}_f^{(k-1)}$ as

$$\hat{\mathbf{X}}_f^{(k)} = \mathbf{K}_{d,f}^{-1}((\mathbf{K}_{d,f} - \mathbf{K}_f)\hat{\mathbf{X}}_f^{(k-1)} + \tilde{\mathbf{Y}}_f). \tag{2.47}$$

2.8 Coded-OFDM-MMIMO system

Fig. 2.11 demonstrates a block diagram of coded-OFDM-MMIMO system, using channel coding technique to reduce the BEP in data communication. The operation of the M-QAM mapper and the OFDM modulator in the transmitter is identical to that of the OFDM-MMIMO system, described in section 2.1. However, the information bits, $\mathbf{d}$, at the transmitter is separated into N_t sub-stream, and the information is then row-wise transformed into the code word $\mathbf{c} \in \mathbb{R}^{N_t \times \log_2(M)N_f/R}$, utilizing channel encoders. R denotes the coding rate, which is the ratio of data block size to code word size. The value of R is less than 1 due to the size of $\mathbf{c}$ is R times larger than that of $\mathbf{d}$. The codeword is then delivered through the OFDM-MMIMO system instead of the information bits to enhance the reliabilities of the data communication. The rest of the operation at the transmitter

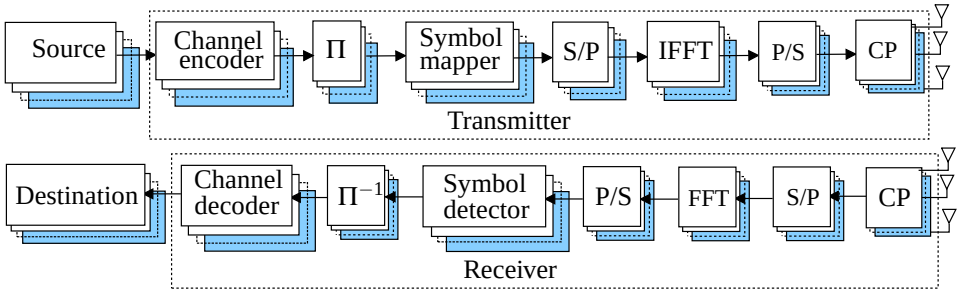

Figure 2.11: Block diagram of coded-OFDM-MMIMO system.

and the receiver is identical to that of the uncoded-OFDM-MMIMO system. If turbo code, LDPC, or other turbo-like codes are chosen to the system, the receiver uses the soft-output symbol detection to produce the LLR $\mathbf{\Lambda} \in \mathbb{R}^{N_t \times \log_2(M) N_f / R}$ corresponding to $\mathbf{Y}$. This soft-information is evaluated by the iterative decoder to estimate the receive information bits $\hat{\mathbf{d}}$. It is worth noting that the MMIMO channel model of the coded-OFDM-MMIMO system is identical to that of the OFDM-MMIMO system, described in the section 2.4. However, the size of code word is R times larger than that of the raw information. Thus, the noise variance for this case is now redefined as

$$\sigma^2_{w,\text{coded}} = \frac{N_t E_s}{2 \log_2(M) R \gamma_b}. \tag{2.48}$$

2.9 Low-density parity-check code

Data communications is generally interfered by the additive white Gaussian noise (AWGN), resulting in reliability degradation. The BEP for the system dramatically increases according to the average noise power and the system requires more transmit energy to maintain the BEP. Therefore, channel coding technique is recommended to the communication system for reducing the BEP[6]. In general, the transmitter utilizes a channel encoder to produce the code word corresponding to the information bits. The raw information is firstly packed into several K-bits groups. A channel coding algorithm is then chosen to generate the N-bits of code words, corresponding to the raw information in each block. Since redundancy bits are added to the information during the encoding process, size of the code word is larger than that of the original information. Let K and N denotes the block size of the information bits and the code word size, respectively, the code rate $R = K/N$ is employed to represent the ratio of the size of the raw information bits and that of the code word. The outcome from the channel encoder is then employed by the transmitter instead of the raw information bits. Although, the size of code word is significantly larger than the number for the original information bits, the redundancy bits in the code word can be utilized by the receiver for bit error correction or detection. The receiver uses channel decoder to estimate the transmitted bits from the received code words. During the operation, the redundancy bits in the code word can be used to detect

or correct errors in data communications. If E_b/N_0 of the system is large enough, channel coding techniques can be significantly detect or correct its information bits.

A number of channel coding techniques have been developed during the pass decades, and they are recommended for communication standards [6]. Turbo code and tail biting convolutional code are efficient channel coding techniques which provide an excellent BEP performance to the system. The techniques were recommended for LTE cellular networks [54]. However, LDPC provides both high coding gain and low-complexity decoder and polar code is more suitable for short frame transmission. Furthermore, the computational complexity of LDPC is lower than that of turbo code [55]. As a result, LDPC and polar codes has been recently applied for data and control channel for the 3GPP 5G NR cellular networks. The 5G NR LDPC codes are chosen in this research work to evaluate the BER performance of the coded-OFDM-MMIMO system. The principle of the channel coding technique and the 5G NR LDPC are then briefly explained in the next sub-sections.

2.9.1 Low-density parity-check code

Low-Density Parity-check (LDPC) code is a linear block code, which was firstly proposed in 1962 by R.G Gallager[32]. The channel coding technique was reintroduced again by D. MacKay in 1998[33]. The BEP performance for the channel coding technique significantly close to the Shannon's capacity limit[56]. As a result, LDPC has been widely recommended for data communications. Generally, LDPC employ parity check matrix $\tilde{\mathbf{H}} \in \mathbb{Z}^{N \times N-K}$ to represent the structure of the channel encoder. The construction of $\tilde{\mathbf{H}}$ can be done through random process, rather than uniform operation[33]. The mean column weight is chosen to be larger than two, whereas each row in the matrix is designed to obtain a uniform weight as possible. As the results, the parity-check matrix becomes a sparse matrix, where the number of non-zeros components in each row and column is less than that of zeros.

In addition, Non-zero components in $\tilde{\mathbf{H}}$ and the operation of LDPC encoder are also demonstrated by using a bipartite graph, named the Tanner graph. Nodes in the Tanner graph are separated into two groups, i.e., check nodes (CN) $\mathbf{N}_c \in \mathbb{Z}^{N-K \times 1}$ and variable nodes (VN) $\mathbf{N}_v \in \mathbb{Z}^{N \times 1}$. The variable nodes in the graph represents all code words, which are required by the detector to produce the syndrome. The CN's size is identical to the size of the column of $\tilde{\mathbf{H}}$. The vertexes between variable nodes and check nodes demonstrate the operation of the LDPC's decoder to estimate syndrome from code words. Fig. 2.12 shows an example of a Tanner graph for the following parity check matrix

$$\tilde{\mathbf{H}} = \begin{bmatrix} 1 & 1 & 0 & 1 & 1 & 0 & 0 \\ 1 & 0 & 1 & 1 & 0 & 1 & 0 \\ 0 & 1 & 1 & 1 & 0 & 0 & 1 \end{bmatrix}. \tag{2.49}$$

The number of one in each row and column of $\tilde{\mathbf{H}}$ is fixed at w_c and w_r, respec-

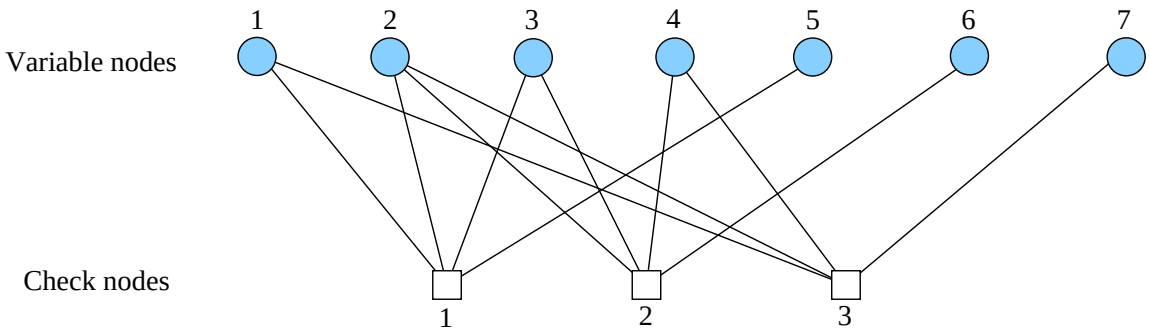

Figure 2.12: Sample of Tanner graph of $\tilde{\mathbf{H}}$ in (2.49).

tively. LDPC uses a symbol "(N, w_c, w_r)" to describe the structure of channel encoder and decoder. LDPC's parity check matrix can be created utilizing random and algebraic construction[6]. The transmitter employs LDPC encoder to produce the code word. Let $\mathbf{m} = \{m_1, m_2, \ldots, m_K\}$ be the information bits at the transmitter, parity check bits $\{c_j\}_{j=1}^{N-K}$ are generated by the encoder and they are combined to the information bits to produce the code word as $\mathbf{c} = \{c_1, c_2, \ldots, c_{N-K}\, m_1, m_2, \ldots, m_K\}$. The LDPC encoder uses generator matrix $\tilde{\mathbf{G}}$ to produce the code words as [6]

$$\mathbf{c} = \mathbf{m}\tilde{\mathbf{G}}. \tag{2.50}$$

The value of $\tilde{\mathbf{G}}$ corresponds to $\tilde{\mathbf{H}}$, making $\mathbf{c}\tilde{\mathbf{H}}^T = 0$. Focusing on a systematic code, where the parity check matrix is constructed as

$$\tilde{\mathbf{H}} = [\mathbf{I}_{N-K} : \mathbf{P}^T], \tag{2.51}$$

where $\mathbf{I}_k$ is an $(k \times k)$ identity matrix. $\mathbf{P}$ is an arbitrary matrix, which is defined by the LDPC code. The parity check matrix can be produced from the parity check matrix as

$$\tilde{\mathbf{G}} = [\mathbf{P} : \mathbf{I}_K]. \tag{2.52}$$

It is worth nothing that if a non-systematic code is applied to the system, the parity check matrix is transformed into a systematic form utilizing Gauss-jordan elimination on GF(2) domain[6]. Furthermore, the computational complexity for the LDPC encoder in (2.50) significantly increases according to the size of $\tilde{\mathbf{G}}$. Thus, a lower-complexity encoding algorithms can be utilized by the channel encoder for producing the code word directly from the parity-check matrix[6].

The receiver estimates the LLR from the received symbol and the LDPC decoder uses the information to recover the transmitted information. A number of decoding algorithms for LDPC have been developed, including bit-flipping, sum-product, and min-sum decoding algorithms[6]. These algorithms use parity check matrix to recover the transmitted information bits. Initially, the receiver estimates the LLR from the received symbol and stores the information in the VN. Next, the extrinsic information for the

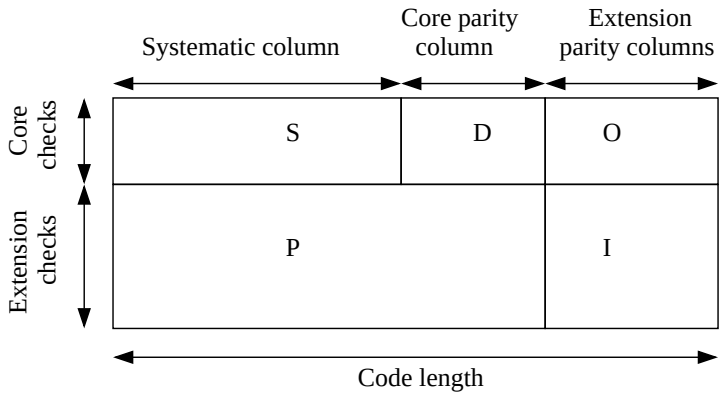

Figure 2.13: Parity check matrix for 5G NR LDPC.

CN is then evaluated utilizing the LLR from the VN which is connected to the CN. The LLR on the VN is then updated utilizing the extrinsic information from the linked CN. The total LLR can be generated by the detector utilizing the LLR on the VN and the extrinsic information from CN. Then, the decoder continue to pass the LLR to the CN and continue the decoding operation again in the next iteration. The decoding process is done iteratively until the number of the iteration is less than the maximal iteration or the product of the code word and $\tilde{\mathbf{H}}^T$ becomes zero. If one of the criterion is met, the decoder employs the LLR from the VN and the extrinsic information at the CN to generate the total LLR and the information bits as the outcome of the detector.

2.9.2 LDPC standard for 5G NR

5G NR LDPC is a Quasi-cyclic LDPC, where the parity checked matrix is generated from a base graph (BG) or protograph. The structure of the BG can be separated into five sub-matrixes as described in Fig 2.13[57]. The sub-matrixes S and D denote the kernel of the base matrix, and they are utilized for producing the systematic bits and the first set of parity bits, respectively. The sub-matrixes O, I, and P are the extension, where the zeros matrix, the identity matrix, and the single parity check rows are contained in the matrix, respectively. 5G NR LDPC deploys 2 standard BGs for producing the codeword, i.e., BG 1 and BG 1. The BGs are chosen from the block size utilization and the coding rate [57], and the structure of the BG 1 and 2 are introduced in the Table 5.3.2-2 and 5.3.2-3 of the 3GPP TS 38.212 v15.2.0 standard [58]. Let Z be the lifting size, all zero-valued components in the BG are replaced by a $Z \times Z$ zeros matrix, whereas non-zero-valued components are replaced by and $Z \times Z$ cyclic permutation identity matrix. According to the standard in [58], the BG 2 is recommended for the data communications if $K \leq 292$, or $K \leq 3824$ and $R \leq 0.67$, or $R \leq 0.25$. Otherwise, the BG 1 is chosen to the channel encoder.

BEP performance of data communications using LDPC depends on parameters for channel coding technique, including block size utilization, coding rate, as well as the number of iteration for iterative decoder. Fig. 2.14a shows the bit error rate (BER) of

single-input, single-output (SISO) data communications over an AWGN channel, using BPSK modulation and 5G NR LDPC. A 1/2 coding rate uplink 5G NR LDPC was chosen to the simulation. The revision number and the number of layer were 0 and 1, respectively. The block size utilization was 1200 bits and the number of iteration I was $\{1, 10, 20, 30\}$. According to the results, the system, using a higher iteration, required less E_b/N_0 to maintain their BER. Focusing on the system with $I = 10$, the BER at $E_b/N_0 = 1.8$ dB was 3.87×10^{-3}. On the other hand, the number for the system using $I = 30$ was 4.23×10^{-6}.

In addition, the effects on choosing block size and code rate in LDPC are demonstrated in Fig. 2.14b. The number of iteration, I, was 30, and the block size utilization was 600, 1200, and 2400 bits. The coding rate was 1/2 and 3/4. The results confirm that the increasing in N makes an improvement in BER performance to the system. The BER for the system, where $K = 600$ and $R = 1/2$ were chosen to the system, at $E_b/N_0 = 1.2$ dB was 1.97×10^{-2}, and the BER was 1.95×10^{-2} higher than that of the number for the system with $K = 2040$. Furthermore, the system, using a lower coding rate, obtained a higher BER performance. The system with $R = 1/2$ and $K = 2400$ required $E_b/N_0 = 1.35$ dB to maintain the BER of 10^{-5}, whereas the system using $R = 3/4$ required 2.81 dB of E_b/N_0 for the operation.

2.10 Classical soft-output linear symbol detection

LDPC decoder employs iterative detection algorithms to estimate the transmitted message from the received information, and soft-output symbol detector is utilized by the receiver to produce the LLRs for the operation. Focusing on a coded-OFDM-MMIMO system where a Gray-coded, M-QAM is chosen to the transmitter, the q-th tuple of the LLRs for the m-th transmit antenna and the f-th sub-carrier, $\Lambda_{m,q}^{(f)}$, can be evaluated from in-phase or quadrature component of $\hat{X}_m^{(f)}$ employing the symbol-by-symbol maximum a posteriori (MAP) algorithm as

$$\Lambda_{m,q}^{(f)} = \ln\left(\frac{\sum\limits_{(\bar{X}_k, d_{m,q}^{(f)}=1} P(\Re(\hat{X}_m^{(f)})|d_{m,q}^{(f)} = 1, \Re(X_m^{(f)}) = \bar{X}_k)}{\sum\limits_{\bar{X}_k, d_{m,q}^{(f)}=0} P(\Re(\hat{X}_m^{(f)})|d_{m,q}^{(f)} = 0, \Re(X_m^{(f)}) = \bar{X}_k)}\right), \tag{2.53}$$

where $\bar{X}_k$ is the referenced constellation point per dimension, i.e., $\{-3, -1, 1, 3\}$ for the 16-QAM. The equation for quadrature component is identical to that of the in-phase component in (2.53). Thus, the equation is neglected in this section. $P(\Re(\hat{X}_m^{(f)})|d_{m,q}^{(f)} = \{0, 1\}, \Re(X_m^{(f)}) = \bar{X}_k)$ is a posterior probability (APP), which is determined from the PDF of $Z_m^{(f)}$. By assuming that the distribution of the received symbol is a $\mathcal{N}(0, \sigma_{z,m}^2)$,

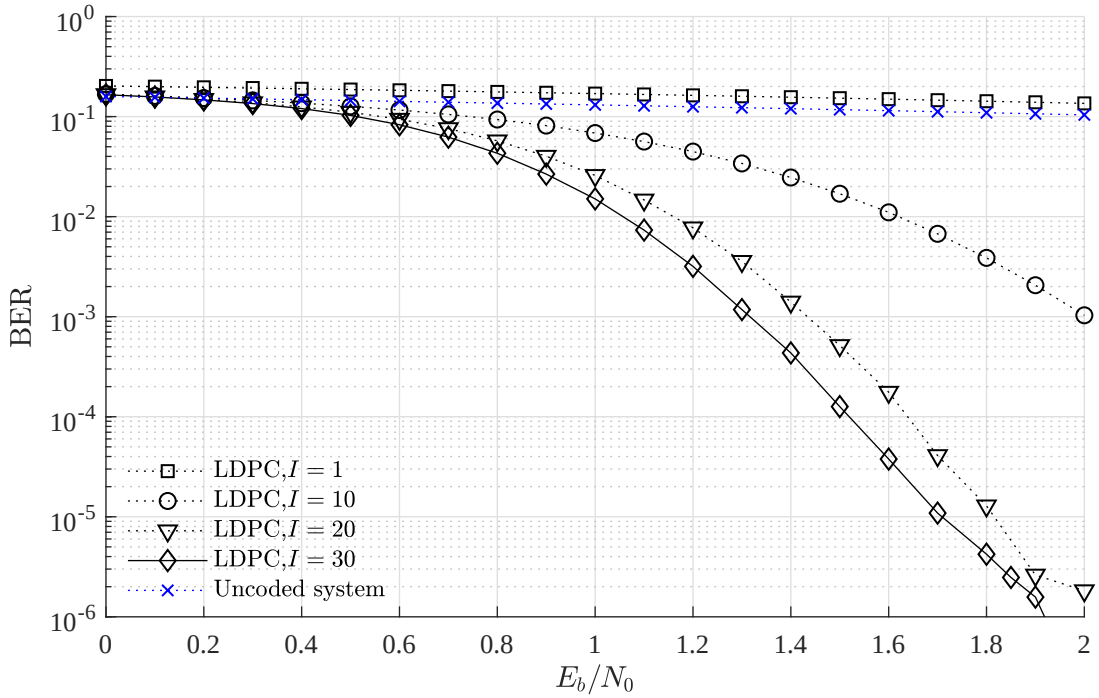

(a) Effects of I in 5G NR LDPC.

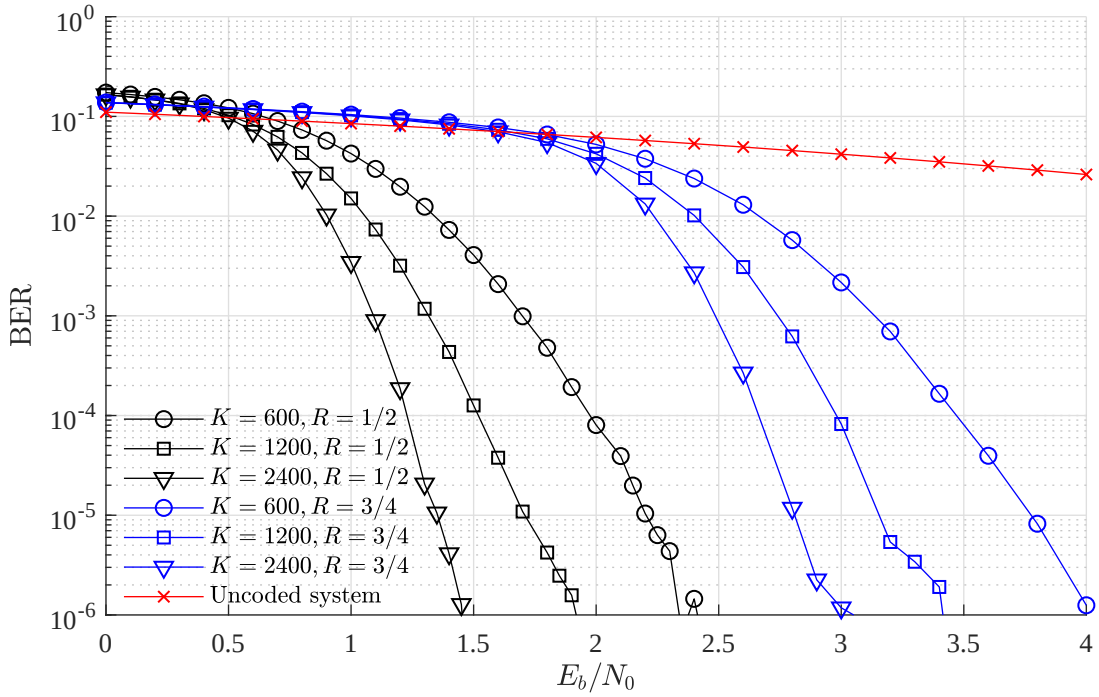

(b) BER for systems using different parameters.

Figure 2.14: BER of SISO system using 5G NR LDPC and BPSK modulation.

the APP becomes

$$P(\Re(\hat{X}_m^{(f)})|d_{m,q}^{(f)} = \{0,1\}, \Re(X_m^{(f)}) = \bar{X}_k) = \frac{1}{\sqrt{2\pi\sigma_{z,m}^2}} \exp\left(\frac{-(\Re(\hat{X}_m^{(f)}) - \bar{X}_k)^2}{2\sigma_{z,m}^2}\right). \quad (2.54)$$

If (2.54) is substituted in (2.53), the LLRs can be approximated as [36]

$$\Lambda_{m,q}^{(f)} = \frac{\min\limits_{\bar{X}_k, d_{m,q}^{(f)}=0} (\Re(\hat{X}_m^{(f)}) - \bar{X}_k)^2 - \min\limits_{\bar{X}_k, d_{m,q}^{(f)}=1} (\Re(\hat{X}_m^{(f)}) - \bar{X}_k)^2}{2\sigma_{z,m}^2}. \tag{2.55}$$

It is worth noting that the LLR computation in (2.55) requires the instantaneous noise variance $\sigma_{z,m}^2$ to estimate the outcome. In general, the distribution of CCI and EN in linear symbol detections is assumed to be the Gaussian distribution. Due to the fact that the variation of the outcome from the detection significantly changes according to the CFR for each sub channel. Thus, instantaneous noise variance $\sigma_{z,m}^2$ is generally chosen to (2.55) for estimating the LLR. The derivation of the instantaneous noise variance for MRC, ZF, and MMSE detections are summarized in appendix D.

Fig. 2.15 shows the BER of LDPC-OFDM-MMIMO system, where 16-QAM and linear symbol detections were chosen to the system. N_t was 10 and $N_r = \{50, 100, 200\}$. The results confirm that the system using MMSE detection received the highest BER performance, compared with other detections. Focusing on the 10×200 system, the MMSE detection required $E_b/N_0 = -8.83$ dB to achieve the BER at 10^{-4}. On the other hand, the E_b/N_0 for ZF and MRC detection were -8.78 and -7.87 dB, respectively. Moreover, the system utilizing a higher N_r obtained a lower BER. The 10×50 system, where MMSE detection was chosen to the mapper, required E_b/N_0 of -2.49 dB for maintaining the BER of 10^{-3}, which was 6.59 dB higher than that of the 10×200 system. It is worth noting that the outcome for the system using MRC, ZF, and MMSE detections in a system with a higher N_r was smaller. Focusing on the 10×50 system, the deviation in E_b/N_0 between MMSE and ZF detection at $BER = 10^{-4}$ was 0.16 dB. On the contrary, the difference in E_b/N_0 for the 10×200 system was smaller at 4.63×10^{-2}.

2.11 Summary

The operation of coded and uncoded OFDM-MMIMO system and MMIMO channel model are summarized in section 2.1 and 2.4, respectively. Due to the fact that the size of N_r is chosen to be much larger than the number for N_t, e.g. 10×100 or 10×1000, the diagonal and off-diagonal of the Gram matrix converge to a constant and a Gaussian distribution. The information regarding the properties of the Gram matrix is summarized in section 2.5. In addition, the block diagram of coded-OFDM-MMIMO system and LDPC are described in section 2.8 and 2.9, respectively.

It is worth noting that a number of methodologies introduced in this chapter will be reused by other chapters. The mathematical expressions for $Z_m^{(f)}$ in (2.25) and (2.29) are chosen to analyze the PDF of in-phase and quadrature components of $Z_m^{(f)}$, BEP, PDF of SINR, and outage probabilities of the OFDM-MMIMO system, using MRC and ZF detection in chapter 3 and 4, respectively. The approximations of the Gram matrix in

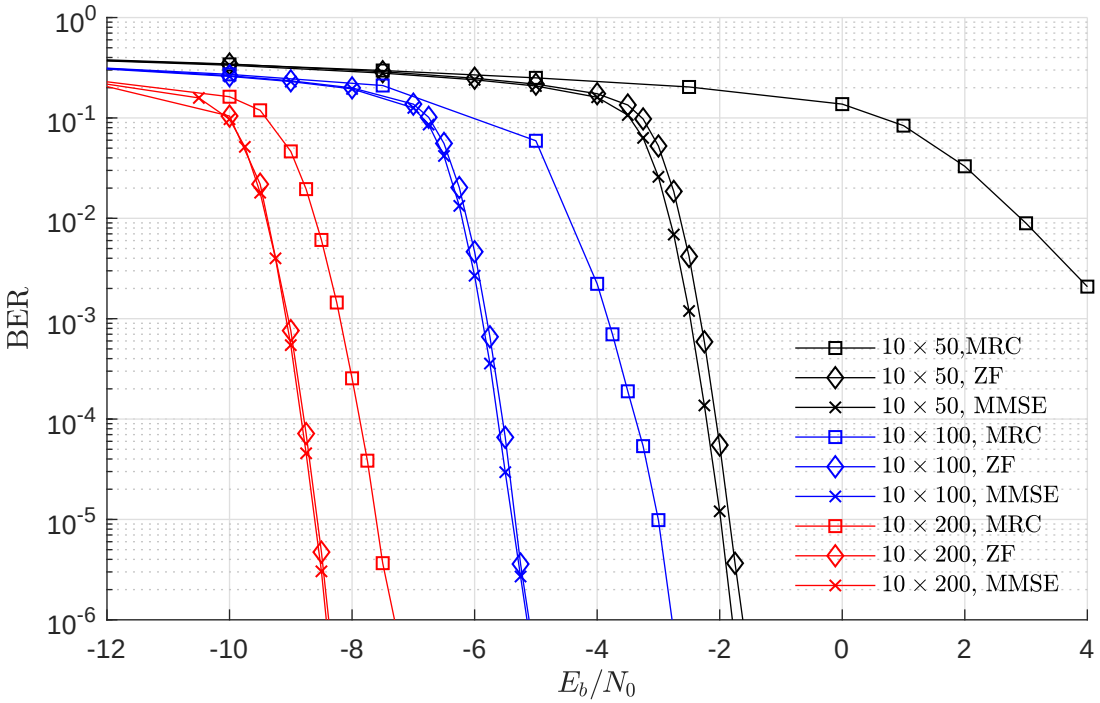

Figure 2.15: BER of coded-OFDM-MMIMO system using linear symbol detection.

section 2.5 and NSE in section 2.7.1 are additionally employed to simplify the derivation in the chapters. Moreover, the simulation results in section 2.6 motivated this research work to improve the operation of the soft-output MRC and ZF detection in chapter 5. According to the simulation results in section 2.6, the PDF of $\Re(Z_m^{(f)})$ for ZF detection in Fig. D.2 approached the Gaussian distribution. Thus, the $p_z(\Re(Z_m^{(f)}))$ is assumed to be the Gaussian distribution, and the closed-form expression of the noise variance in chapter 4 is then employed to simplify the operation of the soft-output ZF detector. On the other hand, there were deviations between the Gaussian distribution and the exact PDF of $\Re(Z_m^{(f)})$ for MRC detection in Fig. 2.10, especially at a higher E_b/N_0 region. As a result, the derived PDF of $\Re(Z_m^{(f)})$ for MRC detection is then chosen to enhance the BER performance of the soft-output MRC detection.

Chapter 3

Performance analysis of MRC detection

In chapter 2, the mathematical expression of the CCI and EN, i.e., $Z_m^{(f)}$ for MRC detection was analyzed in (2.25), where $Z_m^{(f)}$ was assumed to be the complex-valued, Gaussian distribution, $\mathcal{CN}(0, 2\sigma_z^2)$ and the noise variance per dimension, σ_z^2, was given by (2.27). However, the simulation results in Fig. 2.10 revealed deviations between the exact $p_z(\Re(Z_m^{(f)}))$ and the Gaussian distribution, especially at a higher E_b/N_0 region since the PDF of $X_k^{(f)}$ in (2.25) is a combination of impulse functions. Therefore, higher accurate PDFs of $Z_m^{(f)}$ for the OFDM-MMIMO system, utilizing Gray-coded, BPSK, QPSK, and M-QAM modulation are derived in this chapter. The mathematical expression of CCI and the EN in (2.25) and the joint probabilities of the random variables in the equation are employed to derive the PDFs, BEP, PDF of the SINR, and outage probabilities of the OFDM-MMIMO system.

Moreover, enhanced performance analysis for MRC detection is discussed in this chapter. $D_{m,m}^{(f)}$ and $H_{n,m}^{(f)}$ for the mathematical expression of $Z_m^{(f)}$ in (2.25) are correlated random variables, making small deviations between the simulation results and the original analysis for the $p_z(\Re(Z_m^{(f)}))$. Therefore, $D_{m,m}^{(f)}$ in the (2.25) is assumed to be a constant, and the PDF of $Z_m^{(f)}$ is then enhanced by utilizing a PDF transformation. Since the outcomes from the improved PDFs are more closer to the exact PDF than that of the original equations, the improved PDFs are then utilized for analyzing the performance of the OFDM-MMIMO system.

In addition, the asymptotic performance analysis of OFDM-MMIMO system using MRC detection is proposed in this chapter. By utilizing additional approximations, the PDF of $Z_m^{(f)}$ for BPSK and QPSK modulation can be approximated as the Gaussian distribution. Moreover, the PDFs of $\Re(Z_m^{(f)})$ and $\Im(Z_m^{(f)})$ for M-QAM approaches the Gaussian mixture model (GMM), i.e., a combination of scaled Gaussian distributions. As a result, the computational complexity of the performance analysis is significantly minimized by utilizing the approximation.

The derived PDFs and the performance analysis in this chapter were proposed in [59–

61], and the remainder of this chapter is organized as follows. The next section summarizes the methodology of the deriving PDF of the CCI and EN. The random variables in the equation are additionally defined in the section. The analysis from section 3.2 to 3.6 employs the mathematical expression of $Z_m^{(f)}$ to derive the PDF of $Z_m^{(f)}$, and other performance metrics for the system. Furthermore, the derived equations are additionally enhanced and simplified in section 3.7 and 3.8, respectively.

3.1 Derived PDFs of CCI and EN

In this section, the mathematical expression of $Z_m^{(f)}$ in (2.25) and the joint probabilities of random variables in the equation are utilized to derive the PDF of $\Re(Z_m^{(f)})$. The analysis for $\Im(Z_m^{(f)})$ is identical to that of $\Re(Z_m^{(f)})$ since the in-phase and quadrature components of $Z_m^{(f)}$ are symmetrical. As the results, the derivation for the $\Im(Z_m^{(f)})$ is neglected in this section. Since the first and the second terms in (2.25) are calculated from $H_{n,m}^{(f)}$, they are correlated and joint probabilities of the random variables cannot be applied to derive the PDF directly. Therefore, the equation is rewritten to avoid the correlation as

$$Z_m^{(f)} = \frac{\sum_{n=1}^{N_r} H_{n,m}^{(f),*} \left(\sum_{k=1,k\neq m}^{N_t} H_{n,k}^{(f)} X_k^{(f)} + W_n^{(f)} \right)}{D_{m,m}^{(f)}}. \tag{3.1}$$

The PDF of $Z_m^{(f)}$ is analyzed by utilizing joint probabilities for the random variables variables in (3.1) due to $H_{n,m}^{(f)}$, $X_m^{(f)}$, and $W_n^{(f)}$ in the numerator of (3.1) are independent random variables. Moreover, $D_{m,m}^{(f)}$ is generated from $H_{n,m}^{(f)}$ and the variable is assumed to be an independent random variable if the value of N_r is large enough [24]. The analysis for $p_z(\Re(Z_m^{(f)}))$ is now described in the next sub-sections, and a number of variables is defined in this section to simplify the explanation. If $\alpha_{n,m}^{(f)} = \sum_{k=1,k\neq m}^{N_t} H_{n,k}^{(f)} X_k^{(f)}$ and $\beta_{n,m}^{(f)} = \alpha_{n,m}^{(f)} + W_n^{(f)}$ are substituted in (3.1), $Z_m^{(f)}$ becomes

$$Z_m^{(f)} = \frac{\sum_{n=1}^{N_r} H_{n,m}^{(f),*} \beta_{n,m}^{(f)}}{D_{m,m}^{(f)}}. \tag{3.2}$$

Let $\eta_m^{(f)} = \sum_{n=1}^{N_r} H_{n,m}^{(f),*} \beta_{n,m}^{(f)}$ be the numerator in (3.2), $Z_m^{(f)}$ is rewritten as

$$Z_m^{(f)} = \frac{\eta_m^{(f)}}{D_{m,m}^{(f)}}. \tag{3.3}$$

According to (3.3), $Z_m^{(f)}$ is a ratio of $\eta_m^{(f)}$ to $D_{m,m}^{(f)}$, and the PDF of $\Re(Z_m^{(f)})$ can be derived by employing the joint probabilities for the variables. The next sub-sections derive the PDFs of $\alpha_{n,m}^{(f)}$, $\beta_{n,m}^{(f)}$, $\eta_m^{(f)}$, and $Z_m^{(f)}$ of the OFDM-MMIMO system, using M-QAM. Since the PDFs of the variables for BPSK and QPSK modulation are different from the equation for M-QAM, the analysis for the modulation schemes is then summarized in section (3.1.5) separately.

3.1.1 Definition of $p_x(\Re(X_k^{(f)}))$ and $p_x(\Im(X_k^{(f)}))$

The PDFs of in-phase and quadrature elements of $X_k^{(f)}$ are discussed in this section. Squared-shaped, M-QAM constellation points are chosen to the mapper for generating $X_k^{(f)}$. If the symbol mapper utilizes the constellation points for 16-QAM in Fig. 2.2 to generate the transmit symbol, $\Re(X_k^{(f)})$ and $\Im(X_k^{(f)})$ are chosen from an element in $\{-3,-1,1,3\}$, and the number of constellation points per dimension is denoted as $M_\lambda = \log_2(M)$. Since the occurrence of the symbols is uniformly distributed across the constellation points, the PDF of the in-phase and the quadrature components of $X_k^{(f)}$ in (3.5) is defined as M_λ times summation of impulse functions, $\delta(.)$, i.e.,

$$p_x(\Re(X_k^{(f)})) = \frac{1}{M_\lambda}\sum_{v=1}^{M_\lambda}\delta(\Re(X_k^{(f)}) - \bar{X}_v), \tag{3.4a}$$

$$p_x(\Im(X_k^{(f)})) = \frac{1}{M_\lambda}\sum_{v=1}^{M_\lambda}\delta(\Im(X_k^{(f)}) - \bar{X}_v). \tag{3.4b}$$

$\{\bar{X}_v\}_{v=1}^{M_\lambda}$ represents one of the constellation points per dimension. Thus, $\bar{X}_v$ for 16-QAM is chosen from $\{-3,-1,1,3\}$.

3.1.2 Derived PDF of $\alpha_{n,m}^{(f)}$

Since $\alpha_{n,m}^{(f)}$ in (3.2) is a combination of product of $H_{n,m}^{(f)}$ and $X_m^{(f)}$, the in-phase and quadrature components of $\alpha_{n,m}^{(f)}$ are expressed in terms of real arithmetic operators as

$$\Re(\alpha_{n,m}^{(f)}) = \sum_{k=1,k\neq m}^{N_t}\Re(H_{n,k}^{(f)})\Re(X_k^{(f)}) - \Im(H_{n,k}^{(f)})\Im(X_k^{(f)}), \tag{3.5a}$$

$$\Im(\alpha_{n,m}^{(f)}) = \sum_{k=1,k\neq m}^{N_t}\Re(H_{n,k}^{(f)})\Im(X_k^{(f)}) + \Im(H_{n,k}^{(f)})\Re(X_k^{(f)}). \tag{3.5b}$$

$\Re(\alpha_{n,m}^{(f)})$ and $\Im(\alpha_{n,m}^{(f)})$ in (3.5) are calculated from summation and subtraction of $U_n^{(f)} = \wp(H_{n,k}^{(f)})\wp(X_k^{(f)})$, where $\wp(.)$ represents the in-phase or quadrature operators. Since the PDFs of $\wp(H_{n,k}^{(f)})$ and $\wp(X_k^{(f)})$ are symmetric at $\wp(H_{n,k}^{(f)}) = 0$ and $\wp(X_k^{(f)}) = 0$, respectively, additions and subtractions of $U_{n,k}^{(f)}$ are identical. Thus, the in-phase and quadrature elements of $\alpha_{n,m}^{(f)}$ in (3.5) can be rewritten as a $(2N_t - 2)$ times summation of products of in-phase or quadrature components of $U_{n,k}^{(f)}$, i.e.,

$$\wp(\alpha_{n,m}^{(f)}) = \sum_{k=1}^{2N_t-2} U_{n,k}^{(f)}. \tag{3.6}$$

The PDF of $U_{n,k}^{(f)}$ can be derived from the PDF of $\wp(H_{n,k}^{(f)})$ and $\wp(X_k^{(f)})$, using the law

of total probability in (2-41) of [49], and results in

$$p_u(U_{n,k}^{(f)}) = \sum_{v=1}^{M_\lambda} p_u(U_{n,k}^{(f)}|\wp(X_k^{(f)}) = \bar{X}_v) p_x(\wp(X_k^{(f)}) = \bar{X}_v). \tag{3.7}$$

By utilizing PDF transformation in (A.8), the conditional probability $p_u(U_{n,k}^{(f)}|\wp(X_k^{(f)}) = \bar{X}_v)$ in (3.7) is given by

$$p_u(U_{n,k}^{(f)}|\wp(X_k^{(f)}) = \bar{X}_v) = \frac{1}{\sqrt{2\pi\sigma_h^2|\bar{X}_v|^2}} \exp\left(-\frac{(U_n^{(f)}/\bar{X}_v)^2}{2\sigma_h^2}\right). \tag{3.8}$$

If $p_u(U_{n,k}^{(f)}|\wp(X_k^{(f)}) = \bar{X}_v)$ from (3.8) and $p_x(\wp(X_k^{(f)}) = \bar{X}_v^{(f)}) = 1/M_\lambda$ are chosen to (3.7), $p_u(U_{n,k}^{(f)})$ becomes

$$p_u(U_{n,k}^{(f)}) = \frac{1}{M_\lambda\sqrt{2\pi\sigma_h^2}} \sum_{v=1}^{M_\lambda} \frac{1}{|\bar{X}_v|} \exp\left(-\frac{(U_{n,k}^{(f)}/\bar{X}_v)^2}{2\sigma_h^2}\right). \tag{3.9}$$

$p_u(U_{n,k}^{(f)})$ in (3.9) is then employed to derive the PDF of $\Re(\alpha_{n,m}^{(f)})$. According to (3.5), the variable is a $(2N_t - 2)$ times combination of $U_{n,k}^{(f)}$. Although the PDF of the variable can be obtained by utilizing $(2N_t - 2)$ times constitutional integral of $p_u(U_{n,k}^{(f)})$, the outcome from the integration depends on the size of N_t, whereas a closed-form expression is required for the analysis. Therefore, the characteristic function of $U_{n,k}^{(f)}$ is chosen to derive $p_\alpha(\Re(\alpha_{n,m}^{(f)}))$. The probability theory for deriving the PDF of random variables is summarized in section A.2. According to the methodology in the section, the characteristic function of $\Re(\alpha_{n,m}^{(f)})$ can be obtained by substituting $p_u(U_{n,k}^{\lambda})$ from (3.9) in (A.22). After using (2.338) in [62] to solve the integration, the characteristic function of $U_{n,k}^{(f)}$ becomes

$$\Phi_u(\omega) = \frac{1}{M_\lambda} \sum_{v=1}^{M_\lambda} \exp\left(-\frac{\sigma_h^2 \bar{X}_v^2 \omega^2}{2}\right). \tag{3.10}$$

Since $\Re(\alpha_{n,m}^{(f)})$ in (3.6) is a $(2N_t - 2)$ times summation of $U_{n,k}^{(f)}$, the characteristic function of $\alpha_{n,m}^{\lambda}$ is written as

$$\Phi_\alpha(\omega) = \Phi_u(\omega)^{2N_t-2}. \tag{3.11}$$

By substituting $\Phi_u(\omega)$ from (3.10) in (3.11), and using multinomial theorem in (A.32) to expand the equation, the characteristic function is expressed as

$$\Phi_\alpha(\omega) = \frac{(2N_t-2)!}{M_\lambda^{2N_t-2}} \sum_{\sum_{v=1}^{M_\lambda} k_v = (2N_t-2)} \frac{1}{\prod_{v=1}^{M_\lambda} k_v!} \exp\left(-\omega^2 \sum_{v=1}^{M_\lambda} \frac{k_v \sigma_h^2 \bar{X}_v^2}{2}\right), \tag{3.12}$$

where $\{k_v\}_{v=1}^{M_\lambda}$ in (3.12) is an integer that range from 0 to $(2N_t - 2)$. $\Phi_\alpha(\omega)$ in (3.12) demonstrates the characteristic function of $\Re(\alpha_{n,m}^{(f)})$, and the equation can be transformed

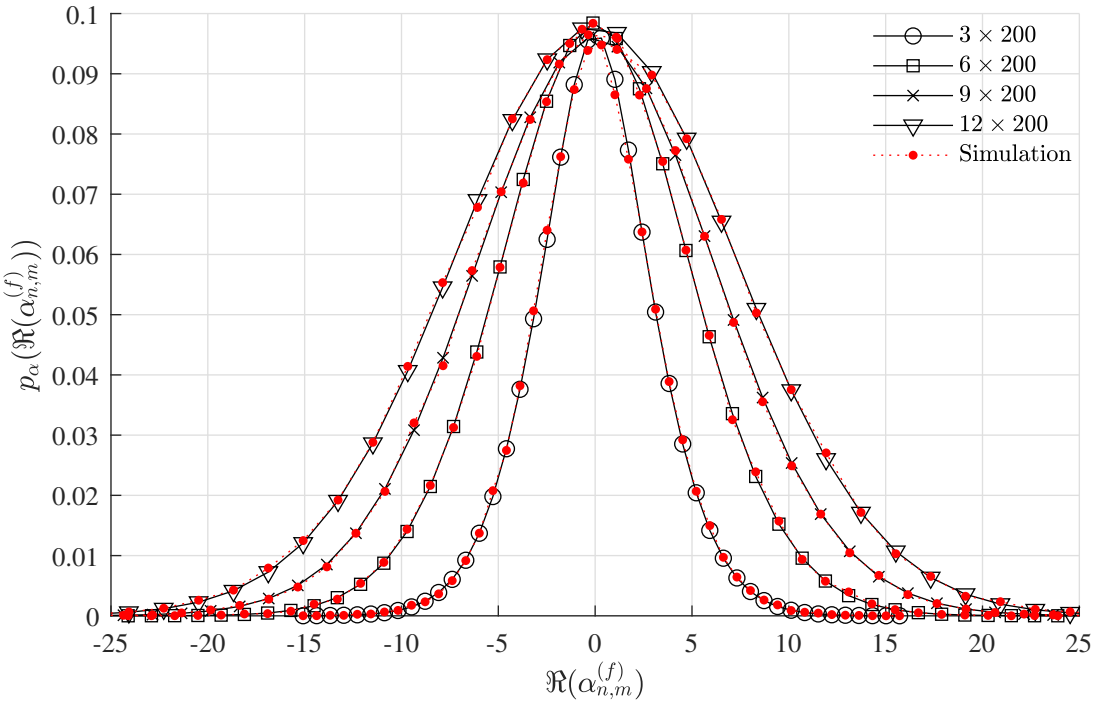

Figure 3.1: Derived PDFs of $\Re(\alpha_{n,m}^{(f)})$ in (3.13).

into the PDF by using (A.23) and (2.338) in [62]. As a result, $p_\alpha(\Re(\alpha_{n,m}^{(f)}))$ is given by

$$p_\alpha(\Re(\alpha_{n,m}^{(f)})) = \frac{(2N_t-2)!}{M_\lambda^{2N_t-2}} \sum_{\sum_{v=1}^{M_\lambda} k_v = 2N_t-2} \frac{\exp\left(-\frac{\Re(\alpha_{n,m}^{(f)})^2}{2\sigma_h^2 \sum_{v=1}^{M_\lambda} k_v \Re(\bar{X}_v)^2}\right)}{\left(\prod_{v=1}^{M_\lambda} k_v!\right)\left(2\pi\sigma_h^2 \sum_{v=1}^{M_\lambda} k_v \Re(\bar{X}_v)^2\right)^{1/2}}. \tag{3.13}$$

According to (3.13), the distribution for the $p_\alpha(\Re(\alpha_{n,m}^{(f)}))$ depends on the size of N_t and M_λ. Fig. 3.1 shows the outcomes from the derived PDF of $\Re(\alpha_{n,m}^{(f)})$ in (3.13) for the system using 16-QAM. $N_t = \{3, 6, 9, 12\}$ and $N_r = 200$. The system operated at $E_b/N_0 = -10$ dB and the constellation points for 16-QAM are as described in Fig. 2.2. Evidently, the derived PDFs significantly matched the simulation results, and the difference between the analytical and the exact PDF was marginal. Focusing on the 12×200 system, the derived $p_\alpha(\Re(\alpha_{n,m}^{(f)}))$ at $\Re(\alpha_{n,m}^{(f)}) = -10$ was 3.85×10^{-2}, and the number for the simulation result was 3.91×10^{-2}. Thus, the outcome from the derived equation was only 1.67% different from the simulation result. By employing the 2-sample Kolmogorov–Smirnov test with the significant level 5% to compare the derived PDFs with that of the exact results, the comparison demonstrated that the differences between the PDFs were negligible.

3.1.3 PDF of $\beta_{n,m}^{(f)}$

$\beta_{n,m}^{(f)}$ in (3.2) is a combination of $\alpha_{n,m}^{(f)}$ and $W_n^{(f)}$. Therefore, the characteristic function of $\Re(\beta_{n,m}^{(f)})$ can be derived from the product of characteristic functions of $\Re(\alpha_{n,m}^{(f)})$ and $\Re(W_n^{(f)})$ as

$$\Phi_\beta(\omega) = \Phi_\alpha(\omega)\Phi_w(\omega). \tag{3.14}$$

$\Re(W_n^{(f)})$ is a $\mathcal{N}(0,\sigma_w^2)$ and the characteristic function for the variable was proved in (A.25) as $\Phi_w(\omega)=\exp(-\sigma_w^2\omega^2/2)$. If $\Phi_\alpha(\omega)$ in (3.12) and $\Phi_w(\omega)$ are substituted in (3.14), $\Phi_\beta(\omega)$ becomes

$$\Phi_\beta(\omega)=\frac{(2N_t-2)!}{M_\lambda^{2N_t-2}}\sum_{\sum_{v=1}^{M_\lambda}k_v=(2N_t-2)}\frac{1}{\prod_{v=1}^{M_\lambda}k_v!}\exp\left(-\omega^2\left(\sum_{v=1}^{M_\lambda}\frac{k_v\sigma_h^2\Re(\bar{X}_v)^2}{2}+\frac{\sigma_w^2}{2}\right)\right). \tag{3.15}$$

Finally, the PDF of $\Re(\beta_{n,m}^{(f)})$ can be obtained by employing the characteristic function from (3.15) in (A.23). After using (2.338) in [62] to solve the integration, the $p_\beta(\Re(\beta_{n,m}^{(f)}))$ is given by

$$p_\beta(\Re(\beta_{n,m}^{(f)}))=\frac{(2N_t-2)!}{M_\lambda^{2N_t-2}}\sum_{\sum_{v=1}^{M_\lambda}k_v=2N_t-2}\frac{\exp\left(-\frac{\Re(\beta_{n,m}^{(f)})^2}{2(\sigma_h^2\sum_{v=1}^{M_\lambda}k_v\Re(\bar{X}_v)^2+\sigma_w^2)}\right)}{(\prod_{v=1}^{M_\lambda}k_v!)\left(2\pi(\sigma_h^2\sum_{v=1}^{M_\lambda}k_v\Re(\bar{X}_v)^2+\sigma_w^2)\right)^{1/2}}. \tag{3.16}$$

Evidently, $p_\beta(\Re(\beta_{n,m}^{(f)}))$ in (3.16) exhibits a combination of scaled Gaussian distributions, i.e.,

$$p_\beta(\beta_{n,m}^{\lambda})=\frac{(2N_t-2)!}{M_\lambda^{2N_t-2}}\sum_{\sum_{v=1}^{M_\lambda}k_v=2N_t-2}\frac{f_g(\Re(\beta_{n,m}^{(f)}),\sigma_{\beta,\{k\}})}{(\prod_{v=1}^{M_\lambda}k_v!)}, \tag{3.17}$$

where the zero-mean, Gaussian distribution with the variance $\sigma_{\beta,\{k\}}^2$ is denoted as $f_g(\Re(\beta_{n,m}^{(f)}),\sigma_{\beta,\{k\}})$, i.e.,

$$f_g(\Re(\beta_{n,m}^{(f)}),\sigma_{\beta,\{k\}})=\frac{1}{\sqrt{2\pi\sigma_{\beta,\{k\}}^2}}\exp\left(-\frac{\Re(\beta_{n,m}^{(f)})^2}{2\sigma_{\beta,\{k\}}^2}\right). \tag{3.18}$$

According to (3.17), the value of $\sigma_{\beta,\{k\}}^2$ for the Gaussian distribution depends on $\{k_v\}_{v=1}^{M_\lambda}$, and is given by

$$\sigma_{\beta,\{k\}}^2=\sigma_h^2\sum_{v=1}^{M_\lambda}k_v\Re(\bar{X}_v)^2+\sigma_w^2. \tag{3.19}$$

Fig. 3.2 compares the derived $p_\beta(\Re(\beta_{n,m}^{(f)}))$ from (3.17) for the system using various parameters. $N_t=\{5,10\}$ and $N_r=200$. The system operated at $E_b/N_0=\{0,-10\}$ dB. The analytical results are compared to that of the empirical, and the outcome from the comparison reveal a good matched between the PDFs. Focusing on the 10×200 system with $E_b/N_0=-10$dB, the derived PDF at $\Re(\beta_{n,m}^{(f)})=10$ was 5.47×10^{-2}, which was 7.85×10^{-4} different from the exact PDF. According to the 2-sample Kolmogorov–Smirnov test with the significant level 5%, the differences between the exact and the derived PDFs were insignificant.

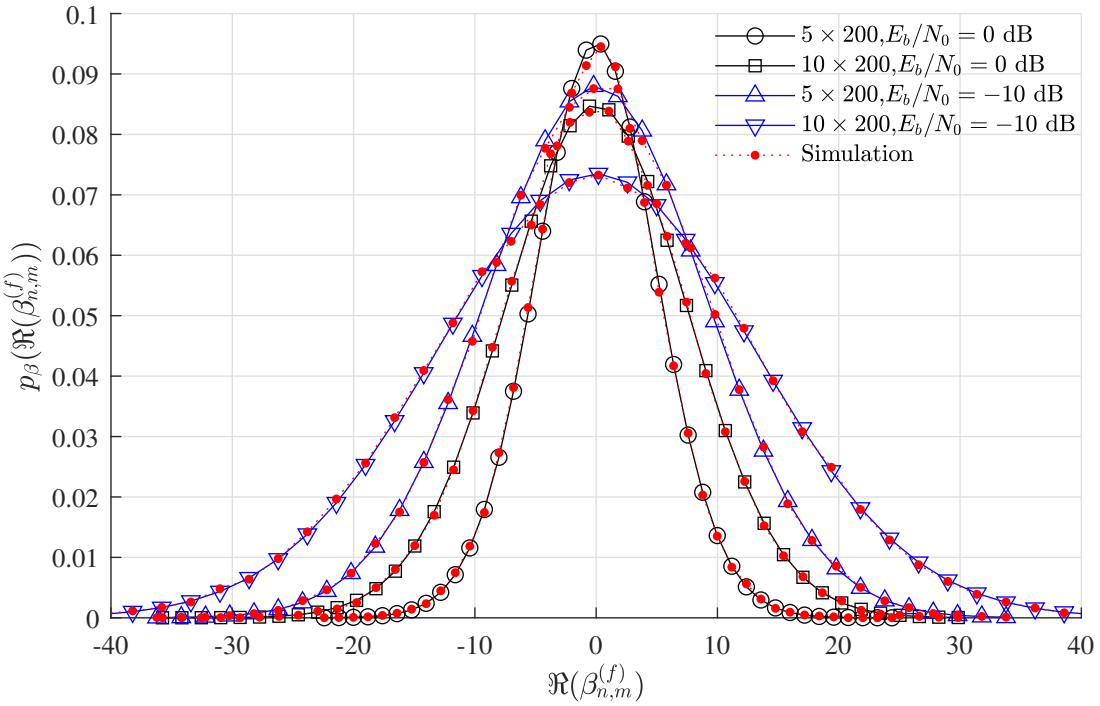

Figure 3.2: Derived PDFs of $\Re(\beta_{n,m}^{(f)})$ in (3.17).

3.1.4 Derived $p_\eta(\Re(\eta_m^{(f)}))$ and $p_z(\Re(Z_m^{(f)}))$

$\Re(\eta_m^f)$ in (3.3) is a $2N_r$ times summation of products of $\Re(H_{n,m}^{(f)})$ and $\Re(\beta_{n,m}^{(f)})$, and $p_\beta(\Re(\beta_{n,m}^{(f)}))$ in (3.17) is a summation of scaled Gaussian distributions. Since the PDF of sum of product of two zero-means Gaussian random variables was previously derived in (6.9) of [63], the equation can be employed to derive $p_\eta(\Re(\eta_m^{(f)}))$. After substituting $p_\beta(\Re(\beta_{n,m}^{(f)}))$ from (3.17) and $p_h(\Re(H_{n,m}^{(f)})) = \mathcal{N}(0, \sigma_h^2)$ in the equation, $p_\eta(\Re(\eta_m^{(f)}))$ becomes

$$p_\eta(\Re(\eta_m^{(f)})) = \frac{(2N_t-2)!}{\Gamma(N_r) M_\lambda^{2N_t-2}} \sum_{\sum_{v=1}^{M_\lambda} k_v = 2N_t-2} \frac{1}{\prod_{v=1}^{M_\lambda} k_v!} \times \exp\left(-\frac{|\Re(\eta_m^{(f)})|}{\sigma_h \sigma_{\beta,\{k\}}}\right) \sum_{i=1}^{N_r} \frac{(N_r+i-2)!}{2^{N_r+i-1} \sigma_h \sigma_{\beta,\{k\}} \Gamma(i)(N_r-i)!} \left(\frac{|\Re(\eta_m^{(f)})|}{\sigma_h \sigma_{\beta,\{k\}}}\right)^{N_r-i}. \tag{3.20}$$

According to (3.3), $Z_m^{(f)}$ is a ratio of $\eta_m^{(f)}$ to $D_{m,m}^{(f)}$. Although both of these variables are a function of CFR, they are assumed to be independent random variables if N_r is large enough[24]. Therefore, $p_z(\Re(Z_m^{(f)}))$ can be derived by using the joint probabilities of the variables in (A.19), and results in

$$p_z(\Re(Z_m^{(f)})) = \int_0^\infty D_{m,m}^{(f)} p_\eta(\Re(Z_m^{(f)}) D_{m,m}^{(f)}) p_d(D_{m,m}^{(f)}) dD_{m,m}^{(f)}. \tag{3.21}$$

By substituting the PDFs of $\Re(\eta_m^{(f)})$ and $D_{m,m}^{(f)}$ from (3.20) and (2.18), respectively, in (3.21) and using (3.351.3) in [62] to solve the integration, the PDF of in-phase component

for $Z_m^{(f)}$ of the system using M-QAM becomes

$$p_z^{M-\mathrm{QAM}}(\Re(Z_m^{(f)})) = \frac{(2N_t-2)!}{\Gamma(N_r)^2 M_\lambda^{2N_t-2}} \sum_{\sum_{v=1}^{M_\lambda} k_v=(2N_t-2)} \frac{\sigma_{\beta,\{k\}}^{N_r}}{\prod_{v=1}^{M_\lambda} k_v!} \times \sum_{i=1}^{N_r} \frac{\sigma_h^{N_r-i+1}(N_r+i-2)!(2N_r-i)!|\Re(Z_m^{(f)})|^{N_r-i}}{2^{2i-2}\Gamma(i)(N_r-i)!(\sigma_{\beta,\{k\}}+2\sigma_h|\Re(Z_m^{(f)})|)^{2N_r-i+1}}. \tag{3.22}$$

Fig. 3.3(a) and (b) show the derived $p_\eta(\Re(\eta_m^{(f)}))$ and $p_z(\Re(Z_m^{(f)}))$, generated from (3.20) and (3.22), respectively. N_t was 10 and $N_r = \{64, 256\}$. 16-QAM was chosen to the mapper, and the system operated at $E_b/N_0 = \{0, -10\}$ dB. The results confirm that the outcomes from the proposed PDFs matched the empirical results. Focusing on the 10×256 system, operating at $E_b/N_0 = -10$ dB, the derived $p_\eta(\Re(\eta_{n,m}^{(f)}))$ at $\Re(\eta_{n,m}^{(f)}) = 100$ was 5.96×10^{-2}, and the number was 4.37×10^{-4} different from the exact PDF. In addition, the derived $p_z(\Re(Z_m^{(f)}))$ at $\Re(Z_m^{(f)}) = 1$ was 5.15×10^{-2}, whereas the number for the exact PDF was 5.19×10^{-2}. Additionally, the 2-sample Kolmogorov–Smirnov test at the significant level 5% confirmed that the deviation between the PDFs was small. It is worth noting that the proposed PDFs is based on $\Re(Z_m^{(f)})$ in (3.3), where $\Re(\eta_m^{(f)})$ and $D_{m,m}^{(f)}$ are assumed to be uncorrelated. However, both variables are generated from CFR, making small deviations between the outcome from the derived $p_z(\Re(Z_m^{(f)}))$ and the exact results.

3.1.5 $p_z(\Re(Z_m^{(f)}))$ for BPSK and QPSK modulation

The PDF of $\Re(Z_m^{(f)})$ of the OFDM-MMIMO system with BPSK and QPSK modulation can be derived from joint probabilities of involving random variables, using the methodology in the previous section. If the modulation schemes are chosen to the system, $M_\lambda = 2$, $\{\bar{X}_v\} = \{-1, 1\}$, and $p_z(\Re(Z_m^{(f)}))$ for this case is less complex than that of M-QAM in (3.22). The characteristic function of $\Re(U_n^{(f)})$ and $\Re(\alpha_{n,m}^{(f)})$ were derived in (3.10) and (3.11), respectively. By substituting M_λ and $\{\bar{X}_v\}$ in the equations, the characteristic function of $\Re(\alpha_{n,m}^{(f)})$ for BPSK and QPSK modulation becomes

$$\Phi_\alpha^{\mathrm{BPSK}}(\omega) = \exp\left(-\frac{\sigma_h^2(N_t-1)\omega^2}{2}\right), \tag{3.23a}$$

$$\Phi_\alpha^{\mathrm{QPSK}}(\omega) = \exp\left(-\sigma_h^2(N_t-1)\omega^2\right). \tag{3.23b}$$

It is worth noting that the $\Phi_\alpha(\omega)$ for BPSK modulation in (3.23) is different from that of QPSK modulation due to there is no quadrature component in the constellation points for BPSK modulation. Thus, $\Re(\alpha_{n,m}^{(f)})$ in (3.5) is a (N_t-1) times combination of $U_n^{(f)}$ for this case. The characteristic function of $\Re(\alpha_{n,m}^{(f)})$ in (3.23) is then transformed to

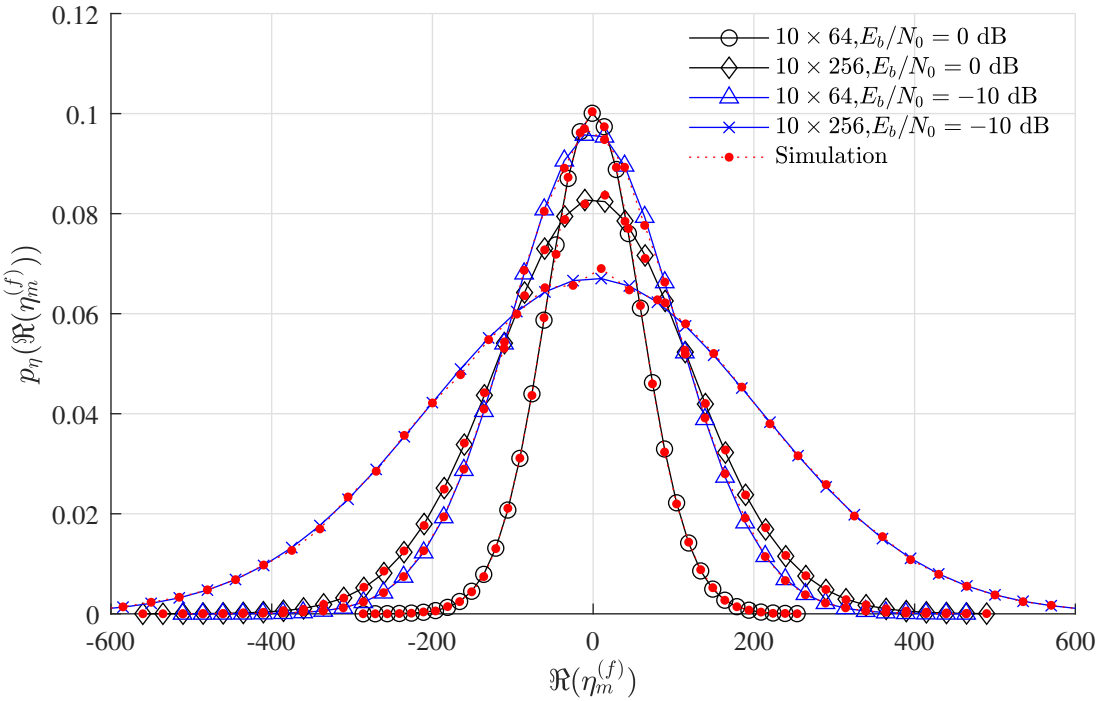

(a) Derived PDF of $\Re(\eta_m^{(f)})$ in (3.20).

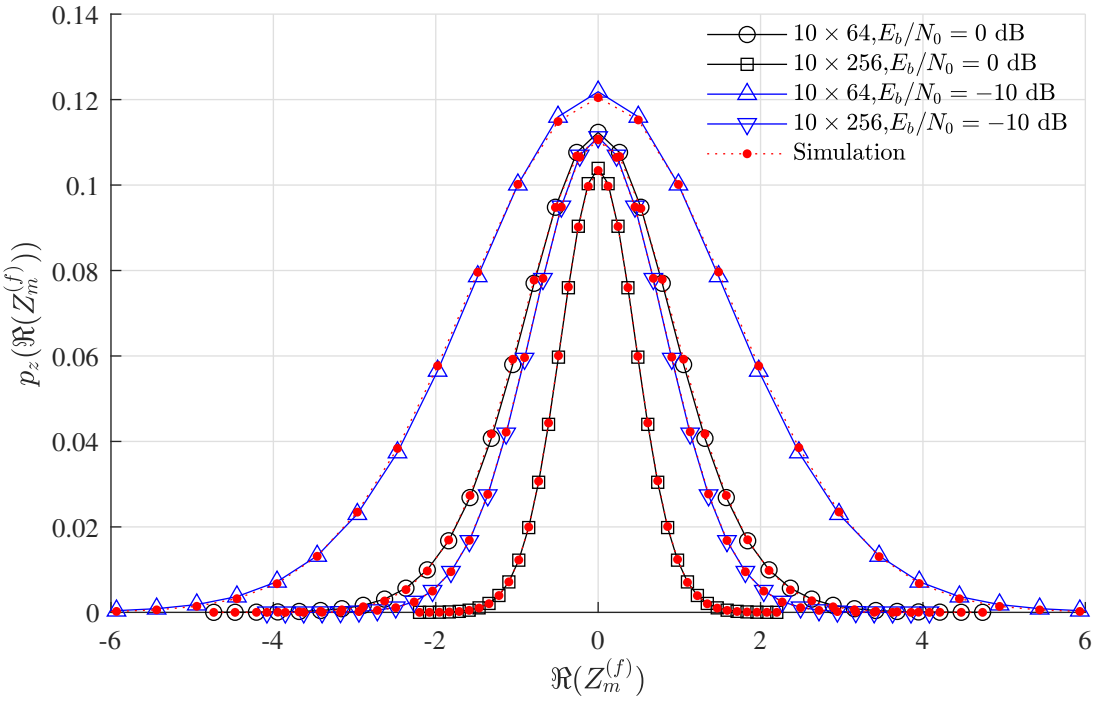

(b) $p_z(\Re(Z_m^{(f)}))$ in (3.22).

Figure 3.3: Derived PDFs of $\Re(\eta_m^{(f)})$ and $\Re(Z_m^{(f)})$ for 16-QAM.

$p_\alpha(\Re(\alpha_{n,m}^{(f)}))$ by utilizing (A.23) and (2.338) in [62], and results in

$$p_\alpha^{\text{BPSK}}(\Re(\alpha_{n,m}^{(f)})) = \frac{1}{\left(2\pi\sigma_h^2(N_t-1)\right)^{1/2}} \exp\left(-\frac{\Re(\alpha_{n,m}^{(f)})^2}{2\sigma_h^2(N_t-1)}\right), \tag{3.24a}$$

$$p_\alpha^{\text{QPSK}}(\Re(\alpha_{n,m}^{(f)})) = \frac{1}{\left(4\pi\sigma_h^2(N_t-1)\right)^{1/2}} \exp\left(-\frac{\Re(\alpha_{n,m}^{(f)})^2}{4\sigma_h^2(N_t-1)}\right). \tag{3.24b}$$

After substituting the $\Phi_\alpha(\omega)$ from (3.23) in (3.14), the characteristic function of $\Re(\beta_{n,m}^{(f)})$ is given by

$$\Phi_\beta^{\text{BPSK}}(\omega) = \exp\left(-\left(\frac{\sigma_h^2(N_t-1)+\sigma_w^2}{2}\right)\omega^2\right), \tag{3.25a}$$

$$\Phi_\beta^{\text{QPSK}}(\omega) = \exp\left(-\sigma_h^2(N_t-1)\omega^2\right). \tag{3.25b}$$

The $p_\beta(\Re(\beta_{n,m}^{(f)}))$ is then derived by using $\Phi_\beta^{\text{BPSK}}(\omega)$ from (3.25) in (A.23). By utilizing (2.338) in [62] to solve the integration, the PDFs become

$$p_\beta^{\text{BPSK}}(\Re(\beta_{n,m}^{(f)})) = \frac{1}{\left(2\pi\sigma_h^2(N_t-1)+2\pi\sigma_w^2\right)^{1/2}} \exp\left(-\frac{\Re(\beta_{n,m}^{(f)})^2}{2\sigma_h^2(N_t-1)+2\sigma_w^2}\right), \tag{3.26a}$$

$$p_\beta^{\text{QPSK}}(\Re(\beta_{n,m}^{(f)})) = \frac{1}{\left(4\pi\sigma_h^2(N_t-1)+2\pi\sigma_w^2\right)^{1/2}} \exp\left(-\frac{\Re(\beta_{n,m}^{(f)})^2}{4\sigma_h^2(N_t-1)+2\sigma_w^2}\right). \tag{3.26b}$$

Evidently, the PDF of $\Re(\beta_{n,m}^{(f)})$ for BPSK and QPSK modulation in (3.26) is a $\mathcal{N}(0,\sigma_\beta^2)$, where the variance is given by

$$\sigma_{\beta,\text{BPSK}}^2 = (N_t-1)\sigma_h^2+\sigma_w^2, \tag{3.27a}$$

$$\sigma_{\beta,\text{QPSK}}^2 = 2(N_t-1)\sigma_h^2+\sigma_w^2. \tag{3.27b}$$

The PDF of $\Re(\eta_m^{(f)})$ is then derived by substituting $p_\beta(\Re(\beta_{n,m}^{(f)}))$ from (3.26) and $p_h(\Re(H_{n,m}^{(f)})) = \mathcal{N}(0,\sigma_h^2)$ in Eq. (6.9) of [63], and results in

$$p_\eta^{\text{BPSK/QPSK}}(\Re(\eta_m^{(f)})) = \frac{1}{\sigma_h\sigma_\beta\Gamma(N_r)} \exp\left(-\frac{|\Re(\eta_m^{(f)})|}{\sigma_h\sigma_\beta}\right) \sum_{i=1}^{N_r} \frac{(N_r+i-2)!}{2^{N_r+i-1}(i-1)!(N_r-i)!} \left(\frac{|\Re(\eta_m^{(f)})|}{\sigma_h\sigma_\beta}\right)^{N_r-i}. \tag{3.28}$$

The PDF of $\Re(Z_m^{(f)})$ is finally obtained by employing $p_\eta(\Re(\eta_m^{(f)}))$ from (3.28) and $p_d(D_{m,m}^{(f)})$ from (2.18) in (3.21). After using (3.351.3) in [62] to solve the integration, the $p_z(\Re(Z_m^{(f)}))$ becomes

$$p_z^{\text{BPSK/QPSK}}(\Re(Z_m^{(f)})) = \frac{\sigma_\beta^{N_r}}{\Gamma(N_r)^2} \sum_{i=1}^{N_r} \frac{\sigma_h^{N_r-i+1}(N_r+i-2)!(2N_r-i)!|\Re(Z_m^{(f)})|^{N_r-i}}{2^{2i-2}\Gamma(i)(N_r-i)!(\sigma_\beta+2\sigma_h|\Re(Z_m^{(f)})|)^{2N_r-i+1}}. \tag{3.29}$$

Fig. 3.4 compares the outcomes from the derived PDF of $\Re(Z_m^{(f)})$ in (3.29) with that of the empirical. QPSK modulation was chosen to the system. $N_t = 10$ and $N_r = \{64, 256\}$. E_b/N_0 was 0 and -10 dB. According to the results, the derived PDFs provided accurate analytical results compared to the exact PDFs. Focusing on the results for the 10×256 system, operating at $E_b/N_0 = -10$ dB, the derived $p_z(\Re(Z_m^{(f)}))$ at $\Re(Z_m^{(f)}) = 1$ was 1.32×10^{-2}, and the deviation between the analysis and the true PDF was 4.73×10^{-5}. However, the deviation became larger in a system with a lower N_r since $\eta_m^{(f)}$ and $d_{m,m}^{(f)}$ in

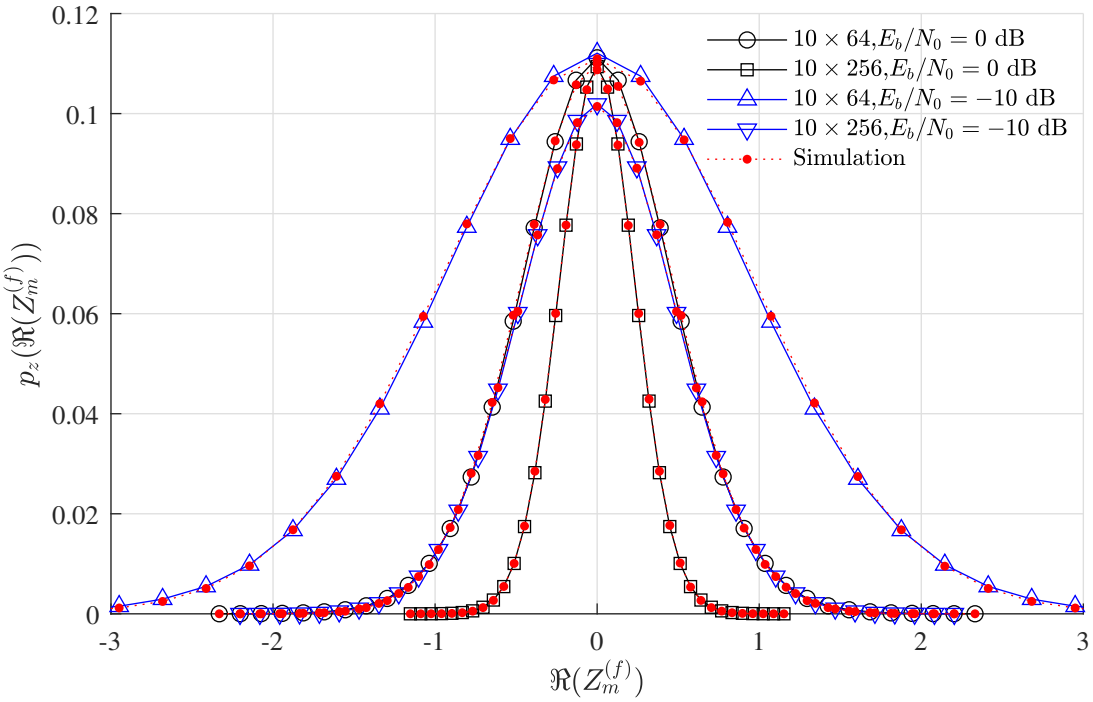

Figure 3.4: PDF of $\Re(Z_m^{(f)})$ of OFDM-MMIMO system using QPSK modulation.

(3.3) are assumed to be uncorrelated and the approximation is imprecise if the size of N_r is inadquate.

3.2 Derived CDF of $\Re(Z_m^{(f)})$

The output from the symbol detection, $\hat{X}_m^{(f)}$, receives the effects of the CCI and EN in $Z_m^{(f)}$, making errors for data transmission. Moreover, the difference between the symbols dramatically increases according to the number of N_t and the noise energy. The pairwise error probability (PEP) and bit error probability (BEP) for the system is generally derived by utilizing the cumulative distribution function (CDF) of $\Re(Z_m^{(f)})$ [39], and the CDF is now derived in this section. Let $\bar{X}_a$ be an element in the constellation points per dimension, which is chosen by the transmitter for generating in-phase and quadrature components of $X_m^{(f)}$, the CDF, $P(\Re(\hat{X}_m^{(f)})|\Re(X_m^{(f)}) = \bar{X}_a, K)$, demonstrates the probability of error event that the value of $\Re(\hat{X}_m^{(f)})$ is closer to a successive constellation point than $\bar{X}_a$. If K represents the distance between $\bar{X}_a$ and the decision boundary for the constellation points, the CDF can be expressed in terms of the $p_z(\Re(Z_m^{(f)}))$ as

$$P(\Re(\hat{X}_m^{(f)})|\Re(X_m^{(f)}) = \bar{X}_a, K) = \int_0^{\infty} p_z(\Re(Z_m^{(f)}) + K) d\Re(Z_m^{(f)}). \tag{3.30}$$

By substituting $p_z(\Re(Z_m^{(f)}))$ for BPSK and QPSK modulation from (3.29) in (3.30),

the CDF becomes

$$P(\Re(\hat{X}_m^{(f)})|\Re(X_m^{(f)}) = \bar{X}_a, K)_{\text{BPSK,QPSK}} = \frac{\sigma_\beta^{N_r}}{\Gamma^2(N_r)} \sum_{i=1}^{N_r} \frac{(N_r+i-2)!}{\Gamma(i)} \sum_{j=0}^{N_r-i} \frac{K^j \sigma_h^j (N_r+j-1)!}{2^{N_r+i-j-1} j! (\sigma_\beta + 2K\sigma_h)^{N_r+j}}. \tag{3.31}$$

It is worth noting that the equation requires the binomial expansion to rewrite the equation in (3.30), and utilizes (3.351.3) in [62] to solve the integration. Likewise, if the PDF of $\Re(Z_m^{(f)})$ in (3.22) is substituted in (3.30), the CDF for M-QAM is given by

$$P(\Re(\hat{X}_m^{(f)})|\Re(X_m^{(f)}) = \bar{X}_a, K)_{M-\text{QAM}} = \frac{(2N_t-2)!}{\Gamma(N_r)^2 M_\lambda^{2N_t-2}} \sum_{\sum_{v=1}^{M_\lambda} k_v = 2N_t-2} \frac{\sigma_{\beta,\{k\}}^{N_r}}{\prod_{v=1}^{M_\lambda} k_v!} \times \sum_{i=1}^{N_r} \frac{(N_r+i-2)!}{\Gamma(i)} \sum_{j=0}^{N_r-i} \frac{K^j \sigma_h^j (N_r+j-1)!}{2^{N_r+i-j-1} j! (\sigma_{\beta,\{k\}} + 2K\sigma_h)^{N_r+j}}. \tag{3.32}$$

3.3 Pairwise error probability

This section utilizes the derived CDFs in (3.31) and (3.32) to derive the PEP of the OFDM-MMIMO system, using MRC detection. If BPSK or QPSK modulation is chosen to the transmitter, the demapper employ decision boundaries at $\Re(\hat{X}_m^{(f)}) = 0$ and $\Im(\hat{X}_m^{(f)}) = 0$ to estimate the transmit message from the in-phase and quadrature elements of $\hat{X}_m^{(f)}$. The distribution of $\Re(\hat{X}_m^{(f)})$ can be demonstrated as the $\mathcal{N}(0, \sigma_z^2)$ in Fig. 3.5a. The σ_z^2 was 0.5 and the center for the PDF was at $\{-1, 1\}$, corresponding to the constellation points. Focusing on the $p_x(\Re(\hat{X}_m^{(f)})|\Re(X_m^{(f)}) = -1)$, where $\Re(X_m^{(f)}) = -1$ is generated by the transmitter, the PEP, P_s, for the symbol can be derived by integrating the PDF from the decision boundary to ∞. Thus, the PEP is expressed in terms of the CDF as

$$P_s^{\text{BPSK,QPSK}} = P(\Re(\hat{X}_m^{(f)})|\Re(X_m^{(f)}) = \bar{X}_a, K). \tag{3.33}$$

K in (3.33) represents the distance between a constellation point and the decision boundary, i.e., $K = 1$ for BPSK and QPSK modulation. Since the $p_x(\Re(\hat{X}_m^{(f)})|\Re(X_m^{(f)}) = -1)$ and $p_x(\Re(\hat{X}_m^{(f)})|\Re(X_m^{(f)}) = 1)$ are symmetrical across the $\Re(\hat{X}_m^{(f)})$ axis, where the axis of symmetry is at $\Re(\hat{X}_m^{(f)}) = 0$, the PEP for both constellation points are identical. Therefore, the analysis in (3.33) additionally represents the average PEP for the system. If the CDF from (3.31) and $K = 1$ are substituted in (3.33) the PEP becomes

$$P_s^{\text{BPSK,QPSK}} = \frac{\sigma_\beta^{N_r}}{\Gamma^2(N_r)} \sum_{i=1}^{N_r} \frac{(N_r+i-2)!}{\Gamma(i)} \sum_{j=0}^{N_r-i} \frac{\sigma_h^j (N_r+j-1)!}{2^{N_r+i-j-1} j! (\sigma_\beta + 2\sigma_h)^{N_r+j}}. \tag{3.34}$$

In addition, if the mapper utilizes a square-shaped, M-QAM with Gray encoding to generate the transmit symbol, the receiver compares the in-phase and the quadrature components of the received symbols with that of the constellation points independently,

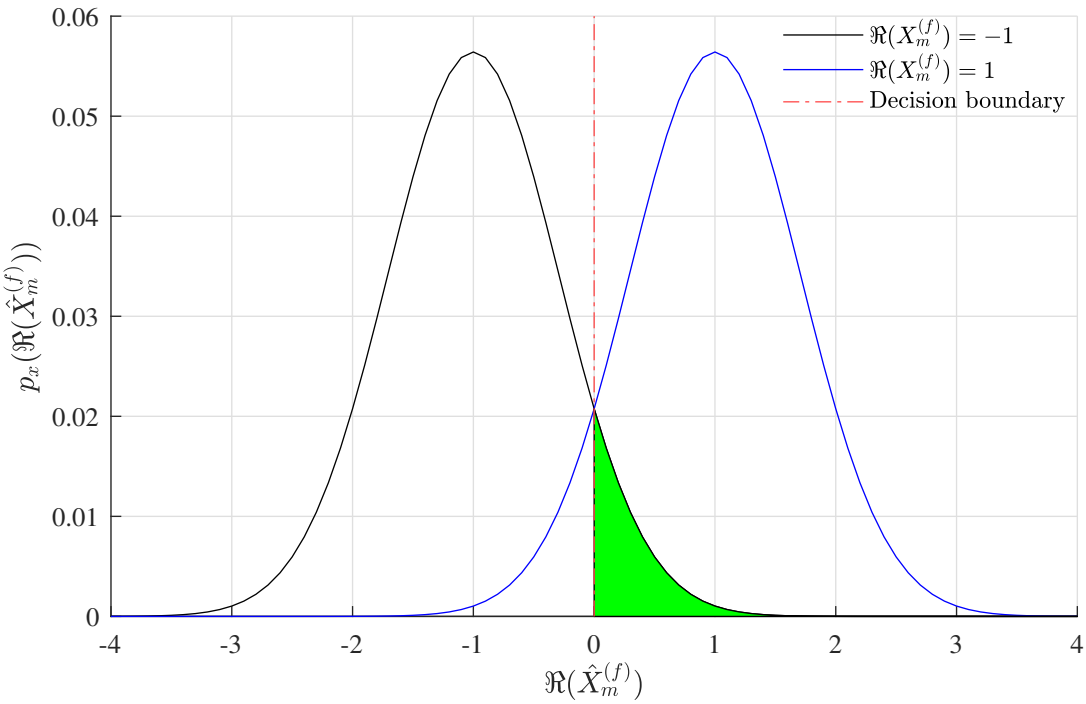

(a) BPSK and QPSK.

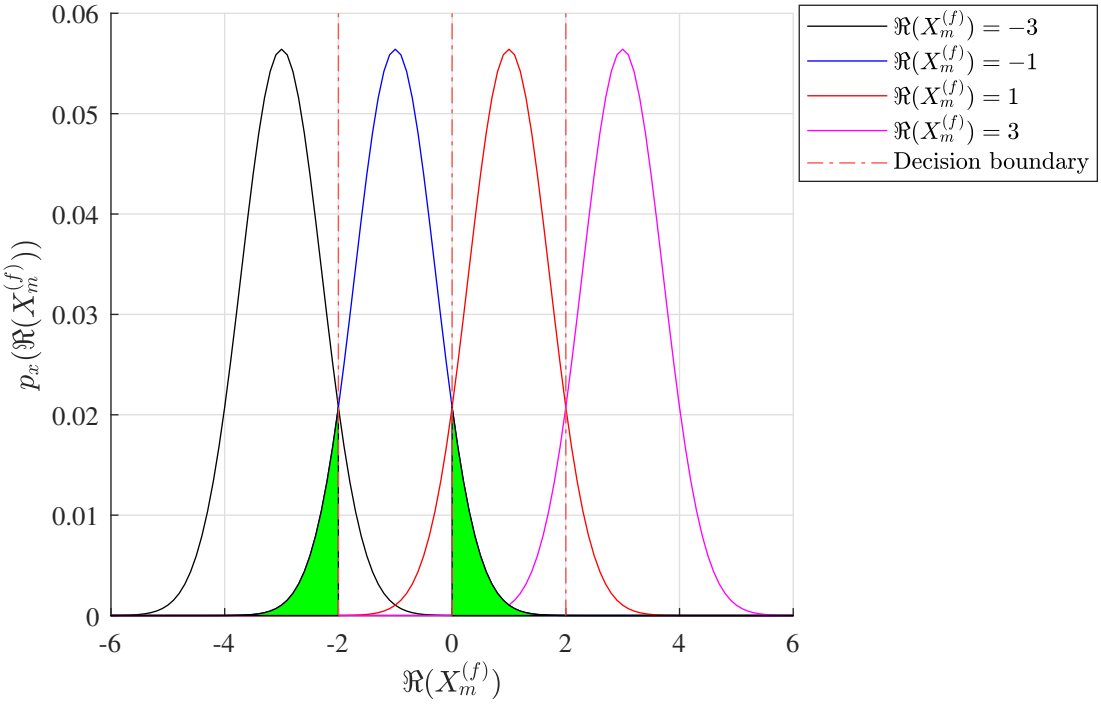

(b) 16-QAM.

Figure 3.5: PDF of $\Re(\hat{X}_m^{(f)})$.

and generates the message as the results. Therefore, the PEP of the OFDM-MMIMO system can be determined by averaging the error probabilities for all M_λ constellation points per dimension[39]. By assuming that the error events, caused by successive constellation points, dominate the PEP, error events from other constellation points are neglected for simplifying the analysis. Focusing on sample of the PDF of $\Re(\hat{X}_m^{(f)})$ for a system using 16-QAM in Fig. 3.5b. The $p_{\hat{x}}(\Re(\hat{X}_m^{(f)}))$ exhibited the $\mathcal{N}(0, \sigma_z^2)$, using $\sigma_z^2 = 0.5$, and $\Re(X_m^{(f)})$ was chosen from a component in $\bar{X}_a = \{-3, -1, 1, 3\}$. According to the PDFs, the center for the PDFs was at $\Re(\hat{X}_m^{(f)}) = \{-3, -1, 1, 3\}$ and the decision boundaries between any symbol and their neighbor were at $\Re(\hat{X}_m^{(f)}) = \{-2, 0, 2\}$. There are $M_\lambda - 2$ inner constellation points in the diagram, where the number of the successive points for the symbol is 2. If $\Re(X_m^{(f)}) = -1$ is generated by the transmitter, the neighbors for the constellation point are at $\Re(X_m^{(f)}) = \{-3, 1\}$. Therefore, the P_s is then obtained by integrating the PDF of $\Re(Z_m^{(f)})$, and the boundary for the integration is from $-\infty$ to -2 and from 0 to ∞. Therefore, the PEP for the inner points is approximated from the $P(\Re(\hat{X}_m^{(f)})|\Re(X_m^{(f)}) = \bar{X}_a, K)$ as

$$P_{s,\text{inner}} = 2P(\Re(\hat{X}_m^{(f)})|\Re(X_m^{(f)}) = \bar{X}_a, K). \tag{3.35}$$

Likewise, the neighbor for the 2 outer constellation points is 1, and the PEP can be evaluated from the CDF as

$$P_{s,\text{outter}} = P(\Re(\hat{X}_m^{(f)})|\Re(X_m^{(f)}) = \bar{X}_a, K). \tag{3.36}$$

The PEP for the OFDM-MMIMO system can be derived by averaging the PEP of the $M_\lambda - 2$ inner and 2 outer constellation points in (3.35) and (3.36). As the results, the PEP becomes[39]

$$P_s = \frac{2(M_\lambda - 1)}{M_\lambda} P(\Re(\hat{X}_m^{(f)})|\Re(X_m^{(f)}) = \bar{X}_a, K). \tag{3.37}$$

After substituting $M_\lambda = 4$ in (3.37), the outcome from the operation is

$$P_s^{16-\text{QAM}} = \frac{3}{2} P(\Re(\hat{X}_m^{(f)})|\Re(X_m^{(f)}) = \bar{X}_a, K). \tag{3.38}$$

If $K = 1$, and the CDF from (3.32) are chosen to (3.38), P_s can be expressed as

$$\begin{aligned} P_s^{16-\text{QAM}} = {} & \frac{3(2N_t - 2)!}{\Gamma(N_r) 2^{4N_t - 2}} \sum_{\sum_{v=1}^{4} k_v = 2N_t - 2} \frac{\sigma_{\beta,\{k\}}^{N_r}}{\prod_{v=1}^{4} k_v!} \\ & \times \sum_{i=1}^{N_r} \frac{(N_r + i - 2)!}{\Gamma(i)} \sum_{j=0}^{N_r - i} \frac{\sigma_h^j (N_r + j - 1)!}{2^{N_r + i - j} j! (\sigma_{\beta,\{k\}} + 2\sigma_h)^{N_r + j}}. \end{aligned} \tag{3.39}$$

3.4 BEP analysis

This section derives the BEP of the OFDM-MMIMO system, utilizing the derived PDFs of the CCI and EN. If BPSK or QPSK modulation is chosen to the system, $M_\lambda = 2$ and each constellation points per dimension corresponds to a binary digit. Therefore, the BEP analysis for this case is identical to that of the PEP in (3.33), i.e.,

$$P_e^{\text{BPSK,QPSK}} = P(\Re(\hat{X}_m^{(f)})|\Re(X_m^{(f)}) = \bar{X}_a, K). \tag{3.40}$$

By substituting $P(\Re(\hat{X}_m^{(f)})|\Re(X_m^{(f)}) = \bar{X}_a, K)$ from (3.31) and $K = 1$ in (3.40), the BEP becomes

$$P_e^{\text{BPSK,QPSK}} = \frac{\sigma_\beta^{N_r}}{\Gamma^2(N_r)} \sum_{i=1}^{N_r} \frac{(N_r+i-2)!}{\Gamma(i)} \sum_{j=0}^{N_r-i} \frac{\sigma_h^j (N_r+j-1)!}{2^{N_r+i-j-1} j! (\sigma_\beta + 2\sigma_h)^{N_r+j}}. \tag{3.41}$$

Furthermore, if Gray encoding, M-QAM is chosen to the mapper, the difference in binary code between any successive constellation points is one. Therefore, the BEP for the system can be approximated from the PEP in (3.37) as $P_s/\log_2(M_\lambda)$, and results in

$$P_e^{M-\text{QAM}} = \frac{2(M_\lambda - 1)}{M_\lambda \log_2(M_\lambda)} P(\Re(\hat{X}_m^{(f)})|\Re(X_m^{(f)}) = \bar{X}_a, K). \tag{3.42}$$

It is worth noting that the analysis in (3.32) requires the CDF for M-QAM in (3.32) for deriving the BEP. If the transmitter utilizes 16-QAM modulation with the constellation points $\{-3, -1, 1, 3\}$, $K = 1$, $M_\lambda = 4$, and the BER analysis in (3.42) becomes

$$P_e^{16-\text{QAM}} = \frac{3}{4} P(\Re(\hat{X}_m^{(f)})|\Re(X_m^{(f)}) = \bar{X}_a, K = 1). \tag{3.43}$$

After using the CDF from (3.32) in (3.43), the BEP is given by

$$\begin{aligned} P_e^{16-QAM} = {} & \frac{3(2N_t-2)!}{\Gamma(N_r)^2 4^{2N_t-2}} \sum_{\sum_{v=1}^{4} k_v = 2N_t-2} \frac{\sigma_{\beta,\{k\}}^{N_r}}{k_1! k_2! k_3! k_4!} \\ & \times \sum_{i=1}^{N_r} \frac{(N_r+i-2)!}{\Gamma(i)} \sum_{j=0}^{N_r-i} \frac{\sigma_h^j (N_r+j-1)!}{2^{N_r+i-j+1} j! (\sigma_{\beta,\{k\}} + 2\sigma_h)^{N_r+j}}. \end{aligned} \tag{3.44}$$

Fig. (3.6) compares the BEP analysis from (3.41) and (3.44) with that of the simulation. The mapper employed QPSK and 16-QAM to generate X_m. N_t was 10 and N_r was $\{64, 128, 256\}$. The block size utilization was 1024 bits. The results confirmed that the derived equations produced an accurate BEP. The analysis for the 10×256 using QPSK at $E_b/N_0 = 0$ dB was 1.96×10^{-5}, which was 8.11×10^{-6} different from the exact BEP. Moreover, the BEP at a higher E_b/N_0 region tend to a constant since the effects of EN became smaller and the CCI dominated the $p_z(\Re(Z_m^{(f)}))$. The analysis for the

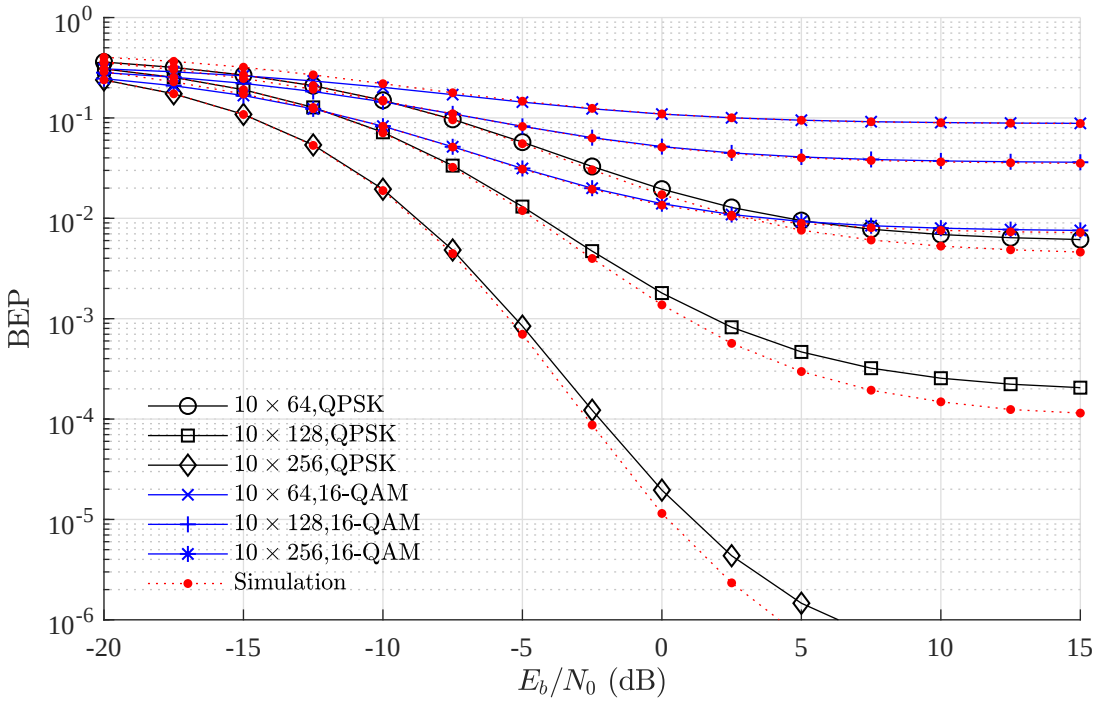

Figure 3.6: BEP analysis from (3.41) and (3.44).

10×256 system using 16-QAM at a higher E_b/N_0 approached an error floor at 7×10^{-3}. In addition, the results confirmed that the BEP performance for the system can be enhanced by the increasing N_r. Focusing on the system, utilizing 16-QAM and operating at $E_b/N_0 = 0$ dB, the derived BEP for the 10×64 was 0.11. If $N_r = 256$ is chosen to the system, the BEP become smaller at 1.4×10^{-2}. It is worth noting that the results reveal small deviations between the exact BEP and the analytical results. The derived BEP in (3.41) and (3.44) assumed that $\Re(\eta_m^{(f)})$ and $D_{m,m}^{(f)}$ are uncorrelated. However, both of the variables are generated from the CFR, and the outcome from the joint probabilities is still inaccurate if N_r is not large enough.

3.5 Derived PDF of SINR

If a Gray-coded, M-QAM is chosen to the OFDM-MMIMO system, the transmit symbols can be estimated from in-phase or quadrature component of $\hat{X}_m^{(f)}$ individually. Moreover, the symbol is uniformly distributed across the constellation points. Therefore, signal-to-interference-plus-noise ratio (SINR) per dimension, γ_s, of $\Re(\hat{X}_m^{(f)})$ can be expressed as

$$\gamma_s = \frac{E_\lambda}{\Re(Z_m^{(f)})^2}, \tag{3.45}$$

where E_λ represents the average transmit energy per dimension, i.e., $E_\lambda = E_s/2$ for QPSK and M-QAM. It is worth noting that there is no quadrature component in the constellation points for BPSK modulation, making $E_\lambda = E_s$ for this case. Since γ_s in (3.45) is a ratio of a constant and $\Re(Z_m^{(f)})$, $p_\gamma(\gamma_s)$ can be derived from $p_z(\Re(Z_m^{(f)}))$, utilizing the PDF

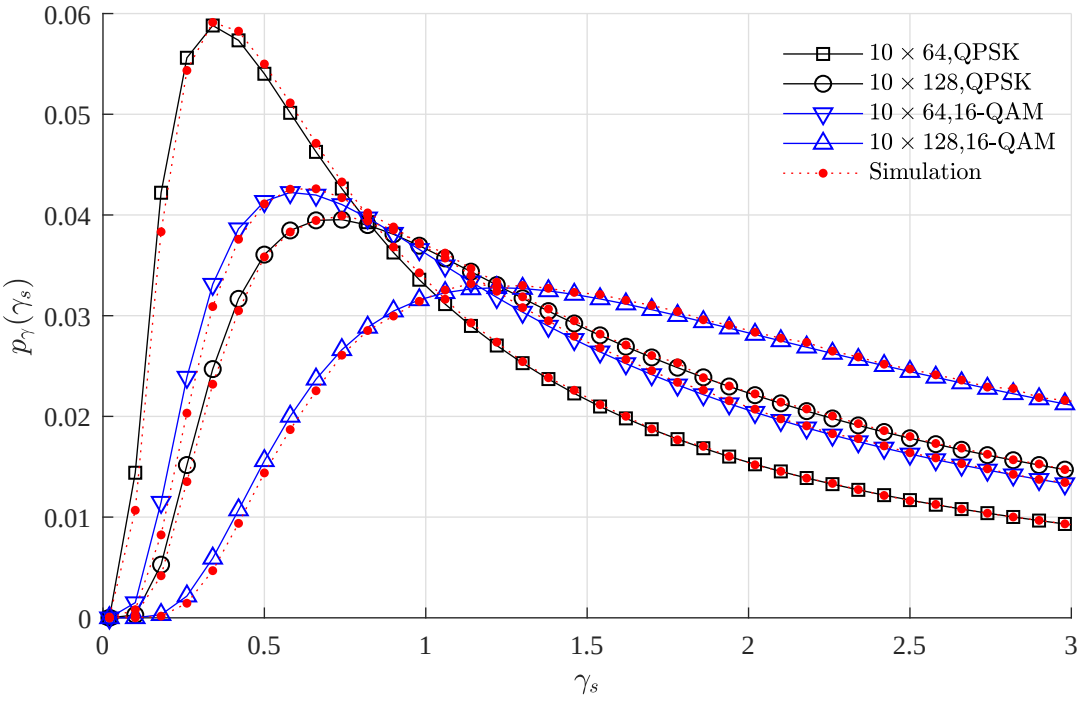

Figure 3.7: Derived PDF of SINR in (3.47) and (3.48).

transformation in (A.12), and results in

$$p_\gamma(\gamma_s) = \sqrt{\frac{E_\lambda}{\gamma_s^3}}\, p_z(\sqrt{E_\lambda/\gamma_s}). \tag{3.46}$$

Substituting $p_z(\Re(Z_m^{(f)}))$ of (3.29) into (3.46), $p_\gamma(\gamma_s)$ for BPSK and QPSK modulation is given by

$$p_\gamma(\gamma_s)^{\text{BPSK,QPSK}} = \frac{\sigma_\beta^{N_r}\sqrt{\gamma_s^{N_r-2}}}{\Gamma(N_r)^2}\sum_{i=1}^{N_r}\frac{\sigma_h^{N_r-i+1}(N_r+i-2)!(2N_r-i)!\sqrt{E_\lambda^{N_r-i+1}}}{2^{2i-2}\Gamma(i)(N_r-i)!(\sigma_\beta\sqrt{\gamma_s}+2\sigma_h\sqrt{E_\lambda})^{2N_r-i+1}}. \tag{3.47}$$

In addition, if $p_z(\Re(Z_m^{(f)}))$ for M-QAM modulation in (3.22) is used by (3.46), $p_\gamma(\gamma_s)$ becomes

$$\begin{aligned} p_\gamma(\gamma_s)^{M-\text{QAM}} = {} & \frac{\sqrt{\gamma_s^{N_r-2}}(2N_t-2)!}{\Gamma(N_r)^2 M_\lambda^{2N_t-2}}\sum_{\sum_{z=1}^{M_\lambda}k_z=(2N_t-2)}\frac{\sigma_{\beta,\{k\}}^{N_r}}{\prod_{z=1}^{M_\lambda}k_z} \\ & \times\sum_{i=1}^{N_r}\frac{\sigma_h^{N_r-i+1}(N_r+i-2)!(2N_r-i)!\sqrt{E_\lambda^{N_r+i-1}}}{2^{2i-2}\Gamma(i)(N_r-i)!(\sigma_{\beta,\{k\}}\sqrt{\gamma_s}+2\sigma_h\sqrt{E_\lambda})^{2N_r-i+1}} \end{aligned}. \tag{3.48}$$

Fig. 3.7 shows the empirical results of $p_\gamma(\gamma)$ for the OFDM-MMIMO system utilizing QPSK and 16-QAM modulation. The results are compared to that of the derived PDF in (3.47) and (3.48). $N_t = 10$ and N_r was $\{64, 128\}$. The system operated at $E_b/N_0 = -10$dB. The results reveal a good match between the exact and the derived PDFs. Focusing on the 10×128 system, using 16-QAM, the outcome from the derived PDF

and the empirical at $\gamma_s = 0.5$ was 1.56×10^{-2} and 1.44×10^{-2}, respectively. Thus, the analysis from the derived equation was only 1.21×10^{-3} different from the exact PDF. According to the 2-sample Kolmogorov–Smirnov test with the significant level 5%, there was no significant difference between the exact and the derived PDFs. It is worth noting that the results revealed small deviations between the PDF since the analysis employ an approximation in (3.3) for the analysis. Furthermore, the derived equation is complex and is still unable to calculate the PDF for a system, using $N_r \geq 172$ and $N_t \geq 10$.

3.6 Outage probability of MRC detection

Outage probability $P_{\text{out}}(\gamma_{\text{th}})$ is a performance metric, demonstrating the probability that the value of the γ_s is less than a threshold, γ_{th}. The outage probability can be expressed in terms of the $p_\gamma(\gamma_s)$ as

$$P_{\text{out}}(\gamma_{\text{th}}) = \int_0^{\gamma_{\text{th}}} p_\gamma(\gamma_s) d\gamma_s. \tag{3.49}$$

Although the analysis in (3.49) can be calculated by using the derived $p_\gamma(\gamma_s)$ from (3.47) and (3.48), the arithmetic operators in the derived PDFs complicate the integration in (3.49). Thus, the $p_\gamma(\gamma_s)$ in the equation is now rewritten in terms of $\Re(\eta_m^{(f)})$ and $D_{m,m}^{(f)}$ by using (3.21) and (3.46), and results in

$$P_{\text{out}}(\gamma_{\text{th}}) = \int_0^{\infty} \sqrt{\frac{E_\lambda}{\gamma_s^3}} \int_0^{\gamma_{\text{th}}} D_{m,m}^{(f)} p_\eta(D_{m,m}^{(f)} \sqrt{E_\lambda/\gamma_s}) p_d(D_{m,m}^{(f)}) d\gamma_s dD_{m,m}^{(f)}. \tag{3.50}$$

After substituting the PDF of $\Re(\eta_m^{(f)})$ and $D_{m,m}^{(f)}$ from (3.28) and (2.18), respectively in (3.50), the outage probability for BPSK and QPSK modulation can be expressed as

$$\begin{aligned} P_{\text{out}}^{\text{BPSK,QPSK}}(\gamma_{\text{th}}) = {} & \frac{\sigma_\beta^{N_r} \sqrt{\gamma_{\text{th}}^{N_r}}}{\Gamma(N_r)^2} \sum_{i=1}^{N_r} \frac{(N_r + i - 2)!}{\Gamma(i)} \\ & \times \sum_{k=0}^{N_r - i} \frac{\sigma_h^{N_r - i - k} \sqrt{E_\lambda^{N_r - i - k}} (2N_r - i - k - 1)!}{2^{2i+k-2} (N_r - i - k)! (\sigma_\beta \sqrt{\gamma_{\text{th}}} + 2\sigma_h \sqrt{E_\lambda})^{2N_r - i - k}}. \end{aligned} \tag{3.51}$$

It is worth noting that (3.51) utilizes (3.351.3) in [62] to solve the integration. Furthermore, if the PDF of $\Re(\eta_m^{(f)})$ for M-QAM modulation in (3.20) is used by (3.50), the $P_{\text{out}}(\gamma_{\text{th}})$ is given by

$$\begin{aligned} P_{\text{out}}^{M-\text{QAM}}(\gamma_{\text{th}}) = {} & \frac{(2N_t - 2)! \sqrt{\gamma_{\text{th}}^{N_r}}}{\Gamma(N_r)^2 M_\lambda^{2N_t - 2}} \sum_{\sum_{z=1}^{M_\lambda} k_z = (2N_t - 2)} \frac{\sigma_{\beta,\{k\}}^{N_r}}{\prod_{z=1}^{M_\lambda} k_z} \\ & \times \sum_{i=1}^{N_r} \frac{(N_r + i - 2)!}{\Gamma(i)} \sum_{p=0}^{N_r - i} \frac{\sigma_h^{N_r - i - p} \sqrt{E_\lambda^{N_r - i - p}} (2N_r - i - p - 1)!}{2^{2i+p-2} (N_r - i - p)! (\sigma_\beta \sqrt{\gamma_{\text{th}}} + 2\sigma_h \sqrt{E_\lambda})^{2N_r - i - p}}. \end{aligned} \tag{3.52}$$

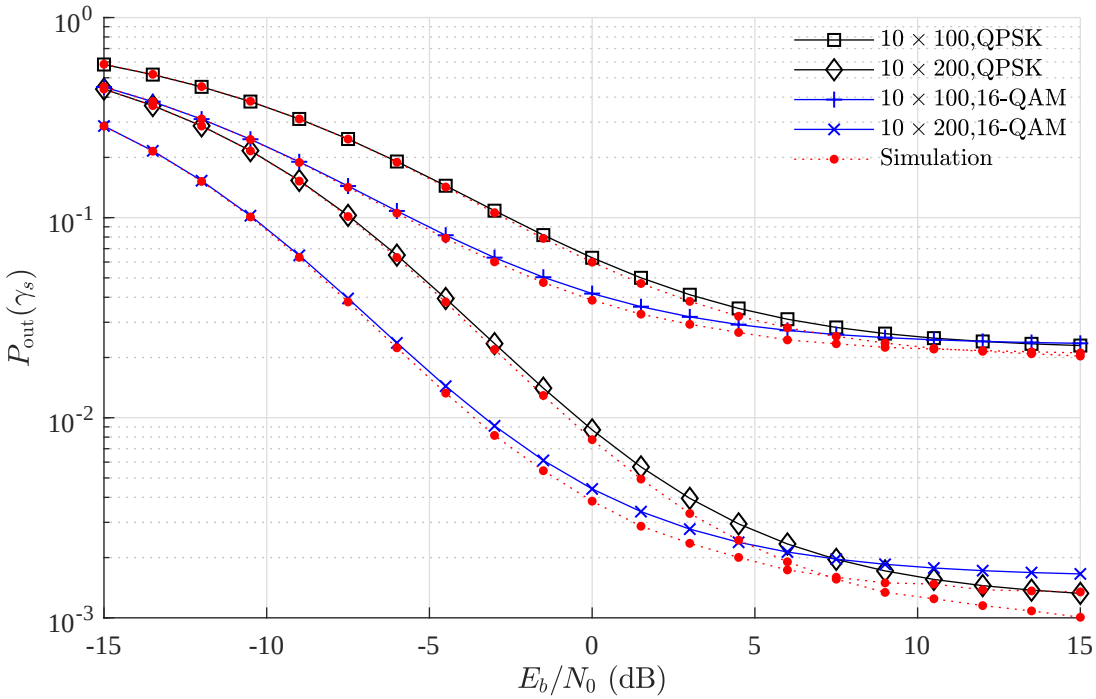

Figure 3.8: Derived outage probabilities in (3.51) and (3.52).

The analytical results for the $P_{\text{out}}(\gamma_{\text{th}})$ in (3.52) are compared to that of the empirical in Fig. 3.8. QPSK and 16-QAM modulation were chosen to the simulation, and the system operated at $E_b/N_0 = -10$ dB. $\gamma_{th} = 3$ dB, $N_t = 10$ and $N_r = \{100, 200\}$. According to the results, the derived equation provided an accurate data, compared to that of the empirical. The derived outage probability for the 10×200 system, where QPSK modulation was chosen to the mapper, at $E_b/N_0 = 0$ dB was 8.7×10^{-3}. The number for the empirical was 7.77×10^{-3}, and there was 9.28×10^{-4} difference between the analytical and empirical results. Furthermore, focusing on a higher E_b/N_0 region, the effects of the EN in (2.25) become smaller, and the CCI dominates the $\Re(Z_m^{(f)})$. Thus, the $P_{\text{out}}(\gamma_{\text{th}})$ tend to a constant in the region. The $P_{\text{out}}(\gamma_{\text{th}})$ for the 10×100 system approached a floor around 2×10^{-2}, whereas the floor for the 10×200 system was around 1×10^{-3}.

3.7 Improved performance analysis

From section 3.1 to 3.6, the mathematical expression of $Z_m^{(f)}$ in (3.3) was employed to analyze the $p_z(\Re(Z_m^{(f)}))$ as well as the performance metrics. However, the empirical results revealed small deviations between the exact results and the outcome from the derived equations since $\eta_m^{(f)}$ and $D_{m,m}^{(f)}$ in (3.3) were generated from $H_{n,m}^{(f)}$, making a correlation between the variables. Thus, this section improves the accuracy for the $p_z(\Re(Z_m^{(f)}))$, and utilizes the PDF to analyze the performance of the OFDM-MMIMO system. According to the analysis for $D_{m,m}^{(f)}$ in section 2.5.1, the variable is the diagonal component of the Gram

matrix and the $p_d(D_{m,m}^{(f)})$ tends to be a constant, Ω, in (2.19) if $N_r >> N_t$. Therefore, $D_{m,m}^{(f)} \simeq \Omega$ and $Z_m^{(f)}$ in (3.3) is approximated as

$$Z_m^{(f)} \simeq \frac{\eta_m^{(f)}}{\Omega}. \tag{3.53}$$

$Z_m^{(f)}$ in (3.53) is a ratio of $\eta_m^{(f)}$ to the constant, Ω. Thus, the $p_z(\Re(Z_m^{(f)}))$ can be derived from the PDF transformation in (A.10), and results in

$$p_z(\Re(Z_m^{(f)})) = \Omega p_\eta(\Omega \Re(Z_m^{(f)})). \tag{3.54}$$

The PDFs of $\Re(\eta_m^{(f)})$ for BPSK, QPSK, and M-QAM were previously derived in (3.28) and (3.20). By substituting the PDFs into (3.54), $p_z(\Re(Z_m^{(f)}))$ becomes

$$p_z^{\text{BPSK/QPSK}}(\Re(Z_m^{(f)})) = f_1(\Re(Z_m^{(f)}), \sigma_\beta), \tag{3.55a}$$

$$p_z^{M-\text{QAM}}(\Re(Z_m^{(f)})) = \frac{(2N_t-2)!}{M_\lambda^{2N_t-2}} \sum_{\sum_{v=1}^{M_\lambda} k_v = 2N_t-2} \frac{f_1(\Re(Z_m^{(f)}), \sigma_{\beta,\{k\}})}{\prod_{v=1}^{M_\lambda} k_v!}, \tag{3.55b}$$

where the function $f_1(\Re(Z_m^{(f)}), \sigma_\beta)$ is defined as

$$\begin{aligned} f_1(\Re(Z_m^{(f)}), \sigma_\beta) = \frac{1}{\Gamma(N_r)} \exp\left(-\frac{2N_r\sigma_h|\Re(Z_m^{(f)})|}{\sigma_\beta}\right) \\ \times \sum_{i=1}^{N_r} \frac{(N_r+i-2)!|\Re(Z_m^{(f)})|^{N_r-i}}{2^{2i-2}\Gamma(i)(N_r-i)!} \left(\frac{N_r\sigma_h}{\sigma_\beta}\right)^{N_r-i+1}. \end{aligned} \tag{3.56}$$

Theoretically, the accuracy of the improved PDFs of $\Re(Z_m^{(f)})$ in (3.55) is higher than that of the original PDFs in (3.29) and (3.22) due to the variables in the equation are uncorrelated. However, the analysis employ Ω to approximate $D_{m,m}^{(f)}$ in (3.53), and the assumption is precise if $N_r >> N_t$.

3.7.1 Improved BEP analysis

In this section, the refined $p_z(\Re(Z_m^{(f)}))$ in (3.55) is employed to evaluate the BEP of the OFDM-MMIMO system. The improved CDFs, $P(\Re(\hat{X}_m^{(f)})|\Re(X_m^{(f)}) = \bar{X}_a, K)$ are analyzed by substituting the derived PDFs in (3.30). After solving the integration with (3.351.3) from [62], the CDF is given by

$$P(\Re(\hat{X}_m^{(f)})|\Re(X_m^{(f)}) = \bar{X}_a, K)_{\text{BPSK,QPSK}} = f_2(\sigma_\beta, K), \tag{3.57a}$$

$$P(\Re(\hat{X}_m^{(f)})|\Re(X_m^{(f)}) = \bar{X}_a, K)_{M-\text{QAM}} = \frac{(2N_t-2)!}{M_\lambda^{2N_t-2}} \sum_{\sum_{v=1}^{M_\lambda} k_v = 2N_t-2} \frac{f_2(\sigma_{\beta,\{k\}}, K)}{\prod_{v=1}^{M_\lambda} k_v!}, \tag{3.57b}$$

where the function $f_2(\sigma_\beta, K)$ is expressed as

$$f_2(\sigma_\beta, K) = \frac{1}{\Gamma(N_r)} \exp\left(-\frac{2N_r\sigma_h K}{\sigma_\beta}\right) \sum_{i=1}^{N_r} \frac{(N_r+i-2)!}{\Gamma(i)} \sum_{r=0}^{N_r-i} \frac{K^r}{2^{N_r+i-r-1}r!} \left(\frac{N_r\sigma_h}{\sigma_\beta}\right)^r. \tag{3.58}$$

The BEP for the OFDM-MMIMO system is then evaluated from the CDFs. Focusing on the system, where BPSK and QPSK modulation is chosen to the mapper, the BEP is derived by substituting $M_\lambda = 2$ and $P(\Re(\hat{X}_m^{(f)})|\Re(X_m^{(f)}) = \bar{X}_a, K)$ from (3.57a) into (3.42), and the outcome from this operation is

$$P_e^{\text{BPSK/QPSK}} = f_2(\sigma_\beta, K). \tag{3.59}$$

If the constellation points per dimension $\bar{X}_v = \{-1, 1\}$ is chosen to the mapper, K in (3.59) becomes 1 for this case. Likewise, the BEP for the system using M-QAM is obtained by substituting the CDF from (3.57b) into (3.42), and the results from the operation is

$$P_e^{M-\text{QAM}} = \frac{2(M_\lambda-1)(2N_t-2)!}{M_\lambda \log_2(M_\lambda) M_\lambda^{2N_t-2}} \sum_{\sum_{v=1}^{M_\lambda} k_v = 2N_t-2} \frac{f_2(\sigma_{\beta,\{k\}}, K)}{\prod_{v=1}^{M_\lambda} k_v!}. \tag{3.60}$$

If the system utilizes 16-QAM with the constellation points $\{-3, -1, 1, 3\}$, the BEP analysis for the system is then evaluated by substituting $M_\lambda = 4$, $K = 1$, and the CDF from (3.57b) into (3.42). As a result, the BEP is given by

$$P_e^{16-\text{QAM}} = \frac{3(2N_t-2)!}{2^{4N_t-2}} \sum_{\sum_{v=1}^{4} k_v = 2N_t-2} \frac{f_2(\sigma_{\beta,\{k\}}, 1)}{\prod_{v=1}^{4} k_v!}. \tag{3.61}$$

3.7.2 Improved PDF of SINR and outage probabilities

This sub-section utilizes the improved $p_z(\Re(Z_m^{(f)}))$ in (3.55) to analyze the PDF of SINR and outage probabilities for the OFDM-MMIMO system. According to (3.46), the $p_\gamma(\gamma_s)$ can be derived from the PDF of $\Re(Z_m^{(f)})$. If the PDF from (3.55a) is chosen to the equation, the improved $p_\gamma(\gamma_s)$ of BPSK and QPSK modulation is given by

$$\begin{aligned} p_\gamma^{\text{BPSK/QPSK}}(\gamma_s) = & \frac{\exp\left(-\frac{2N_r\sigma_h}{\sigma_\beta}\sqrt{\frac{E_\lambda}{\gamma_s}}\right)}{\Gamma(N_r)} \\ & \times \sum_{i=1}^{N_r} \frac{(N_r+i-2)!}{2^{2i-2}\Gamma(i)(N_r-i)!} \sqrt{\frac{E_\lambda^{N_r-i+1}}{\gamma_s^{N_r-i+3}}} \left(\frac{N_r\sigma_h}{\sigma_\beta}\right)^{N_r-i+1}. \end{aligned} \tag{3.62}$$

In addition, the enhanced $p_\gamma(\gamma_s)$ for M-QAM can be obtained by substituting $p_z(\Re(Z_m^{(f)}))$

from (3.55b) in (3.46), and results in

$$p_{\gamma}^{M-\mathrm{QAM}}(\gamma_s) = \frac{(2N_t-2)!}{\Gamma(N_r)M_{\lambda}^{2N_t-2}} \sum_{\sum_{v=1}^{M_\lambda} k_v = 2N_t-2} \frac{\exp\left(-\frac{2N_r\sigma_h}{\sigma_\beta}\sqrt{\frac{E_\lambda}{\gamma_s}}\right)}{\prod_{v=1}^{M_\lambda} k_v!} \times \sum_{i=1}^{N_r} \frac{(N_r+i-2)!}{2^{2i-2}\Gamma(i)(N_r-i)!}\sqrt{\frac{E_\lambda^{N_r-i+1}}{\gamma_s^{N_r-i+3}}}\left(\frac{N_r\sigma_h}{\sigma_{\beta,\{k\}}}\right)^{N_r-i+1}. \tag{3.63}$$

Furthermore, the improved PDF of SINR in (3.62) and (3.63) are then employed to derive the refined outage probabilities of the OFDM-MMIMO system. According to the theoretical analysis in section 3.6, the $P_{\mathrm{out}}(\gamma_{\mathrm{th}})$ can be derived from the PDF using the integral operation in (3.49). By substituting the $p_\gamma(\gamma_s)$ from (3.62) in the equation and using (3.351.2) in [62] to solve the integration, the outage probabilities of the OFDM-MMIMO system using BPSK and QPSK modulation is given by

$$P_{\mathrm{out}}^{\mathrm{BPSK/QPSK}}(\gamma_{\mathrm{th}}) = \frac{\exp\left(-\frac{2N_r\sigma_h}{\sigma_\beta}\sqrt{\frac{E_\lambda}{\gamma_{\mathrm{th}}}}\right)}{\Gamma(N_r)} \times \sum_{i=1}^{N_r} \frac{(N_r+i-2)!}{\Gamma(i)} \sum_{p=0}^{N_r-i} \frac{1}{2^{N_r+i-p-2}p!}\left(\frac{N_r\sigma_h}{\sigma_\beta}\sqrt{\frac{E_\lambda}{\gamma_{\mathrm{th}}}}\right)^p. \tag{3.64}$$

Moreover, if the PDF of SINR from (3.63) is used by (3.49), $P_{\mathrm{out}}(\gamma_{\mathrm{th}})$ for the system, where M-QAM is chosen to the transmitter, becomes

$$P_{\mathrm{out}}^{M-\mathrm{QAM}}(\gamma_{\mathrm{th}}) = \frac{(2N_t-2)!}{\Gamma(N_r)M_{\lambda}^{2N_t-2}} \sum_{\sum_{v=1}^{M_\lambda} k_v = 2N_t-2} \frac{\exp\left(-\frac{2N_r\sigma_h}{\sigma_\beta}\sqrt{\frac{E_\lambda}{\gamma_{\mathrm{th}}}}\right)}{\prod_{v=1}^{M_\lambda} k_v!} \times \sum_{i=1}^{N_r} \frac{(N_r+i-2)!}{\Gamma(i)} \sum_{p=0}^{N_r-i} \frac{1}{2^{N_r+i-p-2}p!}\left(\frac{N_r\sigma_h}{\sigma_\beta}\sqrt{\frac{E_\lambda}{\gamma_{\mathrm{th}}}}\right)^p. \tag{3.65}$$

3.8 Approximate performance analysis using GMM

The derived $p_z(\Re(Z_m^{(f)}))$, BEP, $p_\gamma(\gamma_s)$, and $P_{\mathrm{out}}(\gamma_{\mathrm{th}})$ were improved in section 3.7. Although the outcomes from the analysis matched the exact results, the equations requires several arithmetic operators to calculate the analytical results. Moreover, the computational complexity of the equations dramatically increases according to the value of N_t and M_λ. As the results, the equations are still impractical for analyzing the performance of the system, using a larger number of antennas. Thus, asymptotic PDFs of the CCI and the EN of MRC detection are derived in this section. The approximations are additionally employed to simplify the analysis for the BEPs, PDFs of SINR, and the outage probabilities.

Focusing on the system where BPSK or QPSK modulation are chosen for bit-to-symbol mapping, the PDF of $\Re(\beta_m^{(f)})$ in (3.26) exhibits a zero-mean Gaussian distribution with

variance σ_β^2, i.e., $\mathcal{N}(0, \sigma_\beta^2)$. Moreover, $\Re(\eta_m^{(f)})$ is a $2N_r$ summations of the product of $\Re(H_{n,m}^{(f),*})$ and $\Re(\beta_{n,m}^{(f)})$, and $\Re(H_{n,m}^{(f),*})$ is a $\mathcal{N}(0, \sigma_h^2)$. Therefore, the PDF of $\Re(\eta_m^{(f)})$ can be approximated as the zero-mean, Gaussian distribution function, i.e.,

$$p_\eta^{\text{BPSK/QPSK}}(\Re(\eta_m^{(f)})) \simeq f_g(\Re(\eta_m^{(f)}), \sigma_\eta), \tag{3.66}$$

where the function $f_g(\Re(\eta_m^{(f)}), \sigma_\eta)$ represents the $\mathcal{N}(0, \sigma_\eta^2)$, and is defined as

$$f_g(\Re(\eta_{n,m}^{(f)}), \sigma_\eta) = \frac{1}{\sqrt{2\pi\sigma_\eta^2}} \exp\left(-\frac{\Re(\eta_{n,m}^{(f)})^2}{2\sigma_\eta^2}\right). \tag{3.67}$$

The variance σ_η^2 in (3.66) is given by $2N_r\sigma_h^2\sigma_\beta^2$ due to $\Re(\eta_m^{(f)})$ in (3.3) is a $2N_r$-times combination of the product of $\Re(H_{n,m}^{(f),*})$ and $\Re(\beta_{n,m}^{(f)})$. According to the methodology presented in section 3.7, the $p_z(\Re(Z_m^{(f)}))$ can be derived from the $p_\eta(\Re(\eta_m^{(f)}))$ by utilizing the PDF transformation in (3.54). If the approximation in (3.66) is chosen to the equation, the asymptotic $p_z(\Re(Z_m^{(f)}))$ for BPSK and QPSK modulations becomes a Gaussian distribution too, i.e.,

$$p_z^{\text{BPSK/QPSK}}(\Re(Z_m^{(f)})) \simeq f_g(\Re(Z_m^{(f)}), \sigma_z), \tag{3.68}$$

where $\sigma_z^2 = \sigma_\eta^2/\Omega^2$. By substituting σ_η^2, σ_β^2 and Ω from (3.66), (3.27), and (2.19), respectively, in the equation, the variance per dimension becomes

$$\sigma_{z,\text{BPSK}}^2 = \frac{\sigma_h^2(N_t - 1) + \sigma_w^2}{2N_r\sigma_h^2}, \tag{3.69a}$$

$$\sigma_{z,\text{QPSK}}^2 = \frac{2\sigma_h^2(N_t - 1) + \sigma_w^2}{2N_r\sigma_h^2}. \tag{3.69b}$$

Likewise, the PDF of $\Re(\beta_m^{(f)})$ for M-QAM in (3.17) exhibits a summation of the scaled Gaussian distribution. Thus, the PDF of $\Re(\eta_m^{(f)})$ for this case is approximated as

$$p_\eta^{M-\text{QAM}}(\Re(\eta_m^{(f)})) \simeq \frac{(2N_t - 2)!}{M_\lambda^{2N_t-2}} \sum_{\sum_{v=1}^{M_\lambda} k_v = 2N_t-2} \frac{f_g(\Re(\eta_m^{(f)}), \sigma_{\eta,\{k\}})}{\prod_{v=1}^{M_\lambda} k_v!} \tag{3.70}$$

The variance $\sigma_{\eta,\{k\}}^2$ in (3.70) corresponds to $\{k_v\}_{v=1}^{M_\lambda}$, and is given by $2N_r\sigma_h^2\sigma_{\beta,\{k\}}^2$. If the approximation in (3.70) is substituted in (3.54), the PDF of $\Re(Z_m^{(f)})$ for M-QAM is given by

$$p_z^{M-\text{QAM}}(\Re(Z_m^{(f)})) \simeq \frac{(2N_t - 2)!}{M_\lambda^{2N_t-2}} \sum_{\sum_{v=1}^{M_\lambda} k_v = 2N_t-2} \frac{f_g(\Re(Z_m^{(f)}), \sigma_{z,\{k\}})}{\prod_{v=1}^{M_\lambda} k_v!}, \tag{3.71}$$

where the variance per dimension, $\sigma_{z,\{k\}}^2$, in (3.71) is calculated from $\sigma_{\eta,\{k\}}^2/\Omega^2$. If $\sigma_{\eta,\{k\}}^2$, $\sigma_{\beta,\{k\}}^2$ and Ω from (3.70), (3.19), and (2.19), respectively, are chosen to the equation, the

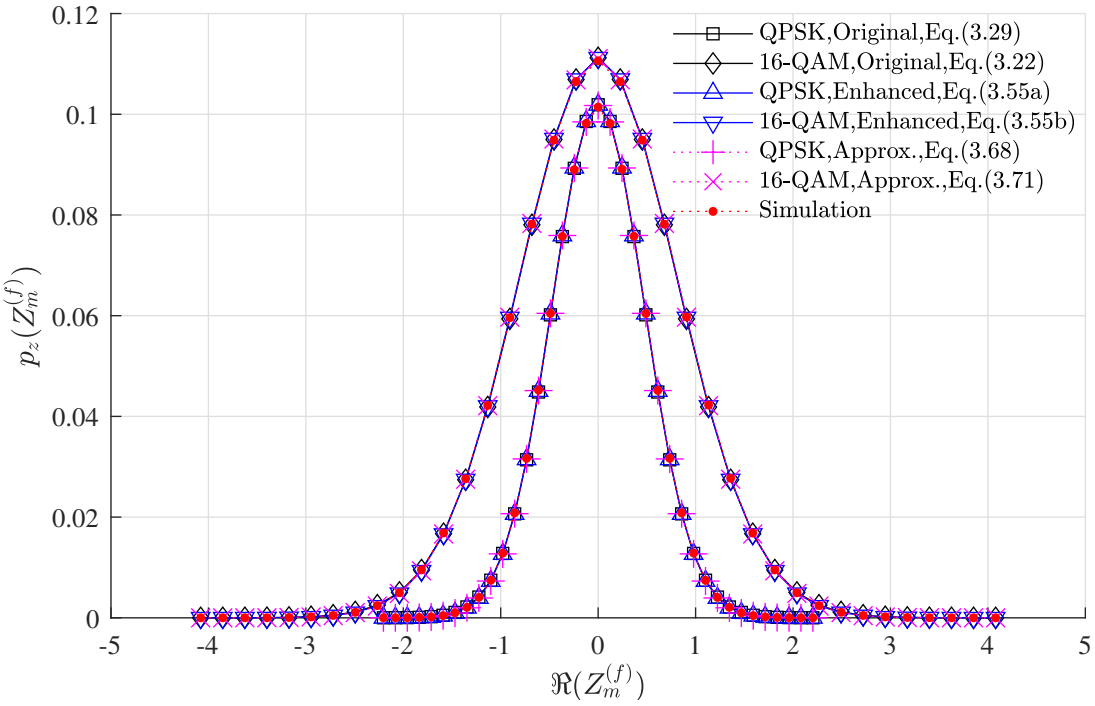

Figure 3.9: Derived $P_z(\Re(Z_m^{(f)}))$ of OFDM-MMIMO system.

variance per dimension becomes

$$\sigma^2_{z,\{k\}} = \frac{\sigma_h^2 \sum_{v=1}^{M_\lambda} k_v \bar{X}_v^2 + \sigma_w^2}{2N_r\sigma_h^2}. \tag{3.72}$$

The approximations in (3.68) and (3.71) confirm that the $p_z(\Re(Z_m^{(f)}))$ for BPSK and QPSK modulation approach the Gaussian distribution. Moreover, if M-QAM is chosen to the mapper, the PDF of $\Re(Z_m^{(f)})$ approaches the combination of Gaussian distribution, i.e., the GMM. According to the experiment, the approximations provide accurate PDFs if $N_r \geq 10N_t$ and $N_r \geq 100$. Fig. (3.9) compares the outcome from the original derived PDFs ((3.22) and (3.29)), the improved PDFs in (3.55), and the approximations ((3.68) and (3.71)) with that of the empirical. A 10×256 system was chosen to the simulation. The system operated at $E_b/N_0 = -10$ dB, and the mapper employed QPSK and 16-QAM modulation for generating the transmit symbols. The results confirmed that the PDF from the derived equations significantly matched the exact PDFs. The analysis from the original equation for 16-QAM at $\Re(Z_m^{(f)}) = -1$ was 5.22×10^{-2}, exhibiting 2.79×10^{-4} different from the empirical. The deviation between the analysis from the enhanced equation and the exact PDF at $\Re(Z_m^{(f)}) = -1$ was 2.03×10^{-5}. Therefore, the enhanced equations provided more accurate PDF than that of the original equations. In addition, the PDF from the approximation matched the exact equations, and the deviation between the PDF from the enhanced equation and the approximation at $\Re(Z_m^{(f)}) = -1$ was only 9.06×10^{-5}. It is worth noting that the deviation between the analysis was marginal. The 2-sample Kolmogorov–Smirnov test with the significant level 5% was utilized to compare the derived equations with that of the exact PDFs, and the results confirmed that the

difference between the outcomes from the analysis and the exact PDFs was insignificant.

3.8.1 Asymptotic BEP analysis

The asymptotic PDFs of $\Re(Z_m^{(f)})$ in (3.68) and (3.71) are now employed in this section to simplify the analysis for the CDFs of $\Re(Z_m^{(f)})$ and BEP. Focusing on the system using BPSK and QPSK modulation, the PDF of $\Re(Z_m^{(f)})$ is assumed to be the $\mathcal{N}(0, \sigma_z^2)$ in (3.68). Thus, the CDF of $\Re(Z_m^{(f)})$ can be obtained by substituting the $p_z(\Re(Z_m^{(f)}))$ in (3.30), and results in

$$P(\Re(\hat{X}_m^{(f)})|\Re(X_m^{(f)}) = \bar{X}_a, K) = \frac{1}{\sqrt{2\pi\sigma_z^2}} \int_0^{\infty} \exp\left(-\frac{(\Re(Z_m^{(f)}) + K)^2}{2\sigma_z^2}\right) d\Re(Z_m^{(f)}). \quad (3.73)$$

Let $Q(x) = \frac{1}{\sqrt{2\pi}} \int_x^{\infty} \exp(-\frac{t^2}{2}) dt$ be the Q-function, (3.73) is then written in terms of the function as

$$P(\Re(\hat{X}_m^{(f)})|\Re(X_m^{(f)}) = \bar{X}_a, K)_{\text{BPSK/QPSK}} \simeq Q\left(\frac{K}{\sigma_z}\right). \quad (3.74)$$

The BEP analysis for BPSK and QPSK modulations is obtained by using (3.42). By substituting the approximate CDF from (3.74) and $M_\lambda = 2$ to the equation, the BEP becomes

$$P_e^{\text{BPSK/QPSK}} \simeq Q\left(\frac{K}{\sigma_z}\right). \quad (3.75)$$

It is worth noting that the BEP for M-QAM can be simplified by employing the approximate $p_z(\Re(Z_m^{(f)}))$ from (3.71). If the PDF is chosen to (3.30), the asymptotic $P(\Re(\hat{X}_m^{(f)})|\Re(X_m^{(f)}) = \bar{X}_a, K)$ is given by

$$P(\Re(\hat{X}_m^{(f)})|\Re(X_m^{(f)}) = \bar{X}_a, K)_{M-\text{QAM}} = \frac{(2N_t - 2)!}{M_\lambda^{2N_t-2}} \sum_{\sum_{v=1}^{M_\lambda} k_v = 2N_t - 2} \frac{1}{\prod_{v=1}^{M_\lambda} k_v!} Q\left(\frac{K}{\sigma_{z,\{k\}}}\right). \quad (3.76)$$

By substituting the CDF from (3.76) in (3.42), the BEP for M-QAM is then approximated as

$$P_e^{M-\text{QAM}} \simeq \frac{2(M_\lambda - 1)(2N_t - 2)!}{M_\lambda^{(2N_t-1)} \log_2(M_\lambda)} \sum_{\sum_{v=1}^{M_\lambda} k_v = 2N_t - 2} \frac{1}{\prod_{v=1}^{M_\lambda} k_v!} Q\left(\frac{K}{\sigma_{z,\{k\}}}\right). \quad (3.77)$$

Focusing on the system with 16-QAM, the BEP is obtained by using $M_\lambda = 4$ in (3.77), and the outcome from this operation is

$$P_e^{16-\text{QAM}} \simeq \frac{3(2N_t - 2)!}{2^{(4N_t-2)}} \sum_{\sum_{v=1}^{4} k_v = 2N_t - 2} \frac{1}{\prod_{v=1}^{4} k_v!} Q\left(\frac{K}{\sigma_{z,\{k\}}}\right). \quad (3.78)$$

Evidently, the approximate BEP for OFDM-MMIMO system in (3.75), (3.77), and

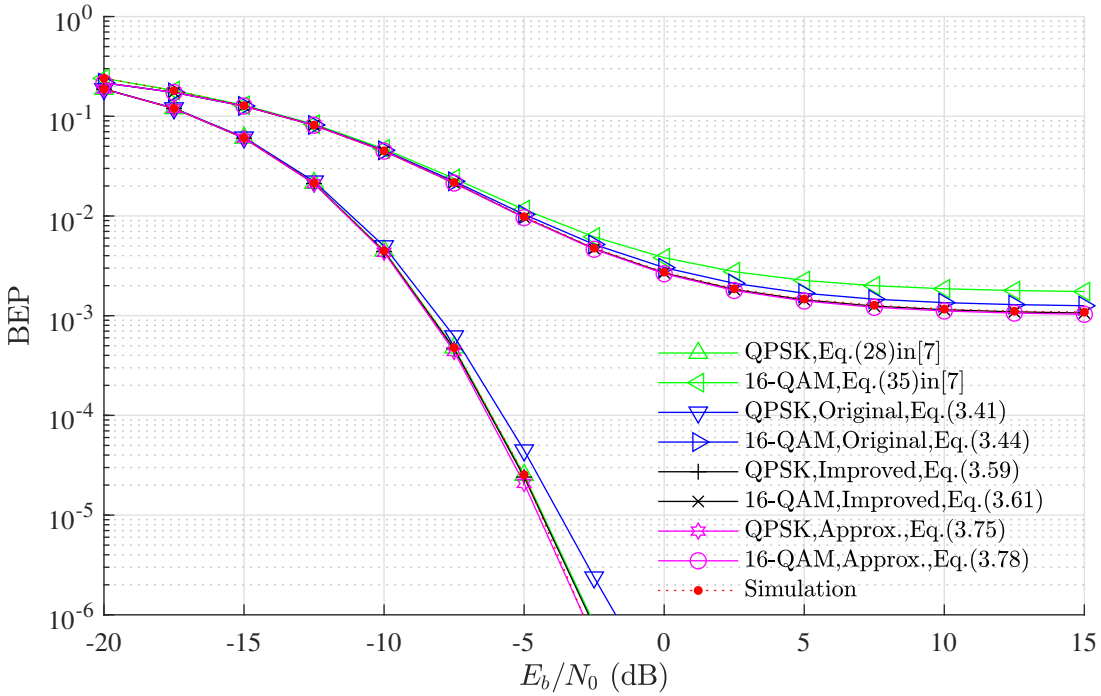

Figure 3.10: Comparison of the BEP analysis.

(3.78) are less complex that that of the exact analysis in section 3.7.1. However, the deviation in BEP between the outcomes from the equations and the exact BEP is higher than that of the exact equation. In Fig. 3.10, the BEP analysis from the original equations in (3.41) and (3.44) are compared to that of the modified equations in (3.59) and (3.61), as well as the approximation in (3.75) and (3.78). The outcomes from the empirical are included in the results. The analytical results from the proposed equations are also compared to that of (28) and (35) from [9]. QPSK and 16-QAM were chosen to the system and the block size utilization was 1024 bits. $N_t = 5$ and $N_r = \{100, 200\}$. Focusing on the BEP for 16-QAM, the enhanced equations outperformed its BEP analysis, compared to other equations. The outcome from the enhanced equation and the empirical results at $E_b/N_0 = 0$ dB were 2.68×10^{-3} and 2.74×10^{-3}. Thus, the deviation BEP was 1.94% different from the exact BEP. On the other hand, the BEP from the derived equation in [9], the original equation, and the approximation were, 3.82×10^{-3}, 3.03×10^{-3}, and 2.63×10^{-3}. In addition, the outcome from the asymptotic equation was only 1.89% different from the enhanced equation. However, the BEP from the enhanced equation for QPSK was slightly less accurate than that of the derived equation in [9]. The outcomes from the improved BEP and the derived equation in [9] at $E_b/N_0 = -5$ dB were 2.41×10^{-5} and 2.52×10^{-5}, respectively. The deviation between the BEPs and the empirical results were 1.32×10^{-6} and 1.82×10^{-7}, respectively.

3.8.2 Asymptotic PDF of SINR and outage probabilities

The methodology to simplify the derived PDF of SINR and the outage probabilities is discussed in this section. According to the analysis in section 3.5, the approximate PDF

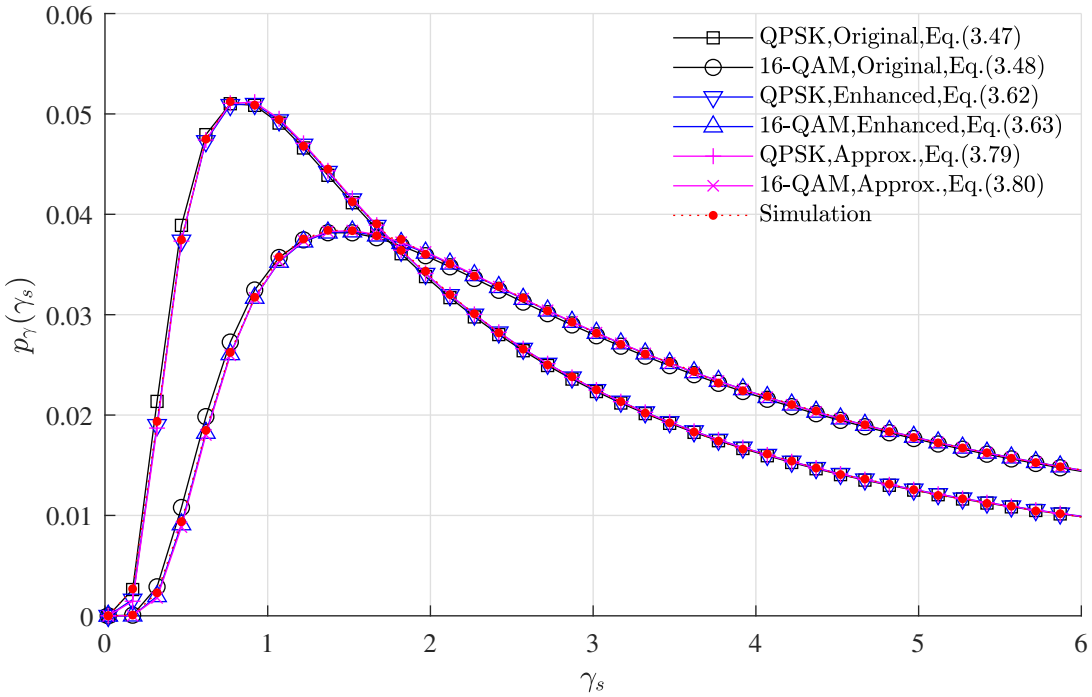

Figure 3.11: PDF of SINR in OFDM-MMIMO systems with MRC detection.

of SINR can be analyzed from $p_z(\Re(Z_m^{(f)}))$ by using (3.46). If the approximate PDF of $\Re(Z_m^{(f)})$ from (3.68) is chosen to (3.46), the asymptotic $p_\gamma(\gamma_s)$ for BPSK and QPSK modulation is given by

$$p_\gamma^{\text{BPSK/QPSK}}(\gamma_s) \simeq \sqrt{\frac{E_\lambda}{2\pi\sigma_z^2\gamma_s^3}}\ \exp\left(-\frac{E_\lambda}{2\gamma_s\sigma_z^2}\right). \tag{3.79}$$

Moreover, by using the $p_z(\Re(Z_m^{(f)}))$ from (3.71) in (3.46), the PDF of SINR for M-QAM becomes

$$\begin{aligned} p_\gamma^{M-\text{QAM}}(\gamma_s) \simeq \frac{(2N_t-2)!}{M_\lambda^{2N_t-2}} \sum_{\sum_{v=1}^{M_\lambda} k_v = 2N_t-2} \frac{1}{\prod_{v=1}^{M_\lambda} k_v!} \\ \times \sqrt{\frac{E_\lambda}{2\pi\sigma_{z,\{k\}}^2\gamma_s^3}}\exp\left(-\frac{E_\lambda}{2\gamma_s\sigma_{z,\{k\}}^2}\right). \end{aligned} \tag{3.80}$$

In Fig. 3.11, the original analysis for $p_\gamma(\gamma_s)$ in (3.47) and (3.48) are compared with that of the enhanced equations in (3.62) and (3.63), as well as the asymptotic equations in (3.79) and (3.80). The mapper employed QPSK and 16-QAM for generating the transmit symbols for a 10×150 system. The number of sub-carriers was 512 symbols, and the system operated at $E_b/N_0 = -10$ dB. The results confirm that the $p_\gamma(\gamma_s)$ from the enhanced equations was more accurate than that of the original analysis as well as the approximation. Moreover, the outcome from the approximation significantly matched the enhanced equation. Focusing on the system with 16-QAM, the exact PDF at $\gamma_s = 3$ was 2.83×10^{-2}. The analytical result from the enhanced equation at $\gamma_s = 3$ was 2.18×10^{-5} different from the simulation result, whereas the number from the original

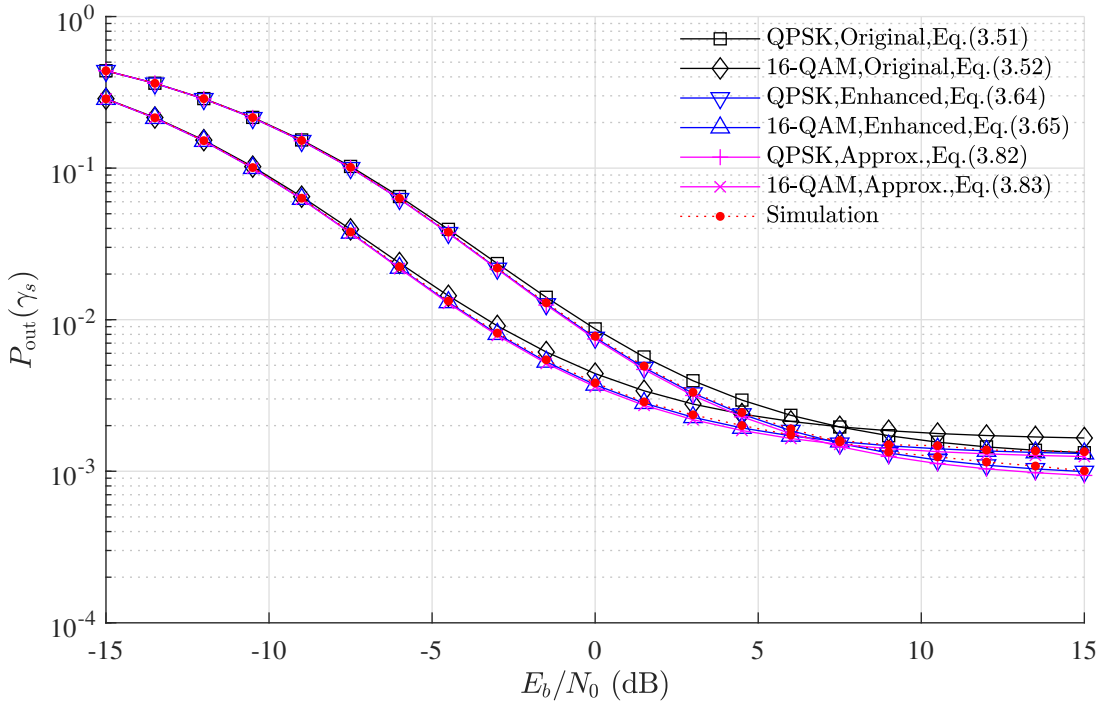

Figure 3.12: Derived $P_{\text{out}}(\gamma_s)$ of OFDM-MMIMO system.

and the approximate equations were 2.60×10^{-4} and 4.63×10^{-5}, respectively.

The approximate outage probabilities for BPSK and QPSK modulation is then derived by substituting the asymptotic $p_\gamma(\gamma_s)$ from (3.79) in (3.49), and results in

$$P_{\text{out}}(\gamma_{\text{th}}) \simeq \sqrt{\frac{E_\lambda}{2\pi\sigma_z^2}} \int_0^{\gamma_{th}} \frac{1}{\sqrt{\gamma_s^3}} \exp\left(-\frac{E_\lambda}{2\gamma_s\sigma_z^2}\right) d\gamma_s. \tag{3.81}$$

After using the substitution method in [64] to solve the integration in (3.81), P_{out} becomes

$$P_{\text{out}}^{\text{BPSK/QPSK}}(\gamma_{\text{th}}) \simeq \Gamma\left(\frac{E_\lambda}{2\sigma_z^2\gamma_{th}}, 1/2\right), \tag{3.82}$$

where $\Gamma(x,a) = (1/\Gamma(a)) \int_x^\infty t^{a-1} \exp(-t) dt$ denotes an upper incomplete Gamma function. Furthermore, if the $p_\gamma(\gamma_s)$ from (3.80) is chosen to (3.49), the $P_{\text{out}}(\gamma_{\text{th}})$ for the system using M-QAM is given by

$$P_{\text{out}}^{M-\text{QAM}}(\gamma_{\text{th}}) \simeq \frac{(2N_t-2)!}{M_\lambda^{2N_t-2}} \sum_{\sum_{v=1}^{M_\lambda} k_v = 2N_t-2} \frac{1}{\prod_{v=1}^{M_\lambda} k_v!} \Gamma\left(\frac{E_\lambda}{2\sigma_z^2\gamma_{th}}, 1/2\right). \tag{3.83}$$

Fig. 3.12 shows the outcomes from the analysis from the original equations in (3.51) and (3.52), the improved equations in (3.64) and (3.65), and the approximations in (3.82) and (3.83). The outcomes from the empirical are additionally included in the results. A 10×200 system was chosen to the simulation, where γ_{th} and the number of sub-carriers were 3 dB and 512 symbols, respectively. The results reveal a good match between the analytical results and that of the simulation, and the enhanced equations outperformed their outage probabilities. If 16-QAM was chosen to the system, the $P_{\text{out}}(\gamma_{\text{th}})$ from the

enhanced equation at $E_b/N_0 = 0$ dB was 3.72×10^{-3} and the number was only 1.10×10^{-4} different from the empirical. The deviation between the original equation and the simulation was larger at 5.78×10^{-4}. In addition, the accuracy for the asymptotic $P_{\text{out}}(\gamma_s)$ was slightly less than that of the enhanced equation, and the deviation between the approximation and the exact $P_{\text{out}}(\gamma_{\text{th}})$ at $E_b/N_0 = 0$ dB was 2.18×10^{-4}.

3.9 Summary

This chapter discussed the performance analysis of MRC detection for the OFDM-MMIMO system. The PDFs of the CCI and EN, the BEP, the PDF of SINR, as well the outage probabilities were derived in this chapter. Monte-Carlo simulation was chosen to evaluate the proposed analysis, and the results confirmed that the outcomes from the derived equations matched the exact results. However, there were small deviations between the analysis and the exact results due to a number of random variables in the mathematical expression of $\Re(Z_m^{(f)})$ are correlated. Thus, the diagonal components of the Gram matrix was assumed to be a constant, and the approximation is then employed to enhance the accuracy for the analysis. Furthermore, the analysis in this chapter confirmed that the $p_z(\Re(Z_m^{(f)}))$ for BPSK and QPSK modulation tends to be the Gaussian distribution if N_r is large enough. On the other hand, the PDF for M-QAM can be approximated as the GMM. Thus, the asymptotic equations can be utilized to simplify the analysis. The simulation results showed that the deviation between the outcome from the approximation and the exact result was slightly higher than that of the exact equations, whereas the asymptotic equations require much less arithmetic operators for producing the output. Thus they are efficient techniques for analyzing the performance of the OFDM-MMIMO system. However, the analysis in this chapter assumed that the diagonal components of the Gram matrix approaches a constant, and the approximation is accurate if $N_r > 10N_t$ and $N_r > 100$. Thus, the proposed equations in this chapter are still inaccurate if N_r is too small.

Chapter 4

Performance analysis of ZF detection

This chapter discusses the performance of ZF detection in OFDM-MMIMO system. The mathematical expression of the EN, $Z_m^{(f)}$, for the detection in (2.29) is now simplified by utilizing the 2-nd order NSE [24], and the $p_z(\Re(Z_m^{(f)}))$, BEP, PDF of the SNR, and the outage probabilities are then derived from the equation. Moreover, if the Gaussian approximation is chosen for the analysis, the $p_z(\Re(Z_m^{(f)}))$ tends to follow the complex-value, zero-mean, Gaussian distribution if $N_r >> N_t$, and a closed-form expression for the noise variance is then derived in this chapter. Due to the fact that the asymptotic equation requires significantly less arithmetic operations than that of the exact equation, the Gaussian approximation is then employed to simplify the performance analysis for the OFDM-MMIMO system.

It is worth highlighting that the methodology presented in this chapter was published in [65]. The remainder of the chapter is organized as follows. The procedure to derive the PDF of $Z_m^{(f)}$ and the approximation are discussed in section 4.1. The derived $p_z(\Re(Z_m^{(f)}))$ and the approximation are then utilized to analyze the BEP, the PDF of SNR, and the outage probabilities of the system, and the methodology is summarized in section 4.2, 4.4, and 4.6, respectively. Monte-Carlo simulation is chosen by this work to evaluate the outcomes from the derived equations, and the comparisons between analytical and empirical results are additionally summarized in the sections.

4.1 Derived PDF of $Z_m^{(f)}$

According to the analysis in (2.29), mathematical expression for the EN can be expressed as $\mathbf{Z}_f = \mathbf{G}_f^{-1}\mathbf{H}_f^{\dagger}\mathbf{W}_f$. Although, the equation can be utilized to analyze the performance for the system, the inverse matrix operator in the equation complicates the analysis. Thus, the NSE is chosen to derive the equation for the m-th elements of $\mathbf{Z}_f$, i.e., $\{Z_m^{(f)}\}_{m=1}^{N_t}$[24]. The background of the NSE was briefly summarized in section 2.7.1, where the technique employs the L-th order Taylor series in (2.38) to approximate the $\mathbf{G}_f^{-1}$. If the 2-nd order

NSE is chosen to (2.29), $L = 2$ and $\mathbf{Z}_f$ is then rewritten as

$$\mathbf{Z}_f = (\mathbf{I} - \mathbf{D}_f^{-1}\mathbf{E}_f)\mathbf{D}_f^{-1}\mathbf{H}_f^{\dagger}\mathbf{W}_f. \tag{4.1}$$

It is worth noting that there are still a small deviation between the outcomes from the approximation in (4.1) and the exact $\mathbf{Z}_f$ in (2.29). However, the number of N_r for the OFDM-MMIMO system is chosen to be much larger than that of N_t, and the diagonal components of $\mathbf{G}_f$ dominate the matrix. Therefore, the differences between the results is marginal if the order of NSE, L, in (2.38) is large enough. It is worth noting that the NSE with $L \geq 3$ is still unable to be applied for this work since the mathematical expression is complex. Due to the fact that $\mathbf{D}_f$ in (2.16) is a diagonal matrix, with the elements $D_{m,m}^{(f)}$, $\mathbf{D}_f^{-1}$ can be simplified as

$$\mathbf{D}_f^{-1} = \begin{bmatrix} 1/D_{1,1}^{(f)} & 0 & 0 & \dots & 0 \\ 0 & 1/D_{2,2}^{(f)} & 0 & \dots & 0 \\ 0 & 0 & 1/D_{3,3}^{(f)} & \dots & 0 \\ \vdots & \vdots & \vdots & \ddots & \vdots \\ 0 & 0 & 0 & 0 & 1/D_{N_t,N_t}^{(f)} \end{bmatrix}. \tag{4.2}$$

If $\mathbf{A}_f = \mathbf{H}_f^{\dagger}\mathbf{W}_f$, with elements $\alpha_m^{(f)} = \sum_{n=1}^{N_r} H_{m,n}^{(f),\dagger} W_n^{(f)}$, each element of $\mathbf{Z}_f$ in (4.1) is given by

$$Z_m^{(f)} = \frac{1}{D_{m,m}^{(f)}} \left(\alpha_m^{(f)} - \sum_{n=1, n\neq m}^{N_t} \frac{E_{m,n}^{(f)} \alpha_n^{(f)}}{D_{n,n}^{(f)}} \right). \tag{4.3}$$

$E_{m,n}^{(f)}$ in (4.3) denotes an off-diagonal component of the Gram matrix in (2.20). According to the mathematical expression of the EN in (4.3), $Z_m^{(f)}$ is a function of uncorrelated random variables. Therefore, joint probabilities of the variables and the probability theory can be utilized to derive the PDF of $Z_m^{(f)}$. However, several arithmetic operators are included in the equation, making complications to the analysis. Thus, approximations are still required for simplifying the equation. According to the methodology in section 2.5.1, $D_{m,m}^{(f)}$ can be approximated as a constant Ω in (2.19) if $N_r >> N_t$. By substituting the constant in $D_{m,m}^{(f)}$ of (4.3), $Z_m^{(f)}$ becomes

$$Z_m^{(f)} = \frac{\alpha_m^{(f)}}{\Omega} - \frac{1}{\Omega^2} \sum_{n=1, n\neq m}^{N_t} E_{m,n}^{(f)} \alpha_n^{(f)}. \tag{4.4}$$

Evidently, the mathematical expression for $Z_m^{(f)}$ in (4.4) is less complex than that of (4.3). Therefore, the equation is employed to derive the PDF of $\Re(Z_m^{(f)})$. A number of variables is additionally defined in this section in order to simplify the explanation. If $\tilde{\alpha}_m^{(f)} = \alpha_m^{(f)}/\Omega$, $\beta_m^{(f)} = \sum_{n=1, n\neq m}^{N_t} E_{m,n}^{(f)} \alpha_n^{(f)}$, and $\tilde{\beta}_m^{(f)} = \beta_m^{(f)}/\Omega^2$, $Z_m^{(f)}$ in (4.4) is then rewritten as

$$Z_m^{(f)} = \tilde{\alpha}_m^{(f)} - \tilde{\beta}_m^{(f)}. \tag{4.5}$$

4.1.1 Deriving PDF of $\alpha_m^{(f)}$ and $\beta_m^{(f)}$

The PDFs of $\alpha_m^{(f)}$ and $\beta_m^{(f)}$ are discussed in this sub-section. According to (4.3), $\mathbf{A}_f$ is a product of $\mathbf{H}_f^{\dagger}$ and $\mathbf{W}_f$. Thus, the in-phase and quadrature elements of $\alpha_m^{(f)}$ can be written in terms of real arithmetic operators as

$$\Re(\alpha_m^{(f)}) = \sum_{n=1}^{N_r} \Re(H_{n,m}^{(f),*})\Re(W_n^{(f)}) - \sum_{n=1}^{N_r} \Im(H_{n,m}^{(f),*})\Im(W_n^{(f)}), \tag{4.6a}$$

$$\Im(\alpha_m^{(f)}) = \sum_{n=1}^{N_r} \Re(H_{n,m}^{(f),*})\Im(W_n^{(f)}) + \sum_{n=1}^{N_r} \Im(H_{n,m}^{(f),*})\Re(W_n^{(f)}). \tag{4.6b}$$

Due to $H_{n,m}^{(f)}$ and $W_n^{(f)}$ are the Gaussian random variables, $\alpha_m^{(f)}$ in (4.6) is identical to the $2N_r$ times combination of product of in-phase or quadrature elements of $H_{n,m}^{(f),*}$ and $W_n^{(f)}$. (6.9) in [63] can be employed to derive the PDF of a combination of products of two Gaussian random variables. By substituting $\mathcal{N}(0, \sigma_h^2)$ and $\mathcal{N}(0, \sigma_w^2)$ in the equation, the $p_\alpha(\Re(\alpha_m^{(f)}))$ is given by

$$p_\alpha(\Re(\alpha_m^{(f)})) = \frac{1}{\Gamma(N_r)} \exp\left(-\frac{|\Re(\alpha_m^{(f)})|}{\sigma_h\sigma_w}\right) \sum_{k=1}^{N_r} \frac{(N_r+k-2)!|\Re(\alpha_m^{(f)})|^{N_r-k}}{2^{N_r+k-1}(\sigma_h\sigma_w)^{N_r-k+1}(N_r-k)!\Gamma(k)}. \tag{4.7}$$

Likewise, (6.9) in [63] can be employed to derive the PDF of $\Re(\beta_m^{(f)})$ in (4.5). The variable is a $2(N_t-1)$ times summation of the product of $\wp(E_{m,n}^{(f)})$ and $\wp(\alpha_m^{(f)})$, where $\wp(.)$ represents in-phase or quadrature component operator. The PDF of both variables tends to be the Gaussian distribution, using the variance per dimension in (2.21) and (4.9), respectively. By using σ_e^2 and σ_α^2 from the equations in (6.9) in [63], $p_\beta(\Re(\beta_m^{(f)}))$ becomes

$$\begin{aligned} p_\beta(\Re(\beta_m^{(f)})) = &\frac{1}{2^{2N_t-2}} \exp\left(-\frac{|\Re(\beta_m^{(f)})|}{2N_r\sigma_h^3\sigma_w}\right) \\ &\times \sum_{k=1}^{N_t-1} \frac{(N_t+k-3)!|\Re(\beta_m^{(f)})|^{N_t-k-1}}{(N_r\sigma_h^3\sigma_w)^{N_t-k}(N_t-2)!(N_t-k-1)!\Gamma(k)}. \end{aligned} \tag{4.8}$$

4.1.2 Approximation of $p_\alpha(\Re(\alpha_m^{(f)}))$ and $p_\beta(\Re(\beta_m^{(f)}))$

According to (4.6), $\alpha_m^{(f)}$ is calculated from multiple Gaussian random variables, using addition, subtraction, and multiplication operators. Therefore, $p_\alpha(\Re(\alpha_m^{(f)}))$ can be approximated as the $\mathcal{N}(0, \sigma_\alpha^2)$, if N_r is large enough. Since $\alpha_m^{(f)}$ in (4.6) is a $2N_r$ times combination of in-phase or quadrature components of $H_{n,m}^{(f),*}$ and $W_n^{(f)}$, σ_α^2 is given as

$$\sigma_\alpha^2 = 2N_r\,\mathbb{E}\,|H_{n,m}^{(f),*}|^2\,\mathbb{E}\,|W_n^{(f)}|^2, \tag{4.9a}$$

$$\sigma_\alpha^2 = 2\sigma_h^2\sigma_w^2 N_r. \tag{4.9b}$$

Likewise, $\beta_m^{(f)}$ in (4.5) is a $2N_r - 2$ times summation of products of $E_{m,n}^{(f)}$ and $\alpha_n^{(f)}$. According to the analysis in (2.21) and (4.9), both $E_{m,n}^{(f)}$ and $\alpha_n^{(f)}$ approaches Gaussian distribution if $N_r >> N_t$. Thus, $p_\beta(\Re(\beta_m^{(f)}))$ can be approximated as the $\mathcal{N}(0, \sigma_\beta^2)$. The variance per dimension for $\beta_m^{(f)}$ is derived by using the definition for the variable in (4.5), and results in

$$\sigma_\beta^2 = 2(N_t - 1)\,\mathbb{E}\,|E_{m,n}^{(f)}|^2\,\mathbb{E}\,|\alpha_n^{(f)}|^2, \tag{4.10a}$$

$$\sigma_\beta^2 = 2(N_t - 1)\sigma_e^2\sigma_\alpha^2. \tag{4.10b}$$

4.1.3 PDF of $\tilde{\alpha}_m^{(f)}$ and $\tilde{\beta}_m^{(f)}$

$\tilde{\alpha}_m^{(f)}$ and $\tilde{\beta}_m^{(f)}$ in (4.5) are the ratio of $\alpha_m^{(f)}$ and $\beta_m^{(f)}$ to the constant, Ω and Ω^2, respectively. Therefore, the PDF transformation in (A.10) is chosen to derive the PDFs of $\tilde{\alpha}_m^{(f)}$ and $\tilde{\beta}_m^{(f)}$, and the results from the operation are

$$p_{\tilde{\alpha}}(\Re(\tilde{\alpha}_m^{(f)})) = \Omega p_\alpha(\Omega\Re(\tilde{\alpha}_m^{(f)})), \tag{4.11a}$$

$$p_{\tilde{\beta}}(\Re(\tilde{\beta}_m^{(f)})) = \Omega^2 p_\beta(\Omega^2\Re(\tilde{\beta}_m^{(f)})). \tag{4.11b}$$

If $p_\alpha(\Re(\alpha_m^{(f)}))$, $p_\beta(\Re(\beta_m^{(f)}))$, and Ω from (4.7), (4.8), and (2.19), respectively, are chosen to (4.11), the PDFs of $\Re(\tilde{\alpha}_m^{(f)})$ and $\Re(\tilde{\beta}_m^{(f)})$ become

$$p_{\tilde{\alpha}}(\Re(\tilde{\alpha}_m^{(f)})) = \sum_{k=1}^{N_r} f_{\tilde{\alpha}}(k)|\Re(\tilde{\alpha}_m^{\lambda})|^{N_r-k} \exp\left(-\frac{2N_r\sigma_h|\Re(\tilde{\alpha}_m^{(f)})|}{\sigma_w}\right), \tag{4.12a}$$

$$p_{\tilde{\beta}}(\Re(\tilde{\beta}_m^{(f)})) = \sum_{k=1}^{N_t-1} f_{\tilde{\beta}}(k)|\Re(\tilde{\beta}_m^{(f)})|^{N_t-k-1} \exp\left(-\frac{2N_r\sigma_h|\Re(\tilde{\beta}_m^{(f)})|}{\sigma_w}\right), \tag{4.12b}$$

where the function $f_{\tilde{\alpha}}(k)$ and $f_{\tilde{\beta}}(k)$ are defined as

$$f_{\tilde{\alpha}}(k) = \frac{(N_r\sigma_h)^{N_r-k+1}(N_r + k - 2)!}{2^{2k-2}\sigma_w^{N_r-k+1}\Gamma(N_r)\Gamma(k)(N_r - k)!}, \tag{4.13a}$$

$$f_{\tilde{\beta}}(k) = \frac{(N_r\sigma_h)^{N_t-k}(N_t + k - 3)!}{2^{2k-2}\sigma_w^{N_t-k}\Gamma(k)(N_t - 2)!(N_t - k - 1)!}. \tag{4.13b}$$

4.1.4 Asymptotic PDF of $\tilde{\alpha}_m^{(f)}$ and $\tilde{\beta}_m^{(f)}$

According to the analysis in section 4.1.2, $p_\alpha(\Re(\alpha_m^{(f)}))$ and $p_\beta(\Re(\beta_m^{(f)}))$ approach the $\mathcal{N}(0, \sigma_\alpha^2)$ and $\mathcal{N}(0, \sigma_\beta^2)$, respectively. If the Gaussian approximation of $p_\alpha(\Re(\alpha_m^{(f)}))$, $p_\beta(\Re(\beta_m^{(f)}))$ are substituted in (4.11), the asymptotic PDFs of $\Re(\tilde{\alpha}_m^{(f)})$ and $\Re(\tilde{\beta}_m^{(f)})$ become

$$p_{\tilde{\alpha}}(\Re(\tilde{\alpha}_m^{(f)})) \simeq \mathcal{N}(0, \sigma_\alpha^2/\Omega^2), \tag{4.14a}$$

$$p_{\tilde{\beta}}(\Re(\tilde{\beta}_m^{(f)})) \simeq \mathcal{N}(0, \sigma_\beta^2/\Omega^4). \tag{4.14b}$$

The approximations in (4.14) confirm that $p_{\tilde{\alpha}}(\Re(\tilde{\alpha}_m^{(f)}))$ and $p_{\tilde{\beta}}(\Re(\tilde{\beta}_m^{(f)}))$ approach the Gaussian distribution, where the variance per dimension are σ_α^2/Ω^2 and σ_β^2/Ω^4, respectively. If σ_α^2, σ_β^2, and Ω in (4.9), (4.10), and (2.19) are substituted in (4.14), the $\sigma_{\tilde{\alpha}}^2$ and $\sigma_{\tilde{\beta}}^2$ becomes

$$\sigma_{\tilde{\alpha}}^2 = \frac{\sigma_w^2}{2N_r\sigma_h^2}, \tag{4.15a}$$

$$\sigma_{\tilde{\beta}}^2 = \frac{(N_t-1)\sigma_w^2}{2N_r^2\sigma_h^2}. \tag{4.15b}$$

Fig. 4.1 compares the outcomes from the derived $p_\alpha(\Re(\alpha_m^{(f)}))$ and $p_{\tilde{\alpha}}(\Re(\tilde{\alpha}_m^{(f)}))$ in (4.7) and (4.12a), respectively, with that of the empirical. The asymptotic PDFs of $\Re(\alpha_m^{(f)})$ and $\Re(\tilde{\alpha}_m^{(f)})$ from the approximations in (4.9) and (4.15a) are additionally included in the results. N_t was 10, and N_r was $\{50, 100, 200\}$. The system operated at $E_b/N_0 = -10$ dB. The results confirm that the proposed equations produced accurate analytical results, compared to the exact PDFs. Focusing on the 10×50 system, the exact $p_\alpha(\Re(\alpha_m^{(f)}))$ at $\Re(\alpha_m^{(f)}) = 100$ was 4.32×10^{-2}. The outcome from the derived PDF was 1.13×10^{-4} different from the exact result, whereas the number for the approximate PDF was slightly less accurate at 5.41×10^{-4}. In addition, the results show that the variation in $\Re(\alpha_m^{(f)})$ dramatically increases according to the size of N_r. By changing the value of N_r from 50 to 200, the exact $p_\alpha(\Re(\alpha_m^{(f)}))$ at $\Re(\alpha_m^{(f)}) = 100$ increased from 4.32×10^{-2} to 8.0×10^{-2}. On the contrary, the variation of $\Re(\tilde{\alpha}_m^{(f)})$ for the system using a smaller N_r becomes larger. If N_r increased from 50 to 200, the PDF at $\Re(\tilde{\alpha}_m^{(f)}) = 1$ decreased from 7.62×10^{-2} to 4.57×10^{-2}. The 2-sample Kolmogorov–Smirnov test with the significant level 5% was chosen to compare the outcome from the derived PDFs and the simulation results. The comparisons confirmed that the deviation between the PDFs was negligible.

In addition, Fig. 4.2 shows the derived $p_\beta(\Re(\beta_m^{(f)}))$ and $p_{\tilde{\beta}}(\Re(\tilde{\beta}_m^{(f)}))$ from (4.8) and (4.12b), the approximations from (4.10) and (4.15b), and the simulation results. $N_t = \{5, 10, 20\}$ and $N_r = 200$. The system operated at $E_b/N_0 = -10$ dB. Evidently, the output from the derived PDFs matched the empirical results. The derived PDF $p_\beta(\Re(\beta_m^{(f)}))$ and the simulation result for the 5×200 system at $\Re(\beta_m^{(f)}) = 0.5$ were 5.21×10^{-2} and 5.23×10^{-2}, respectively. Thus, the analytical was only 1.92×10^{-4} different from the exact PDF. However, there were deviations between the outcome from the approximate $p_\beta(\Re(\beta_m^{(f)}))$ and $p_{\tilde{\beta}}(\Re(\tilde{\beta}_m^{(f)}))$ with that of the exact PDFs, especially for the system using a smaller N_t. The asymptotic PDF of $\Re(\tilde{\beta}_m^{(f)})$ for the 5×200 system at $\Re(\tilde{\beta}_m^{(f)}) = 0.1$ was 5.87×10^{-2}, and the number was 6.49×10^{-3} different from the exact PDF. According to the 2-sample Kolmogorov–Smirnov test at the significant level 5%, the differences between the derived PDFs, the approximations and the empirical results were insignificant.

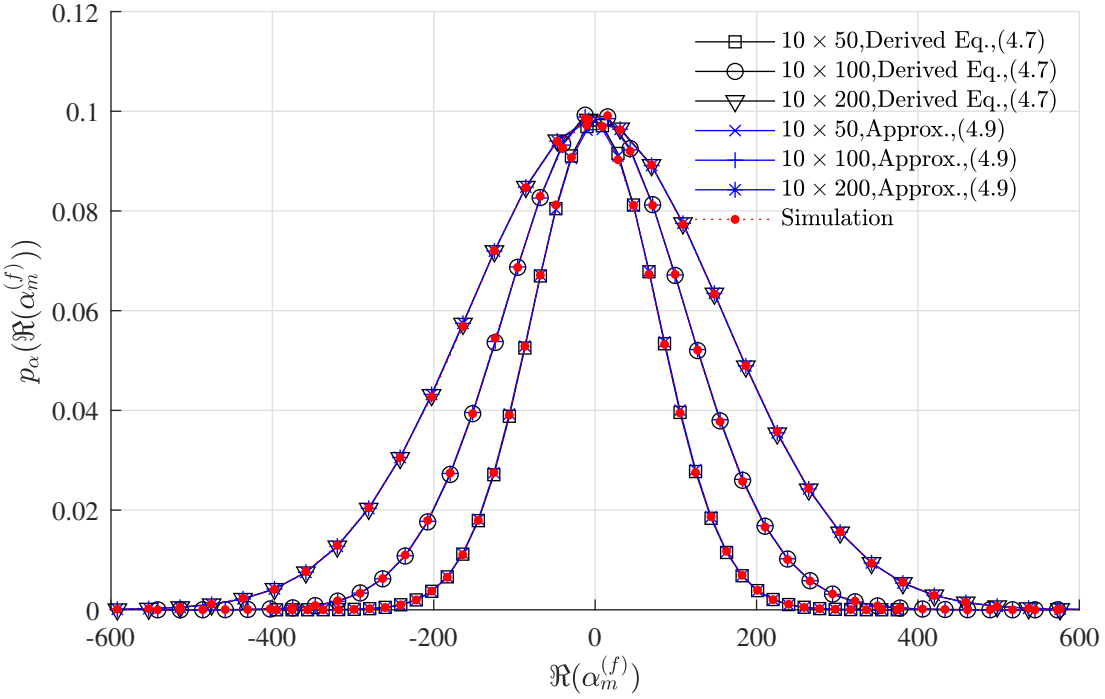

(a) $p_\alpha(\Re(\alpha_m^{(f)}))$.

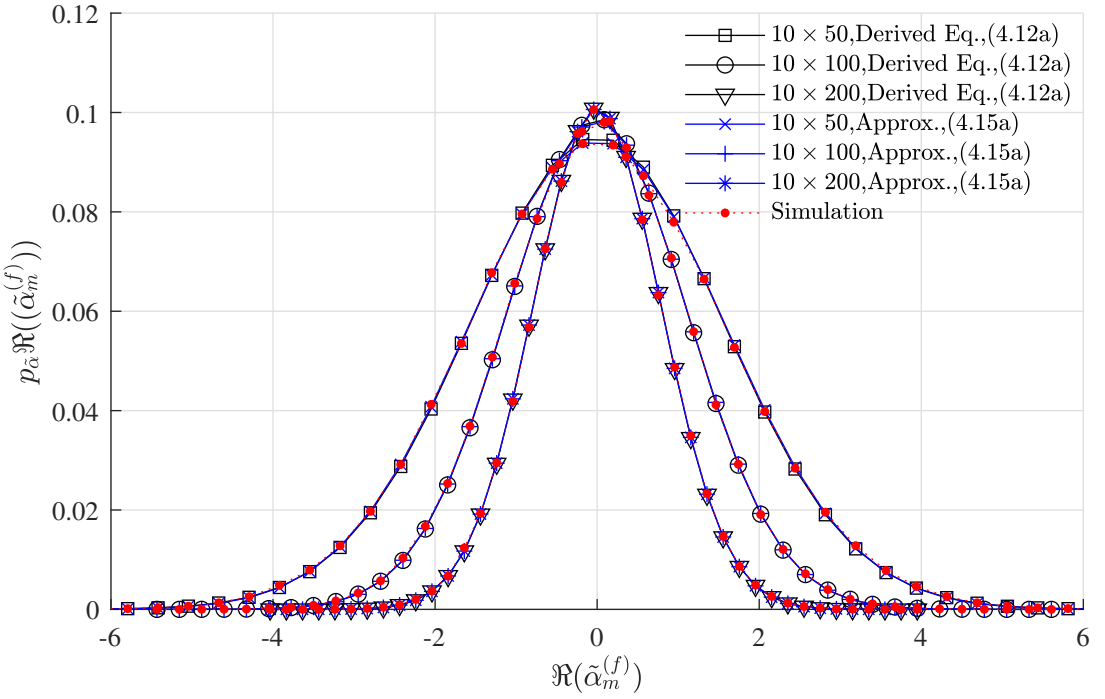

(b) $p_{\tilde{\alpha}}(\Re(\tilde{\alpha}_m^{(f)}))$.

Figure 4.1: Derived PDFs of $\Re(\alpha_m^{(f)})$ and $\Re(\tilde{\alpha}_m^{(f)})$.

4.1.5 Derived PDF of EN

The PDF of $\Re(Z_m^{(f)})$ and the asymptotic equation are derived in this section. Although $Z_m^{(f)}$ in (4.5) is calculated from a subtraction of $\tilde{\alpha}_m^{(f)}$ and $\tilde{\beta}_m^{(f)}$, both $p_{\tilde{\alpha}}(\Re(\tilde{\alpha}_m^{(f)}))$ and $p_{\tilde{\beta}}(\Re(\tilde{\beta}_m^{(f)}))$ are even functions. As a result, $Z_m^{(f)}$ is identical to a summation of $\tilde{\alpha}_m^{(f)}$ and

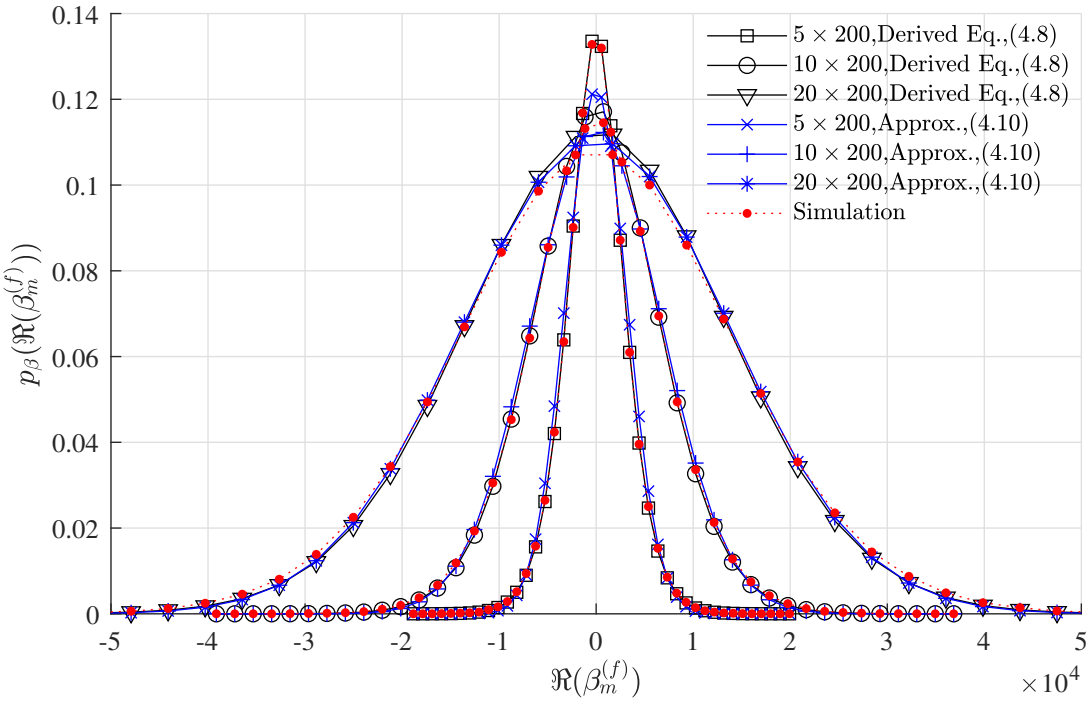

(a) $p_\beta(\Re(\beta_m^{(f)}))$.

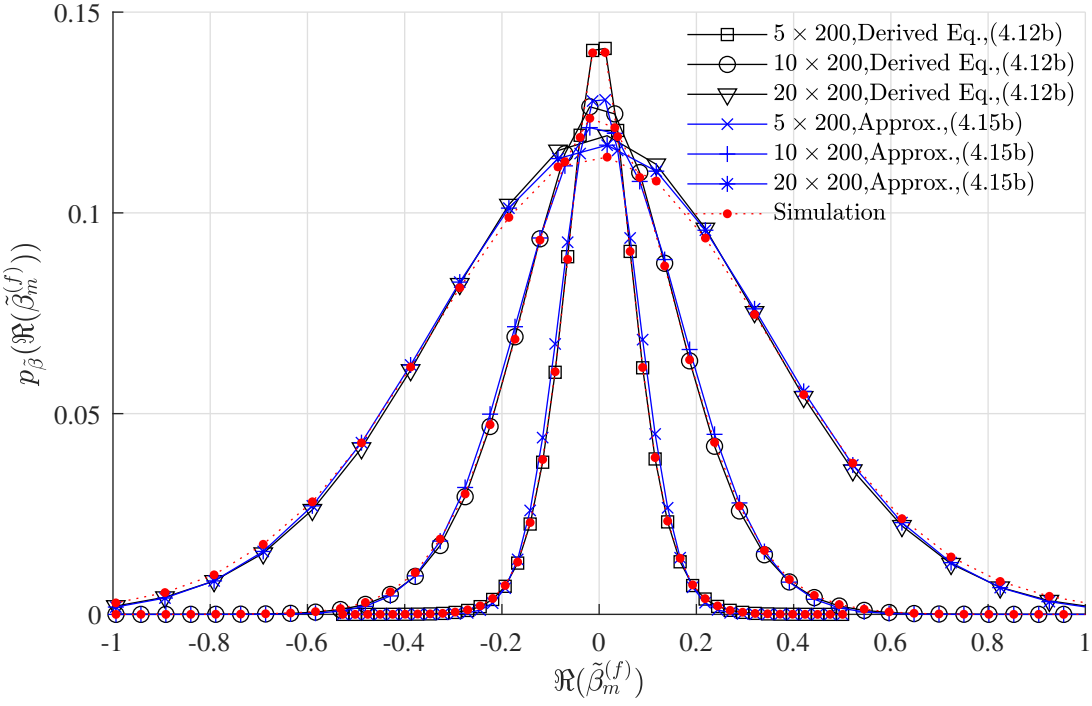

(b) $p_{\tilde{\beta}}(\Re(\tilde{\beta}_m^{(f)}))$.

Figure 4.2: Derived PDFs of $\Re(\beta_m^{(f)})$ and $\Re(\tilde{\beta}_m^{(f)})$.

$\tilde{\beta}_m^{(f)}$, and $p_z(\Re(Z_m^{(f)}))$ is then derived by using convolution integral operation[48], i.e.,

$$p_z(\Re(Z_m^{(f)})) = p_{\tilde{\alpha}}(\Re(\tilde{\alpha}_m^{(f)})) * p_{\tilde{\beta}}(\Re(\tilde{\beta}_m^{(f)})). \tag{4.16}$$

By substituting the $p_{\tilde{\alpha}}(\Re(\tilde{\alpha}_m^{(f)}))$ and $p_{\tilde{\beta}}(\Re(\tilde{\beta}_m^{(f)}))$ from (4.12) in (4.16), and using bi-

nomial expansion to decompose the equation, the outcome from the integration becomes

$$p_z(\Re(Z_m^{(f)})) = \exp\left(-\frac{2N_r\sigma_h|\Re(Z_m^{(f)})|}{\sigma_w}\right)\sum_{k=1}^{N_r}\sum_{p=1}^{N_t-1} f_z(k,p)\sum_{q=0}^{N_t-p-1}\frac{1}{(N_t-p-q-1)!q!}$$
$$\times\left(\frac{(-1)^q|\Re(Z_m^{(f)})|^{N_t+N_r-k-p}}{N_r-k+q+1} + (N_t+N_r-k-p-q-1)!|\Re(Z_m^{(f)})|^q\left(\frac{\sigma_w}{4N_r\sigma_h}\right)^{N_t+N_r-k-p-q}\right.$$
$$\left.+\sum_{r=0}^{N_t+N_r-k-p-q-1}\frac{(-1)^q(N_t+N_r-k-p-q-1)!|\Re(Z_m^{(f)})|^{N_t+N_r-k-p-r-1}}{(N_t+N_r-k-p-q-r-1)!}\left(\frac{\sigma_w}{4N_r\sigma_h}\right)^{r+1}\right), \tag{4.17}$$

where the function $f_z(k,p)$ in (4.17) is defined as

$$f_z(k,p) = \frac{(N_r+k-2)!(N_t+p-3)!}{2^{2k+2p-4}(N_t-2)!(N_r-k)!\Gamma(N_r)\Gamma(k)\Gamma(p)}\left(\frac{N_r\sigma_h}{\sigma_w}\right)^{N_t+N_r-k-p+1}. \tag{4.18}$$

4.1.6 Asymptotic $p_z(\Re(Z_m^{(f)}))$

Although the analysis for the $p_z(\Re(Z_m^{(f)}))$ in (4.17) provided accurate results, several arithmetic operators are still required by the equation for computing the outcomes. As a result, the derived equation is still inconvenient for deriving the performance of the OFDM-MMIMO system. Therefore, an asymptotic PDF of $\Re(Z_m^{(f)})$ is derived in this section. According to (4.5), $Z_m^{(f)}$ is a subtraction of $\tilde{\alpha}_m^{(f)}$ to $\tilde{\beta}_m^{(f)}$. Moreover, the $p_{\tilde{\alpha}}(\Re(\tilde{\alpha}_m^{(f)}))$ and $p_{\tilde{\beta}}(\Re(\tilde{\beta}_m^{(f)}))$ approach the Gaussian distribution, using the variance per dimension in (4.15). Therefore, the PDF of $\Re(Z_m^{(f)})$ can be approximated as the $\mathcal{N}(0,\sigma_z^2)$ too, i.e.,

$$p_z(\Re(Z_m^{(f)})) \simeq \frac{1}{\sqrt{2\pi\sigma_z^2}}\exp\left(-\frac{\Re(Z_m^{(f)})^2}{2\sigma_z^2}\right). \tag{4.19}$$

σ_z^2 in (4.19) can be obtained from the combination of $\sigma_{\tilde{\alpha}}^2$ and $\sigma_{\tilde{\beta}}^2$ in (4.15), and results in

$$\sigma_z^2 = \frac{\sigma_w^2}{\sigma_h^2}\left(\frac{1}{2N_r}+\frac{N_t-1}{2N_r^2}\right). \tag{4.20}$$

Fig. 4.3 compares the outcomes from the derived $p_z(\Re(Z_m^{(f)}))$ and the Gaussian approximation in (4.17) and (4.20), respectively, with that of the empirical. 10×64, 10×128, and 10×256 systems were chosen to the simulation, where the systems operated at $E_b/N_0 = -10$ dB and the number of sub-carriers was 512 symbols. Overall, the outcomes from the derived PDFs matched the empirical results. The derived PDF for the 10×256 system at $\Re(Z_m^{(f)}) = 1$ was 3.38×10^{-2}, and the analytical result was only 1.47×10^{-4} different from the exact PDF. However, the deviation between the analysis and the exact PDF became larger in the system, using a smaller N_r. Focusing on the 10×64 system, the deviation between the derived PDF and the exact result at $\Re(Z_m^{(f)}) = 1$ increased from 1.47×10^{-4} to 8.32×10^{-4}. Due to $D_{m,m}^{(f)}$ was assumed to be the constant, Ω, and the approximation is inaccurate if N_r is too small. In addition, the asymptotic equation

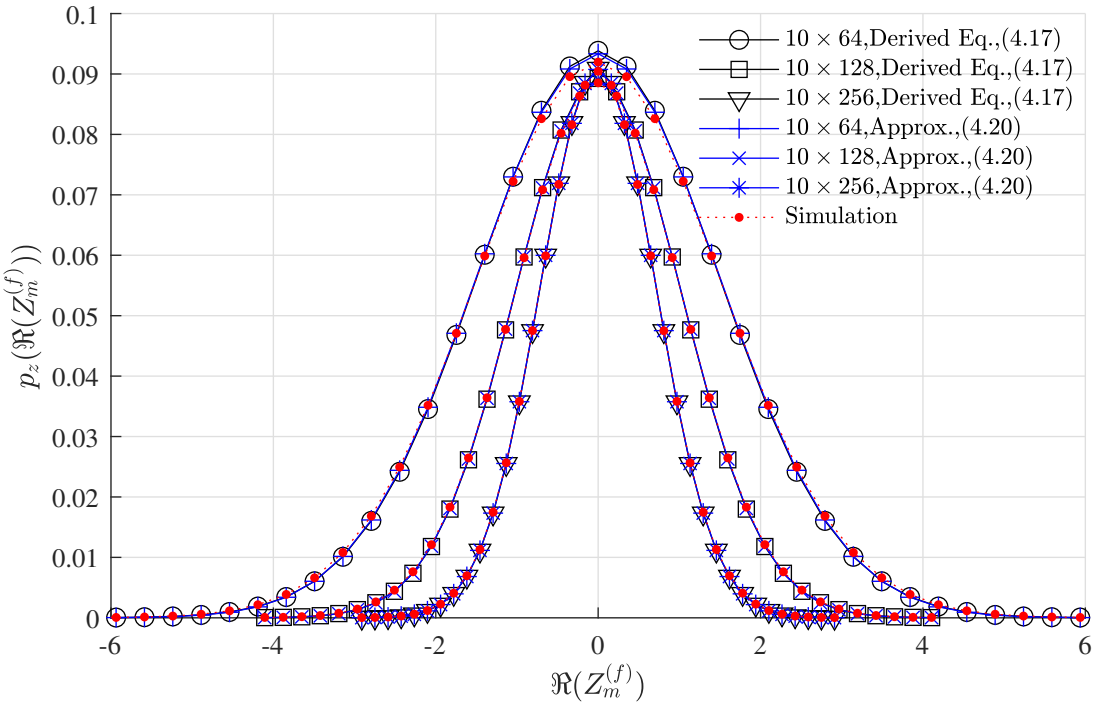

Figure 4.3: Derived PDFs of $\Re(Z_m^{(f)})$.

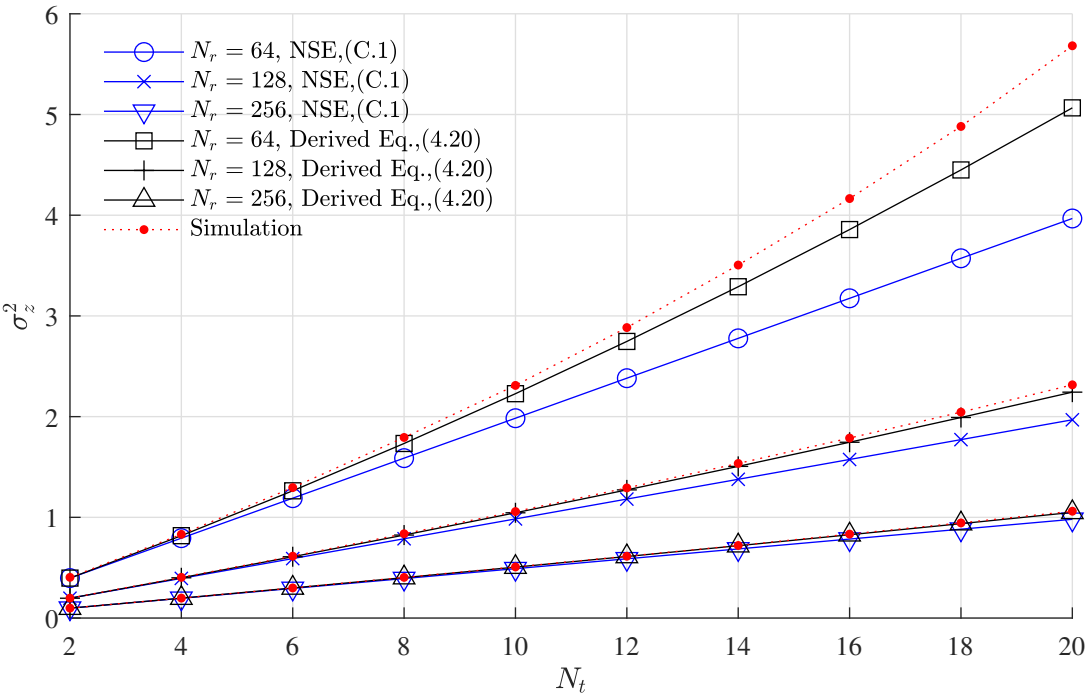

Figure 4.4: Derived effective noise variance for the OFDM-MMIMO system.

generated an accurate results, compared to the exact PDFs. If $N_r = 256$ was chosen to the system, the Gaussian approximation at $\Re(Z_m^{(f)}) = 1$ was only 7.77×10^{-5} different from the derived $p_z(\Re(Z_m^{(f)}))$. According to the 2-sample Kolmogorov–Smirnov test with the significant level 5%, there was no significant difference between the analytical and the simulation results.

In addition, Fig. 4.4 evaluates the outcomes from the derived noise variance in (4.20). The analytical results are compared to that of the empirical and the NSE in (C.1). 16-

QAM was chosen to the mapper and the system operated at $E_b/N_0 = -10$ dB. $N_r = \{64, 128, 256\}$, and N_t was varied from 2 to 20. The results show that the derived noise variance generated accurate outcomes, especially for the system with a larger N_r. The analysis for a 20×256 system was 1.049, exhibiting 1.17×10^{-2} difference from the exact variance. Moreover, the derived noise variance was more accurate than that of the NSE, and the deviation between the NSE and the exact variance was larger at 8.03×10^{-2}. However, there was a accuracy reduction in the analysis for a system using a smaller N_t due to the approximation for $D^{(f)}_{m,m}$ in (4.4) was imprecise for this case. The deviation between the analytical and the exact results for a 20×64 system increased to 0.62. Furthermore, the results reveal a reduction in the distribution of $\Re(Z^{(f)}_m)$ on the system using a larger N_r. The derived noise variance for a 20×64 system was 5.07, whereas the number of a 20×256 system decreased to 1.05. These results confirm that the distribution of $\Re(Z^{(f)}_m)$ can be efficiently reduced by increasing the number of N_r in the OFDM-MMIMO system.

4.2 BEP analysis

The BEP for the OFDM-MMIMO system is now analyzed in this section by using the derived PDF of the EN and the approximation in (4.17) and (4.20), respectively. The analysis for BEP was previously derived in (3.42) of chapter 3, and the analysis for M-QAMs was written in forms of the CDF of $Z^{(f)}_m$ as

$$P_e^{M-\mathrm{QAM}} = \frac{2(M_\lambda - 1)}{M_\lambda \log_2(M_\lambda)} P(\Re(\hat{X}^{(f)}_m)|\Re(X^{(f)}_m) = \bar{X}_a, K). \tag{4.21}$$

$P(\Re(\hat{X}^{(f)}_m)|\Re(X^{(f)}_m) = \bar{X}_a, K)$ in (4.21) denotes the CDF of $Z^{(f)}_m$, which is derived by utilizing the integration of the $p_z(\Re(Z^{(f)}_m))$ in (3.30). By substituting the PDF from (4.17) in (3.30), and using the binomial expansion to expand the polynomial, the CDF is given

by

$$
\begin{aligned}
&P(\Re(\hat{X}_m^{(f)})|\Re(X_m^{(f)}) = \bar{X}_a, K) = \\
&\exp\left(-\frac{2N_r\sigma_h K}{\sigma_w}\right)\sum_{k=1}^{N_r}\sum_{p=1}^{N_t-1} f_z(k,p)\sum_{q=0}^{N_t-p-1}\frac{1}{(N_t-p-q-1)!q!} \\
&\times\left(\frac{(-1)^q(N_t+N_r-k-p)!}{N_r-k+q+1}\sum_{s=0}^{N_t+N_r-k-p}\frac{K^s}{s!}\left(\frac{\sigma_w}{2N_r\sigma_h}\right)^{N_t+N_r-k-p-s+1}\right. \\
&+(N_t+N_r-k-p-q-1)!q!\sum_{s=0}^{q}\frac{K^s}{2^{2N_t+2N_r-2k-2p-q-s+1}s!}\left(\frac{\sigma_w}{N_r\sigma_h}\right)^{N_t+N_r-k-p-s+1} \\
&+\sum_{r=0}^{N_t+N_r-k-p-q-1}\sum_{s=0}^{N_t+N_r-k-p-r-1}\frac{(-1)^q K^s(N_t+N_r-k-p-q-1)!}{2^{N_t+N_r-k-p+r-s+2}(N_t+N_r-k-p-q-r-1)!s!} \\
&\left.\times\,(N_t+N_r-k-p-r-1)!\left(\frac{\sigma_w}{N_r\sigma_h}\right)^{N_t+N_r-k-p-s+1}\right).
\end{aligned}
\tag{4.22}
$$

Focusing on a system, using BPSK or QPSK modulation, the BEP is obtained by substituting $M_\lambda = 2$ in (4.21), and results in

$$
P_e^{\text{BPSK,QPSK}} = P(\Re(\hat{X}_m^{(f)})|\Re(X_m^{(f)}) = \bar{X}_a, K). \tag{4.23}
$$

Likewise, if 16-QAM modulation is chosen to the mapper, $M_\lambda = 4$, and the BEP for the system is then derived by using the variable in (4.21). As a result, the P_e becomes

$$
P_e^{16-\text{QAM}} = \frac{3}{4}P(\Re(\hat{X}_m^{(f)})|\Re(X_m^{(f)}) = \bar{X}_a, K). \tag{4.24}
$$

4.3 Approximation of BEP analysis

It is worth noting that the BEP analysis in (4.23) and (4.24) requires the derived CDF in (4.22) to calculate the outcome, and the computational complexity for the CDF dramatically increases according to the size of N_t and N_r. As a result, the analysis still requires several arithmetic operators to calculate the outcome. Thus, an asymptotic BEP for the system is additionally derived in this section. As previously stated, the $p_z(\Re(Z_m^{(f)}))$ for the OFDM-MMIMO system tends to be the $\mathcal{N}(0,\sigma_z^2)$ in (4.19). If the approximation is chosen to (3.30), the CDF can be simplified as

$$
P(\Re(\hat{X}_m^{(f)})|\Re(X_m^{(f)}) = \bar{X}_a, K) \simeq Q\left(\frac{K}{\sigma_z}\right). \tag{4.25}
$$

By substituting the CDF from (4.25) in (4.21), the BEP becomes

$$
P_e^{M-\text{QAM}} \simeq \frac{2(M_\lambda-1)}{M_\lambda\log_2(M_\lambda)}Q\left(\frac{K}{\sigma_z}\right). \tag{4.26}
$$

The value of M_λ for BPSK and QPSK modulation is 2, and the number for 16-QAM is 4. Therefore, the asymptotic BEP for the system can be obtained by using $M_\lambda = \{2, 4\}$ in (4.26), and results in

$$P_e^{\text{BPSK,QPSK}} \simeq Q\left(\frac{K}{\sigma_z}\right), \tag{4.27a}$$

$$P_e^{\text{16-QAM}} \simeq \frac{3}{4} Q\left(\frac{K}{\sigma_z}\right). \tag{4.27b}$$

Evidently, the approximations in (4.27) require less arithmetic operators than that of the exat analysis in (4.23) and (4.24). On the contrary, the outcomes from the asymptotic equations are less accurate than that of the exact BEP. However, the $p_z(\Re(Z_m^{(f)}))$ converges to the Gaussian distribution if $N_r > 10N_t$ and $N_r \geq 100$. Therefore, the deviation between the exact and the approximate equations becomes smaller for this case. Fig. 4.5 compares the BEP analysis for 16-QAM from (4.24) and the approximations in (4.27) with the empirical results. The BEP analysis from (29) in [24] is additionally included in the results. The 16-QAM constellation points in Fig. 2.2 with $K = 1$ were employed by the transmitter to generate the transmit symbols. The block size utilization was 1024 bits. According to the results, the deviation between the analysis and the exact BEP was marginal. The exact BEP for the 10×200 system, operating at $E_b/N_0 = 0$ dB, was 4.14×10^{-5}. The analysis from the derived equation and the approximation were 3.83×10^{-5} and 3.42×10^{-5}, respectively, exhibiting a difference of 3.17×10^{-6} and 7.25×10^{-6} from the exact result, respectively. Moreover, the deviation between the analysis from [24] and the simulation result was 6.39×10^{-6}. Therefore, the outcome from the exact BEP analysis was more accurate than that of [24]. However, there was a accuracy reduction in the analysis for the system using a lower N_r due to the analysis assumed that $D_{m,m}^{(f)}$ approach the constant. The outcome from the exact BEP for the 10×50 system at $E_b/N_0 = 6$ dB was 1.91×10^{-4}, which was 7.62×10^{-5} smaller than the simulation result.

In addition, Fig. 4.6 compares the BEP analysis for QPSK modulation from (4.23), the asymptotic BEP from (4.27a), with those obtained from the empirical. The BEP analysis for QPSK modulation (Eq. (27) in [24]) and BPSK modulation (Eq. (39) in [16]) are included in the results. N_t and N_r was $\{5, 10, 15\}$ and 100, respectively. K and the block size utilization were 1 and 1024, respectively. Focusing on the results for the 5×100 system at $E_b/N_0 = -4$ dB, the outcomes from the exact analysis and the approximation were 5.68×10^{-5} and 4.56×10^{-5}, which were 5.89×10^{-6} and 1.71×10^{-5}. Thus, the exact equation generates accurate BEP analysis for the system, whereas the accuracy for the asymptotic equation was slightly less than that of the exact equation. In addition, the analysis for the 5×100 system from [16] and [24] at $E_b/N_0 = -4$ dB were 1.25×10^{-6} and 4.96×10^{-5}. The results confirm that the proposed BEP analysis was more accurate than the analysis from [24]. However, the deviation in BEP between the analytical result from the proposed equation and the exact BEP was still higher than that of the BEP in

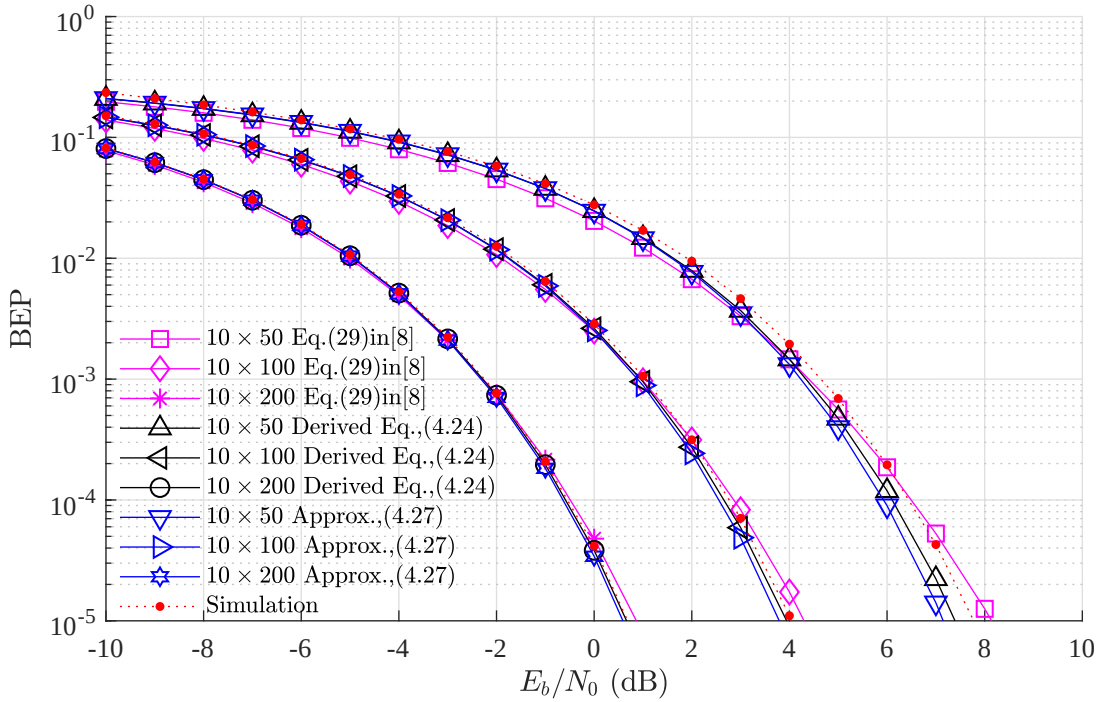

Figure 4.5: BEP analysis for 16-QAM.

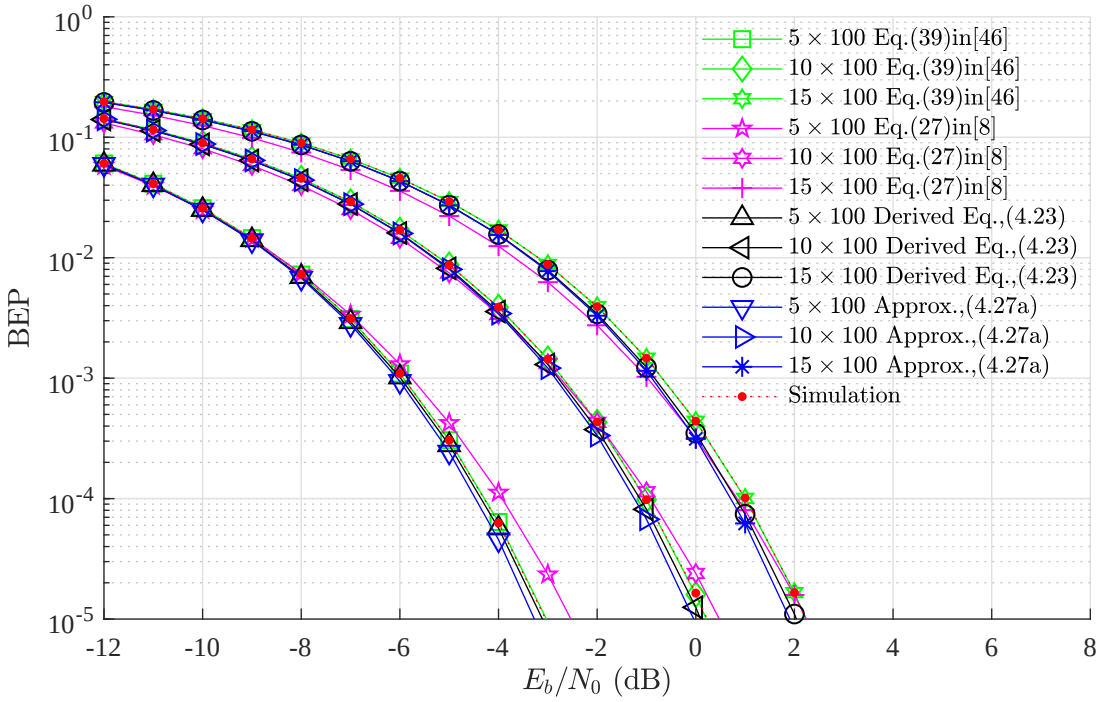

Figure 4.6: Comparison of BEP analysis for QPSK modulation.

[16].

4.4 Derived PDF of SNR

The PDF of the output SNR, $p_\gamma(\gamma_s)$, and the asymptotic PDF are derived in this section. According to the methodology in section 3.5, γ_s is a function of $Z_m^{(f)}$ in (3.45) and the PDF of γ_s can be expressed in terms of $p_z(\Re(Z_m^{(f)}))$ in (3.46). If the PDF of $Z_m^{(f)}$ in

(4.17) is substituted in (3.46), the derived $p_\gamma(\gamma_s)$ for the OFDM-MMIMO system, using ZF detection, becomes

$$\begin{aligned} p_\gamma(\gamma_s) = \exp\left(-\frac{2N_r\sigma_h}{\sigma_w}\sqrt{\frac{E_\lambda}{\gamma_s}}\right) \sum_{k=1}^{N_r}\sum_{p=1}^{N_t-1} f_z(k,p) \sum_{q=0}^{N_t-p-1} \frac{1}{(N_t-p-q-1)!q!} \\ \times \left(\frac{(-1)^q}{N_r-k+q+1} \left(\frac{E_\lambda^{N_t+N_r-k-p+1}}{\gamma_s^{N_t+N_r-k-p+3}}\right)^{1/2} \right. \\ + (N_t+N_r-k-p-q-1)! \left(\frac{E_\lambda^{q+1}}{\gamma_s^{q+3}}\right)^{1/2} \left(\frac{\sigma_w}{4N_r\sigma_h}\right)^{N_t+N_r-k-p-q} \\ + \sum_{r=0}^{N_t+N_r-k-p-q-1} \frac{(-1)^q(N_t+N_r-k-p-q-1)!}{(N_t+N_r-k-p-q-r-1)!} \left(\frac{E_\lambda^{N_t+N_r-k-p-r}}{\gamma_s^{N_t+N_r-k-p-r+2}}\right)^{1/2} \\ \left. \times \left(\frac{\sigma_w}{4N_r\sigma_h}\right)^{r+1} \right). \end{aligned} \tag{4.28}$$

4.5 Asymptotic $p_\gamma(\gamma_s)$

It is worth noting that the derived PDF in (4.28) involves several arithmetic operators, making a high computational complexity to the analysis. Therefore, the approximate $p_\gamma(\gamma_s)$ is additionally derived to simplify the analysis. According to the analysis in (4.19), the $p_z(\Re(Z_m^{(f)}))$ approaches the $\mathcal{N}(0,\sigma_z^2)$. If the approximate PDF is chosen to (3.46), the asymptotic $p_\gamma(\gamma_s)$ is given by

$$p_\gamma(\gamma_s) \simeq \sqrt{\frac{E_\lambda}{2\pi\sigma_z^2\gamma_s^3}}\ \exp\left(-\frac{E_\lambda}{2\gamma_s\sigma_z^2}\right). \tag{4.29}$$

The analysis from the derived PDF of γ_s and the approximation in (4.28) and (4.29), respectively, were evaluated through Monte-Carlo simulation and the results are shown in Fig. 4.7. The system employed 16-QAM to generate the transmit symbol and operated at $E_b/N_0 = 5$ dB. $N_t = 10$ and $N_r = \{50, 100, 200\}$. The results reveal a good match between the derived $p_\gamma(\gamma_s)$ and the empirical results. Moreover, the outcome from the approximation was slightly less accurate than the exact analysis. The true $p_\gamma(\gamma_s)$ for a 10×200 system at $\gamma_s = 18$ was 9.84×10^{-3}. The analysis from the derived and the asymptotic equations were 1.23×10^{-4} and 9.79×10^{-5} different from the true PDF, respectively. In addition, according to the 2-sample Kolmogorov–Smirnov test with a significance level of 5%, the difference between the outcomes from the derived PDFs and those from the empirical was negligible. It is worth noting that the deviation between simulation and analytical results became larger for the system using a smaller N_r due to the underlying assumptions made in the derivations. Focusing on a 10×50 system, the deviation between the derived PDF and the empirical results at $\gamma_s = 10$ increased to 3.02×10^{-3}.

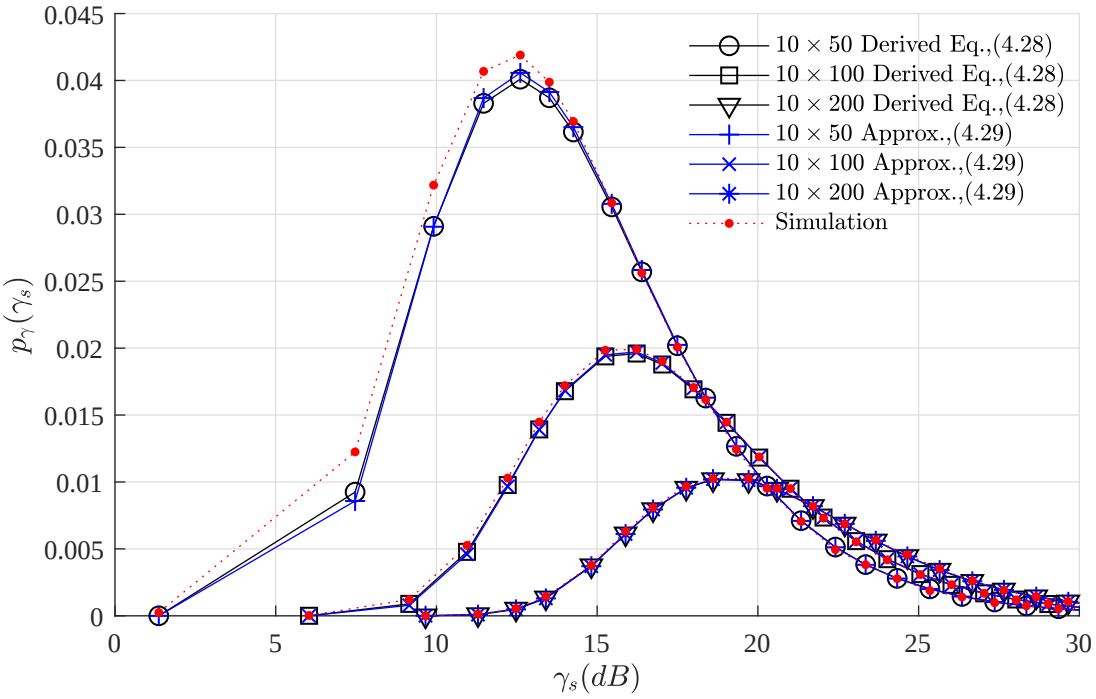

Figure 4.7: Derived PDF of γ_s.

4.6 Derived outage probabilities

According to the methodology in section 3.6, the outage probabilities for the OFDM-MMIMO system can be determined by the integration of $p_\gamma(\gamma_s)$, where the integral boundary of γ_s is from zero to γ_{th}, i.e., (3.49). If the PDF from (4.28) is chosen to the equation, the $P_{\text{out}}(\gamma_{\text{th}})$ becomes

$$
\begin{aligned}
P_{\text{out}}(\gamma_{\text{th}}) = & \sum_{k=1}^{N_r}\sum_{p=1}^{N_t-1} f_z(k,p) \sum_{q=0}^{N_t-p-1} \frac{1}{(N_t-p-q-1)!q!} \\
& \times \left(\frac{(-1)^q}{(N_r-k+q+1)} E_\lambda^{(N_t+N_r-k-p+1)/2} \int_0^{\gamma_{th}} \frac{e^{\left(-\frac{2N_r\sigma_h}{\sigma_w}\sqrt{\frac{E_\lambda}{\gamma_s}}\right)}}{\gamma_s^{(N_t+N_r-k-p+3)/2}} d\gamma_s \right. \\
& + (N_t+N_r-k-p-q-1)! E_\lambda^{(q+1)/2} \left(\frac{\sigma_w}{4N_r\sigma_h}\right)^{N_t+N_r-k-p-q} \int_0^{\gamma_{th}} \frac{e^{\left(-\frac{2N_r\sigma_h}{\sigma_w}\sqrt{\frac{E_\lambda}{\gamma_s}}\right)}}{\gamma_s^{(q+3)/2}} d\gamma_s \\
& + \sum_{r=0}^{N_t+N_r-k-p-q-1} \frac{(-1)^q (N_t+N_r-k-p-q-1)!}{(N_t+N_r-k-p-q-r-1)!} E_\lambda^{(N_t+N_r-k-p-r)/2} \left(\frac{\sigma_w}{4N_r\sigma_h}\right)^{r+1} \\
& \left. \times \int_0^{\gamma_{th}} \frac{e^{\left(-\frac{2N_r\sigma_h}{\sigma_w}\sqrt{\frac{E_\lambda}{\gamma_s}}\right)}}{\gamma_s^{(N_t+N_r-k-p-r+2)/2}} d\gamma_s \right).
\end{aligned}
\tag{4.30}
$$

After employing (3.351.2) in [62] and the substitution method in [64] to solve the

integration in (4.30), the $P_{\text{out}}(\gamma_{\text{th}})$ becomes

$$P_{\text{out}}(\gamma_{\text{th}}) = 2\exp\left(-\frac{2N_r\sigma_h}{\sigma_w}\sqrt{\frac{E_\lambda}{\gamma_{th}}}\right)\sum_{k=1}^{N_r}\sum_{p=1}^{N_t-1} f_z(k,p)\sum_{q=0}^{N_t-p-1}\frac{1}{(N_t-p-q-1)!q!}$$
$$\times\left(\frac{(-1)^q(N_t+N_r-k-p)!E_\lambda^{(N_t+N_r-k-p+1)/2}}{N_r-k+q+1}\sum_{r=0}^{N_t+N_r-k-p}\frac{1}{r!\sqrt{\gamma_{th}^r}}\left(\frac{\sigma_w}{2N_r\sigma_h\sqrt{E_\lambda}}\right)^{N_t+N_r-k-p-r+1}\right.$$
$$+ q!(N_t+N_r-k-p-q-1)!E_\lambda^{(q+1)/2}\left(\frac{\sigma_w}{4N_r\sigma_h}\right)^{N_t+N_r-k-p-q}\sum_{r=0}^{q}\frac{1}{r!\sqrt{\gamma_{th}^r}}\left(\frac{\sigma_w}{2N_r\sigma_h\sqrt{E_\lambda}}\right)^{q-r+1}$$
$$+\sum_{r=0}^{N_t+N_r-k-p-q-1}\frac{(N_t+N_r-k-p-q-1)!(N_t+N_r-k-p-r-1)!}{(N_t+N_r-k-p-q-r-1)!}\left(\frac{\sigma_w}{4N_r\sigma_h}\right)^{r+1}$$
$$\left.\times(-1)^q E_\lambda^{(N_t+N_r-k-p-r)/2}\sum_{s=0}^{N_t+N_r-k-p-r-1}\frac{1}{s!\sqrt{\gamma_{th}^s}}\left(\frac{\sigma_w}{2N_r\sigma_h\sqrt{E_\lambda}}\right)^{N_t+N_r-k-p-r-s}\right). \tag{4.31}$$

4.7 Approximation of derived outage probabilities

The analysis for $P_{\text{out}}(\gamma_{\text{th}})$ can be simplified by using the asymptotic PDF of γ_s in (4.29). If the approximation is chosen to (3.49), the asymptotic $P_{\text{out}}(\gamma_{\text{th}})$ is given by

$$P_{\text{out}}(\gamma_{\text{th}}) \simeq \sqrt{\frac{E_\lambda}{2\pi\sigma_z^2}}\int_0^{\gamma_{th}}\frac{1}{\sqrt{\gamma_s^3}}\exp\left(-\frac{E_\lambda}{2\gamma_s\sigma_z^2}\right)d\gamma_s. \tag{4.32}$$

If the substitution method in [64] is chosen to solve the integration in (4.32), the $P_{\text{out}}(\gamma_{\text{th}})$ becomes

$$P_{\text{out}}(\gamma_{\text{th}}) \simeq \Gamma\left(\frac{E_\lambda}{2\sigma_z^2\gamma_{th}}, 1/2\right). \tag{4.33}$$

As previously stated, the proposed equations in this chapter utilize a number of approximations to simplify the analysis. Therefore, the outcomes from the equations are still inaccurate if N_r is too small compared to the size of N_t. Fig. 4.8 shows the $P_{\text{out}}(\gamma_{\text{th}})$ from the derived equation in (4.31), the asymptotic outage probabilities from (4.33) and the empirical results. The number of transmit antennas was $\{6, 9, 12\}$ and N_r varied from 20 to 200 in steps of 20. The Gray-coded 16-QAM was chosen to the system. E_b/N_0 and γ_{th} were -5 and 3 dB, respectively. According to the findings, the deviations between the analytical and the empirical results were marginal if $N_r >> N_t$. The exact $P_{\text{out}}(\gamma_{\text{th}})$ for a 6×200 system was 7.78×10^{-6}. The difference between the result and the derived outage probabilities was only 7.79×10^{-7}, whereas the deviation for the approximation was slightly larger at 2.17×10^{-6}. However, the accuracy of the analysis for the system, using a lower N_r significantly decreased since the approximation of the value of $D_{m,m}$ utilizing the constant Ω was imprecise.

Fig. 4.9 compares the analysis for the $P_{\text{out}}(\gamma_{\text{th}})$ from (4.31) and the approximation

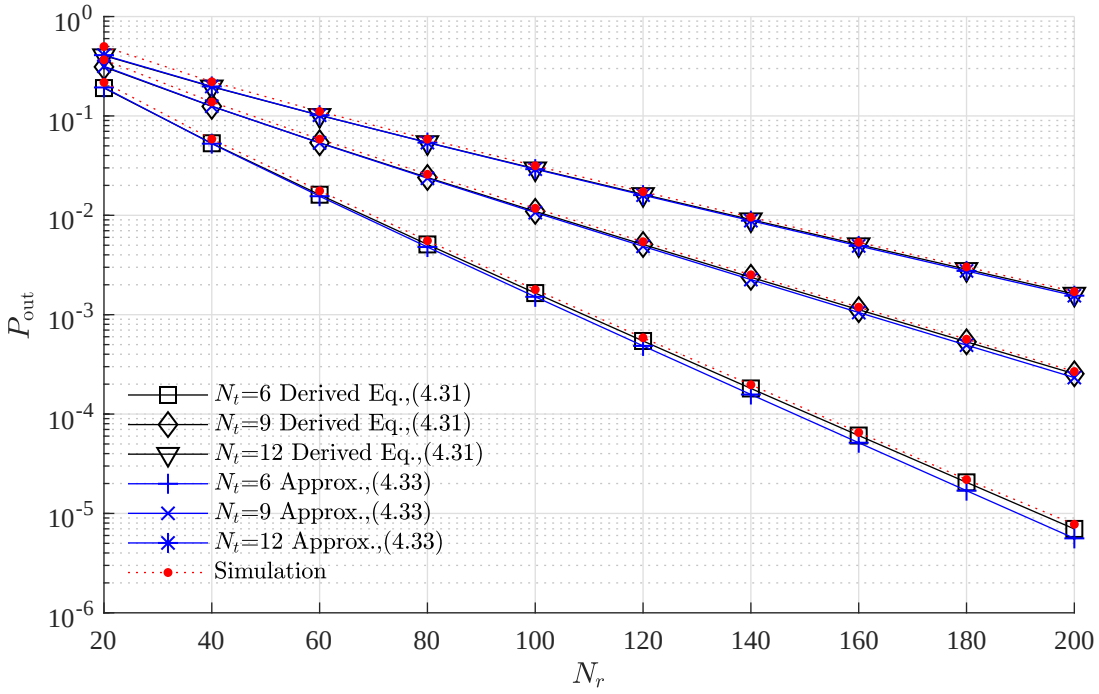

Figure 4.8: Outage probabilities of OFDM-MMIMO system.

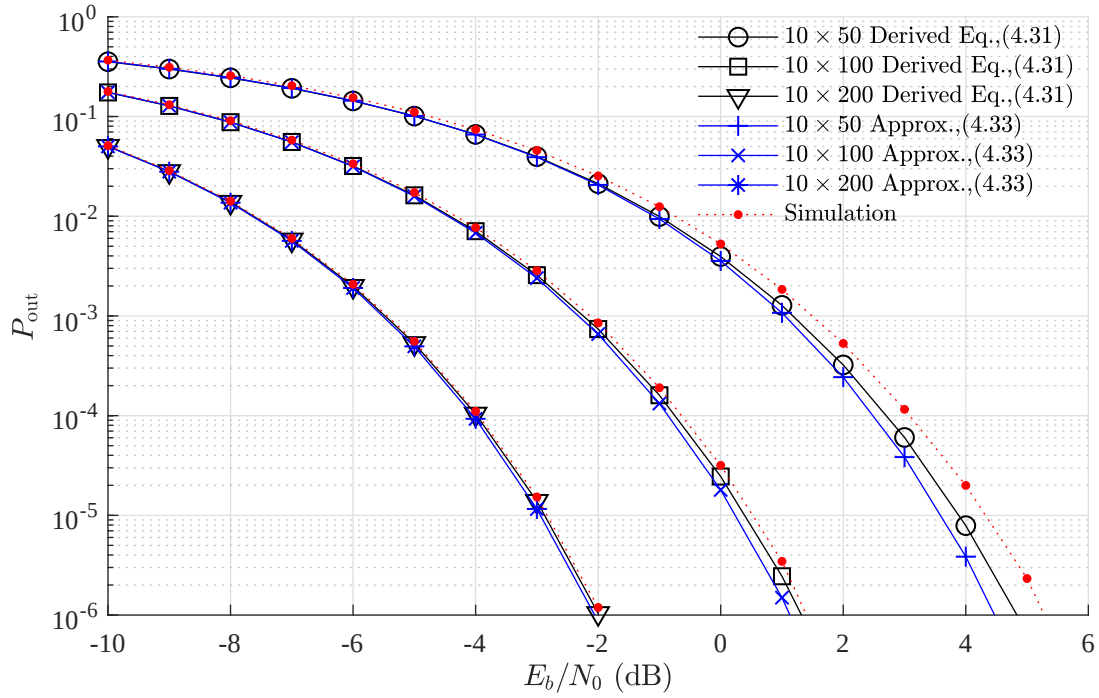

Figure 4.9: Outage probabilities of OFDM-MMIMO system.

in (4.33) to that of the empirical. The mapper employed 16-QAM with Gray encoding to generate the transmit symbols. 10×50, 10×100, and 10×200 systems were chosen to the simulation. The number of sub-carrier and γ_{th} were 512 and 3 dB, respectively. According to the results, the deviations between the analysis and the exact $P_{\text{out}}(\gamma_{\text{th}})$ were small, especially for the system with a larger N_r. Focusing the 10×200 system, the analysis from the derived equation and the approximation at $E_b/N_0 = -1$ dB were 5.31×10^{-4} and 4.93×10^{-4}, exhibiting a difference of 2.53×10^{-5} and 6.06×10^{-5} from the

exact result, respectively. However, the analysis for the system using a lower N_r became smaller, and the difference between the outcome from the derived equation for the 10×50 system at $E_b/N_0 = 0$ dB increased to 1.33×10^{-3}.

4.8 Summary

The performance of ZF detection in the OFDM-MMIMO system was discussed in this chapter. The analysis utilize a simplified mathematical expression of $Z_m^{(f)}$ to derive the PDF of $\Re(Z_m^{(f)})$, BEP, PDF of SNR, and the outage probabilities. Moreover, the analysis confirmed that the $p_z(\Re(Z_m^{(f)}))$ approaches the Gaussian distribution if $N_r >> N_t$, and the approximation can be utilized for simplifying the analysis. Monte-Carlo simulation results confirmed that the outcome from the proposed equations significantly matched the exact results, and the deviation between the analysis from the asymptotic and the exact equation was marginal. Therefore, the proposed equations can be efficiently used to evaluate performance of OFDM-MMIMO system.

Furthermore, the 2-nd order NSE is chosen by this work to approximate the inverse matrix operation, which was found to be precise if $N_r >> N_t$ is assumed. According to the numerical simulations, the derived equations generate accurate analytical results if $N_r > 10N_t$ and $N_r \geq 100$. Thus, a more accurate approximation is still required to enhance the performance analysis. Furthermore, in this chapter, the CFR is assumed to follow a Gaussian distribution and the OFDM-MMIMO channel model is then expressed as a linear matrix equation. However, there are still deviations between the exact PDF of the CFR and the classical distribution. Therefore, more accurate channel model for the system using OFDM waveform should be included in the analysis for improving the performance analysis.

Chapter 5

Soft-output linear symbol detections utilizing derived PDF

The derived PDF of the CCI and EN, $\Re(Z_m^{(f)})$, for MRC and ZF detections from chapter 3 and 4 are now employed in this chapter to enhance the performance of the coded-OFDM-MMIMO system. If the non-line-of-sight propagation between transmitter and receiver is neglected, the $p_z(Z_m^{(f)})$ is generally assumed to be the Gaussian distribution[39] and the LLR is then estimated from the received symbol $\hat{X}_m^{(f)}$ using the approximate symbol-by-symbol MAP algorithm in (2.55). However, the analysis in chapter 3 confirmed that the exact PDF of the CCI and the EN for MRC detection is different from the Gaussian distribution, especially in a higher E_b/N_0 region. Therefore, the derived PDFs are now utilized to estimate more accurate LLR for the soft-output MRC detector. Due to the derived PDFs require several arithmetic operators to calculate the outcomes, the equations are unable to be applied for the MRC detector directly. Thus, polynomial is chosen to approximate the LLR calculation, where the coefficients in the polynomial are generated from a sample of exact LLRs by utilizing the Newton's method[40][24].

In addition, the approximate PDF of EN in chapter 4 is chosen to reduce the computational complexity of soft-output ZF detection. In general, the PDF of the EN in the detection is assumed to be the $\mathcal{CN}(0, 2\sigma_z^2)$, and the asymptotic symbol-by-symbol MAP algorithm in (2.55) is then chosen to estimate the LLR, corresponding to the received symbol. However, as far as the literature survey goes, there is no research work derives a closed-form expression for the PDF and the noise variance for the EN of the detection. As a result, the detection requires additional operators in (D.4) to calculate the noise variance for every estimated symbol. It is worth noting that the 1-st order NSE can be chosen to reduce the computational complexity for the calculation and the methodology was briefly explained in appendix C. Although the NSE noise variance in (C.1) requires much less arithmetic operators than the conventional equation in 4, the computational complexity for the operation still dramatically increases according to the N_t and N_r. Moreover, there are still small deviations between the outcomes from the asymptotic nose variance and the exact result. Therefore, the derived noise variance in (4.20) is now utilized to generate the

LLR instead of the classical equation, making a reduction in computational complexity to the detector.

The improved soft-output MRC and ZF detections are explained in section 5.1 and 5.2, respectively. The simulation results and the complexity analysis are additionally discussed in the sections. It is worth pointing out that the improved soft-output MRC and ZF detections were proposed in [66] and [65].

5.1 Enhanced soft-output MRC detection

This section introduces the technique to enhance the BER performance of soft-output MRC detection in the OFDM-MMIMO system, using the derived PDF of the CCI and EN. In general, the soft-output MRC detector estimates the LLRs from in-phase and quadrature components of $\hat{X}_m^{(f)}$ by utilizing symbol-by-symbol MAP algorithm in (2.53). The PDFs of $\Re(Z_m^{(f)})$ and $\Im(Z_m^{(f)})$ are assumed to be the $\mathcal{N}(0, \sigma_{z,m}^2)$, and the instantaneous noise variance per dimension for each transmit antenna $\sigma_{z,m}^2$ is estimated from CFR in (D.3). However, the numerical results in chapter 2 revealed deviations between the exact PDF of $\Re(Z_m^{(f)})$ and the Gaussian distribution, especially in a higher E_b/N_0 region. Thus, the derived $p_z(\Re(Z_m^{(f)}))$ from (3.55) is now chosen instead of the $\mathcal{N}(0, \sigma_{z,m}^2)$ to generate the LLR in (2.53). As a result, the LLR for the m-th transmit symbol, the f-th sub-carrier, and the q-th tuple becomes

$$\Lambda_{m,q}^{(f)} = \ln\left(\frac{\sum\limits_{\bar{X}_k, d_{m,q}=1} p_z(\Re(\hat{X}_m^{(f)}) - \bar{X}_k)}{\sum\limits_{\bar{X}_k, d_{m,q}^{(f)}=0} p_z(\Re(\hat{X}_m^{(f)}) - \bar{X}_k)}\right). \tag{5.1}$$

5.1.1 LLR Approximation utilizing Newton interpolation

Theoretically, the LLR from (5.1) is more accurate than that of the general detection in (2.53) due to the outcome from the derived $p_z(\Re(Z_m^{(f)}))$ is closer to the exact result than that of the Gaussian distribution. However, the arithmetic operators of the $p_z(\Re(Z_m^{(f)}))$ from (3.55) complicate the computation in (5.1). Thus, the MAP algorithm in (5.1) is still impractical for generating LLR for the receiver directly. Therefore, a function in forms of N_p-th order polynomial $f_{\text{Poly}}(\Re(\hat{X}_m^{(f)}))$ is chosen to approximate outcomes of the MAP algorithm in (5.1). The methodology of Newton interpolation is chosen to this research work for computing coefficients for $f_{\text{Poly}}(\Re(\hat{X}_m^{(f)}))$, and the methodology was briefly summarized in appendix B. An N_p-th order polynomial in (B.5) is chosen to approximate outcome of mathematical functions, and the algorithm requires $N_p + 1$ samples of input and output from the exact equation in (5.1), i.e., $\{\Re(\hat{X}_m^{(f)}), \Lambda_{m,q}^{(f)}\}$, to compute the coefficients for the polynomial[67].

Focusing on a system, utilizing BPSK or QPSK modulation, the number of constellation points per dimension is 2 and the decision boundary between the points is at

$\Re(\hat{X}_m^{(f)}) = 0$ and $\Im(\hat{X}_m^{(f)}) = 0$. The range of exact $\Lambda_{m,q}^{(f)}$ is from $-\infty$ to ∞, and the value of the variable gradually changes according to the in-phase and quadrature element of $\hat{X}_m^{(f)}$. As a result, the detector directly utilizes the polynomial in (B.5) to estimate the LLR, corresponding to $\Re(\hat{X}_m^{(f)})$ as

$$\Lambda_{m,q}^{(f)} = f_{\text{Poly}}(\Re(\hat{X}_m^{(f)})). \tag{5.2}$$

It is worth noting that the polynomial produces an incorrect LLR if the value of $\Re(\hat{X}_m^{(f)})$ is larger or smaller than than the largest and the smallest sample in $\bar{X}_m$. According to the experiment, the probability of the occurrence of $|\Re(\hat{X}_m^{(f)})|$, which is larger than $4\sigma_z$, is marginal, where the value of σ_z^2 is evaluated from the average $\sigma_{z,m}^2$ in (D.3). Therefore, the value of $\Lambda_{m,q}^{(f)}$ from (5.2) is additionally forced to be a constant if $|\Re(\hat{X}_m^{(f)})| > 4\sigma_z$.

Likewise, if 16-QAM constellation points in Fig. 2.2 is chosen to the mapper, $M_\lambda = 4$, and the MAP algorithm in (2.53) employs a decision boundary at $\Re(\hat{X}_m^{(f)}) = 0$ to estimate $\Lambda_{m,1}^{(f)}$ and $\Lambda_{m,3}^{(f)}$ from $\Re(\hat{X}_m^{(f)})$. Thus, the detector requires odd functions to approximate the LLR. On the other hand, $\Lambda_{m,2}^{(f)}$ and $\Lambda_{m,4}^{(f)}$ are calculated from even functions since the MAP algorithm utilizes the decision boundary at $\Re(\hat{X}_m^{(f)}) = \{-2, 2\}$ to estimate the LLR. Therefore, $\Lambda_{m,q}^{(f)}$ for 16-QAM is calculated from the polynomial as

$$\Lambda_{m,1}^{(f)} = f_{\text{Poly}}(|\Im(\hat{X}_m^{(f)})|), \tag{5.3a}$$

$$\Lambda_{m,2}^{(f)} = \begin{cases} f_{\text{Poly}}(|\Im(\hat{X}_m^{(f)})|), & \Im(\hat{X}_m^{(f)}) > 0 \\ -f_{\text{Poly}}(|\Im(\hat{X}_m^{(f)})|), & \text{otherwise} \end{cases}, \tag{5.3b}$$

$$\Lambda_{m,3}^{(f)} = f_{\text{Poly}}(|\Re(\hat{X}_m^{(f)})|), \tag{5.3c}$$

$$\Lambda_{m,4}^{(f)} = \begin{cases} f_{\text{Poly}}(|\Re(\hat{X}_m^{(f)})|), & \Re(\hat{X}_m^{(f)}) > 0 \\ -f_{\text{Poly}}(|\Re(\hat{X}_m^{(f)})|), & \text{otherwise} \end{cases}. \tag{5.3d}$$

Since partial LLRs for 16-QAM in (5.3) exhibits the even function, the coefficients of the polynomial in the equation are generated from the sampled LLRs, where the range of $\bar{X}_m$ is from 0 to $4\sigma_z$. It is worth noting that the coefficients $a_{p,q}$ are still required for generating the outcome for the polynomial, $f_{\text{Poly}}(|\Re(\hat{X}_m^{(f)})|)$, in (5.2) and (5.3). According to the methodology in appendix B, the Newton interpolation requires N_p+1 data points of input $\bar{X}_m$ and output $\Lambda_{m,q}^{(f)}$ of the MAP algorithm in (5.1) to generate the coefficients $a_{p,q}$ for the N_p-th order polynomial $f_{\text{Poly}}(|\Re(\hat{X}_m^{(f)})|)$ in (5.2) and (5.3). Thus, the coefficients for the polynomial in (5.2) and (5.3) are calculated from $N_p + 1$ data points of the input and output of the MAP algorithm in (5.1), i.e., $\{\bar{X}_m, \bar{\Lambda}_{m,q}^{(f)}\}$. $\bar{X}_m$ and $\Lambda_{m,q}^{(f)}$ are uniformly sampled from the LLR, generated by (5.1).

Fig. 5.1 compares $\Lambda_{m,1}^{(f)}$ and $\Lambda_{m,2}^{(f)}$ from the enhanced detection for 16-QAM in (5.3) with that of the symbol-by-symbol MAP algorithm from (5.1). The improved derived PDF of $\Re(Z_m^{(f)})$ in (3.55) was chosen to generate the LLR for the enhanced detection and the MAP algorithm. The outcomes from the detectors are additionally compared to that of the the conventional detection in (2.55), where the $p_z(\Re(Z_m^{(f)}))$ was assumed to

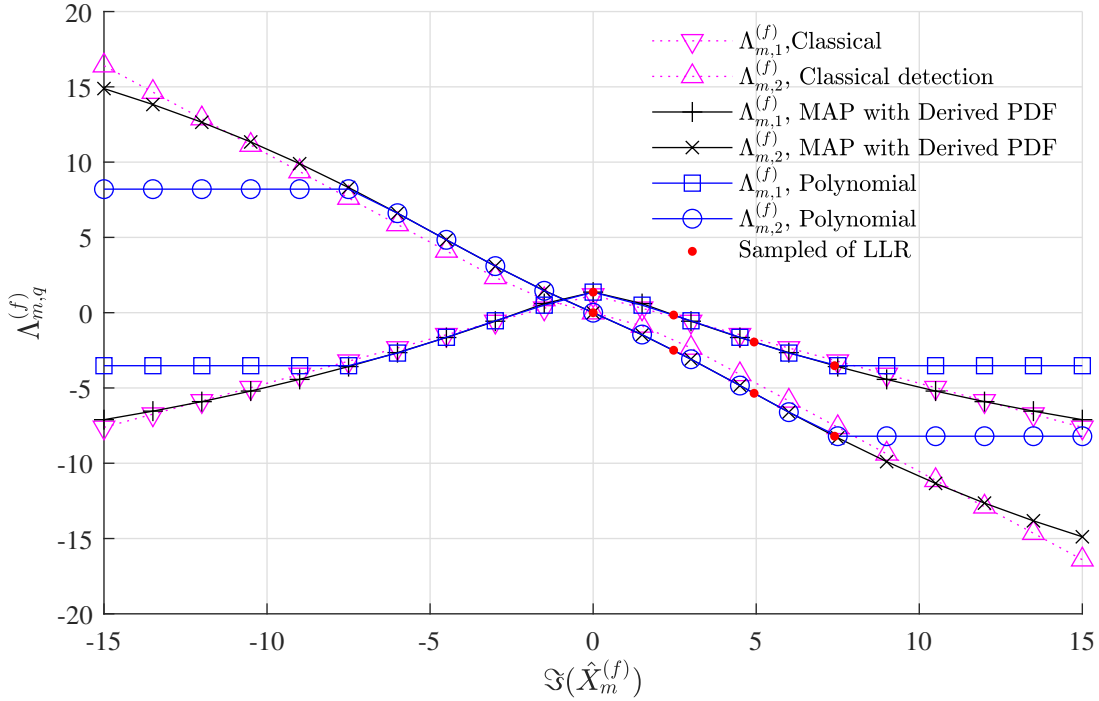

(a) $E_b/N_0 = -10$ dB

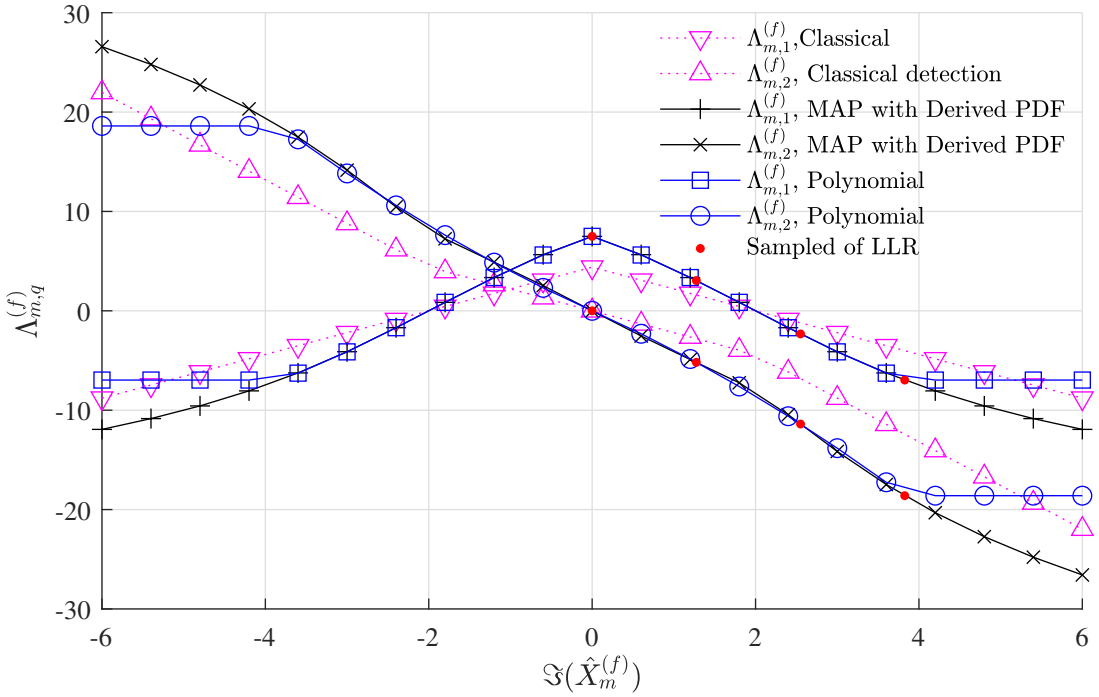

(b) $E_b/N_0 = 10$ dB

Figure 5.1: LLR for a 10×50 system utilizing 16-QAM.

be the $\mathcal{N}(0, \sigma^2_{z,m})$ and the noise variance was given by (D.3). The enhanced detection utilized the 3-rd order polynomial to calculate the LLR, where sample of 4 LLRs from the MAP algorithm in (5.1) was chosen for generating the coefficients in the polynomial. The sample of the LLRs is additionally included in the results. A 10×100 system was chosen to the simulation, where the system operated at $E_b/N_0 = \{-10, 10\}$ dB. Evidently, the outcomes from the enhanced detection significantly matched the exact LLR from the MAP algorithm. If $E_b/N_0 = -10$ dB, the $\Lambda^{(f)}_{m,1}$ from the polynomial at $\Im(\hat{X}^{(f)}_m) = 6$ was

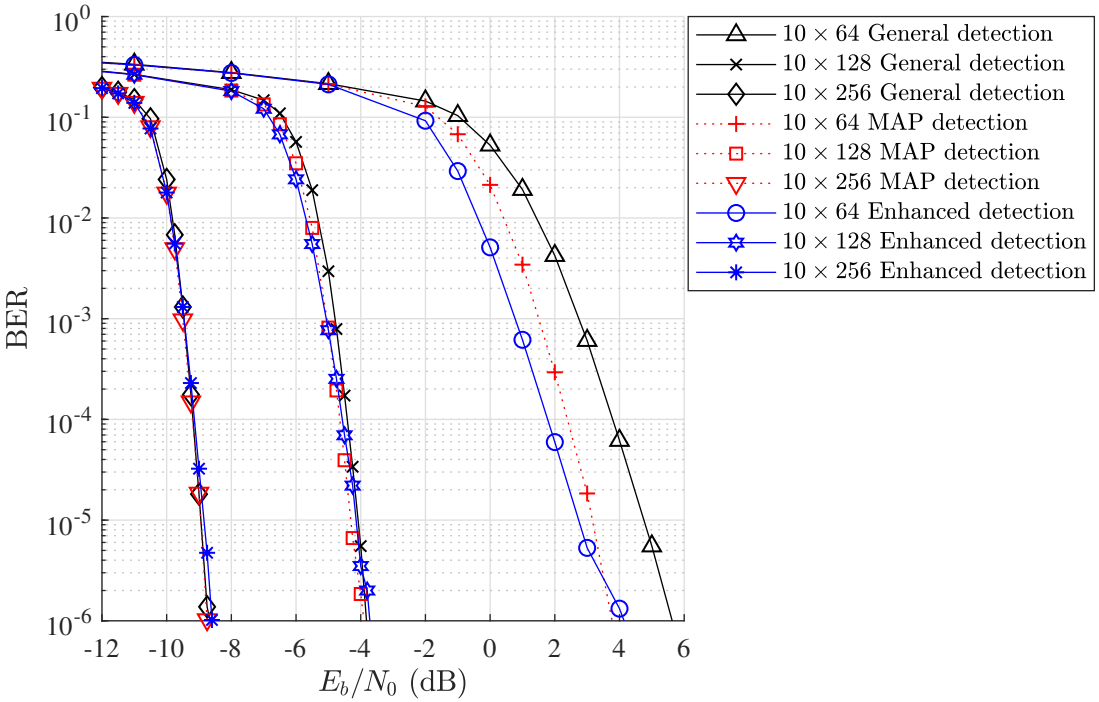

Figure 5.2: BER of enhanced soft-output MRC detection.

-2.65, and the number for MAP algorithm was -2.683. Thus, the LLR from the proposed detection was only 1.15% different from that of the MAP algorithm. It is worth noting that there were deviations between the LLR from the classical detection and that of the enhanced detection since both schemes utilizes a different equation to estimate the PDF of the CCI and EN, and the deviation became larger in a higher E_b/N_0 region. Focusing on the $\Lambda_{m,1}^{(f)}$ for $E_b/N_0 = -10$ dB, the deviation at $\Im(\hat{X}_m^{(f)}) = 6$ was 0.31, whereas the number for the system with $E_b/N_0 = 10$ dB at $\Im(\hat{X}_m^{(f)}) = 3$ increased to 1.93.

5.1.2 BER performance

BER performance of the coded-OFDM-MMIMO system, utilizing the enhanced soft-output MRC detection for 16-QAM in (5.3) was evaluated through Monte-Carlo simulation. The channel model in (2.3) was chosen to the simulation. τ, the number of tap coefficients, and the maximum delay spread for the channel model were 1.2, 8, and 50, respectively. The effects of channel estimation errors were neglected by the simulation. the number of CP symbols was 55. A 5G new radio LDPC for uplink data communication was chosen to the simulation[68]. The base matrix and the revision number were 1 and 0, respectively. The coding rate, block size utilization, and the number of iterations were 0.5, 1024 bits, and 25, respectively. The enhanced detector utilized the 3-rd order polynomial in (5.3) to estimate the LLR. The number of loop for the simulation was 5×10^4. As a result, the number of samples of information bits for computing BER was 5.12×10^7 bits, which is large enough to generate empirical results if the BER is greater than 10^{-6}.

Fig. 5.2 compares the BER of LDPC-OFDM-MMIMO system, utilizing the enhanced detection for 16-QAM in (5.3) with that of the classical detection in (2.55). The BER

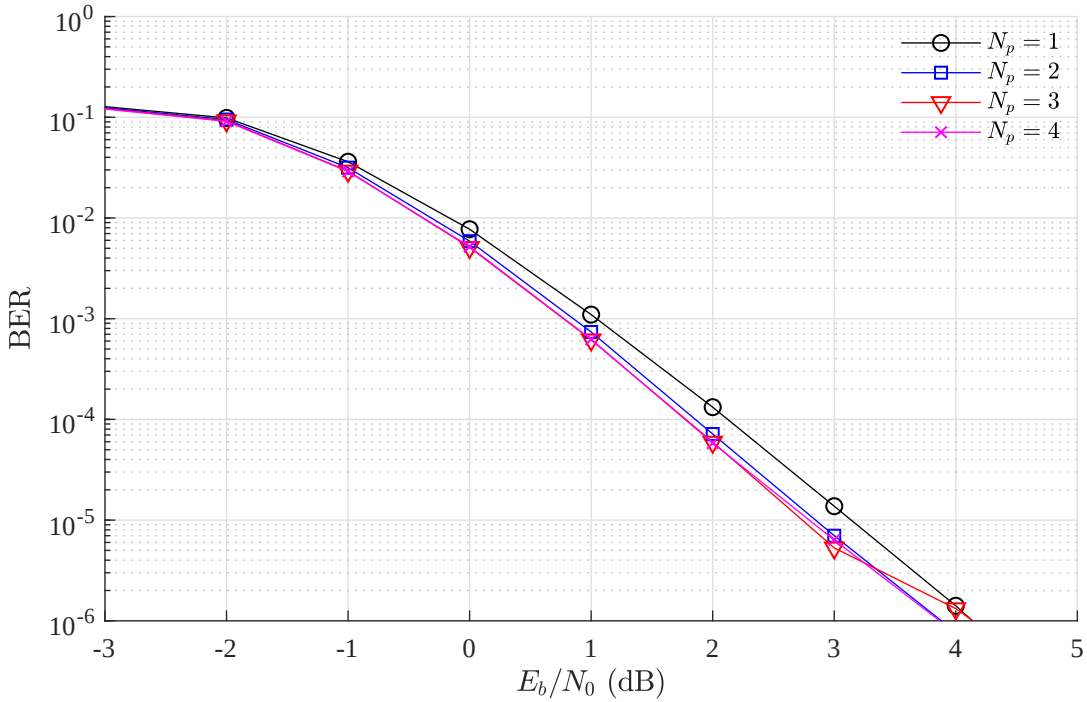

Figure 5.3: Effects of N_p in BER performance.

for the system with the MAP detection in (2.53), utilizing the Gaussian approximation of the EN PDF, is additionally included in the results. N_t was 10 and $N_r = \{64, 128, 256\}$. According to the results, the proposed detection outperforms its BER compared to the conventional detections, especially on a higher E_b/N_0 region. Focusing on a 10×64 system, the system with the enhanced detection required $E_b/N_0 = 1.78$ dB to maintain the BER of 10^{-4}, whereas the number for the general MAP and the approximate MAP detections were 2.39 dB and 3.79 dB, respectively. However, the deviations in BER between the detections became smaller in a lower E_b/N_0 region since the effects of the EN dominate the PDF of $\Re(Z_m^{(f)})$, making the PDF approaches the Gaussian distribution for this case. The BER for a 10×128 system, employing the enhanced detection, at $E_b/N_0 = -9.5$ dB was 7.75×10^{-4}, and the number was only 4.24×10^{-5} lower than the number for the MAP detection. However, the BER of the enhanced detection in a lower E_b/N_0 region was still higher than that of the MAP detection since the polynomial was chosen to approximate the LLR from MAP algorithm. For a 10×256 system, the E_b/N_0 at the BER of 10^{-5} for the enhanced detection was -8.85 dB, exhibiting 9.94×10^{-2} dB higher than that of the MAP detection.

In addition, the effects of N_p in BER of the enhanced detection for 16-QAM in (5.3) are shown in Fig. 5.3. The value of N_p for the detection was varied from 1 to 4. Evidently, the system with a higher N_p required a lower E_b/N_0 to maintain the BER. If $N_p = 1$, the BER at $E_b/N_0 = 2$ dB was 1.32×10^{-4}, and the number was 6.07×10^{-5} higher than that of system with $N_p = 2$. However, the differences in BER for the system with a higher N_p became smaller, and the differences in BER between the system with $N_p = \{3, 4\}$ was only 1.33×10^{-6}.

Table 5.1: Computational complexity of soft-output detections for 16-QAM.

Real arithmetic operators	**General detection**	**Enhanced detection**
Addition and Subtraction	$(4N_rN_t^2 + 18N_t)N_f$	$8N_tN_pN_f$
Multiplication	$(2N_t^2(2N_r + 1) + 10N_t)N_f$	$4N_tN_f(2N_p - 1)$
Division	$5N_tN_f$	0
Comparison	$8N_tN_f$	$2N_tN_f$

5.1.3 Complexity analysis

Table 5.1 compares the computational complexity the enhanced soft-output detections for 16-QAM in (5.3) with that of the asymptotic MAP detection from (2.55), utilizing the noise variance in (D.3). The equations in the table represents the number of real arithmetic operators, required for computing the LLRs of $\Re(\hat{X}_m^{(f)})$ from all N_f sub-carriers. The analysis assumed that X comparators are required to determine the minimum value of $X + 1$ random variables, and a summation of X random variables employed $X - 1$ additions. The computation of the coefficients of the polynomial in (**??**) and (B.7a) was neglected in the analysis since the coefficients can be pre-determined and stored into the memory at the receiver. According to the analysis, the computational complexity for the classical soft-output detection was $O(N_r)$, whereas the result for the enhanced detection was $O(N_p)$. Since $N_r >> N_p$, the equations confirm that the enhanced detection required less arithmetic operators than that of the conventional detection.

In addition, Fig. 5.4 compares the number of additions, subtractions, multiplications, and comparisons for generating the LLRs of the enhanced and conventional detections. The analytical results are calculated from the equations on Table 5.1. 16-QAM was chosen to the analysis. N_f and N_t were 512 and 10, respectively. N_r was varied from 20 to 200. Evidently, the computational complexity for the classical detection dramatically increased according to N_r. On the contrary, the number for the enhanced detection depended on N_p, and the number exhibited a constant. If $N_r = 200$, the number of multiplications in the general detection was 4.11×10^8. The number for the enhanced detection was only 1.02×10^5. Thus, the enhanced detection required 99.97% less multiplications than that of the conventional detection.

5.2 Low-complexity soft-output ZF detection

This section discusses a technique for minimizing the computational complexity of the soft-output ZF detector in the OFDM-MMIMO system by employing the derived PDF of the EN for ZF detection. Generally, the conventional soft-output ZF detection utilizes

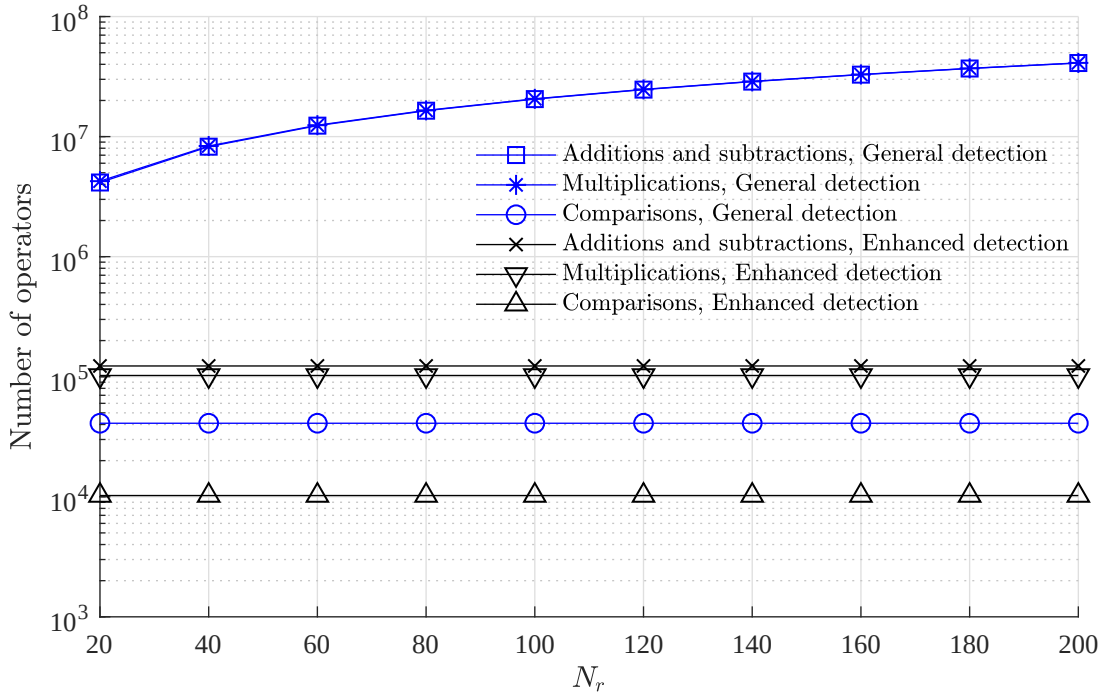

Figure 5.4: Number of real arithmetic operators.

the asymptotic symbol-by-symbol MAP algorithm in (2.55) to estimate the LLR from X_m^{λ}. The noise variance $\sigma_{z,m}^2$ in (D.4) is required by the MAP algorithm to estimate the LLR for all $\Re(X_m^{(f)})$, and the computational complexity for the calculation significantly increases according to the size of antennas. Thus, the 1-order NSE is additionally chosen to simplify the operation in (C.1), and the approximation was summarized in appendix C. Although the requirement in arithmetic operators for the NSE approximation in (C.1) is less than that of the conventional equation in (D.4), the operation still requires a large number of the arithmetic operators for generating the outcome. Furthermore, there are still small deviations between the asymptotic and exact noise variance, making a reduction in BER performance. According to the methodology in chapter 4, the $p_z(\Re(Z_m^{(f)}))$ for the OFDM-MMIMO system approached the $\mathcal{N}(0, \sigma_z^2)$, where the noise variance σ_z^2 was given by (4.20). If the derived noise variance from (4.20) is chosen to the asymptotic symbol-by-symbol MAP algorithm in (2.55), the LLR estimation can be simplified as

$$\Lambda_{m,q}^{(f)} = \frac{\min\limits_{\bar{X}_k, d_{m,q}=0} (\Re(\hat{X}_m^{(f)}) - \bar{X}_k)^2 - \min\limits_{\bar{X}_k, d_{m,q}=1} (\Re(\hat{X}_m^{(f)}) - \bar{X}_k)^2}{2\sigma_z^2}. \tag{5.4}$$

Theoretically, the computational complexity for the detection can be significantly reduced by utilizing the derived noise variance since the derived PDF requires much less arithmetic operators than that of the general equation in (D.4) to generate the outcome.

Table 5.2: Comparison of real-arithmetic operations in soft-output ZF detection.

Real arithmetic operators	**ZF detection using NSE noise variance**	**ZF detection using derived noise variance**
Addition and subtraction	$N_t N_f(\log_2(M) + 2M_\lambda + 2N_r - 1)$	$N_t N_f(\log_2(M) + 2M_\lambda) + 2$
Multiplication	$N_t N_f(2M_\lambda + 2N_r + 3)$	$N_t N_f(2M_\lambda + 1) + 3$
Division	$N_t N_f(\log_2(M) + 1)$	$N_t N_f \log_2(M) + 3$
Comparison	$N_t N_f \log_2(M)(M_\lambda - 2)$	$N_t N_f \log_2(M)(M_\lambda - 2)$

5.2.1 BER comparison

The BER of the coded-OFDM-MMIMO system, utilizing the low-complexity ZF detection from (5.4) was evaluated through Monte-Carlo simulation, and the results are shown in Fig. 5.5. The detector utilized the derived σ_z^2 from (4.20), the classical noise variance in (D.4), and the NSE noise variance in (C.1) to estimate the LLR. The 3-rd order NSE was chosen to the ZF detector to simplify the inverse matrix operator in (2.28). The mapper utilized 16-QAM constellation points to generate the transmit symbol, and the block size utilization was 1024 bits. N_t was 10 and $N_r = \{50, 100, 200\}$. An uplink 5G NR LDPC was chosen to the simulation, where the coding rate, base matrix and revision number were 1/2, 1 and 0, respectively. The receiver utilized iterative decoders and the Belief propagation to estimate the transmitted information from the LLR, where number of iteration was 25. A pseudo-random interleaver was chosen for the simulation for converting burst errors to random error events. The parameters for the OFDM-MMIMO channel model were as described in section 5.1.2. Focusing on a system where $N_r >> N_t$, the deviations in BER between the detections were marginal, since the $p_z(\Re(Z_m^{(f)}))$ approached the Gaussian distribution for this case. For a 10×256 system, the BER for the system with general, NSE, and derived noise variances at $E_b/N_0 = -9$ dB were 8.74×10^{-4}, 9.97×10^{-4}, and 9.26×10^{-4} respectively. Therefore, BER for the derived noise variance was only 5.11×10^{-5} higher than that of the conventional noise variance, and 7.13×10^{-5} lower than the number for the NSE noise variance. However, the deviation in BER between the detections tended to increase for a system using a smaller N_r. The BER for a 10×50 system using the derived noise variance at $E_b/N_0 = -2$ dB was 1.02×10^{-3}, exhibiting 2.48×10^{-4} higher than that of the classical noise variance, and 1.47×10^{-3} smaller than that of the NSE noise variance.

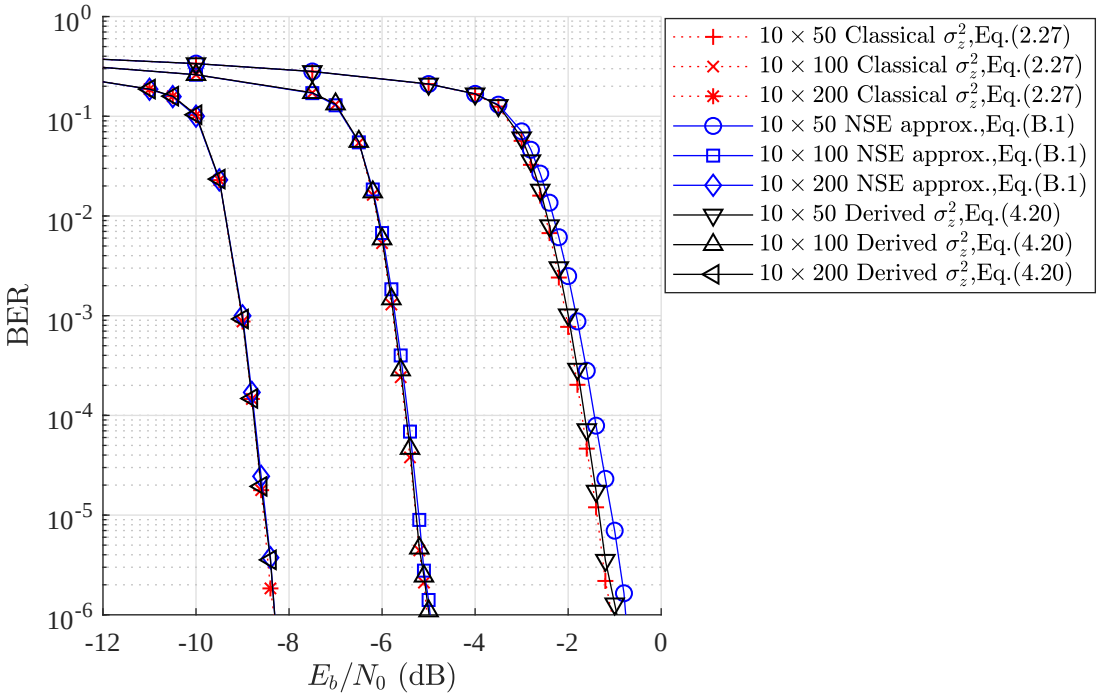

Figure 5.5: BER of low-complexity soft-output ZF detection.

5.2.2 Complexity analysis

Table 5.2 compares the number of real arithmetic operators for the soft-output ZF detection to calculate the LLR, corresponding to $\Re(\hat{X}_m^{(f)})$ from all N_f sub-carriers. The detectors utilized the asymptotic MAP algorithm in (2.55) to estimate the LLR, where the derived noise variance in (4.20) and the NSE noise variance in (C.1) were utilized by the operation. Due to The derived noise variance was a constant, the variable was estimated by the detector only one time for all sub-carriers. In addition, the number of arithmetic operations, required for producing $\mathbf{D}_f$ for the NSE noise variance was neglected by the analysis since the diagonal components of the Gram matrix were previously generated by detection for producing $\Re(\hat{X}_m^{(f)})$. According to the analytical results, the number of comparisons in both detections was identical. Likewise, the number of the divisions for both schemes was a function of M, thus, the deviation between the number was small. On the other hand, the number of the additions, subtractions, and multiplications for the NSE noise variance was $O(N_r)$, whereas the number for the derived noise variance was $O(M_\lambda)$. Since $N_r >> M_\lambda$, the proposed detection required less additions, subtractions, multiplications, and divisions than that of the general detection.

In addition to the complexity analysis, the number of real arithmetic operators, obtained by the equations in Table 5.2, is shown in Fig. 5.6. The number of additions, subtractions, multiplications, and divisions for the 16-QAM OFDM-MMIMO system, where the detector utilized the derived noise variance in (4.20) and the NSE noise variance in (C.1) to estimate the LLR. N_t and N_f were 10 and 512 symbols, respectively. The size of N_r was varied from 20 to 200. The numerical results confirm that the derived noise variance required less arithmetic operators than that of the conventional detection. If

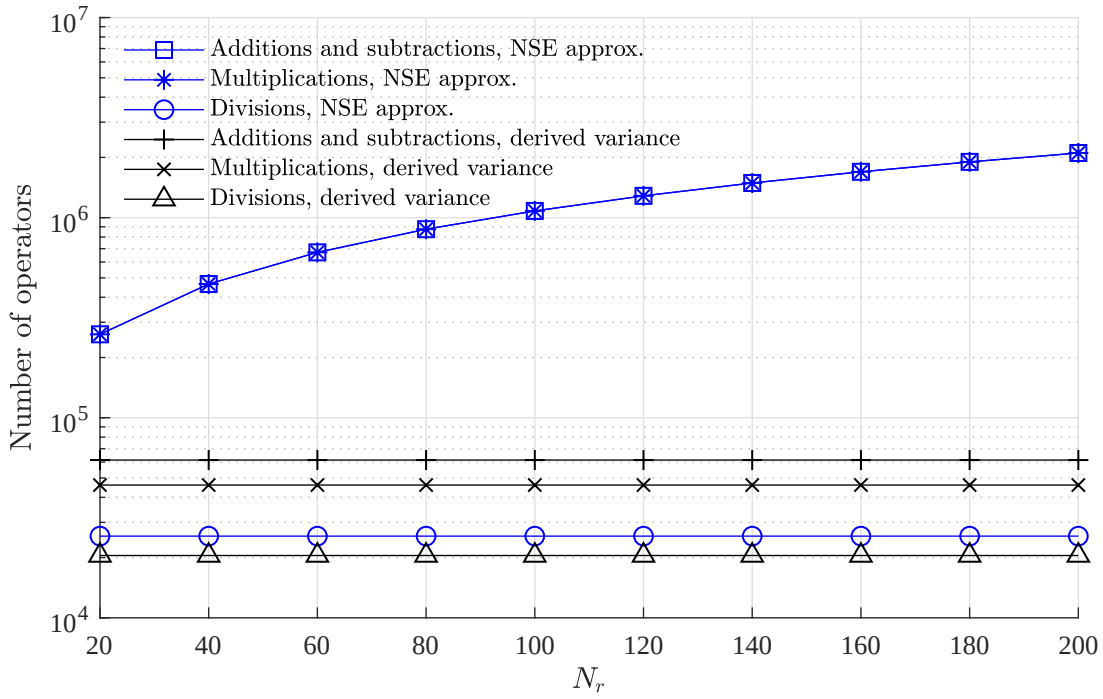

Figure 5.6: Computational complexity of soft-output ZF detection.

$N_r = 200$, the number of additions and subtractions for the NSE noise variance and the derived noise variance was 2.1×10^6 and 6.14×10^4, respectively. Therefore, 97.08% of additions and subtractions can be reduced by utilizing the derived noise variance. Furthermore, the number of multiplications in the system with the derived noise variance at $N_r = 200$ was only 4.61×10^4, exhibiting 97.81% smaller than that of the NSE noise variance.

5.3 Summary

The derived PDFs of the CCI and EN for MRC detection were chosen to enhance the BER performance of the soft-output MRC detection in section 5.1, and the numerical results confirmed that the BER performance of the system with the enhanced soft-output MRC detection was higher than that of the classical detection, especially at a higher E_b/N_0 region. In addition, a low-complexity soft-output ZF detection was introduced in section 5.2, where the detector utilized the derived noise variance to estimate the LLR, making a significantly reduction in computational complexity. According to the numerical results, the number of arithmetic operators in the proposed detection was significantly less than that of the conventional detection, whereas the deviations in BER performance between the detections were small. Furthermore, the BER for the system, utilizing the derived noise variance, was lower than that of the NSE noise variance due to the derived equation generates more accurate noise variance than that of the NSE approximation.

Although, the derived PDFs of $\Re(Z_m^{(f)})$ can be efficiently applied to enhance the performance of the OFDM-MMIMO system, approximations were employed to the analysis

in chapter 3 and 4, and the approximation is precise if $N_r >> N_t$. Therefore, the proposed soft-output detections in this chapter are still impractical for a system, employing a smaller N_r. In addition, the enhanced soft-output MRC detection utilized the polynomial to approximate the LLR from MAP algorithm, making a performance degradation in a lower E_b/N_0 region. Therefore, more accurate calculation is still required to enhance the BER performance.

Chapter 6

Conclusion and future works

The BEP, the PDF of SINR, and outage probability of the OFDM-MMIMO system, utilizing MRC and ZF detections were essentially derived in chapter 3 and 4. The analysis in the chapters utilized the mathematical expression of the CCI and EN to analyze the performance metrics. Furthermore, the analytical results proved that the PDF of the CCI and EN of MRC detection for M-QAM approached the summation of Gaussian distribution, i.e., GMM, if $N_r >> N_t$. On the other hand, the PDF of the EN for ZF detection tended to the zero-mean, Gaussian distribution. The noise variances for the distributions were firstly derived in this thesis. By utilizing the asymptotic PDF of $\Re(Z_m^{(f)})$, The analysis for the BEP, the PDF of SINR, and outage probability for MRC and ZF detections were then simplified in forms of the Q, exponential, and upper incomplete Gamma functions, respectively. Numerical results confirmed that the outcomes from the derived equations significantly matched the exact results. The derived equations provided an accurate analytical results if $Nr \geq 10Nt$ and $Nr > 100$. Moreover, the deviation between the outcomes from the exact and asymptotic equations were marginal. Thus, the derived equations in chapter 3 and 4 can be efficiently utilized to analyze the performance of the OFDM-MMIMO system.

Moreover, the derived PDFs for MRC and ZF detection were additionally chosen to enhance the performance of the coded-OFDM-MMIMO system in chapter 5. The enhanced soft-output MRC detection utilized the derived PDF of the CCI and EN with Newton's method to estimate the LLRs instead of the Gaussian distribution. According to the numerical results, the enhanced soft-output MRC detection outperformed its BER performance compared to the conventional detection, especially in a higher E_b/N_0 region since the outcomes from the derived PDF were more accurate than that of the Gaussian distribution. In addition, the analysis for ZF detection confirmed that the PDF of the EN for the detection approached the Gaussian distribution. Thus, the derived noise variance was employed to reduce the computational complexity in the soft-output ZF detection. The arithmetic operators for computing the derived noise variance was smaller than that of the conventional equation, and the parameters in the equation were constants. As a result, the computational complexity of the proposed soft-output ZF detector can be

significantly minimized by utilizing the derived noise variance.

6.1 Future works

It is worth pointing out that a number of approximations was chosen to simplify the analysis in this thesis, resulting in the limitation of the derived equations and the enhanced soft-output detection. The imperfection is now summarized in this section. Moreover, the author received constructive suggestions for the reviewer during the peer review process, and the recommendation is additionally included in this section.

6.1.1 Improving performance analysis

Due to several approximations were chosen to simplify the analysis in chapter 3 and 4, the outcomes from the derived equations MRC and ZF detections were slightly different from the exact results. The analysis assumed that the diagonal components of the Gram matrix approached a constant, and the off-diagonal components tended to the Gaussian distribution. Furthermore, the 2-nd order NSE was chosen to derive the performance metrics for ZF detection. Since the assumptions are still imprecise if N_r was too small, more accurate calculation is still required to enhance the accuracy for the analysis. However, the BEP analysis for the MIMO system, utilizing ZF detection and BPSK modulation, over uncorrelated frequency-flat Rayleigh fading channel at high SNR region was previously proposed in [16]. Although the BEP for M-QAM and other type of modulation schemes was neglected in the work, the readers can employ the PDF of the derive SNR to derive the BEP using the equations in [45]. Thus, the analysis in the work should be taken into account for the comparison.

6.1.2 Limitation on enhanced soft-output MRC detection

Although the enhanced soft-output MRC detection in chapter 5 outperformed its BER performance, compared to the conventional detection, the BER of the proposed detection was slightly higher than that of the general detection in a lower BER region. The proposed detector utilized the polynomial to estimate the LLRs, and there were still deviations between the outcomes from the approximation and the exact LLR from MAP algorithm. Thus, more accurate approximation could be utilized to enhance the BER performance of the OFDM-MMIMO system. Furthermore, the analysis in chapter 3 confirmed that the PDF of the CCI and EN of MRC detection approached the GMM. Therefore, machine learning and other computation techniques could be utilized to simplify the mathematical model of the CCI and EN and the detection.

6.1.3 Exact OFDM-MMIMO channel model

This thesis employed the linear matrix equation in (2.11) to simplify the analysis for the OFDM-MMIMO channel model and the CFR was assumed to be the Gaussian distribution. However, numerical results revealed small deviations between the exact PDF of the CFR and the Gaussian distribution. Therefore, more accurate mathematical expressions of the received symbol is still required to enhance the performance analysis. It is worth pointing out that the exact channel model for data communication links, utilizing OFDM waveforms, and the performance analysis were essentially proposed by a number of research work[69–72].

6.1.4 BEP analysis for coded-OFDM-MMIMO system

The BEP analysis in this thesis is derived for the uncoded-OFDM-MMIMO system. However, LDPC, polar codes, and other channel coding techniques are widely applied to the 5G and other communication standards for enhancing the reliability of data communication. Therefore, the BEP analysis for the coded-OFDM-MMIMO system would be more relevant in practice. Although the BEP analysis for the coded-OFDM-MMIMO system is complex, the BEP for convolution code can be derived by utilizing error weight list[23, 73, 74]. Furthermore, the BEP analysis for turbo codes can be approximated by utilizing conditional weight enumerating function[75].

6.1.5 Performance analysis for MMSE detection

According to the literature survey in chapter 1, MRC and MMSE detections are focused by a number of research works. MRC detection requires only a matrix multiplication to produce an estimated symbol, thus, becomes an attractive technique to detect transmitted information symbols in practical MMIMO systems. On the other hand, the MMSE detection outperforms its BER performance, compared to other linear symbol detections. Therefore, the performance analysis for the MMSE detection in the OFDM-MMIMO system would be of interest.

6.1.6 Novel waveforms for 5G and 6G

Although the OFDM waveform is suitable for the practical transceiver, and the technique has been widely chosen to the communication standards, the waveform is still receive the effects of inter-carrier interference (ICI), caused by Doppler and phase noise. As the results, orthogonal time frequency space modulation (OTFS), non-orthogonal multiple access (NOMA), and other number of new waveform has been currently focused for the next generation cellular network[76, 2]. Thus, the performance analysis for the waveforms in the MMIMO system would be required.

Appendix A

Mathematics tools

The analysis in chapter 3 and 4 involves with the probability theory and mathematics. A number of formulas was chosen to simplify the analysis in this thesis, and the methodology is now summarized in this appendix. Section A.1 discusses the techniques to transform the equation from linear to logarithm domain for reducing the range of outcome from function of random variables. Then, the methodology to derive PDF of output of function of random variables is then described in section A.2. Joint probability and characteristic function of random variables are included in the section. Furthermore, binomial and multinomial expansion are chosen by this research work to rewrite equations in chapter 3 and 4. The expansions are finally summarized in section A.3.

A.1 Calculation in logarithm domain

The derived equations in this thesis involves with several mathematics operators in linear domain. The range of the outcome of the equations dramatically increases according to the input variables, making complication to prepare the simulation software. Therefore, a number of derived equations in this thesis is transformed into the logarithm domain to minimize the range of the outcome. Focusing on an equation, where a variable y is calculated from x as

$$y = (x+1)^x. \tag{A.1}$$

According to the experimental, the value of y in (A.1) dramatically increases according to the value of x, and the number is too large for the numerical software if $x \geq 150$. By using logarithm to the both sides of (A.1), the equation becomes

$$\tilde{y} = \ln(y) = x\ln(x+1). \tag{A.2}$$

$\tilde{y}$ in (A.2) represents y in the logarithm domain, and the range of $\tilde{y}$ is much smaller that of y from (A.1). If $x = 100$, $\tilde{y} = 461.51$, whereas the number for y is 2.7×10^{200}. It is worth noting that derived equations in this thesis involve with factorial operator, $N! = \prod_{n=1}^{N} n$, where the outcome from the operator dramatically increases according to

the input, N. Therefore, the factorial operator is then rewritten in logarithm domain as

$$\tilde{y} = \ln(N!), \qquad N \leq 100, \tag{A.3a}$$

$$\tilde{y} = \sum_{n=1}^{N} \ln(n), \qquad N \leq 100. \tag{A.3b}$$

Although the range of $\tilde{y}$ in (A.3) is much smaller than that of $N!$, the equation is still unable to calculate the outcome if N is too large. Therefore, the Sterling's approximation is chosen by this thesis to approximate the outcome of $N!$ in the logarithm domain as

$$\tilde{y} \simeq N\ln(N) - N + \frac{1}{2}\ln(2\pi N), \qquad N > 100. \tag{A.4}$$

However, there is still deviations between the outcome from the approximation in (A.4) and the exact factorial operator, and the difference becomes larger if N is smaller. Therefore, the Sterling's approximation in (A.4) is chosen by this thesis to approximate the factorial operator if $N > 100$. In addition, $\tilde{y}$ in logarithm domain can be transformed to linear domain by utilizing an exponential function, i.e.,

$$y = \exp(\tilde{y}). \tag{A.5}$$

A.2 PDF transformation

Generally, random variables are chosen to demonstrate parameters in the OFDM-MMIMO system and the channel model, e.g., thermal noise, CIR, and CFR. Moreover, the operation of the OFDM-MMIMO system can be expressed as function of the variables. If the random variables are uncorrelated, probability theory can be efficiently applied to analyze the performance of the system. PDF transformation, joint probabilities and characteristic functions of random variables are chosen by this research work to derive the PDF of the output of the function of random variables. The methodology to derived the PDF is now summarized in this section.

A.2.1 PDF of function of a random variable

Let X be a random variable with a PDF $p_x(X)$, and $Y = g(X)$ is calculated from a function of X. If $X = h(Y) = g^{-1}(Y)$ represents the inverse function of $g(.)$ with N solutions $\{x_1, x_2, \ldots, x_N\}$, the PDF of Y can be derived from $p_x(X)$ as [48]

$$p_y(Y) = \sum_{k=1}^{N} \frac{p_x(X_k)}{|g'(X_k)|}, \tag{A.6}$$

where the derivative of $g(X_k)$ is denoted as $g'(X_k)$. Focusing on a linear equation, where the outcome, Y, is generated from a random variable, X, as

$$Y_{\text{linear}} = AX + B. \tag{A.7}$$

If A and B in (A.7) are constants, the PDF of Y in (A.9) is derived by utilizing (A.9) in (A.6), and results in[48]

$$p_y(Y_{\text{linear}}) = \frac{1}{|A|} p_x\left(\frac{Y-B}{A}\right). \tag{A.8}$$

The PDF transformation in (A.6) can be chosen to analyze the PDF of a ratio of a random variable X to a positive constant A, i.e.,

$$Y_{X/A} = \frac{X}{A}, \quad A > 0. \tag{A.9}$$

The PDF of Y in (A.9) is derived by substituting (A.9) in (A.6), and results in

$$p_y(Y_{X/A}) = A p_x(AX). \tag{A.10}$$

Likewise, if Y is the outcome from a function of X, which is given by

$$Y_{A/X^2} = \frac{A}{X^2}. \tag{A.11}$$

$X = h(Y) = \pm\sqrt{A/Y}$ and $g'(X_k) = -2A/X^3$. By utilizing $g'(X_k)$ in (A.6), $p_y(Y)$ becomes

$$p_y(Y_{A/X^2}) = \sqrt{\frac{A}{Y^3}} p_x\left(\sqrt{\frac{A}{Y}}\right). \tag{A.12}$$

A.2.2 PDF of function of two random variables

Let $Z = f(X, Y)$ be a function of two independent random variables X and Y, The CDF of Z can be derived from the joint probabilities of the random variables as [48, 49]

$$P(a < X < b, c < Y < d) = \int_c^d \int_a^b f(X, Y) dX dY, \tag{A.13}$$

where $\{a, b\}$, and $\{c, d\}$ are the integral bounds of X and Y, respectively. Focusing on a variable Z, which is calculated from a product of X and Y, .i.e.,

$$Z_{XY} = XY, \qquad -\infty < X < \infty, -\infty < Y < \infty. \tag{A.14}$$

If $f(X,Y)$ in (A.14) is substituted in (A.13), the CDF of Z becomes

$$P_z(Z) = \int_0^{\infty} \int_{-\infty}^{z/y} p_x(X)p_y(Y)dXdY + \int_{-\infty}^{0} \int_{z/y}^{\infty} p_x(X)p_y(Y)dXdY. \tag{A.15}$$

The $p_z(Z)$ is the derivative from the CDF in (A.15). By utilizing the Leibniz integral rule[49], the PDF becomes

$$p_z(Z_{XY}) = \int_{-\infty}^{\infty} \frac{1}{|y|} p_x\left(\frac{Z}{Y}\right) p_y(Y)dY. \tag{A.16}$$

In addition, If Z is a ratio of two random variables X and Y, i.e.,

$$Z_{X/Y} = \frac{X}{Y}, \qquad -\infty < X < \infty, Y \geq 0. \tag{A.17}$$

After substituting $f(X,Y)$ from (A.17) in (A.13), the CDF of Z is given by

$$P_z(Z_{X/Y}) = \int_0^{\infty} \int_{-\infty}^{zy} p_x(X)p_y(Y)dXdY. \tag{A.18}$$

The PDF of Z is then derived from the CDF in (A.18), and results in

$$p_z(Z_{X/Y}) = \int_0^{\infty} Y p_x(ZY)p_x(X)dY. \tag{A.19}$$

Furthermore, if Z is a summation of X and Y, i.e.,

$$Z_{X+Y} = X + Y, \qquad -\infty < X < \infty, -\infty < Y < \infty. \tag{A.20}$$

The PDF of Z in (A.20) is derived by utilizing the joint probabilities of X and Y in (A.13). As a result, the $p_z(Z)$ is calculated from the convolutional integral as

$$p_z(Z_{X+Y}) = \int_{-\infty}^{\infty} p_x(Z-Y)p_y(Y)dY, \tag{A.21a}$$

$$p_z(Z_{X+Y}) = p_x(X) * p_y(Y). \tag{A.21b}$$

A.2.3 Characteristic function of random variable

Characteristic function of random variable is additionally chosen by this research work to derive the PDF of outcome from function of random variables. Let X be a random variable, the characteristic function of X is derived from $p_x(X)$ as [48]

$$\Phi_x(\omega) = \int_{-\infty}^{\infty} \exp(j\omega x)p_x(X)dX. \tag{A.22}$$

On the contrary, the characteristic function can be transformed into the PDF by using

the following equation

$$p_x(X) = \frac{1}{2\pi}\int_{-\infty}^{\infty} \exp(-j\omega x)\Phi_x(\omega)dX. \tag{A.23}$$

For example, let $X = \mathcal{N}(0, \sigma_x^2)$ with the variance σ_x^2, the characteristic function of X is determined by substituting $p_x(X)$ in (A.23), i.e.,

$$\Phi_x(\omega) = \frac{1}{\sqrt{2\pi\sigma_x^2}}\int_{-\infty}^{\infty} \exp\left(j\omega x - \frac{X^2}{2\sigma_x^2}\right) dX. \tag{A.24}$$

After solving the integration in (A.24), the $\Phi_x(\omega)$ becomes

$$\Phi_x(\omega) = \exp\left(-\frac{\sigma_x^2\omega^2}{2}\right). \tag{A.25}$$

In addition, characteristic function can be utilized to derive the PDF of outcome of a variable, which is calculated by a combination of random variable. Focusing on a variable Y, which is calculated from the random variables $\{X_n\}_{n=1}^N$ as

$$Y = \sum_{n=1}^{N} X_n. \tag{A.26}$$

If $\Phi_{x_n}(\omega)$ represents the characteristic function of X_n, the $\Phi_y(\omega)$ is given by

$$\Phi_y(\omega) = \prod_{n=1}^{N} \Phi_{x_n}(\omega). \tag{A.27}$$

The $p_y(Y)$ can be then obtained by substituting $\Phi_y(\omega)$ from (A.27) in (A.23). It is worth noting that the analysis in (A.27) can be utilized to derive the PDF of combination of multiple Gaussian random variables. If $\{X_n\}_{n=1}^N$ in (A.26) denote the zero-mean, Gaussian random variables with variance $\sigma_{x_n}^2$, Y is a summation of the variables and the characteristic function of Y can be derived by substituting (A.25) in (A.27). As a result, the characteristic function becomes

$$\Phi_y(\omega) = \exp\left(-\frac{\omega^2}{2}\sum_{n=1}^{N}\sigma_{x_n}^2\right). \tag{A.28}$$

After substituting $\Phi_y(\omega)$ from (A.28) in (A.28), the PDF of Y is given by

$$p_y(Y) = \frac{1}{\sqrt{2\pi\sum_{n=1}^{N}\sigma_{x_n}^2}} \exp\left(-\frac{Y^2}{2\sum_{n=1}^{N}\sigma_{x_n}^2}\right). \tag{A.29}$$

The analysis in (A.29) confirms that the PDF of a combination of zero-mean, Gaussian random variables exhibits the Gaussian distribution.

A.3 Binomial and multinomial expansions

Research on performance analysis of digital communications involves with integration of complicated equations, and a number of theorem is required to simplify the analysis. Focusing on an equation, which is a power of a binomial, the binomial expansion can be employed to decompose the equation as[77]

$$(x+y)^N = \sum_{k=0}^{N} \binom{N}{k} x^{N-k} y^k = \sum_{k=0}^{N} \binom{N}{k} x^k y^{N-k}, \tag{A.30}$$

where the binomial coefficients $\binom{N}{k}$ are calculated from N and k as

$$\binom{N}{k} = \frac{N!}{k!(N-k)!}. \tag{A.31}$$

In addition, if 3 or more variables are chosen to the equation, the equation can be expanded by utilizing the multinomial expansion as[77]

$$(x_1 + x_2 + \cdots + x_m)^N = \sum_{k_1+k_2+\cdots+k_m=N}^{N} \binom{N}{k_1, k_2, \ldots, k_m} \prod_{v=1}^{m} x_v^{k_v}, \tag{A.32}$$

where

$$\binom{N}{k_1, k_2, \ldots, k_m} = \frac{N!}{\prod_{v=1}^{m} k_v!}. \tag{A.33}$$

$\{k_v\}_{v=1}^{N}$ in (A.33) is the integer, and the range of the variables is from 0 to N. The binomial and multinomial expansions in (A.30) and (A.32) were chosen by this research work to simplify the integration in chapter 3 and 4.

Appendix B

Newton interpolation

Interpolation is a technique to construct a curve from a set of data points from a mathematical function. The technique can be chosen to generate a smooth curve from Monte-Carlo simulation, where random variables scatter the data set[67]. This chapter discusses the Newton interpolation, which was utilized by this thesis to approximate outcomes of complex equations. Focusing on an example of function $f(\hat{x})$, where the outcome $\hat{y}$ is calculated from a function of $\hat{x}$, i.e.,

$$\hat{y} = f(\hat{x}). \tag{B.1}$$

Newton interpolation utilizes a polynomial to estimate the outcome from (B.1), and the technique requires N_p+1-points of data points of input and output in (B.1), $\{(x_k, y_k)\}_{k=1}^{N_p+1}$, to calculate coefficients for the N_p-th order polynomial. The methodology to generate coefficients for linear equation and N_p-th order polynomial is now described in the next sub-sections.

B.1 Linear interpolation

Linear equation can be chosen to approximate the outcome from $f(\hat{x})$ in (B.1), where $\hat{y}$ is generated from $\hat{x}$ as

$$\hat{y} = a_1 + a_2(\hat{x} - x_1). \tag{B.2}$$

a_1 and a_1 in (B.2) represent coefficients, and (B.2) requires two samples of $\hat{x}$ and $\hat{y}$ from (B.1) to calculate coefficients $\{a_k\}_{k=1}^{2}$. Let (x_1, y_1) and (x_2, y_2) denote samples of input and output of $f(\hat{x})$ in (B.1), coefficients in linear equation are determined as

$$a_1 = y_1, \tag{B.3a}$$

$$a_2 = \nabla y_1, \tag{B.3b}$$

where ∇y_k in (B.3a) represents the divided difference, which is defined as

$$\nabla y_k = \frac{y_{k+1} - y_i}{x_{k+1} - x_k}. \tag{B.4}$$

B.2 Non-linear interpolation

Although the outcomes from the linear equation in (B.2) approach the exact results, there are still deviations between the exact $\hat{y}$ from (B.1) and the approximation in (B.2), especially if $f(\hat{x})$ is a non-linear equation. Thus, N_p-th order non-linear equation is utilized to enhance the approximation, where $\hat{y}$ is estimated from $\hat{x}$ by using a polynomial, $f_{\text{Poly}}(\hat{x})$, as

$$\hat{y} = f_{\text{Poly}}(\hat{x}), \tag{B.5}$$

where the polynomial, $f_{\text{Poly}}(\hat{x})$, is given by

$$\begin{aligned} f_{\text{Poly}}(\hat{x}) =& a_1 + a_2(\hat{x} - x_1) + a_3(\hat{x} - x_1)(\hat{x} - x_2) + \dots \\ &+ a_{N_p-1}(\hat{x} - x_1)(\hat{x} - x_2)\dots(\hat{x} - x_{N_p}). \end{aligned} \tag{B.6}$$

Coefficients $\{a_k\}_{k=1}^{N_p-1}$ in (B.6) are calculated from $N_p + 1$ samples of $\hat{x}$ and $\hat{y}$ of $f(\hat{x})$ in (B.1) as

$$a_{1,q} = x_1, \tag{B.7a}$$
$$a_{2,q} = \nabla y_2, \tag{B.7b}$$
$$a_{3,q} = \nabla^2 y_3, \tag{B.7c}$$
$$a_{N_p,q} = \nabla^{N_p-1} y_{N_p}. \tag{B.7d}$$

$\nabla^n y_m$ in (B.7a) is computed from the data points as

$$\nabla y_m = \frac{y_m - y_1}{x_m - x_1}, \quad p = 2, 3, \dots, N_p, \tag{B.8a}$$
$$\nabla^2 y_m = \frac{y_m - y_2}{x_m - x_2}, \quad p = 3, 4, \dots, N_p, \tag{B.8b}$$
$$\nabla^3 y_m = \frac{y_m - y_3}{x_m - x_3}, \quad p = 4, 5, \dots, N_p, \tag{B.8c}$$
$$\nabla^{N_p} y_m = \frac{y_m - y_{N_p}}{x_m - x_{N_p}}. \tag{B.8d}$$

B.3 Numerical results

Fig. B.1 compare the approximations from linear equation in (B.2) and polynomial in (B.5) with that of the exact outcomes from the following equation

Table B.1: Linear and non-linear interpolation.

Sampled data of (x_k, y_k)	**k = 1**	**k = 2**	**k = 3**	**k = 4**
Linear eq. in (B.2)	$(0, 0)$	$(10, 0.90)$	-	-
The 2-nd order polynomial in (B.5)	$(0, 0)$	$(5, 1.42)$	$(10, 0.90)$	-
The 3-rd order polynomial in (B.5)	$(0, 0)$	$(3, 1.02)$	$(7, 1.48)$	$(10, 0.90)$

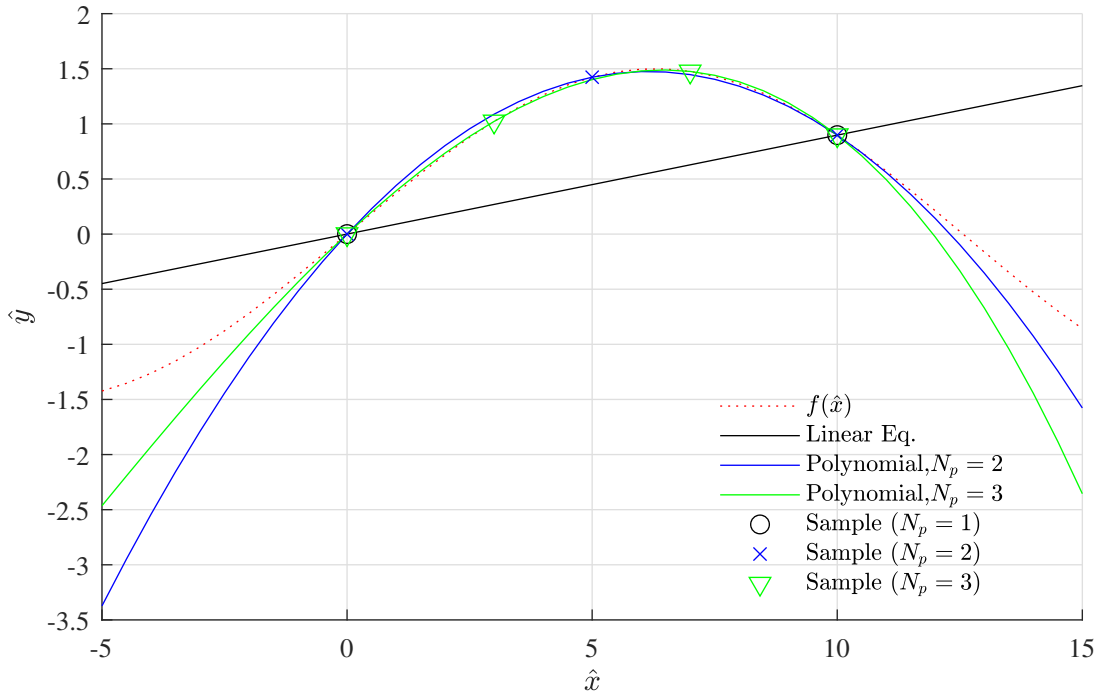

Figure B.1: Linear and non-linear interpolation.

$$\hat{y} = 1.5 \sin\left(\frac{\hat{x}}{4}\right). \tag{B.9}$$

Linear equation requires 2 data points for computing coefficients in (B.2), whereas the number of data points for the 2-nd and the 3-rd polynomial are 3 and 4, respectively. The data points are uniformly sampled from the exact $(\hat{x}, \hat{y})$ in (B.9), and the information is summarized in Table. (B.1). The numerical results in Fig. B.1 confirms that the outcomes from the approximations in (B.2) and (B.2) matched the exact results from (B.9). The asymptotic $\hat{y}$ from linear equation at $\hat{x} = 4$ was 0.36, and the number was 0.9 different from the exact result. Furthermore, a higher order polynomial produced more accurate $\hat{y}$, and the approximation for 3-rd polynomial at $\hat{x} = 4$ was only 1.54×10^{-2} different from the exact result.

Appendix C

Approximate noise variance for ZF detection using NSE

According to the methodology in chapter 2, the soft-output ZF detector utilizes the symbol-by-symbol MAP algorithm in (2.53) and the approximation in (2.55) to estimate the LLR, corresponding to $\hat{X}_m^{(f)}$. The noise variance $\sigma_{z,m}^2$ is required by the equations to calculate the outcome, and the ZF detector utilizes (D.4) to determine the variance from CFR. However, the equation requires $\mathbf{G}_f^{-1}$ to produce the outcome and the size of the Gram matrix is very large, and several arithmetic operators are required by the detector to generate the noise variance. Therefore, the authors in [52] utilized the 1-st order NSE to simplify the calculation for the noise variance. Although the methodology was proposed for the soft-output MMSE detection, the operation of ZF detection is slightly different from the MMSE detection, and the NSE can be applied for this case. If the 1-st order NSE from (2.38) is chosen to (D.4), the $\sigma_{z,m}^2$ is simplified as

$$\sigma_{z,m}^2 = \frac{\sigma_w^2}{(D_{m,m}^{(f)})^2} \sum_{n=1}^{N_r} |H_{m,n}^{(f),*}|^2. \tag{C.1}$$

It is worth noting that the NSE approximation in (C.1) requires less arithmetic operators than that of the general equation in (D.4), however, the size of N_r should larger than the number for N_t to minimize the difference between the exact and the approximate equations.

Appendix D

Derivation of instantaneous noise variance for linear symbol detections

Soft-output detection is generally chosen to estimate LLR for iterative decoder in coded-OFDM-MMIMO sytem. Focusing on soft-output linear symbol detection, the detector compares receive symbol with the Gaussian distribution for computing the LLR. Instantaneous noise variance is required for the LLR computation, and the value of the noise variance dramatically change according to the CFR for each sub-channel. Thus, the soft-output detector estimate the instantaneous noise variance from the CFR. In general, the outcome for the detection is generally modeled as[52]

$$\hat{X}_m^{(f)} = X_m^{(f)} + \frac{e_m^{(f)}}{\underbrace{\mu_m^{(f)}}_{Z_m^{(f)}}}, \tag{D.1}$$

where $\mu_m^{(f)}$ denotes the effective channel gain and $e_m^{(f)}$ represents post equalization CCI and EN. The value of $\mu_m^{(f)}$ corresponds to CFR for each sub-channel. If $e_m^{(f)}$ is assumed to be the Gaussian distribution, the second term in (D.1), $Z_m^{(f)}$, becomes the $\mathcal{CN}(0, 2\sigma_z^2)$. The instantaneous noise variance is estimated from CFR for each sub-channel, and the variance for soft-output MRC, ZF, and MMSE detections are now summarized in section D.1, D.2, and D.3, respectively.

D.1 MRC detection

The principle of MRC detection was previously explained in section 2.6.1, where the mathematical expression of the outcome for the detection, $\hat{X}_m^{(f)}$, was derived in (2.25). $\hat{X}_m^{(f)}$ receives the effects of CCI and EN, i.e. $Z_m^{(f)}$ in (2.25). If $X_m^{(f)}$ and $W_n^{(f)}$ are assumed to be the Gaussian distribution, the instantaneous noise variance per dimension $\sigma_{z,m}^2$ for the m-th transmit antenna is estimated from CFR as[52]

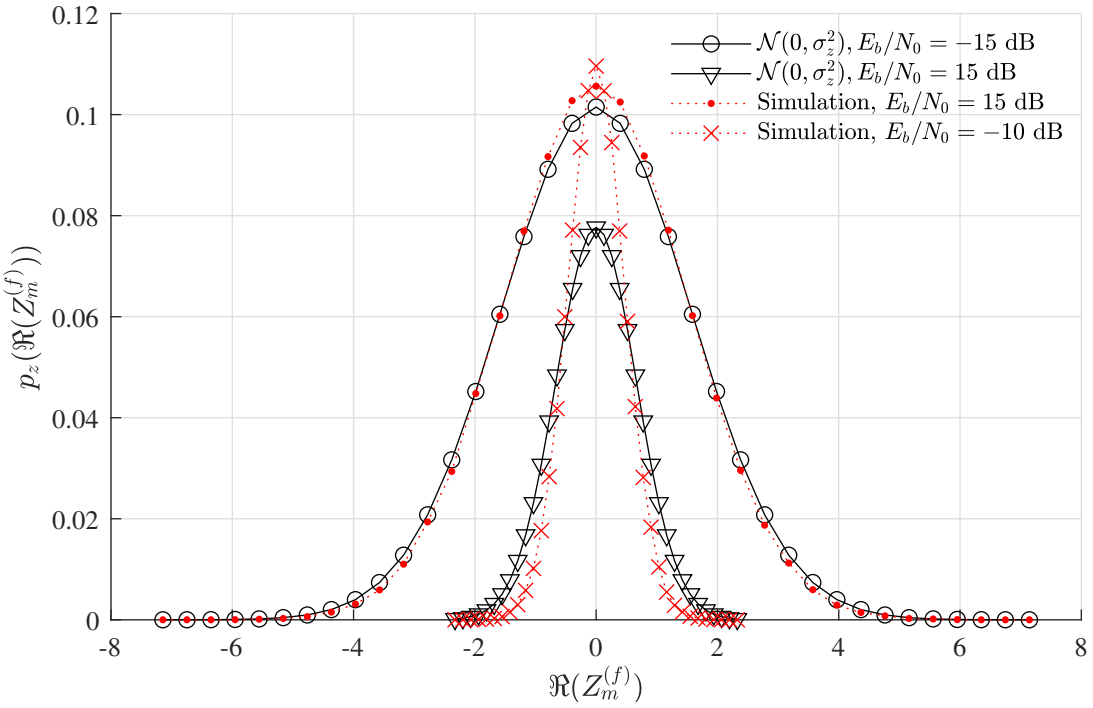

Figure D.1: PDF of the CCI and the EN of OFDM-MMIMO system, utilizing MRC detection.

$$\sigma_{z,m}^2 = \frac{\sum_{k=1,k\neq m}^{N_t} |E_{m,k}^{(f)}|^2 \mathbb{E}\left(|X_k^{(f)}|^2\right) + \sum_{n=1}^{N_r} |H_{n,m}^{(f),*}|^2 \mathbb{E}\left(|W_n^{(f)}|^2\right)}{2(D_{m,m}^{(f)})^2}. \tag{D.2}$$

By substituting $\mathbb{E}\left(|X_k^{(f)}|^2\right) = E_s$ and $\mathbb{E}\left(|W_n^{(f)}|^2\right) = 2\sigma_w^2$, the $\sigma_{z,m}^2$ becomes

$$\sigma_{z,m}^2 = \frac{E_s \sum_{k=1,k\neq m}^{N_t} |E_{m,k}^{(f)}|^2 + \sigma_w^2 \sum_{n=1}^{N_r} |H_{n,m}^{(f),*}|^2}{(D_{m,m}^{(f)})^2}. \tag{D.3}$$

Fig. D.1 compares the PDF of $\Re(Z_m^{(f)})$ in a 10×200 OFDM-MMIMO system from the simulation results with that of the $\mathcal{N}(0, \sigma_{z,m}^2)$ using the average $\sigma_{z,m}^2$ in (D.3). 16-QAM was chosen to the system and $E_b/N_0 = \{-15, 15\}$ dB. The simulation employed (2.11), (2.22), and (2.24), respectively, to generate $\hat{X}_m^{(f)}$ corresponding to $X_m^{(f)}$. $Z_m^{(f)}$ is then calculated from a subtraction of $\hat{X}_m^{(f)}$ and $X_m^{(f)}$. The $H_{n,m}^{(f)}$ in (2.11) was assumed to be a $\mathcal{CN}(0, 2\sigma_h^2)$. According to the results, the exact PDF of Z_m^I at a lower E_b/N_0 region tends to be the Gaussian distribution since the effects of the EN in (2.25) dominated the PDF. The exact $p_z(\Re(Z_m^{(f)}))$ for the system operating at $E_b/N_0 = -15$ dB at $\Re(Z_m^{(f)}) = 0$ was 0.11, which was only 4.13×10^{-3} higher than that of the $\mathcal{N}(0, \sigma_z^2)$. However, the deviation for the system operating at $E_b/N_0 = 15$ dB at $\Re(Z_m^{(f)}) = 0$ increased to 3.19×10^{-2}. Therefore, there is still a deviation between the Gaussian distribution and the exact PDF of $\Re(Z_m^{(f)})$, especially at a higher E_b/N_0 region.

D.2 ZF detection

According to the methodology in section 2.6.2. The outcome from ZF detection receive the effects of EN, and the EN was given by $Z_m^{(f)} = \sum_{n=1}^{N_r} U_{n,m}^{(f)} W_n^{(f)}$ in (2.30). Since $W_n = \mathcal{CN}(0, 2\sigma_h^2)$, $Z_m^{(f)}$ in (2.30) approaches the $\mathcal{CN}(0, 2\sigma_{z,m}^2)$, and the instantaneous noise variance per dimension for the m-th transmit antenna can be determined from the $U_{n,m}^{(f)}$ as

$$\sigma_{z,m}^2 = \frac{1}{2} \sum_{n=1}^{N_r} |U_{n,m}^{(f)}|^2 \, \mathbb{E}\left(|W_n^{(f)}|^2\right), \tag{D.4a}$$

$$\sigma_{z,m}^2 = \sigma_w^2 \sum_{n=1}^{N_r} |U_{n,m}^{(f)}|^2. \tag{D.4b}$$

D.3 MMSE detection

The derivation for the instantaneous noise variance for MMSE detection is now discussed in this section. In general, the CCI and the EN in MMSE detection are given by $Z_m^{(f)}$ in (2.37). If $X_k^{(f)}$ and $W_n^{(f)}$ in (2.37) are assumed to be the complex-valued, Gaussian distribution, the instantaneous noise variance per dimension of $Z_m^{(f)}$ is expressed as [78]

$$\sigma_{z,m}^2 = \frac{\sum_{n=1, n\neq m}^{N_t} |\acute{K}_{m,n}^{(f)}|^2 \, \mathbb{E}\left(|X_k^{(f)}|^2\right) + \sum_{n=1}^{N_r} \breve{K}_{m,n}^{(f)} \, \mathbb{E}\left(|W_n^{(f)}|^2\right)}{2|\acute{K}_{m,m}^{(f)}|^2}, \tag{D.5a}$$

$$\sigma_{z,m}^2 = \frac{E_s \sum_{k=1, j\neq N_t}^{N_t} |\acute{K}_{m,k}^{(f)}|^2}{2(\acute{K}_{m,m}^{(f)})^2} + \frac{\sigma_w^2 \sum_{n=1}^{N_r} |\breve{K}_{m,n}^{(f)}|^2}{(\acute{K}_{m,m}^{(f)})^2}. \tag{D.5b}$$

Fig. D.2(a) and (b) show the $p_z(\Re(Z_m^{(f)}))$ of the OFDM-MMIMO system, using ZF and MMSE detection from the simulation results. The empirical results are additionally compared to that of the $\mathcal{N}(0, \sigma_z^2)$, where the noise variance per dimension of $\Re(Z_m^{(f)})$ for the detections is employed by averaging $\sigma_{z,m}^2$ from (D.4) and (D.5), respectively. $N_t = 10$ and $N_r = \{50, 100, 200\}$. 16-QAM was chosen to the system and the number of subcarrier was 512 symbols. The system operated at $E_b/N_0 = -10$ dB. Evidently, the exact PDFs of $\Re(Z_m^{(f)})$ matched the Gaussian distribution. According to the 2-sample Kolmogorov–Smirnov test at a significance level of 5%, there is no major difference between the exact PDF and the Gaussian distribution.

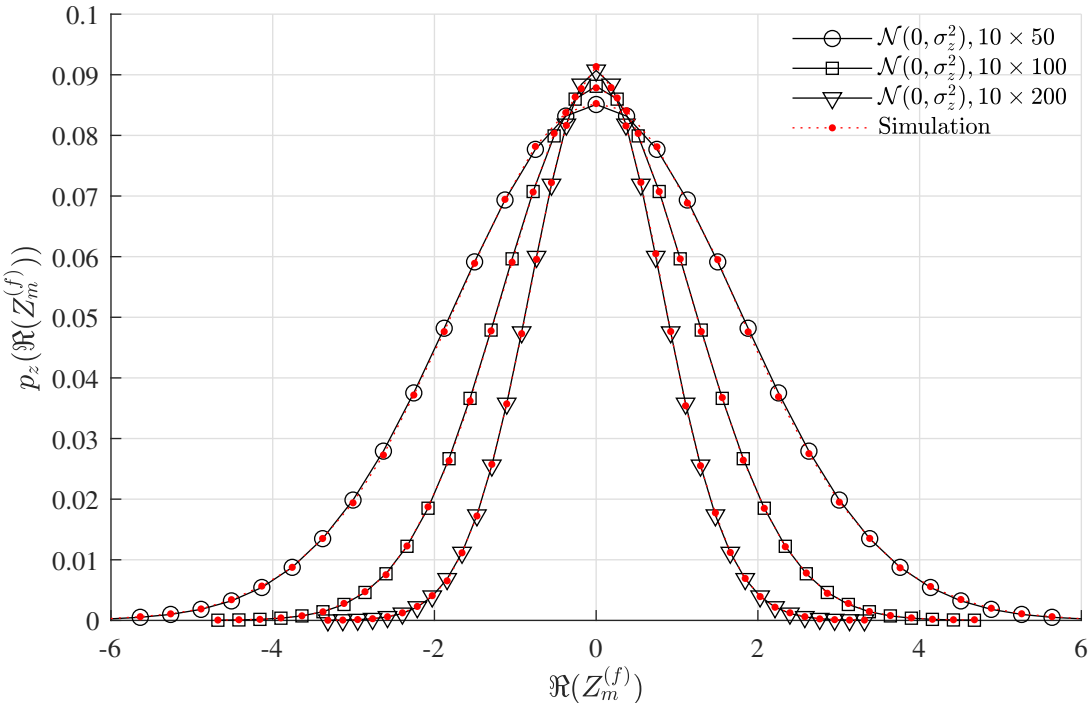

(a) ZF detection.

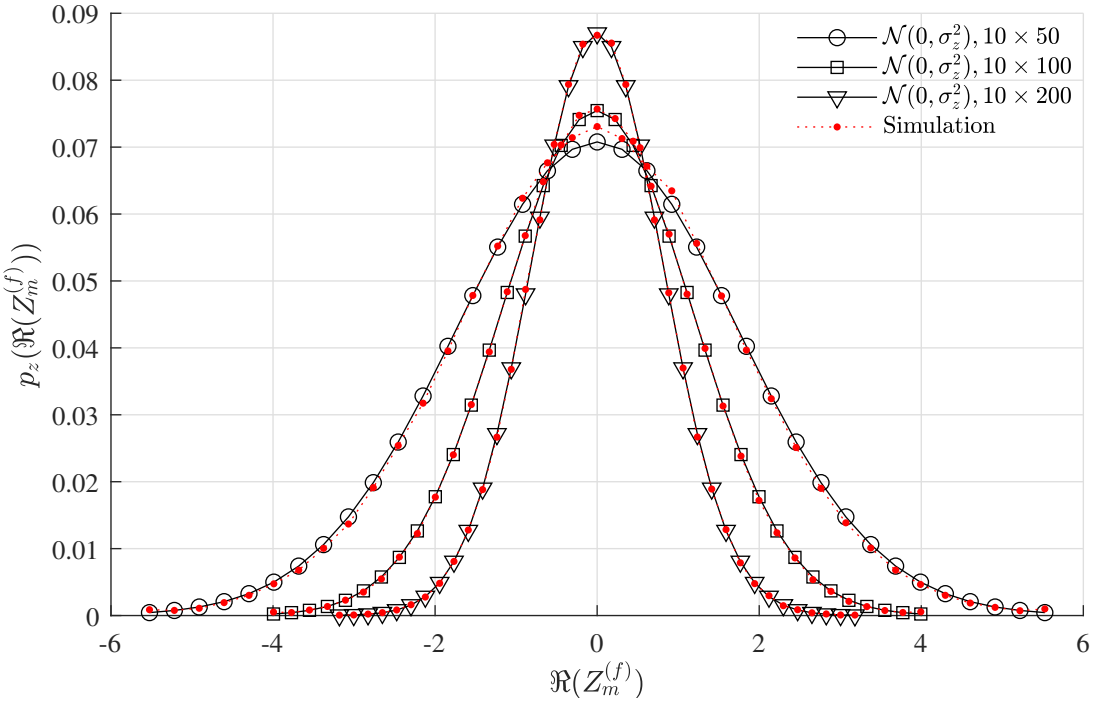

(b) MMSE detection.

Figure D.2: PDF of $\Re(Z_m^{(f)})$ of ZF and MMSE detections.

Bibliography

[1] F. Tariq, M. R. A. Khandaker, K.-K. Wong, M. A. Imran, M. Bennis, and M. Debbah, "A speculative study on 6G," *IEEE Wireless Commun.*, vol. 27, no. 4, pp. 118–125, 2020.

[2] W. Jiang, B. Han, M. A. Habibi, and H. D. Schotten, "The road towards 6G: a comprehensive survey," *IEEE Open J. Commun. Soc.*, vol. 2, pp. 334–366, 2021.

[3] E. G. Larsson, O. Edfors, F. Tufvesson, and T. L. Marzetta, "Massive MIMO for next generation wireless systems," *IEEE Commun. Mag.*, vol. 52, no. 2, pp. 186–195, 2014.

[4] M. A. Albreem, M. Juntti, and S. Shahabuddin, "Massive mimo detection techniques: A survey," *IEEE Commun. Surv. Tut.*, vol. 21, no. 4, pp. 3109–3132, 2019.

[5] A. Chockalingam and B. S. Rajan, *Large MIMO systems*. Cornwall, United Kingdom: Cambridge University, 2014.

[6] K. D. Rao, *Channel Coding Techniques for Wireless Communications*. Forum for interdisciplinary mathematics, Gateway East, Singapore: Springer Nature Singapore, 2nd ed., 2019.

[7] J. Beiranvand and H. Meghdadi, "Analytical performance evaluation of MRC receivers in massive MIMO systems," *IEEE Access*, vol. 6, pp. 53226–53234, 2018.

[8] C. D. Altamirano, J. Minango, H. C. Mora, and C. De Almeida, "BER evaluation of linear detectors in massive MIMO systems under imperfect channel estimation effects," *IEEE Access*, vol. 7, pp. 174482–174494, 2019.

[9] Y. Hama and H. Ochiai, "Performance analysis of matched-filter detector for MIMO spatial multiplexing over rayleigh fading channels with imperfect channel estimation," *IEEE Trans. Commun.*, vol. 67, no. 5, pp. 3220–3233, 2019.

[10] J. Winters, J. Salz, and R. Gitlin, "The capacity of wireless communication systems can be substantially increased by the use of antenna diversity," in *Proc. 1st Int. Conf. Univers. Personal Commun.*, pp. 02.01/1–02.01/5, 1992.

[11] J. Winters, J. Salz, and R. Gitlin, "The impact of antenna diversity on the capacity of wireless communication systems," *IEEE Trans. Commun.*, vol. 42, no. 234, pp. 1740–1751, 1994.

[12] R. Xu and F. Lau, "Performance analysis for MIMO systems using zero forcing detector over Rice fading channel," in *Proc. IEEE Int. Symp. Circuits Syst.*, pp. 4955–4958 Vol. 5, 2005.

[13] H. A. Saleh and W. Hamouda, "Performance of zero-forcing detectors over MIMO flat-correlated Ricean fading channels," *IET Commun.*, vol. 3, pp. 10–16(6), January 2009.

[14] D. Gore, R. Heath, and A. Paulraj, "On performance of the zero forcing receiver in presence of transmit correlation," in *Proc. IEEE Int. Symp. Inf. Theory*, p. 159, 2002.

[15] H.-Y. Fan, *MIMO Detection Schemes for Wireless Communications.* Hong Kong: MPhil. thesis, Dept. Elect. Electron., Hong Kong Univ. Sci. Technol., 2002.

[16] Y. Jiang, M. K. Varanasi, and J. Li, "Performance analysis of ZF and MMSE equalizers for MIMO systems: An in-depth study of the high SNR regime," *IEEE Trans. Inf. Theory*, vol. 57, no. 4, pp. 2008–2026, 2011.

[17] G. Alfano, C.-F. Chiasserini, and A. Nordio, "SINR and multiuser efficiency gap between MIMO linear receivers," *IEEE Trans. Wireless Commun.*, vol. 19, no. 1, pp. 106–119, 2020.

[18] C. Siriteanu, Y. Miyanaga, S. D. Blostein, S. Kuriki, and X. Shi, "MIMO zero-forcing detection analysis for correlated and estimated Rician fading," *IEEE Trans. Veh. Technol.*, vol. 61, no. 7, pp. 3087–3099, 2012.

[19] C. Wang, E. K. Au, R. D. Murch, W. H. Mow, R. S. Cheng, and V. Lau, "On the performance of the MIMO zero-forcing receiver in the presence of channel estimation error," *IEEE Trans. Wireless Commun.*, vol. 6, no. 3, pp. 805–810, 2007.

[20] F. Jiang, C. Li, and Z. Gong, "Accurate analytical BER performance for ZF receivers under imperfect channel in low-SNR region for large receiving antennas," *IEEE Signal Process. Lett.*, vol. 25, no. 8, pp. 1246–1250, 2018.

[21] C. D. Altamirano, J. Minango, H. C. Mora, and C. De Almeida, "BER evaluation of linear detectors in massive mimo systems under imperfect channel estimation effects," *IEEE Access*, vol. 7, pp. 174482–174494, 2019.

[22] J. Lu, K. Letaief, J.-I. Chuang, and M. Liou, "M-PSK and M-QAM BER computation using signal-space concepts," *IEEE Trans. Commun.*, vol. 47, no. 2, pp. 181–184, 1999.

[23] J. G. Proakis, *Digital communications*. New York, USA: McGraw-Hill, 5th ed., 2008.

[24] A. J. Al-Askery, C. C. Tsimenidis, S. Boussakta, and J. A. Chambers, "Performance analysis of coded massive mimo-ofdm systems using effective matrix inversion," *IEEE Trans. Commun.*, vol. 65, no. 12, pp. 5244–5256, 2017.

[25] G. P. Leibo Liu and S. Wei, *Massive MIMO Detection Algorithm and VLSI Architecture*. Beijing, China: Science Press, 2019.

[26] P. Li, D. Paul, R. Narasimhan, and J. Cioffi, "On the distribution of SINR for the MMSE MIMO receiver and performance analysis," *IEEE Trans. Information Theory*, vol. 52, no. 1, pp. 271–286, 2006.

[27] N. Kim, Y. Lee, and H. Park, "Performance analysis of MIMO system with linear MMSE receiver," *IEEE Trans. Wireless Commun.*, vol. 7, no. 11, pp. 4474–4478, 2008.

[28] R. Corvaja and A. G. Armada, "SINR degradation in MIMO-OFDM systems with channel estimation errors and partial phase noise compensation," *IEEE Trans. Commun.*, vol. 58, no. 8, pp. 2199–2203, 2010.

[29] M. R. McKay, I. B. Collings, and A. M. Tulino, "Achievable sum rate of MIMO MMSE receivers: A general analytic framework," *IEEE Trans. Inf. Theory*, vol. 56, no. 1, pp. 396–410, 2010.

[30] E. Eraslan, B. Daneshrad, and C.-Y. Lou, "Performance indicator for MIMO MMSE receivers in the presence of channel estimation error," *IEEE Wireless Commun. Lett.*, vol. 2, no. 2, pp. 211–214, 2013.

[31] H. Fu, S. Roy, and L. Peng, "Asymptotic performance analysis of MMSE receivers in multicell MU-MIMO systems," *IEEE Trans. Veh. Technol.*, vol. 70, no. 9, pp. 9174–9189, 2021.

[32] R. Gallager, "Low-density parity-check codes," *IRE Trans. Inf. Theory*, vol. 8, no. 1, pp. 21–28, 1962.

[33] M. C. Davey and D. MacKay, "Low-density parity check codes over gf(q)," *IEEE Communications Lett.*, vol. 2, no. 6, pp. 165–167, 1998.

[34] C. Berrou, A. Glavieux, and P. Thitimajshima, "Near shannon limit error-correcting coding and decoding: Turbo-codes. 1," in *Proc. IEEE Int. Conf. Commun*, vol. 2, pp. 1064–1070, 1993.

[35] L. Fang, L. Xu, and D. D. Huang, "Low complexity iterative MMSE-PIC detection for medium-size massive MIMO," *IEEE Wireless Commun. Lett.*, vol. 5, no. 1, pp. 108–111, 2016.

[36] M. Zhang and S. Kim, "Evaluation of MMSE-based iterative soft detection schemes for coded massive MIMO system," *IEEE Access*, vol. 7, pp. 10166–10175, 2019.

[37] S. Chan and S. Kim, "Min-sum soft symbol estimation for iterative MMSE detection," *IEEE Access*, vol. 8, pp. 226240–226247, 2020.

[38] I. A. Khoso, X. Zhang, I. A. Khoso, Z. A. Dayo, and X. Dai, "Computationally efficient data detection in massive MIMO wireless systems via semi-iterative method," *IEEE Trans. Veh. Technol.*, vol. 70, no. 10, pp. 10252–10264, 2021.

[39] G. L. Stüber, *Principles of Mobile Communication*. Cham, Switzerland: Springer, 4th ed., 2017.

[40] J. Kiusalaas, *Numerical methods in engineering with MATLAB*. New York, USA: Cambridge university, 2nd ed., 2010.

[41] R. W. Chang, "Synthesis of band-limited orthogonal signals for multichannel data transmission," *Bell Syst. Tech. J.*, vol. 45, no. 10, pp. 1775–1796, 1966.

[42] S. Weinstein and P. Ebert, "Data transmission by frequency-division multiplexing using the discrete fourier transform," *IEEE Trans. Commun. Technol.*, vol. 19, no. 5, pp. 628–634, 1971.

[43] M. S. John G. Proakis and G. Bauch, *Modern communication systems using MATLAB*. S.l.: Cengage Learning, 2013.

[44] J. Leis, *Communication systems principles using MATLAB*. 2018.

[45] M. S. John G. Proakis and G. Bauch, *Contemporary communication systems using MATLAB and Simulink*. Belmont, CA, USA: Thomson–Brooks/Cole, 2nd ed., 2004.

[46] D. P. Travis F. Collins, Robin Getz and A. M. Wyglinski, *Software-defined radio for engineers*. 2018.

[47] B. Sklar, *Digital communications:fundamental and applications*. New Jersey, USA: Prentice-Hall, 2nd ed., 2001.

[48] A. Grami, *Probability, random variables, statistics, and random processes : fundamentals and applications*. NJ, USA: John Wiley & Son, 2019.

[49] A. Papoulis and S. U. Pillai, *Probability, random variables, and stochastic processes*. London: McGraw-Hill, 4th ed., 2002.

[50] S. Yang and L. Hanzo, "Fifty years of mimo detection: The road to large-scale mimos," *IEEE Commun. Surv. Tut.*, vol. 17, no. 4, pp. 1941–1988, 2015.

[51] L. Dai, X. Gao, X. Su, S. Han, C.-L. I, and Z. Wang, "Low-complexity soft-output signal detection based on gauss–seidel method for uplink multiuser large-scale MIMO systems," *IEEE Trans. Veh. Technol.*, vol. 64, no. 10, pp. 4839–4845, 2015.

[52] M. Wu, B. Yin, G. Wang, C. Dick, J. R. Cavallaro, and C. Studer, "Large-scale MIMO detection for 3GPP LTE: algorithms and FPGA implementations," *IEEE J. Sel. Topics Signal Process.*, vol. 8, no. 5, pp. 916–929, 2014.

[53] X. Qin, Z. Yan, and G. He, "A near-optimal detection scheme based on joint steepest descent and jacobi method for uplink massive MIMO systems," *IEEE Commun. Lett.*, vol. 20, no. 2, pp. 276–279, 2016.

[54] G. Liva, W. E. Ryan, and M. Chiani, "Quasi-cyclic generalized ldpc codes with low error floors," *IEEE Trans. Commun.*, vol. 56, no. 1, pp. 49–57, 2008.

[55] T. Richardson and S. Kudekar, "Design of low-density parity check codes for 5G new radio," *IEEE Commun. Mag.*, vol. 56, no. 3, pp. 28–34, 2018.

[56] W. E. Ryan and S. Lin, *Channel Codes: Classical and Modern*. Cambridge University, 2009.

[57] D. H. Morais, *Key 5G Physical Layer Technologies: Enabling Mobile and Fixed Wireless Access*. Cham, Switzerland: Springer, 2020.

[58] 3GPP TS 36.212, *LTE; Evolved Universal Terrestrial Radio Access (E-UTRA); Multiplexing and channel coding*.

[59] D. Chumchewkul and C. Tsimenidis, "Maximal-ratio combining detection in massive multiple-input multiple-output systems with accurate probability distribution function," *IET Electron. Lett.*, vol. 57, no. 9, pp. 381–383, 2021.

[60] D. Chumchewkul and C. Tsimenidis, "Probability of bit error of MRC detection in OFDM-MMIMO systems utilizing gaussian mixture model," in *Proc. Asia Pacific Conf. Commun.*, pp. 220–225, 2022.

[61] C. T. D. Chumchewkul and S. Mumtaz, "Outage probability analysis of MRC detection in OFDM-MMIMO system utilizing incomplete gamma function," in *Proc. IEEE Int. Conf. Commun. (Workshop)*, pp. 1826–1831, 2023.

[62] A. Jeffrey and D. Zwillinger, *Table of integrals, series, and products*. New York, USA: Academic, 6th ed., 2000.

[63] M. K. Simon, *Probability distributions involving Gaussian random variables a handbook for engineers and scientists*. New York, USA: Springer, 2006.

[64] G. R. Iversen, *Calculus*. Thousand Oaks, California: SAGE, 1996.

[65] D. Chumchewkul and C. C. Tsimenidis, "Closed-form bit error probability of ZF detection for OFDM-M-MIMO systems using effective noise PDF," *IEEE Access*, vol. 10, pp. 104384–104397, 2022.

[66] D. Chumchewkul and C. Tsimenidis, "MRC detection for LDPC-OFDM, massive MIMO, NR-5G-based systems utilizing accurate PDF of effective noise and co-channel interference," in *Proc. IEEE Int. Conf. Commun.*, pp. 775–780, 2022.

[67] C. Woodford, *Numerical methods with worked examples : Matlab edition*. Dordrecht ; London: Springer, 2nd ed.. ed., 2012.

[68] 3GPP, "NR; multiplexing and channel coding," *3rd Generation Partnership Project; Technical Specification Group Radio Access Network*.

[69] P. Dharmawansa, N. Rajatheva, and H. Minn, "An exact error probability analysis of OFDM systems with frequency offset," *IEEE Trans. Commun.*, vol. 57, no. 1, pp. 26–31, 2009.

[70] D. Singh and H. D. Joshi, "Performance analysis of SFBC-OFDM system with channel estimation error over generalized fading channels," *Trans. Emerg. Telecommun. Technol.*, vol. 29, no. 3, p. e3293, 2018.

[71] D. Singh and H. D. Joshi, "Error probability analysis of STBC-OFDM systems with CFO and imperfect CSI over generalized fading channels," *AEU - Int. J. Electron. Commun.*, vol. 98, pp. 156–163, 2019.

[72] D. Singh, A. Kumar, H. D. Joshi, M. Magarini, and R. Saxena, "Symbol error rate analysis of OFDM system with CFO over TWDP fading channel," *Wireless Pers. Commun.*, vol. 109, no. 4, pp. 2187–2198, 2019.

[73] J. Conan, "The weight spectra of some short low-rate convolutional codes," *IEEE Transac. Commun.*, vol. 32, no. 9, pp. 1050–1053, 1984.

[74] P. Frenger, P. Orten, and T. Ottosson, "Convolutional codes with optimum distance spectrum," *IEEE Commun. Lett.*, vol. 3, no. 11, pp. 317–319, 1999.

[75] S. Benedetto and G. Montorsi, "Unveiling turbo codes: some results on parallel concatenated coding schemes," *IEEE Trans. Inf. Theory*, vol. 42, no. 2, pp. 409–428, 1996.

[76] S. S. Das and R. Prasad, *OTFS: Orthogonal Time Frequency Space Modulation A Waveform for 6G*. Gistrup Denmark: River, 2021.

[77] L. Rade and B. Westergren, *Mathematics Handbook for Science and Engineering*. Lund, Sweden: Springer, 5th ed., 2004.

[78] B. Yin, M. Wu, J. R. Cavallaro, and C. Studer, "Conjugate gradient-based soft-output detection and precoding in massive MIMO systems," in *Proc. IEEE Global Commun. Conf.*, pp. 3696–3701, 2014.